Stony Brook University

Fabrication, Characterization, and Environmental Impacts of Multifunctional Nanomaterials for Energy Conversion

A Dissertation Presented

by

Xiaohui Peng

to

The Graduate School

in Partial Fulfillment of the

Requirements

for the Degree of

Doctor of Philosophy

in

Chemistry

Stony Brook University

August 2011

Stony Brook University

The Graduate School

Xiaohui Peng

We, the dissertation committee for the above candidate for the

Doctor of Philosophy degree, hereby recommend

acceptance of this dissertation.

Stanislaus S. Wong – Dissertation Advisor
Professor, Department of Chemistry

John Parise – Chairperson of Defense
Professor, Department of Chemistry

Joseph W. Lauher – Third Member
Professor, Department of Chemistry

Michael Dudley – Outside Member
Professor and Chair, Department of Materials Science and Engineering

This dissertation is accepted by the Graduate School

Lawrence Martin
Dean of the Graduate School

Abstract of the Dissertation

Fabrication, Characterization, and Environmental Impacts of

Multifunctional Nanomaterials for Energy Conversion

by

Xiaohui Peng

Doctor of Philosophy

in

Chemistry

Stony Brook University

2011

Solar energy has been considered to be an alternative energy source to meet the exponential demand for renewable energy. To date, the use of nanomaterials has provided alternative and promising ways to improve solar device performance. In particular, nanoscale heterostructures hold great promise in the improvement of energy conversion efficiency, due to their advantages of possessing diverse functionalities in a single structure and their unique properties arising from strong interfacial interaction. Moreover, the safety risk associated with nanomaterials needs to be comprehensively assessed prior to their widespread use. In this dissertation, we have attempted to develop facile and reliable routes to two different categories of nanoscale heterostructures, namely (a) zero-dimensional (0D) – one-dimensional (1D) heterostructures and (b) 1D coaxial heterostructures, and to study their intriguing properties in applications associated with the energy conversion process. Specifically, the first part of the dissertation, including Chapter 2 and 3, will demonstrate the rational design of heterostructures consisting of carbon nanotubes and one or more types of nanocrystals, with precise control over the location and coverage of nanocrystals on the nanotube surface. The investigation of their photophysical properties reveals insight into the dynamics of charge carriers in the heterostructures. Moreover, the fabrication of SnO_2/TiO_2 1D radial heterostructures by coaxial

electrospinning technique will be discussed as an example of creating discrete multifunctional 1D heterostructures. The applicability of such inorganic radial heterostructures in energy conversion applications is manifested by their photocatalytic activity in the degradation of organic dyes (Chapter 4). Finally, the morphology effect upon the toxicity of ZnO nanostructures towards marine diatoms has been studied, revealing the impact of nanomaterials on the environment (Chapter 5). Overall, these studies have provided valuable insight into the fabrication and utilization of nanostructures to resolve problems with global significance as well as to provide useful implications for evaluating the potential environmental risks of nanomaterials during the course of their life cycle.

Table of Contents

List of Abbreviations

0D	zero-dimensional
1D	one-dimensional
2D	two-dimensional
AET	aminoethanethiol
ALD	atomic layer deposition
AM 1.5	1.5 atmosphere thickness
ANOVA	analysis of variance
BET	Brunauer-Emmett-Teller
C_s	solubility
CB	conduction band
CBE	chemical beam epitaxy
CdSe	cadmium selenide
CdTe	cadmium telluride
CNTs	carbon nanotubes
CT	charge transfer
CVD	chemical vapor deposition
DCC	dicyclohexylcarbodiimide
DLS	dynamic light scattering
DMF	dimethylformamide
DSSCs	dye-sensitized solar cells
DWNTs	double-walled carbon nanotubes

E_g	band gap
EC_0	concentration leading to depression of cell division rates by 100%
EC_{50}	concentration leading to depression of cell division rates by 50%
EDC	*N*-(3-dimethylaminopropyl)-*N*'-ethylcarbodiimide
FESEM	field emission scanning electron microscopy
GFAAS	graphite furnace atomic absorption spectroscopy
HDA	hexadecylamine
HOMO	highest occupied molecular orbital
HRTEM	high resolution transmission electron microscopy
IPCE	incident photon to photocurrent efficiency
ITO	indium tin oxide
J_{SC}	short circuit current density
LS	large spherical nanoparticles
LUMO	lowest unoccupied molecular orbital
MO	molecular orbital
MWNTs	multi-walled carbon nanotubes
NHE	normal hydrogen electrode
NIR	near infrared
NN	nanoneedle
NP	nanoparticle
NR	nanorod
NW	nanowire
OA	oleic acid

OPV	organic photovoltaic
P25	titanium dioxide produced by Degussa
P3HT	poly (3-hexylthiophene)
PL	photoluminescence
PV	photovoltaic
PVP	poly (vinylpyrrolidone)
RET	resonance energy transfer
RhB	rhodamine B
SEM	scanning electron microscopy
SILAR	successive ionic layer adsorption and reaction
SS	small spherical nanoparticle
TBP	tributylphosphine
TCSPC	time-correlated single-photon counting
TDPA	tetradecylphosphonic acid
TEM	transmission electron microscopy
TGA	thermogravimetric analysis
TOP	tri-n-octylphosphine
TOPO	tri-n-octylphosphine oxide
TRPL	time-resolved photoluminescence
TW	terawatt
V_{OC}	open-circuit voltage
VB	valence band
VLS	vapor-liquid-solid

List of Figures

List of Tables

Acknowledgments

First, I would like to thank my advisor, Professor Stanislaus S. Wong for providing me with the valuable opportunities to participate in various projects, learn a number of different skills and collaborate with many outstanding scientists. I sincerely appreciate my committees: Professor John Parise and Professor Joseph Lauher, for their insightful advice, encouragement and support towards the successful completion of my studies. In addition, I would like to thank Professor Michael Dudley for serving on my committee as an outside member. His kindness is highly appreciated. I am also grateful to my former Chair, Professor Michelle Millar, for her encouragement and useful suggestion on my research work.

I am also immensely grateful to my collaborators, Dr. Matthew Sfeir and Professor Nicholas Fisher, for not only all the help they provided on my projects, but also their influence on me for being a great scientist. Many thanks to the members in Wong's group: Jingyi, Hongjun, Fen, Alex, Jon, Amanda, Chris, Yan, David, Maurizio, Caroline, and all the undergraduats, for all the useful discussions, support and entertainment they have given me during my Ph.D. study.

In addition, I also acknowledge all the technical supports provided by Dr. Eli Sutter (Brookhaven National Laboratory), Dr. Susan van Horn (CMIC, Stony Brook University), Dr. Shelagh Palma (Stony Brook University). In particular, I would like to appreciate Dr. James Quinn not only for his assistance with scanning electron microscopy, but also for being a nice friend giving me advice on my research and life.

Lastly, I am really grateful to all the friends I have met at Stony Brook, for all the happiness they have brought into my life. Special thanks to Jing for all his understanding and support along my way towards today's success. And I thank my parents for their unconditional love and support.

List of Publications

1. **Peng, X.H.**; Santulli, A.C.; Sutter, E.; and Wong, S.S. "Fabrication and Enhanced Photocatalytic Activity of Inorganic Core-shell Nanofibers Produced by Coaxial Electrospinning", *Chem. Sci.* submitted
2. **Peng, X.H.**; Misewich, J.A.; Wong, S.S.; and Sfeir, M.Y. "Efficient Charge Separation in Multidimensional Nanohybrids", *Nano Lett*. submitted.
3. Patete, J.M.; **Peng, X.H.**; Serafin, J.M.; and Wong, S.S. "Quantitatively Probing Means of Controlling Nanoparticle Assembly on Surfaces", *Langmuir* **2011**, *27*, 5792-5805.
4. **Peng, X.H.**; Fisher, N.S.; and Wong, S.S. "Relating the Morphology of ZnO Nanostructures on Marine Algal Toxicity", *Aquat. Toxicol.* **2011**, *102*, 186-196.
5. Patete, J.M.; **Peng, X.H.**; Koenigsmann, C.; Xu, Y.; Karn, B.; and Wong, S.S. "Viable Methodologies for the Synthesis of High-Quality Nanostructures", *Green Chem*. (invited review) **2011**, *13*, 482-519.
6. **Peng, X.H.**; Sfeir, M.Y.; Zhang, F.; Misewich, J.A.; and Wong, S.S. "Covalent Synthesis and Optical Characterization of Double-Walled Carbon Nanotube-Nanocrystal Heterostructures", *J. Phys. Chem. C* **2010**, *114*, 8766–8773.
7. **Peng, X.H.**; Chen, J.Y.; Misewich, J.A. and Wong, S.S. "Carbon Nanotube-Nanocrystal Heterostructures", *Chem. Soc. Rev*. (invited review and inside cover) **2009**, *38*, 1076-1098.
8. **Peng, X.H.** and Wong, S.S. "Controlling Nanocrystal Density and Location on Carbon Nanotube Templates", *Chem. Mater*. **2009**, *21*, 682–694.
9. **Peng, X.H.** and Wong, S.S. "Functional Covalent Chemistry of Carbon Nanotube Surface", *Adv. Mater*. (invited review) **2009**, *21*, 625–642.

Chapter 1 Introduction

1.1 Global Energy Issue and the Applications of Nanostructures in Energy Conversion

Ensuring a reliable energy supply has arguably become one of the most important problems facing humanity. The exponential demand for energy has been exacerbated by dwindling fossil fuel resources and record-high oil prices because of explosive global population growth and rapid economic development. The energy crisis has been further complicated by major concerns about global warming from greenhouse gas emissions emanating from indiscriminate fossil fuel consumption. Therefore, obtaining alternatives sources of clean energy is imperative. One such strategy to meet our energy needs involves the use of solar energy conversion. The sun continuously delivers to the earth ~120,000 TW of energy, which dramatically exceeds our current rate of energy needs (13 TW).[1] This implies that covering only 0.1% of the earth's surface with solar cells of 10% efficiency would satisfy our current energy demands.[2] The major barriers for the large-scale use of solar energy are the high cost and inadequate efficiencies of current solar devices.

Solar cells, also known as photovoltaic (PV) cells, can convert sunlight directly into electricity. PV gets its name from the process of converting light (photons) into electricity (voltage), which is called the *PV effect*. The PV effect was discovered in 1954, when scientists at Bell Labs discovered that silicon created an electric charge when exposed to sunlight. Soon solar cells were being used to power space satellites and smaller items such as calculators and watches. Today, thousands of people power their homes and businesses with individual solar PV systems.

In 2006, SunPower announced that it would commercialize silicon solar cells with power conversion efficiencies of 22%, approaching the theoretical Shockley-Queisser limiting efficiency of 33%. These *first generation* devices are generally the most efficient. However, they suffer from the high cost of manufacturing and installation. *Second generation* devices, consisting of polycrystalline semiconducting thin films (e.g. CdTe and $CuIn_xGa_{(1-x)}Se_2$), have been under intense development during the 1990s and 2000s. They can potentially bring down the price significantly, but their efficiency needs to be enhanced in order to render them practically viable. Currently, the focus is on *third generation* devices, such as dye-sensitized solar cells (DSSCs)[3, 4], bulk heterojunction cells,[5, 6] and hybrid cells, which aim to couple the high electrical performance of the first generation devices with the low production costs of those of the second generation.

In recent years, nanomaterials have emerged as the new building blocks applicable in the development of photovoltaic devices. Compared with bulk materials, low-dimensional nanoscale materials, with their large surface areas and possible quantum confinement effect, exhibit distinctive electronic, optical, chemical, and thermal properties. Meanwhile, a natural progression from single-component nanomaterials has been made towards the synthesis and design of more complex, multi-component nanostructures. In particular, nanoscale heterostructures, consisting of two or more chemically distinct components, have demonstrated great potential for revolutionizing nanomaterials research by providing a means to incorporate diverse functionalities within a single nanostructure and, moreover, to generate novel properties which are nonexistent in the individual component but arise from the strong interfacial interactions at the nanoscale junction. To this end, the fabrication of high-quality nanostructures with desirable properties via effective, reliable approaches, as well as a fundamental

understanding of their electronic and optical properties are essential to promote a breakthrough in the development of sources of renewable energy. Meanwhile, with the increasing expansion associated with the academic investigation and commercial manufacturing of nanomaterials, there is a growing concern about the impact of nanomaterials on the environment as well as the health of human beings. A full risk assessment of nanoscale materials is crucial before their widespread use in energy conversion applications.

In this dissertation, we have attempted to develop facile and reliable routes in order to fabricate two different categories of nanoscale heterostructures, namely (a) zero-dimensional (0D) – one-dimensional (1D) heterostructures and (b) 1D coaxial heterostructures, and study their intriguing properties in applications associated with the energy conversion process. Specifically, the rational design of heterostructures consisting of carbon nanotubes and one or more types of nanocrystals, with precise control over the location and coverage of nanocrystals on the nanotube surface, has been demonstrated (Chapter 2), shedding light on the possibility of the manipulation of 0D –1D heterostructures via a facile and simple route. Furthermore, we have thoroughly investigated photophysical properties of carbon nanotube-quantum dot 0D –1D heterostructures (Chapter 3), which not only provides a better understanding of the dynamic of charge carriers within heterostructures, but also provides valuable guidance for the construction of high-efficiency solar devices. We also pioneered the use of coaxial electrospinning technique in development of inorganic 1D radial heterostructures and further demonstrated the applicability of such inorganic radial heterostructures in energy conversion applications (Chapter 4). Lastly, the environmental impact of nanostructures has been assessed and this has been manifested in the morphology effect on the toxicity of ZnO nanostructures towards marine diatoms (Chapter 5). Overall, these studies have provided valuable insight into the fabrication and utilization of

nanostructures to resolve problems with global significance, as well as useful implications for evaluating the potential environmental risk of nanomaterials during the course of their life cycle.

1.2 Zero-dimensional (0D) Nanostructures: Quantum Dots

Materials that are nanoscale in three dimensions are termed "zero-dimensional" (0D) nanomaterials. In particular, semiconductor materials will exhibit quantization effects when the charge carriers of these materials are confined within very small regions of space by potential barriers along all three spatial dimensions. It results in an increasing bandgap accompanied by the quantization of the energy levels to discrete values. For most semiconductors, this observation normally occurs when the particle size is reduced to a few nanometers. Colloidal semiconductor nanocrystals, which experience quantum confinement, are also termed "quantum dots" (QDs). They were discovered at the beginning of the 1980s by Alexei Ekimov in a glass matrix and by Louis E. Brus in colloidal solutions.[7] Afterwards, the size-dependent optical properties of QDs have been the focus of significant research over the past three decades.

1.2.1 *Synthesis of quantum dots*

The synthesis of nanosized crystals usually takes place in solution-based reactions involving the process of precipitation of a solid phase from solution. The separation of nucleation and growth of nanocrystals has been found to be necessary to ensure the synthesis of high-quality monodisperse nanocrystals. The rapid addition of the reagents is usually required to increase in the concentration of a supersaturated precursor solution above the nucleation threshold, therefore leading to a short nucleation burst. Then the system enters the growth stage as the concentration of precursor is below the threshold wherein new nuclei cannot be formed

(Figure 1.1A-B). At any given monomer concentration, there is a critical size (Figure 1.1C). At the initial growth stage, the smaller particles grow more rapidly than the larger ones because the free energy driving force is larger for smaller particles when the particle size is slightly larger than the critical size. This phenomenon is called "focusing" of size distributions.[8] When the monomer concentration is depleted due to growth, the critical size becomes larger than the average size present. Therefore, the system enters into a second, distinctive growth stage called Ostwald ripening. In this process, smaller QD species with a high surface energy thermodynamically tend to dissolve faster than the bigger ones, and the dissolved materials are re-deposited onto the larger QDs. As such, the precise control over the size of QDs depends critically upon the kinetics of the initial nucleation and subsequent growth.

The synthesis of quantum dots via colloidal methods is based upon a three-component system composed of precursors, organic surfactants, and solvents. The "green" approach for synthesizing high-quality QDs has been well developed by Peng's group,[9-14] wherein metal oxides (e.g. cadmium oxide, CdO) are employed as cationic precursors in order to substitute the conventional toxic precursor reagents (e.g. dimethyl cadmium, $Cd(CH_3)_2$) . In a typical experiment, an aliquot of solution containing chalcogenide precursors stabilized by organic ligands is rapidly injected into the cationic precursor solution containing surfactants (e.g. phosphonic acid, phosphine oxide, fatty acid and/or amine) at a temperature of 200 – 330°C in order to induce nucleation, followed by a growth phase at a relatively low temperature. Alivisatos and co-workers have investigated this reaction mechanism, suggesting that the cleavage of phosphorus chalcogenide double bond (TOP = E, E = Se, Te, S) is activated by the nucleophilic attack of either phosphonate or oleate on a (TOP=E)-Cd complex, thereby generating the initial Cd-E bond. The surfactants such as phosphonic acid and fatty acid have

been found to be responsible for the cleavage of the phosphorus chalcogenide double bond in addition to the binding to the nanocrystal surface. Specifically, trialkylphosphine chalcogenides deoxygenate the alkylphosphonate or alkylcarboxylate surfactants, liberating the chalcogen atom, accompanied by the generation of trialkylphosphine oxide and anhydride products of either oleic or phosphonic acid.[15, 16]

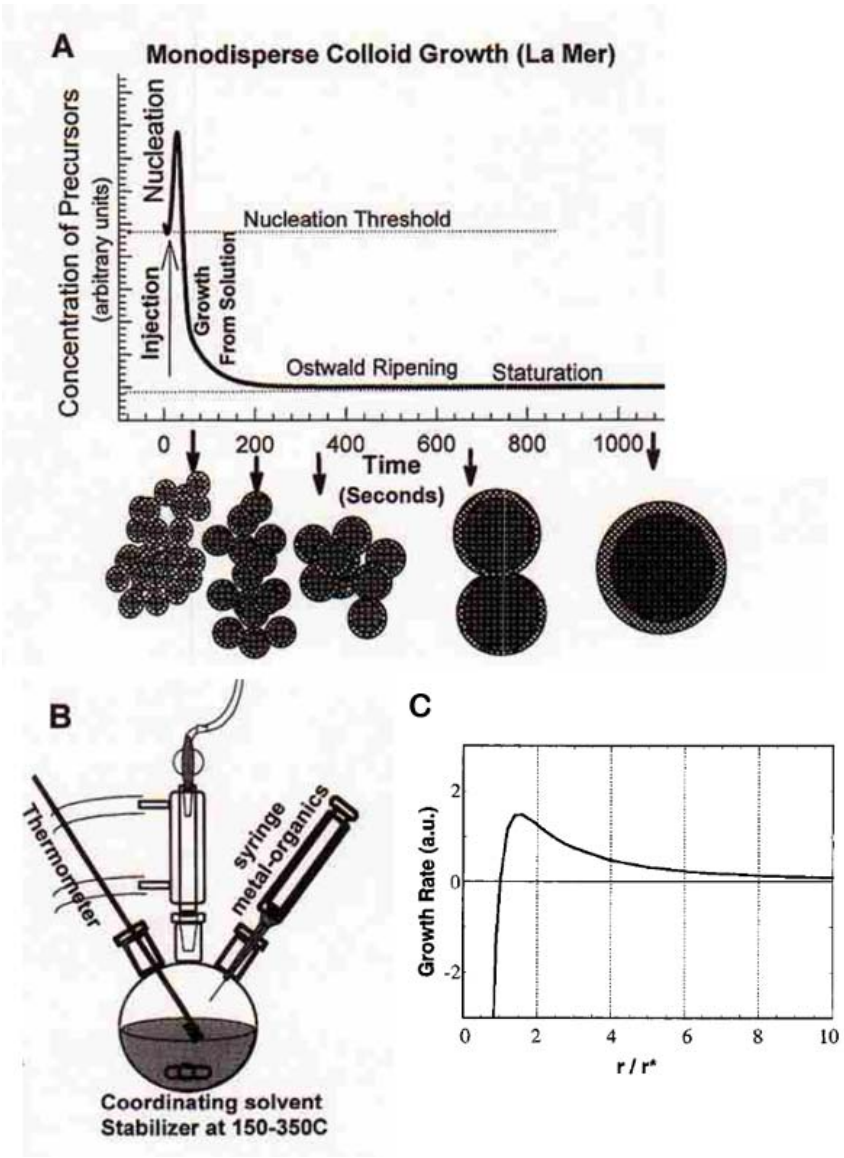

Figure 1.1: Schematic and the model for synthesis of quantum dots. (A) Cartoon depicting the stages of nucleation and growth for the preparation of monodisperse QDs in the framework of the La Mer model. The addition of reagents induced the nucleation burst, followed by a slower controlled growth on the existing nuclei. (B) Representation of the simple synthetic experimental setup employed in the preparation of monodisperse QD samples. (A-B) Reproduced from Murray *et al. Annu. Rev. Mater. Sci*. **2000**, 30, 545-610.[17] (C) Variation of the growth rate versus size, according to the model of Sugimoto. r is the radius of the nanocrystals and r^* is the critical radius for which the solubility of the nanocrystal is exactly the concentration of the monomers in solution (zero growth rate). Reproduced from Peng *et al. J. Am. Chem. Soc*. **1998**, 120, 5343-4344.[8]

1.2.2 *Optical properties of quantum dots and related characterization techniques*

With the absorption of a photon with energy greater than the band gap energy (E_g), the excitation of an electron leaves a hole in the valence band. The lowest energy state of an electrostatically bound electron-hole pair is known as an exciton. Relaxation of the excited electron back to the valence band annihilates the exciton, accompanied by the emission of a photon, a process known as radiative recombination. The exciton has a finite size within the crystal defined by the Bohr exciton diameter, which can vary from 1 nm to more than 100 nm depending on the material.[18] If the size of a semiconductor nanocrystal is smaller than the Bohr exciton diameter, the charge carriers become strongly spatially confined, therefore resulting in discrete energy levels. As a result, the optical and electronic properties of nanocrystals become size-dependent. For semiconductor nanocrystals in the quantum confinement regime, the effective band gap, $E_{g,eff}(R)$, is given by

$$E_{g,eff}(R) = E_g + \frac{\hbar^2 \pi^2}{2R^2}\left(\frac{1}{m_e} + \frac{1}{m_h}\right) - \frac{1.8e^2}{\varepsilon R} \qquad (1.1)$$

where E_g is the bulk band gap, m_e and m_h are the effective masses of the electron and hole, and ε is either the bulk optical dielectric constant or relative permittivity.[19]

Even though the quantum efficiency for radiative recombination of QDs can approach unity due to the strong overlap between the electron and hole wave functions in the confined structure as compared with bulk semiconductors, there are a number of non-radiative relaxation pathways influencing the quantum efficiency of QDs, including hot-carrier relaxation, trapping processes, charge carrier transfer, and carrier-carrier interaction. Figure 1.2 illustrates the major relaxation pathways for charge carriers formed upon illumination with energies above the band

gap energy. The first step of relaxation should be electron relaxation in the conduction band and hole relaxation in the valence band, which usually occurs rapidly on the time scale of hundreds of femtoseconds or several picoseconds.[20] Once charge carriers have relaxed to the lowest-energy states, they can recombine radiatively to emit strong band-edge luminescence if there are no other competing non-radiative pathways. This process should be on the order of nanoseconds or longer.[19] If there are trap states with energies within the band gap, the charge carriers are more likely to be trapped by the trap states due to the faster kinetics of the trapping process itself (~picoseconds).[21, 22] Recombination of trapped charge carriers can give rise to trapping emission, which is red shifted with respect to band-edge emission. Alternatively, the extra charge carriers residing on the QDs can trigger another non-radiative process, called Auger recombination, wherein the energy released by the recombination of the second electron-hole pair promotes this extra charge carrier to a high energy level. In the case where the QDs are connected with another charge-carrier acceptor, two other external non-radiative de-excitation processes can occur, namely (a) resonance energy transfer (RET) of both charge carriers via a near-field electromagnetic interaction and (b) charge transfer (CT) involving one of the charge carriers. Both processes are highly dependent upon the separation between QDs and acceptors.

A number of state-of-the-art spectroscopies with high spatial and temporal resolution have been developed and utilized in order to study the photophysical properties of semiconductor materials. In particular, the time-resolved photoluminescence (TRPL) technique is a common method used to measure the dynamics of fluorescence from photoexcited QDs. Most experiments excite the sample with a pulsed laser source, and subsequently detect the photoluminescence with either a photodiode or photomultiplier tube (PMT), set up for single-photon counting. Among a wide variety of experimental configurations, the time-correlated

single photon counting (TCSPC) technique possesses the advantages of a short acquisition time, high sensitivity, high accuracy, and high time resolution, which can be as low as 25 ps. This technique is based on the fact that for low intensity level, high repetition rate signals, the light intensity is usually so low that the probability of detecting one photon in one signal period is much less than one. When a photon is detected, the time of the corresponding detector pulse is recorded. Afterwards, the histogram of detection time derived from many collection events can be generated, thereby reconstructing the waveform of the photoluminescence decay of the sample. In a simplified classic TCSPC set up, the laser pulse is split into two beams with a beam splitter. The first beam triggers a time-amplitude converter (TAC) to start ramping up a voltage. The second beam excites photoluminescence from the sample. The photoluminescence is passed through a long pass filter and monochromator onto a PMT. The first emitted photon detected by the PMT sends a stop signal to the TAC. The output signal generated from the TAC is proportional to the time elapsed between the start and the stop pulse, which is then amplified, converted to digital signal by analog-to-digital converter (ADC), and ultimately stored in memory. As such, the reconstructed waveform based on memory reflects the dynamics of the excited state associated with the samples.

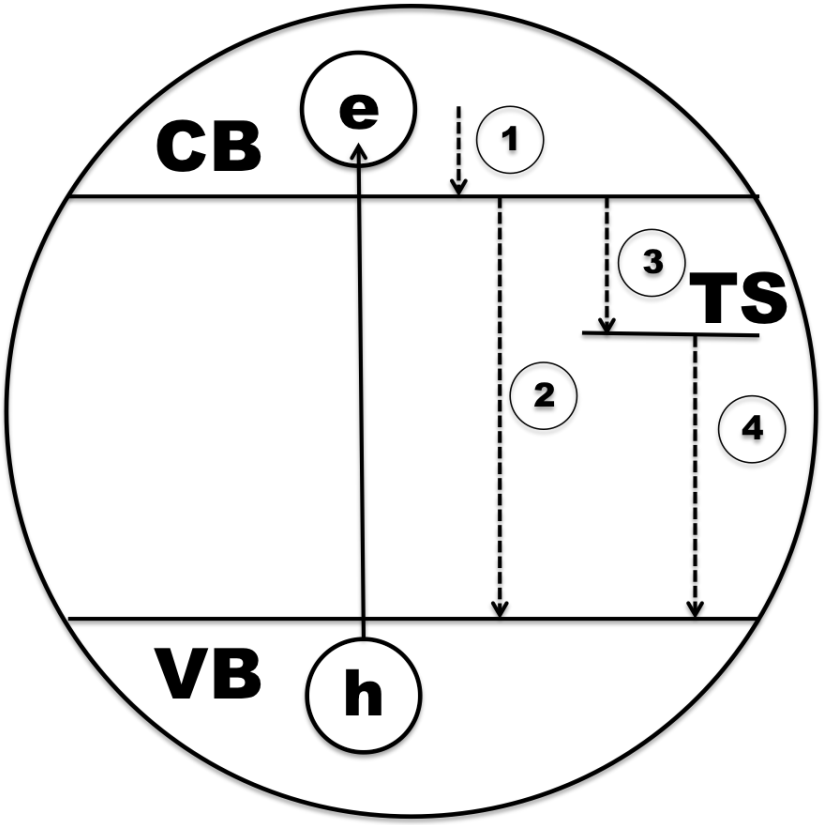

Figure 1.2: Schematic illustration of charge carrier relaxation in semiconductor nanocrystals. The solid line with upward arrows indicates an excitation process and the dashed lines with downward arrows indicate different relaxation processes: (1) electronic relaxation within the conduction band (CB), (2) band-edge electron-hole recombination, (3) trapping into trap states (TS), and (4) trapped electron-hole recombination.

1.2.3 *Surface modification*

Since the atoms on the surface of a crystal facet are incompletely bonded within the crystal lattice, it often leaves one or more "dangling orbitals" on each atom pointing outwards from the crystal. The energy of surface states formed by these unpassivated orbitals may lie within the band gap of the semiconductor, thereby giving rise to non-radiative pathways for the recombination of electrons and holes, which could be detrimental to the overall quantum efficiency. Because of the high surface-to-volume ratio inherent to nanocrystals, surface ligands have a strong influence on physical properties of QDs including photophysics[23] and charge transport.[24] Hence, proper surface chemistry is considered key to generate a viable QD-based solar device or other optoelectronic device. A number of surface ligands have been tried and their corresponding properties are summarized in Figure 1.3.[25]

The most common surface ligands are based on organic hydrocarbon molecules with anchoring end groups (e.g. alkyl phosphine oxides, alkyl phosphonic acids, alkyl phosphines, fatty acids, and amines). These molecules all contain metal coordinating groups as well as solvophilic groups. According to the molecular orbital (MO) diagrams, in the absence of a ligand, an electron-poor Cd^{2+} surface site on a QD forms an electron-trapping surface state whose energy lies between the highest occupied molecular orbital (HOMO) and lowest unoccupied molecular orbital (LUMO) of CdSe QDs.[26] Since the participating orbitals of Cd^{2+} have mostly 5s character, they interact most strongly with *σ-donating* ligands to form bonding and antibonding MOs. The relative energies of these MOs depend on the strength of the Cd^{2+}-ligand interaction, which in turn depends on the *σ-donating* ability of the ligand as given by its electronegativity and basicity. A strong *σ-donating* ligand can effectively passivate surface sites

by removing an electron-trapping mid-gap state, whereas a weak *σ-donating* ligand may achieve weak passivation. Most of the organic ligands on the surface of the as-prepared QDs are strong σ-*donating* ligands, such as trioctylphosphine oxide (TOPO) or hexadecylamine (HDA). Therefore, the as-prepared QDs generally exhibit excellent quantum yield with a high degree of surface passivation.

However, most organic ligands act as bulky insulating barriers, hindering charge transport. A simple exchange of the original bulky ligands with smaller molecules is a widely used approach for improving charge transport. The ligand exchange procedure typically involves exposure of colloidal QDs to a large excess of competing ligands. In order to achieve complete exchange of the original surface ligands, the procedure can be prolonged up to a few days, repeated multiple times, or even accelerated by gentle heating. One of the most common ligands used to modify nanocrystal surfaces are thiols, which exhibit a high affinity with metal atoms in II-VI semiconductors as well as a great flexibility in terms of ligand length and chemical functionality. Depending upon the size and functional groups present, thiol ligands can either stabilize the excited charge so as to increase the quantum yield or withdraw excited electrons or holes, therefore doing the reverse and quenching the QDs.[27] In addition, it has been found that thiol ligands at low concentrations can passivate existing electron trap states of QDs, accompanied by enhancement of the photoluminescence. However, a high concentration of thiol ligands can lead to a decrease in QD photoluminescence as a result of the formation of hole trap states because of the presence of two non-bonding electron pairs of the sulfur atom associated with the thiol group.[21, 28]

Apart from surface ligands, the application of an inorganic shell onto the QD core is another viable approach towards passivating the surface of QDs. That is, when the band gap of

the shell materials is wider than that of core, the charge carriers can be confined to the nanocrystal core. As such, surface defect states will have a diminished impact on the fluorescence efficiency, and the optical properties of the nanocrystal core will be less likely affected by environmental factors, such as the presence of either oxygen or water molecules. The first published prototype system demonstrating core-shell nanocrystal structures was CdSe/ZnS. The ZnS shell significantly improved the amount of fluorescence QY as well as stability against photobleaching.[29] In addition to appropriate band alignment, obtaining a decent crystallinity of the shell material as well as minimizing any lattice mismatch between shell and core materials play key roles in optimizing optical properties. As another factor, the strain induced by the growth of shells and the formation of defect states at the core/shell interface or within shells will essentially undermine the amount of fluorescence QY.[30]

Ligand type	Molecular structure	Interparticle spacing	Functions, characteristics, typical examples
Molecules with single head group and a long hydrocarbon chain	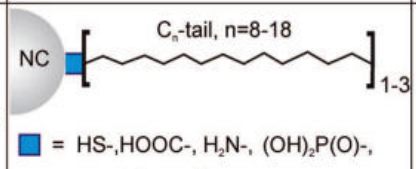	>1.5 nm	• Most common ligands used for NC synthesis • Form stable colloidal solutions • Hydrophobic surface • Form highly insulating NC solids, $\sigma \sim 10^{-12}$-10^{-9} S cm^{-1}
Short-chain molecules with single head group	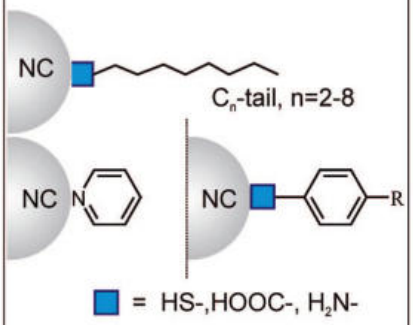	0.3-1 nm	• Treatment of NC solids or ligand-exchange in solutions • Decreased colloidal stability • Improved electronic transport compared to long-chain ligands • Reported detectivity of $\sim 10^{12}$-10^{13} Jones in photodetectors on PbS NCs caped with butylamine[270] • Conductivities of up to 10^{-1} S cm^{-1} in arrays of metallic NCs[267]
Cross-linking molecules with two end groups	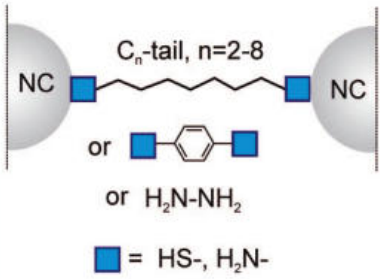	0.3-1 nm	• Mainly prepared by treating NC solids • μ up to 2 cm^2 V^{-1} s^{-1} in arrays of PbSe NCs treated with N_2H_4[23] • μ~10^{-2} cm^2 V^{-1} s^{-1} in arrays of CdSe NCs treated with 1,4-phenylenediame[185] • Solar cells based on PbS and PbSe NC solids showed power conversion efficiencies of up to 2.1%[253,271,272]
Metal chalcogenide complexes	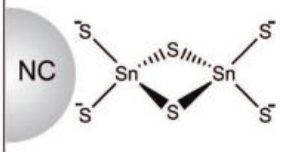	≥ 0.5 nm	• Prepared via solution phase ligand-exchange • Complete removal of original organic ligands • Hydrophilic surface • High conductivities of ~200 S cm^{-1} in Au-$Sn_2S_6^{4-}$NC solids[273]

Figure 1.3: Different types of surface ligands used in nanocrystals. Reproduced from Talapin *et al. Chem. Rev.* 2010, 110, 389-458.[25]

1.2.4 *Quantum dot-based solar cells*

QD-based solar cells have attracted a lot of attention recently owing to the advantageous properties of QDs including (i) the higher absorption of a QD coating than a single molecular layer of organic dye, (ii) a greater stability of QDs as compared with conventional organic dyes, and (iii) a highly tunable optical absorption capability over a wide wavelength range, which could be highly matched to the full region of the solar spectrum. Moreover, the possibility of multiple exciton generation in some of QDs allows for potential quantum efficiency higher than 100%.[31]

The efficiency of QD-based solar cells has been increased to 3.6% using an elegantly simple Schottky junction configuration, wherein the QDs are deposited onto an indium tin oxide (ITO) substrate followed by evaporation of a top metal contact as the negative electrode. A remarkable short-circuit photocurrent density (J_{SC}) of 24.5 mA cm^{-2} has been achieved when PbSe QDs were used, a result that can be ascribed to the strong absorption of PbSe in the infrared region.[32] Further significant progress on QD-based solar cells has been achieved by sensitizing a nanoporous TiO_2 electrode with a layer of QDs. In such a configuration, upon light absorption, the photogenerated electrons are injected from QDs into a TiO_2 electrode, while the holes can be transported via a suitable electrolyte to the counter electrode. The direction of the current flow is determined by relative energy levels of the semiconductors and the oxides, rather than band bending as in the Schottky junction-based configuration.

Either chemical bath deposition or linker-assisted self-assembly has been used to prepare QDs onto TiO_2 in order to achieve greater contact between QDs and oxides, while post-treatments such as the deposition of a semiconductor shell have been applied in order to greatly prevent serious recombination between electrons and holes at the QD/electrolyte interface. 3.2%

of photon conversion efficiency in this configuration has been attained.[33] However, it is worth mentioning that even though optimization of the oxide coverage with QDs can yield high optical absorption, an increase in the thickness of QDs beyond more than one monolayer may inherently undermine the overall efficiency due to possible attenuation of charge transfer. Therefore, such configurations usually experience low photocurrent.

1.3 One-dimensional (1D) Nanostructures: Carbon Nanotubes (CNTs)

Materials that are nanoscale in two dimensions are termed "one-dimensional" (1D) nanomaterials and include nanowires, nanotubes, nanobelts, and nanoribbons. 1D nanomaterials have attracted considerable interest in the scientific community due to their advantageous properties. For example, the large surface area-to-volume ratio of 1D nanostructures allows for their distinctive structural and chemical behavior as well as great chemical reactivity. In addition, their large aspect ratio is favorable for their uses in a number of technological applications. For instance, 1D structures are recommended as ideal materials for interconnects and as functional building blocks in fabricating nanoscale electronic, optoelectronic, and electrochemical devices.[34] Furthermore, a number of studies have been conducted to improve the processability and efficiency of solar devices by utilizing 1D nanostructures.[6, 35, 36] In particular, carbon nanotubes (CNTs) have been widely studied since their discovery in 1991.[37] Due to their unique electronic and chemical properties, they are considered as attractive candidates for a number of diverse photochemical and electronic applications, ranging from photovoltaic devices to field effect transistors.

1.3.1 *Chemical functionalization of CNTs*

However, there still is a huge gulf between the theoretical potential and practical reality of using pristine nanotubes in applications conducted on a widespread scale. First, strong van der Waals interaction among pristine nanotubes results in their bundling and aggregation. Second, pristine nanotubes are hardly soluble or dispersible in aqueous media as well as organic solvents. Third, as-prepared nanotubes tend to be contaminated with a number of impurities such as metal catalyst particles, amorphous carbon, and other carbonaceous species. Hence, given these challenges with pristine tubes, chemical functionalization of carbon nanotubes is one of the most effective means for manipulating and processing nanotubes.

Prior research has demonstrated that CNTs can be reliably modified by a number of chemical treatments.[38, 39] Generally, chemical functionalization falls into two major categories, namely, non-covalent functionalization and covalent functionalization, according to the nature of the interaction between the nanotubes and functional moieties. With regard to non-covalent functionalization, CNTs are usually wrapped by either polymers or other biological molecules[40] through π-π stacking interactions, thereby obtaining the desired solubility or biological functionality for various applications, including biosensors and electronic detectors. Even though covalent functionalization is suggested to disrupt the electronic structure of CNTs by destroying the intrinsic nanotube sp^2 structure, it provides a robust and effective methodology with a high degree of flexibility in introducing a variety of chemical moieties onto the surfaces of CNTs in order to improve nanotube processability, accessibility, and performance.

At this stage, a number of key conclusions about the reactivity of nanotubes subjected to covalent functionalization are evident. First, nanotubes tend to be most reactive at their tips in order to relieve the strain arising from pyramidalization of the carbon atom at the end caps of the

carbon nanotubes. Second, π-orbital misalignment between adjacent carbon atoms on the nanotube sidewall plays a large influence in determining overall reactivity of CNTs. Furthermore, since π-orbital misalignment as well as pyramidalization scale inversely with nanotube diameter, CNTs with smaller diameters are expected to be far more reactive than larger diameter tubes. To date, molecular moieties have been covalently introduced onto the surface of CNTs by (i) either linking to oxygenated groups at the ends or the defect sites of oxidized CNTs via amidation or esterification reactions,[41-44] or (ii) utilizing polar, pericyclic, as well as radical reactions to construct carbon-carbon and carbon-heteroatom bonds on the sidewalls of carbon nanotubes.[45-49]

1.3.2 *Application of CNTs in photovoltaic devices*

Owing to a number of advantageous properties of CNTs, such as their great thermal and mechanical stability[50], excellent carrier mobility (100,000 cm^2/ V·s at room temperature)[51], and high surface area (~ 400 m^2/g), CNTs have been incorporated into polymer solar cells in order to improve the device performance.[52, 53] Extensive studies have reported that transparent thin films of CNTs can be prepared to replace high-cost ITO in PV devices due to the excellent conductivity of CNTs[54] (Figure 1.4). With a sheet resistance value comparable to that of ITO, CNT thin films have exhibited not only optical transmittance similar to that of commercial ITO in the visible spectrum but also superior transmittance in the 2 to 5 μm infrared spectral band.[55] An organic solar cell with an efficiency of 2.65% can be fabricated while using SWCNTs as the transparent electrode (Figure 1.4).[56] In addition to acting as charge carrier conducting channels, CNTs can also provide a high field at polymer/CNT interfaces for exciton dissociation in a typical organic photovoltaic device (OPV).[57-59] Femtosecond transient absorption studies on photochemical solar cells consisting of single-walled CNT (SWCNT) –porphyrin (H_4P^{2+})

composites have confirmed that the enhancement in the incident photon to photocurrent efficiency (IPCE) can be attributed to the electron transfer between photoexcited H_4P^{2+} and SWCNTs as well as to improved charge transport enhanced by SWCNTs (6.5% for SWCNT–H_4P^{2+} vs. 1.5% for H_4P^{2+}).[60] Recently, the Strano group[61] has demonstrated that efficient exciton dissociation can be achieved at the interface of a planar nanoscale heterojunction comprising of well-isolated perfectly aligned SWCNTs underneath a poly(3-hexylthiophene) (P3HT) layer. The photovoltaic efficiencies per nanotube of this heterojunction ranging in 3% – 3.82% exceeded those of polymer/nanotube bulk heterojunctions by a factor of 50 – 100, a result attributed to the fast charge transport in this planar device geometry. In another study, the incorporation of CNTs in ITO/P3HT/C_{60}/Al OPV resulted in the increase in open-circuit voltage (V_{OC}) to 0.7 – 0.8 V (vs. 0.45 V in the absence of CNTs) and the improvement of short-circuit current (J_{SC}) by a factor of 5.[57]

Overall, CNTs have demonstrated their potential advantages in the construction of high-efficiency photovoltaic devices. Enormous research is still ongoing in order to better understand the interaction of CNTs with other components in these devices and to exploit the properties of CNTs for improving device performance.

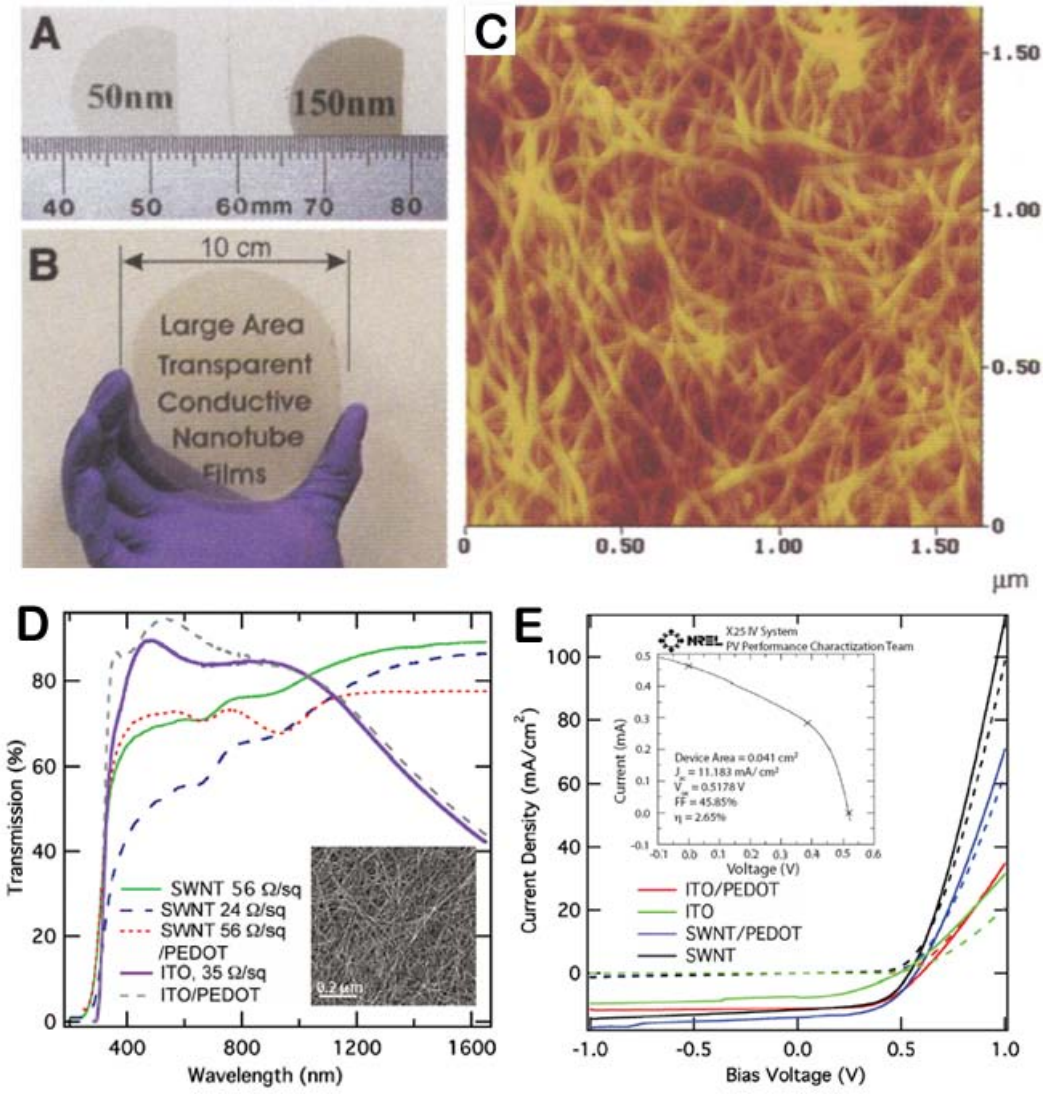

Figure 1.4: Transparent single-walled carbon nanotube (SWCNT) films used for solar device fabrication. (A) Transparent single-walled carbon nanotube (SWCNT) films with the indicated thickness on quartz substrates. (B) 80-nm-thick SWCNT film on a sapphire substrate with a diameter of 10 cm. (C) AFM image of a 150-nm-thick SWCNT film surface. (A-C) Reproduced from Wu *et al. Science* 2004, 305, 1273-1276.[55] (D) Transmission spectra for transparent electrodes used for device fabrication. Inset: inverted-contrast transmission electron microscopy image of sprayed SWCNTs. (E) Light (solid lines) and dark (dashed lines) J-V curves for devices on SWCNT and ITO transparent electrodes. Inset: National Renewable Energy Laboratory (NREL)-certified light I-V data for bulk heterojunction (BHJ) device on a SWCNT electrode without the hole transport layer. (D-E) Reproduced from Barnes *et al. Appl. Phys. Lett.* 2010, 96, 243309.[56]

1.4 0D – 1D Nanoscale Heterostructures

Due to the high surface area-to-volume ratio of both 0D nanocrystals and 1D nanostructures, the nature of the interaction occurring at the large interfacial area between these two motifs has a significant influence on the overall behavior of the heterostructures.[62] Specifically, the electronic coupling between these two components, highly dependent upon the spatial separation and nature of the chemical functionalities, can potentially bias either the charge flow or energy flow within these systems, thereby raising significant interest in the utilization of these 0D – 1D heterostructures in electronic device design. In addition, the tunability in terms of size, shape, and chemistry of 1D nanostructures and 0D nanocrystals allows for the properties at the junction interface to be inherently manipulable and hence, predictable. Thus, the rational design of these nanoscale heterostructures is critical for understanding the intrinsic factors affecting their electronic and optical properties (e.g. carrier mobility and carrier recombination). Results based on a thorough understanding of these systems will be useful when 0D – 1D heterostructures are incorporated as building blocks in either electronic or other photovoltaic devices.

1.4.1 *Synthesis of 0D – 1D heterostructures*

As suggested by the previous section, semiconductor nanocrystals can be assembled or deposited onto the mesoporous metal oxide film in order to construct semiconductor-sensitized solar devices. In the light of the various uses of 1D nanostructures, enormous effort has been expended for the fabrication of nanoscale heterostructures comprised of QDs deposited onto metal oxide nanowire (nanotube) arrays for improving solar device performance.[63] The *in situ* preparation of QDs onto the 1D nanostructures can be realized by either chemical bath

deposition or successive ionic layer adsorption and reaction (SILAR) protocols. As opposed to the limited control over the size and size distribution associated with *in situ* preparation, linker-assisted approaches provide for more inherent flexibility in terms of controlling the monodispersity of QDs.

In terms of the broad range of 0D –1D heterostructures that can be possibly fabricated, CNT-nanocrystal heterostructures stand out as being of exceptional interest in that such heterostructures take advantage of the unique physical and chemical properties of both carbon nanotubes and nanoparticles in one discrete structure with potential applications spanning a broad range of diverse fields from heterogeneous catalysis[64-66], chemical sensing[67], drug delivery[68, 69], to optoelectronic device development.[70, 71]

Similarly, CNT– nanocrystal heterostructures have been fabricated via either *in situ* growth, non-covalent, or covalent approaches. The *in situ* synthesis of nanocrystals on the CNT scaffolds usually possesses the difficulty of precise control over the morphology of nanocrystals, whereas non-covalent approaches, relying on electrostatic interactions and/or π-π stacking, are not generally practical for a number of applications due to the lack of long-term stability, high sensitivity to changes in pH and ionic strength, and difficulty in terms of control of stoichiometry.[72]

In contrast with *in situ* growth and non-covalent approaches, the advantages of covalent conjugation of nanocrystals onto the surface of CNTs are at least three-fold: (i) the shape and size of nanocrystals can be easily controlled prior to attachment onto CNTs, thereby avoiding the influence of CNTs on the nucleation and growth of nanocrystals; (ii) covalent bonds can rigidly connect the linker molecules and CNTs in a reliable and robust manner, such that the nanoparticles will not become easily dislodged even after sonication or extensive washing; and

(iii) the spatial coverage and exact positions of nanocrystals depend upon the precise nature of the chemical functionalities on CNT surfaces, and these can be reasonably governed by controlling oxidation treatments and/or chemical reaction conditions. In recent years, extensive research has been conducted to covalently attach the nanoparticles onto the surfaces of CNTs via the formation of either amide or ester bonds through the use of organic molecular linkers. For example, nanocrystals, either metallic or semiconducting, have been linked onto oxidized CNTs by the formation of amide bonds in the presence of a carbodiimide agent such as *N*-(3-dimethylaminopropyl)-*N*'-ethylcarbodiimide (EDC) or dicyclohexylcarbodiimide (DCC).[73-75] Most importantly, it has been found that nanocrystals tend to be concentrated at either the ends or defect sites of SWNTs where the largest concentration of carboxylic groups is present.

1.4.2 *Application of 0D – 1D heterostructures in photoconversion*

Since QDs have been considered as one of most promising 0D nanomaterials capable of being utilized in solar devices, there has been a growing interest in developing QDs-based 0D – 1D heterostructures, which take advantage of 1D nanostructures to overcome the difficulties associated with charge separation and transport in the ensemble of QDs alone. In particular, the development of nanoscale hybrids consisting of CNTs and semiconducting QDs has been of great interest in recent years. In such nanohybrids, CNTs are expected to provide for the physical scaffolds onto which semiconductor particles are attached, thereby not only facilitating photoinduced charge carrier separation but also aiding in collecting and transporting photogenerated charge carriers to the respective electrodes. (Figure 1.5) Indeed, a significant decrease of the photoluminescence of QDs upon conjugation with CNTs has been observed, which can be attributed to either charge transfer or energy transfer from QDs to CNTs.[76, 77] It has

been suggested that the charge carrier recombination in QDs can be efficiently suppressed due to the presence of CNTs. In addition, it has been found that carbon nanotubes with different chemical functional groups (e.g. carboxyl, hydroxyl, and amine) can quench the luminescence of mercaptoacetic acid-capped CdSe quantum dots to different degrees.[78] This observation was attributed to the charge difference on the surfaces of CNTs, which can affect the electrostatic forces between CNTs and QDs. As a result, the separation between CNTs and QD was altered thereby influencing the degree of quenching. One recent photophysical investigation employing both luminescence and transient absorption measurement has demonstrated that charge transfer in CdTe–pyrene–SWCNT nanohybrids can occur at 62 ps, which is strongly competitive with the radiative recombination of charge carriers (i.e. 35 ns), thereby transforming excited CdTe QDs into a charge-separated state with a lifetime of several nanoseconds.[72]

Recently, photovoltaic devices with an external quantum efficiency of 2.6% have been achieved by utilizing CNT–PbSe composites with a high-density coverage of PbSe (up to 20 wt%), as compared with the 1.2% value associated with isolated quantum dots alone. (Figure 1.5) The improvement in efficiency was attributed to not only efficient harvesting of infrared photons but also the fast charge transfer and enhanced conduction due to the presence of CNTs.[79] Another study has revealed that an IPCE up to 2.3% could be achieved in hybrid cells consisting of SWCNT/pyrene^{+}/red-emitting CdTe stacks.[80] Strong electronic interactions in the ground and excited states were thought to be responsible for the favorable charge-transfer characteristics observed. Similarly, hybrid solar cells consisting of CdS-grafted SWCNTs on a Si substrate have been constructed, exhibiting a fairly high efficiency of up to 1.4%.[81, 82] CdSe-SWCNT nanohybrids have also been incorporated into flexible, lightweight polymer solar devices composed of either poly(3-octylthiophene) (P3OT)[83] or thiol derivative perylene compounds[84] in

order to facilitate exciton dissociation and carrier transport. These nanocomposites evinced a ~2-4-fold enhancement in their photoconductivity. The flow of electrons and holes in the nanocomposites intrinsically was found to rely on the energy levels of different components in the solar devices including QDs, CNTs, and organic polymers. The point is that the degree to which the QDs can produce excitons, the degree to which CNTs and the polymer can absorb light, as well as the degree to which excitons can be dissociated at the junctions ultimately depend on the nature and the tunability of materials as well as the types of junctions that can be created. All of these parameters are fundamentally a function of material composition as well as the precise morphology (e.g. shape and size) of each individual building block.

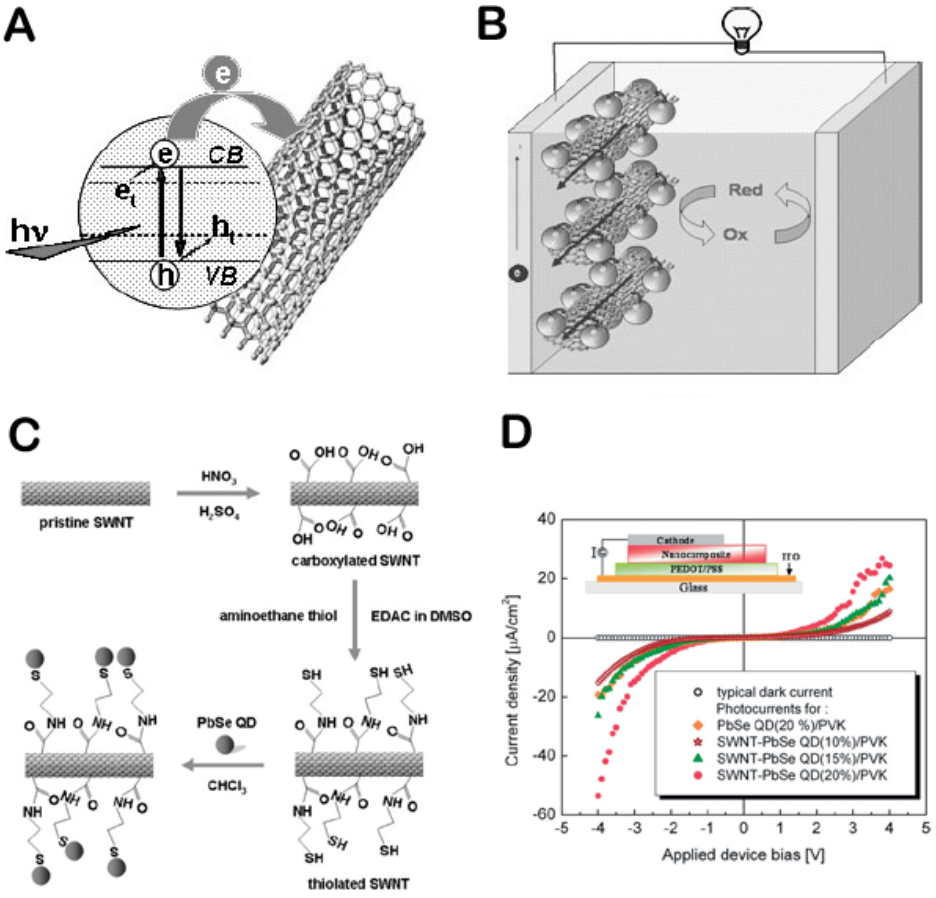

Figure 1.5: Carbon nanotube – nanocrystal heterostructures used for solar device.(A) Photoinduced charge injection from excited semiconductor particles into SWCNT. (B) SWCNTs as conducting scaffolds to transport photogenerated charge carriers in a photoelectrochemical cell. (A-B) Reproduced from Vietmeyer *et al. Adv. Mater.* 2007, 19, 2935-2940. (C) Synthetic route for the preparation of SWNTs coupled with PbSe. (EDAC: *N*-(3-dimethylaminopropyl)-*N*-ethylcarbodiimide hydrochloride, DMSO: dimethyl sulfoxide.) (D) Current density-voltage (I-V) curves of PbSe QD/poly(vinyl carbazole) (PVK) and SWNT-PbSe/PVK devices in the dark and under illumination. Inset: structure of the IR photodetector device employed in this study. (C-D) Reproduced from Cho *et al. Adv. Mater.* 2007, 19, 232-236.

1.5 1D Nanoscale Heterostructures

As implied by the previous section, 1D nanostructures, exhibiting attractive properties, have demonstrated potential in a host of applications. Therefore, combining different materials into a single 1D nanostructure can allow us to potentially exploit the combined benefits of the 1D morphology and the unique function of the multicomponent heterojunction. Different 1D heterojunctions can be classified by the nature of the junction, including segmented[85, 86], core-shell (or radial)[87-89], cross junctions (or T junctions)[90], hyperbranched[91], or multibranched ("nanobrushes")[92] heterojunctions. Figure 1.6 demonstrates several examples of various types of 1D nanoscale heterojunctions. The type of junctions plays an important role in determining their ultimate properties and applicability. For example, segmented heterostructures are thought to be useful as either nanoswitches or nanoscale diodes in nanoelectronic devices[93], as well as "barcodes" in applications associated with tracking and bio-diagnosis.[94] In particular, 1D radial heteroscale structures have been considered as promising materials in photo-energy conversion applications.

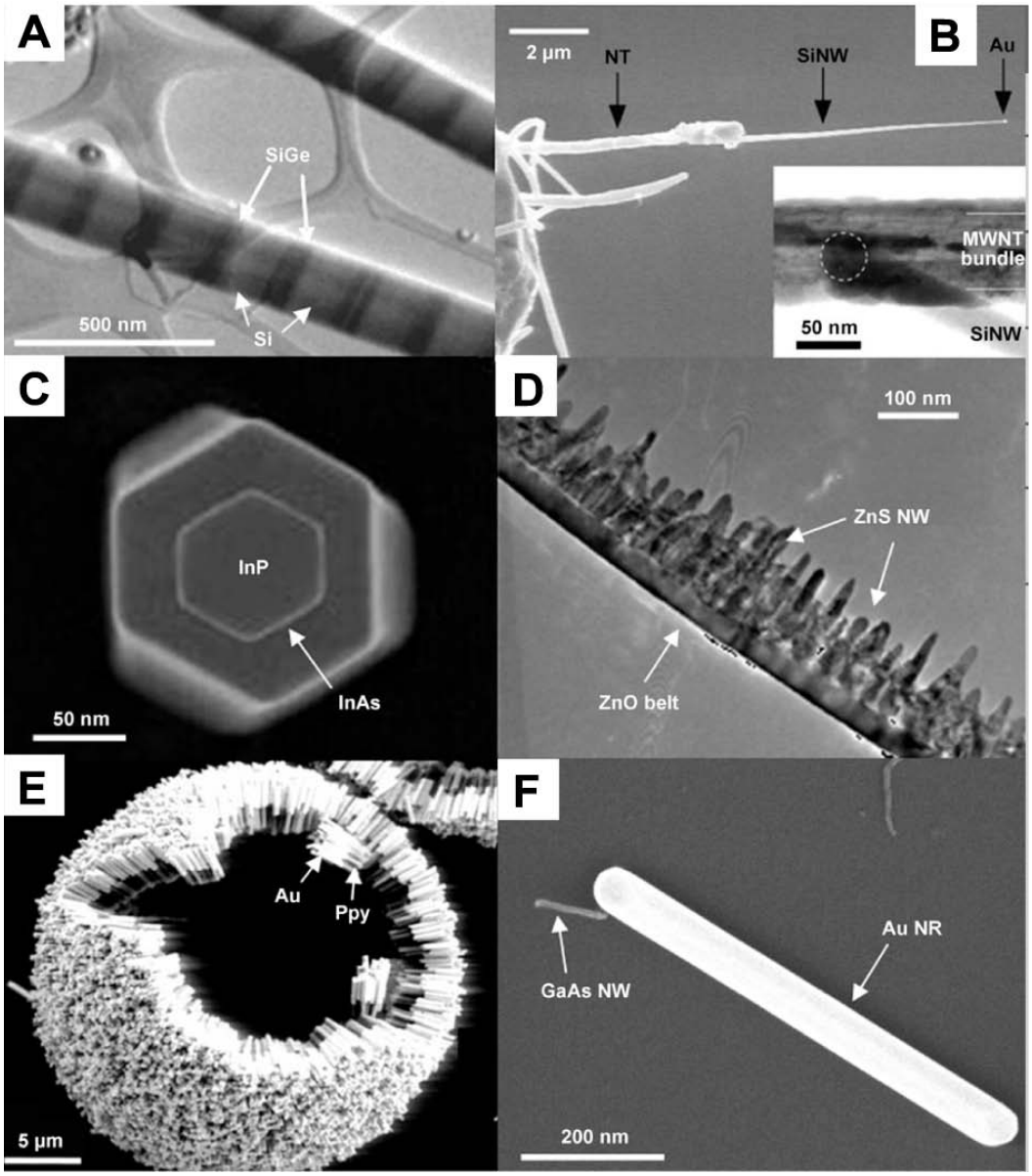

Figure 1.6: Examples of a wide variety of one-dimensional nanoscale heterostructures: (A) STEM image of the Si/SiGe segments of the nanowire (NW) prepared by vapor-liquid-solid (VLS) synthesis. (B) FESEM image of a CNT/Si NW end-to-end heteroscale junction formed on a Pt-Ir STM tip from a Au catalyst. (C) SEM image of the cross section of an InP/InAs/InP NW showing a hexagonal shape composition. (D) TEM image of a sawlike heterojunction of ZnS NWs grown on a ZnO belt by a two-step vapor-solid process. (E) SEM image of assembled Au-polypyrrole segmented nanorods (NRs) prepared by electrochemical deposition. (F) SEM image of GaAs NW/Au NR heterojunction synthesized by combining VLS growth of GaAs NWs and seed-mediated growth of Au NRs. (A-F) Reproduced from Mieszawska *et al. Small* 2007, 3, 722-756.[95]

1.5.1 *Synthesis of 1D heterostructures*

Extensive effort has been devoted to synthesizing 1D heterostructures in recent years. 1D heterojunctions have been fabricated via the vapor-liquid-solid (VLS) growth mechanism by using various types of deposition methods, including chemical vapor deposition (CVD), pulsed-laser deposition (PLD) and chemical beam epitaxy (CBE). The fabrication process usually entails the use of specific chemicals as precursor materials, with or without appropriate catalysts pre-deposited on the substrate, and the utilization of specialized equipment in order to achieve elevated temperatures in the range of 500 – 1200°C and/or low vacuum environments.

In order to obtain segmented structures, two or more different types of precursors are introduced to the chamber in either sequential or alternating fashion. For example, Si/SiGe segmented NW heterojunctions have been synthesized in the reaction chamber wherein the Ge reactant vapor was controllably supplied by laser ablation of solid targets and Si was provided by the constant supply of the vapor-phase precursors, $SiCl_4$ and H_2. Alternate switching of the laser between 'on' and 'off' states led to the formation of the segmented structures of Si/SiGe with control over the length of the segments.[86] Similarly, switching of the reactant gas or applying a completely different experimental condition can lead to the homogeneous deposition of the second material onto the nanowire surface of the first material, therefore forming a uniform core-shell heterostructure. In one study, ZnO–Al_2O_3 core-shell NWs were obtained by pre-synthesizing ZnO NWs with a diameter of 10 – 30 nm via VLS growth, followed by growth of the Al_2O_3 shell with a thickness of 10 nm in the atomic layer deposition (ALD) chamber, by using $Al(CH_3)_3$ and H_2O as precursors.[96]

Heteroscale junctions can also be successfully synthesized by solution-phase methods. The synthesis can occur (i) by introducing all of the precursors at once in one step, (ii) by

alternating the precursors in the solution, or (iii) by synthesizing the core in the first place and then transferring it to a new solution for the subsequent formation of the shell. Stabilizing ligands and surfactants are usually necessary in order to confine the morphology of the resulting materials. For instance, ZnO/CdS core-shell QDs[97] and CdSe/CdS core-shell nanorods[98] have been synthesized by first synthesizing core materials in the coordinating solvent mixture and then growing the CdS shell by slowly adding the tri-n-octylphosphine (TOP) solution containing dimethylcadmium and bis(trimethylsilylsulfide). Another study has demonstrated that hematite nanoparticles were able to epitaxially grow onto multiple nucleation sites on the CdS nanowires (i.e. $\left(10\bar{1}0\right)_{CdS}$ // $\left(4\bar{3}0\right)_{\alpha-Fe_2O_3}$) via a two-step hydrothermal method, thereby successfully yielding CdS/Fe_2O_3 core-shell heterostructures.[99]

Template-assisted approaches are another key route for fabricating 1D nanoscale heterostructures. In the early 1990s, Martin and co-workers pioneered the use of hard templates in the synthesis of NWs by either electrochemical or electroless deposition in porous membranes followed by removal of templates in the presence of proper solvents.[100, 101] By adapting the same principle of preparing single-component NWs in the polycarbonate or alumina membrane template by electrochemical deposition, NWs with different segments can be prepared by using either single bath or alternating baths. The dimensions of NWs are highly restricted to both the pore width and length of the membranes. Nonetheless, such methods have been generalized for a wide variety of materials including metals[102, 103], semiconductors[104] and polymers[105]. For example, metal–CdSe–metal NWs have been prepared by sequentially electrodepositing either Au or Ni NWs as well as CdSe NWs from a plating solution consisting of 0.3 M $CdSO_4$, 0.25 M H_2SO_4 and 0.7 mM SeO_2.[104] In more sophisticated experiments, core-shell 1D nanostructures

have also been prepared by either a one-step or two-step electrodeposition procedure. Zhu *et al.* has demonstrated that Ni/TiO_2 core-shell nanorod arrays can be formed by a one-step electrodeposition process in electrolyte containing 0.04 M TiF_4 and 0.08 M $NiCl_2 \cdot 6H_2O$ at -1.30 V for 10 min.[106] The authors suggested that the TiO_2 shell was rapidly deposited onto the inner surface of the channels of the template due to the presence of hydroxyl ions along its inner surface, produced at a negative potential, whereas Ni NW core was formed slowly from the bottom of the channels wherein a thin layer of Au was pre-sputtered as working electrode, thereby giving rise to the final core-shell structures.

Apart from advanced technical methodologies, well-known chemical conversion processes (e.g. ion exchange[107], sulfidation[108], and the Kirkendall effect[96]) have been successfully used for the preparation of 1D heterostructures. For instance, Alivisatos and co-workers have developed a facile, colloidal route to convert nanorods with a single chemical composition into a striped pattern through a single-step partial cation exchange.[109, 110] The diffusion-limited growth and strain arising from the lattice mismatch between CdS and Ag_2S were suggested to account for the spontaneous superlattice-pattern formation. Recently, Shuai *et al.* demonstrated that ZnO/ZnS core-shell nanorods could be obtained through the reaction of ZnO NWs with thioacetamide. The sulfidation conversion could took place at the surface of the ZnO NWs, thereby leading to the formation of a ZnS shell composed of nanoparticles with a mean size of 18 nm.

In addition, the use of a combination of these aforementioned approaches is a common strategy to open up more possibilities for generating 1D heterojunctions with a broad-spectrum range of chemical compositions. For instance, vertically aligned ZnO/CdTe core-shell nanocable arrays deposited onto ITO have been fabricated by electrochemical deposition of CdTe onto ZnO

nanorod arrays which were pre-synthesized by VLS.[88] Multilayered core-shell NWs consisting of SiO_2, Fe_2O_3, and Ni have been successfully prepared by a combination of ALD and electrodeposition methods.[111] However, as compared with the progress in the synthesis of homogeneous 1D nanowires and nanotube systems, the reliable synthesis of 1D heterostructures with well-defined interfaces via a facile, scalable, and cost-effective route with precise control over chemical composition and spatial dimension still remains an elusive objective, prior to any consideration about their potential widespread use in commercialized industry applications.

1.5.2 *Applications of 1D radial heterostructures in photoconversion*

The study of 1D nanoscale heterostructures is rapidly growing because of the numerous potential applications for these multicomponent structures. According to the band offset, the heterojunction formed at the interface between two different materials can be classified as either type I, where both the conduction and valence bands of one material are located within the bandgap of the other, or type II, where one material has higher conduction and valence bands than the other. In particular, 1D radial heterostructures with a type II configuration can yield efficient charge separation at the interface and carrier transport in the orthogonal direction, which is a desirable outcome for applications related to the photoconversion process.

1.5.2.a Photovoltaic devices

In applications of photovoltaic devices, the use of 1D radial heterostructures has been theoretically[112] and experimentally[88, 113, 114] demonstrated to provide improvements in photoconversion efficiency as compared with the conventional planar geometry heterostructures. For instance, in a typical photovoltaic device, three major processes need to be optimized in

order to achieve a highly efficient device. These factors include light absorption, carrier separation, and charge collection. For the conventional planar geometry heterojunction, even though an increase of the light-absorbing layer can enhance light absorption, the collection efficiency of charge carriers can be compromised as it is highly limited by the minority carrier diffusion length in the semiconductor. By contrast, 1D nanostructures with heterojunctions in the radial direction would enable a decoupling of the requirements for light absorption and carrier extraction in orthogonal spatial directions. Specifically, each individual nanowire in the cell could be sufficiently long in the direction of incident light, allowing for optimal light absorption, but thin in the other dimension, thereby allowing for effective carrier collection.

In the example of a photodetector consisting of a ZnO/CdTe nanocable on ITO, the photogenerated electrons were more likely to be injected from the CdTe shell into the ZnO nanowire core, driven by the type II band alignment between ZnO and CdTe, (Figure 1.7A) and then rapidly transported to the ITO substrate by means of single-crystalline ZnO, which can serve as an electron-transport highway. Both the nanocable array configuration (Figure 1.7B) as well as the interfacial interaction of two materials (Figure 1.7C) were believed to contribute to the impressive photocurrent density of ~ 5.9 mA/cm^2 as compared with previously reported results obtained from similar devices.[88] In 2006, the Yang group developed dye-sensitized solar cells based on arrays of ZnO NWs coated with thin shells of either Al_2O_3 or TiO_2 by ALD, with an overall conversion efficiency up to 2.25%. The superior performance of these solar cells based upon ZnO-TiO_2 core-shell NWs was attributed to the radial surface field generated at the interface within each NWs, which can repel electrons from the NW surface and thus decrease the recombination rate in these devices.[115]

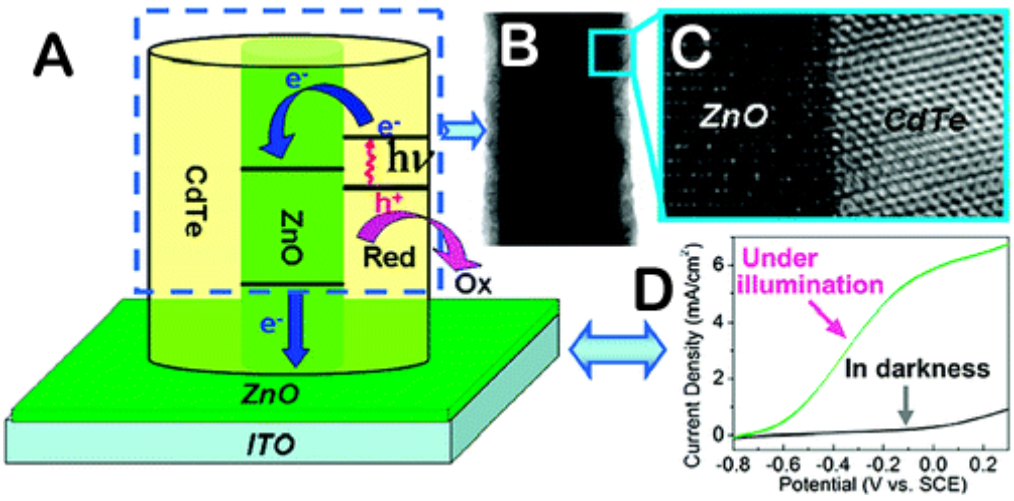

Figure 1.7: (A) Schematic of the operation of a semiconductor-sensitized solar cell composed of ZnO/CdTe nanocable arrays on ITO. (B) TEM image of the uniform morphology of a single ZnO/CdTe nanocable. (C) HRTEM image showing the interface of the nanocable. (D) I-V curves for ZnO/CdTe nanocable arrays-on-ITO photoelectrodes measured in the dark and under an illumination of AM 1.5 light at 100 mW/cm^2. (A-D) Reproduced from Wang *et al. ACS Nano,* 2010, 4, 3302-3308.[88]

1.5.2.b Photocatalysis

In addition to the fabrication of photovoltaic devices, 1D radial heterostructures hold great promise in terms of a significant improvement in the photocatalysis and photo-degradation of organic pollutants owing to their remarkable advances in terms of charge separation and charge transport.

Over the last decade, growing scientific and engineering interest in the application of easily available, chemically stable semiconductor photocatalysis has emerged because of the increasingly substantial concern about hazardous waste remediation. However, one of the barriers hindering the effective photocatalytic efficiency of semiconductor nanocatalysts is the occurrence of charge carrier recombination prior to charge transfer from the semiconductors to the species adsorbed onto the surfaces of these semiconductor nanocatalysts.

In principle, when the energy of the incident photons either matches or exceeds the bandgap energy of the semiconductor, an electron is promoted from the valence band into the conduction band, leaving a hole behind. The photoexcited electrons and holes can then recombine, dissipating the input energy as heat or emitted photons, get trapped in surface states, or react with electron donors/acceptors adsorbed onto the semiconductor surface. Therefore, competition between the charged carrier recombination and trapping, as well as between trapped carrier recombination and interfacial charge transfer can play important roles in determining the photocatalytic reactivity of semiconductor photocatalysts. It has been reasonably argued that either increasing the interfacial charge transfer or lowering the possibility of charge carrier recombination will effectively enhance semiconductor photoreactivity. In this regard, the

formation of heterostructures between two materials provides a promising resolution in terms of eliminating charge recombination by separating charge carriers at the interface.[116, 117]

For example, *p*-type NiO/*n*-type ZnO heterojunction nanofibers exhibited excellent photocatalytic activity and are in fact superior to the NiO and ZnO nanofibers alone.[118] Figure 1.8A-B highlights a distinctive structural interface and a continuity of lattice fringes between NiO and ZnO nanoparticles, indicative of the formation of a reasonable *p*-*n* heterojunction in the NiO/ZnO nanofibers. Owing to the electronic characteristics of these two materials, electrons tend to diffuse from *n*-type ZnO to *p*-type NiO at the interface, whereas holes migrate in the opposite direction, thereby generating a depletion region at the interfacial surface. This local exchange of charge causes a change in the energy of charge carriers at the junction, leading to the formation of band bending at the interface, a phenomenon in this case that can facilitate the separation of photogenerated charge carriers at the junction upon UV illumination (Figure 1.8C). It is believed that such heterojunctions account for the outstanding photocatalytic activity of NiO/ZnO fibers. In a separate study, SnO_2/Fe_2O_3 nanoscale heterostructures prepared by hydrothermal method exhibited a higher photocatalytic reactivity for the degradation of methylene blue than that associated with Fe_2O_3 itself.[119] Similarly, this improvement was ascribed to the type II band configuration at the interface of SnO_2/Fe_2O_3 nanoheterostructures. Photogenerated electrons and holes separated at the interface migrated effectively to the surface of SnO_2 and Fe_2O_3, respectively, so as to form the hydroxyl radicals, thereby leading to the decomposition of the probed organic molecules.

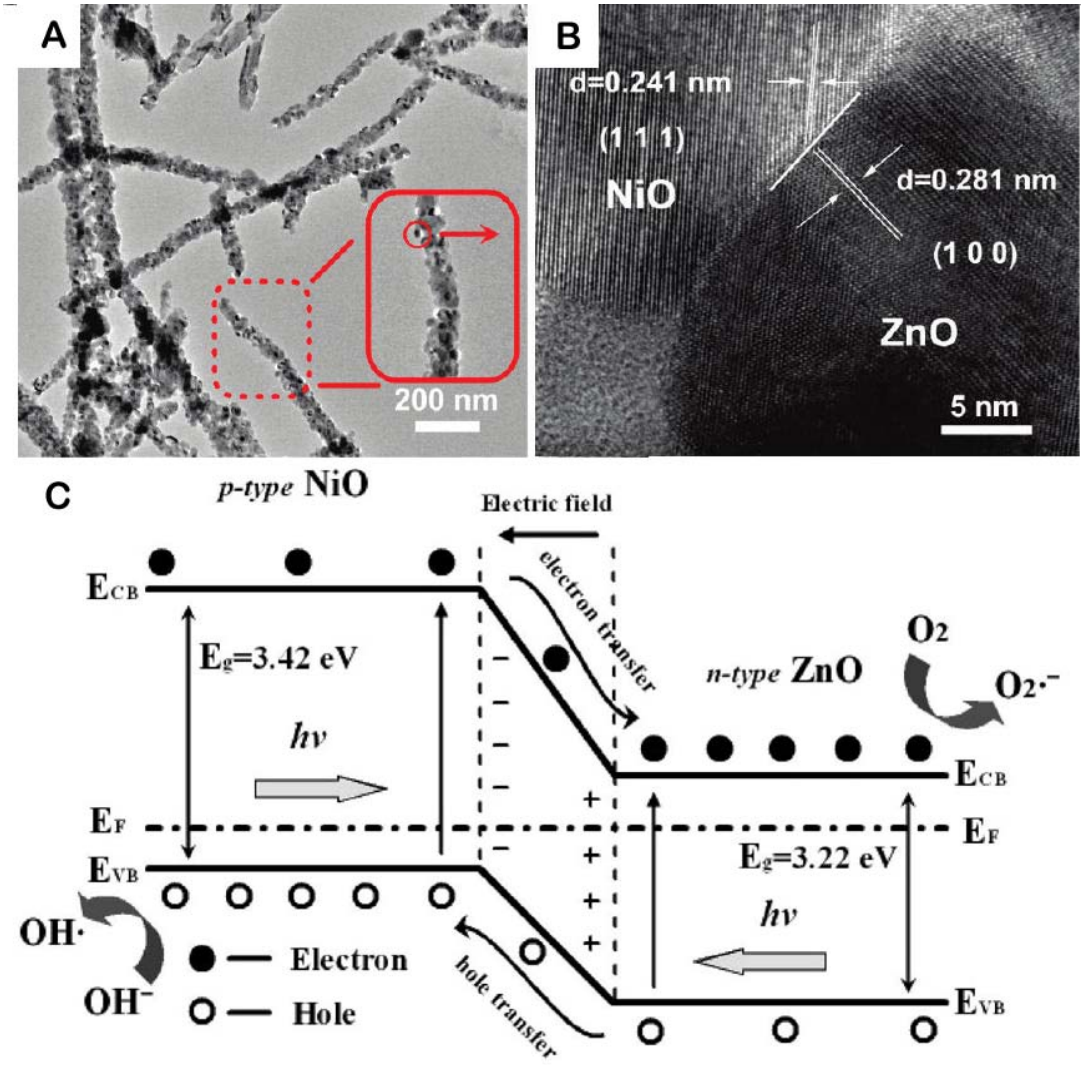

Figure 1.8: *p*-type NiO/*n*-type ZnO heterojunction. (A) TEM image of as-prepared NiO-ZnO nanofibers. (B) HRTEM of p-type NiO/n-type ZnO heterojunction region in the nanofibers. (C) Schematic diagram showing the energy band structure and electron-hole pair separation in the *p*-type NiO/*n*-type ZnO heterojunction.(A-C) Reproduced from Zhang *et al. ACS Appl. Mater. Interfaces*, 2010, 2, 2915-2923.[118]

1.6 Environmental Impact of Nanostructures

According to the Project on Emerging Nanotechnologies (PEN), over 1,300 manufacturer-identified, nanotechnology-enable products have entered the commercial marketplace around the world, and the number could reach over 3,400 by 2020. Since the use of nanotechnology in consumer products continues to grow at a rapid and consistent pace, the unforeseen environmental problems associated with nanoscale materials has raised great concern. While the issue of nanoscale toxicity is still unresolved to a large extent due to a comprehensive lack of conclusive studies on the matter, there is a wealth of evidence supporting the harmful effects of certain nanoscale particulates, which can cause a number of pulmonary pathologies in mammals as well as human beings when inhaled. The US Environmental Protection Agency (EPA) has attributed 60,000 deaths per year to the inhalation of atmospheric nanoparticles.[120] Apart from nanoparticles produced unintentionally from natural sources (e.g. volcanic eruptions, forest fires, and pollen fragments) as well as from anthropogenic sources (e.g. power plants, vehicles, and coal combustion), nanoparticles have been purposely generated for use in sunscreens, detergents, paints, or printer inks, which can also enter the environment through accidental spills during their production and transportation, wear and tear throughout their usage, as well as their final disposal.

For example, semiconducting nanoparticles (e.g. TiO_2 and ZnO) have been produced for the purpose of environmental remediation, such as the de-chlorination of groundwater pollutants.[121] However, the environmental impact of the release of these manufactured nanoparticles into the aquatic environment is largely unknown. Moreover, once in the environment, free nanoparticles tend to form aggregates that can be trapped or eliminated

through sedimentation. Subsequently, aggregated nanoparticles can be uptaken by either filter feeders or sediment-dwelling animals. As a result, the environmental impact of nanoparticles essentially is magnified through the food chain, potentially having an adverse effect upon human health. Therefore, a life cycle assessment for risk to the health of the environment is necessary and required, concomitant with a safety evaluation of nanomaterials. Hence, while the field of nanoecotoxicology is still in its infancy, it represents an important and growing research area in the USA and Europe.

At the cellular level, most internalization of nanoparticles will occur via endocytosis. Typical endocytic mechanisms include phagocytosis, pinocytosis (which implies internalization of fluid surrounding the cell), clathrin-mediated endocytosis, and clathrin-independent endocytosis (e.g. caveolae-mediated endocytosis and Cdc42-dependent endocytosis). By contrast with animal cells, most plant, algae, and fungi cells possess cell walls that constitute a primary site for interaction and a barrier for the entrance of nanoparticles. For example, cell walls in plants and algae mainly consist of cellulose, while diatom algae typically possess hydrated silicon dioxide. Cell walls are typically semipermeable, with pores across the cell wall possessing diameters in the range of 5 – 20 nm. Thus, only nanoparticles/aggregates with sizes smaller than that of the largest pore are expected to pass through the cell wall and reach the plasma membrane. Moreover, the interactions of the cells with nanoparticles might induce the formation of new pores, which might be bigger than normal, and hence increase the possibility of internalization of the nanoparticles through the cell wall.[122] After passing through the cell wall, the nanoparticles will be uptaken into the cells across the plasma membrane either via the endocytic processes or using embedded transport carrier proteins. As soon as the particles enter the cell, they may bind with different types of organelles and interfere with the metabolic

processes. In such a case, one of the possible cell responses would be to produce reactive oxygen species (ROS), including superoxide anions, hydrogen peroxide, hydroxyl radicals, and peroxynitrites. Furthermore, the nucleus may experience degeneration due to oxidative DNA damage.

1.6.1 *Direct toxic effects of nanoparticles*

The extent of the direct toxic effects of nanoparticles upon organisms is mainly determined by their surface reactivity and chemical composition. It is known for example that the surface chemistry and reactivity of materials are different when their dimensions shrink down to the order of 100 nm or less. For example, carbon fullerenes, with diameters on the order of several nm, may have a different toxicity as compared with micron-sized graphite particles, even though both particles are made of carbon.[123] In addition, the size of nanoparticles is directly correlated with their ability to penetrate into and accumulate within cells and organisms.[124-128] For example, the oxidative stress induced inside of alveolar macrophages in the presence of Ag nanoparticles with sizes of 15, 30, and 55 nm has revealed that smaller Ag nanoparticles can evoke a more significant inflammatory response, partially because they were more accessible to cell membranes and hence, undergo internalization.[125] Once they are uptaken, nanoscale materials exhibit greater reactivity and thus induce severe oxidation inside the cells, owing to their much higher specific surface area as compared with their bulk-like counterparts. Therefore, this can have an adverse impact upon the normal photosynthetic or respiratory processes of algae or plants.[129] In addition, the size of nanoparticles also governs other physical/physicochemical properties of nanomaterials, such as the degree of aggregation and surface charge, which, in turn, can also affect their ecological toxicity.

The chemical composition of nanomaterials plays an important role in determining the toxicity of nanomaterials as well. Evaluation of the toxicity of several metal oxides (e.g. ZnO, TiO_2 and Al_2O_3) on zebrafish embryos has revealed that ZnO caused severe tissue damage and delayed zebrafish embryo development, whereas the presence of TiO_2 and Al_2O_3 did not give rise to any obvious toxicity.[130] In order to understand the influence of chemical composition of nanoparticles on their toxicity to cells, lung epithelial cells were exposed to iron-, manganese-, cobalt-, and titania-containing nanoparticles possessing the same morphology and degree of agglomeration. Afterwards, the release of ROS was quantitatively measured, and then correlated with either the catalytic activity or chemical composition of nanoparticles. These results confirmed that the oxidative damage noted varied with both the chemical and catalytic properties of nanomaterials, apart from their physical properties, such as size, shape, and degree of agglomeration.[131]

1.6.2 *Indirect toxic effects of nanoparticles*

Apart from these direct toxic effects, the presence of nanoparticles can perceptibly influence the metabolic processes of biological species by either releasing toxic ions [132] or imposing physical restraints (e.g. through aggregation and adsorption of nanoparticles). Even though some of these ions are considered as nutrients at low concentrations, an excess amount of ions may disrupt cellular metabolic processes by preventing the uptake of other ions essential for physiological needs.[133]

A comparative assessment, for example, of the toxicity of Au, Ag, and Ag–Au bimetallic nanoparticles conducted on *Daphnia magna* indicated that Ag-containing nanoparticles were much more toxic than pure Au ones. This observation could be ascribed to the fact that Ag^+ can

inhibit sodium influx in aquatic species.[134] The use of cysteine, a strong silver ligand, can completely inhibit the toxicity of Ag nanoparticles to freshwater algae, *Chlamydomonas reinhardtii*, by greatly reducing silver bioavailability due to the formation of an Ag–cysteine complex. This observation further suggested that the released Ag^+ was the main factor contributing to the observed toxicity of Ag nanoparticles.[132] A more systematic study about the role of dissolution in governing the toxic effect of various metallic nanoparticles (e.g. Ag, Cu, Ni, and Co) has revealed that the presence of soluble copper ions is not necessarily responsible for the overall toxicity of copper nanoparticles due to the low dissolution of copper, even though soluble copper ions are extremely toxic. However, the toxicity of Ni nanoparticles largely resulted from the presence of dissolved Ni, because of its large dissolution capability.[135] Therefore, the dissolution ability of nanomaterials is another key parameter that needs to be taken into account in determining the overall risk assessment of nanomaterials.

The aggregation of nanoparticles is strongly affected by the particle size, shape, pH value, and ionic strength of aqueous solutions.[136, 137] In turn, the degree of the aggregation of nanoparticles can influence the nature of particle dissolution,[138] the available reactive surface area, and ultimately, their interaction with biological species.[139] For example, a comparison of the toxic effects of bulk TiO_2 and aggregated TiO_2 nanoparticles has demonstrated that algal cells (*P. subcapitata*) tended to become entrapped in small TiO_2 aggregates, while experiencing growth inhibition because the light essential for growth was shielded by nanoparticles.[140] As such, the toxicity evaluation of nanostructures should take into consideration not only the chemical but also the physical properties of the nanomaterials.

1.7 References

1. G. W. Crabtree and N. S. Lewis, *Physics Today*, **2007**, *60*, 37-42.
2. M. Gratzel, *Inorganic Chemistry*, **2005**, *44*, 6841-6851.
3. U. Bach, D. Lupo, P. Comte, J. E. Moser, F. Weissortel, J. Salbeck, H. Spreitzer and M. Gratzel, *Nature*, **1998**, *395*, 583-585.
4. A. Hagfeldt, G. Boschloo, L. Sun, L. Kloo and H. Pettersson, *Chemical Reviews*, **2010**, *110*, 6595-6663.
5. G. Yu, J. Gao, J. C. Hummelen, F. Wudl and A. J. Heeger, *Science*, **1995**, *270*, 1789-1791.
6. W. U. Huynh, J. J. Dittmer and A. P. Alivisatos, *Science*, **2002**, *295*, 2425-2427.
7. R. Rossetti, S. Nakahara and L. E. Brus, *Journal of Chemical Physics*, **1983**, *79*, 1086-1088.
8. X. Peng, J. Wickham and A. P. Alivisatos, *Journal of the American Chemical Society*, **1998**, *120*, 5343-5344.
9. Z. A. Peng and X. G. Peng, *Journal of the American Chemical Society*, **2001**, *123*, 183-184.
10. Z. A. Peng and X. G. Peng, *Journal of the American Chemical Society*, **2002**, *124*, 3343-3353.
11. L. H. Qu and X. G. Peng, *Journal of the American Chemical Society*, **2002**, *124*, 2049-2055.
12. W. W. Yu, L. H. Qu, W. Z. Guo and X. G. Peng, *Chemistry of Materials*, **2003**, *15*, 2854-2860.
13. L. H. Qu, Z. A. Peng and X. G. Peng, *Nano Letters*, **2001**, *1*, 333-337.

14. W. W. Yu, Y. A. Wang and X. G. Peng, *Chemistry of Materials*, **2003**, *15*, 4300-4308.

15. J. S. Owen, E. M. Chan, H. Liu and A. P. Alivisatos, *Journal of the American Chemical Society*, **2010**, *132*, 18206-18213.

16. H. Liu, J. S. Owen and A. P. Alivisatos, *Journal of the American Chemical Society*, **2007**, *129*, 305-312.

17. C. B. Murray, C. R. Kagan and M. G. Bawendi, *Annual Review of Materials Science*, **2000**, *30*, 545-610.

18. A. M. Smith and S. M. Nie, *Accounts of Chemical Research*, **2010**, *43*, 190-200.

19. J. Z. Zhang, *Journal of Physical Chemistry B*, **2000**, *104*, 7239-7253.

20. W. A. Tisdale, K. J. Williams, B. A. Timp, D. J. Norris, E. S. Aydil and X. Y. Zhu, *Science*, **2010**, *328*, 1543-1547.

21. P. Guyot-Sionnest, M. Shim, C. Matranga and M. Hines, *Physical Review B*, **1999**, *60*, R2181-R2184.

22. T. C. Kippeny, M. J. Bowers, A. D. Dukes, J. R. McBride, R. L. Orndorff, M. D. Garrett and S. J. Rosenthal, *Journal of Chemical Physics*, **2008**, *128*, 084713.

23. M. Kuno, J. K. Lee, B. O. Dabbousi, F. V. Mikulec and M. G. Bawendi, *Journal of Chemical Physics*, **1997**, *106*, 9869-9882.

24. N. Y. Morgan, C. A. Leatherdale, M. Drndicacute, M. V. Jarosz, M. A. Kastner and M. Bawendi, *Physical Review B*, **2002**, *66*, 075339.

25. D. V. Talapin, J.-S. Lee, M. V. Kovalenko and E. V. Shevchenko, *Chemical Reviews*, **2009**, *110*, 389-458.

26. K. E. Knowles, D. B. Tice, E. A. McArthur, G. C. Solomon and E. A. Weiss, *Journal of the American Chemical Society*, **2009**, *132*, 1041-1050.

27. F. Dong, H. Y. Han, J. G. Liang and D. L. Lu, *Luminescence*, **2008**, *23*, 321-326.

28. S. Jeong, M. Achermann, J. Nanda, S. Ivanov, V. I. Klimov and J. A. Hollingsworth, *Journal of the American Chemical Society*, **2005**, *127*, 10126-10127.

29. M. A. Hines and P. Guyot-Sionnest, *Journal of Physical Chemistry*, **1996**, *100*, 468-471.

30. P. Reiss, M. Protiere and L. Li, *Small*, **2009**, *5*, 154-168.

31. A. J. Nozik, M. C. Beard, J. M. Luther, M. Law, R. J. Ellingson and J. C. Johnson, *Chemical Reviews*, **2010**, *110*, 6873-6890.

32. J. M. Luther, M. Law, M. C. Beard, Q. Song, M. O. Reese, R. J. Ellingson and A. J. Nozik, *Nano Letters*, **2008**, *8*, 3488-3492.

33. S.-Q. Fan, D. Kim, J.-J. Kim, D. W. Jung, S. O. Kang and J. Ko, *Electrochemistry Communications*, **2009**, *11*, 1337-1339.

34. Y. N. Xia, P. D. Yang, Y. G. Sun, Y. Y. Wu, B. Mayers, B. Gates, Y. D. Yin, F. Kim and Y. Q. Yan, *Advanced Materials*, **2003**, *15*, 353-389.

35. M. Law, L. E. Greene, J. C. Johnson, R. Saykally and P. D. Yang, *Nature Materials*, **2005**, *4*, 455-459.

36. Z. Y. Fan, H. Razavi, J. W. Do, A. Moriwaki, O. Ergen, Y. L. Chueh, P. W. Leu, J. C. Ho, T. Takahashi, L. A. Reichertz, S. Neale, K. Yu, M. Wu, J. W. Ager and A. Javey, *Nature Materials*, **2009**, *8*, 648-653.

37. S. Iijima, *Nature*, **1991**, *354*, 56-58.

38. S. Banerjee, T. Hemraj-Benny and S. S. Wong, *Advanced Materials*, **2005**, *17*, 17-29.

39. X. H. Peng and S. S. Wong, *Advanced Materials*, **2009**, *21*, 625-642.

40. M. Zheng, A. Jagota, M. S. Strano, A. P. Santos, P. Barone, S. G. Chou, B. A. Diner, M. S. Dresselhaus, R. S. McLean, G. B. Onoa, G. G. Samsonidze, E. D. Semke, M. Usrey and D. J. Walls, *Science*, **2003**, *302*, 1545-1548.

41. Y. B. Zhang, M. Kanungo, A. J. Ho, P. Freimuth, D. van der Lelie, M. Chen, S. M. Khamis, S. S. Datta, A. T. C. Johnson, J. A. Misewich and S. S. Wong, *Nano Letters*, **2007**, *7*, 3086-3091.

42. M. Alvaro, C. Aprile, B. Ferrer and H. Garcia, *Journal of the American Chemical Society*, **2007**, *129*, 5647-5655.

43. H. M. Li, F. O. Cheng, A. M. Duft and A. Adronov, *Journal of the American Chemical Society*, **2005**, *127*, 14518-14524.

44. N. W. S. Kam, T. C. Jessop, P. A. Wender and H. J. Dai, *Journal of the American Chemical Society*, **2004**, *126*, 6850-6851.

45. C. A. Dyke and J. M. Tour, *Journal of the American Chemical Society*, **2003**, *125*, 1156-1157.

46. J. L. Delgado, P. de la Cruz, F. Langa, A. Urbina, J. Casado and J. T. L. Navarrete, *Chemical Communications*, **2004**, 1734-1735.

47. T. Hemraj-Benny and S. S. Wong, *Chemistry of Materials*, **2006**, *18*, 4827-4839.

48. W. Zhang and T. M. Swager, *Journal of the American Chemical Society*, **2007**, *129*, 7714-7715.

49. D. Pantarotto, C. D. Partidos, R. Graff, J. Hoebeke, J. P. Briand, M. Prato and A. Bianco, *Journal of the American Chemical Society*, **2003**, *125*, 6160-6164.

50. J. J. Ge, H. Q. Hou, Q. Li, M. J. Graham, A. Greiner, D. H. Reneker, F. W. Harris and S. Z. D. Cheng, *Journal of the American Chemical Society*, **2004**, *126*, 15754-15761.

51. T. Durkop, S. A. Getty, E. Cobas and M. S. Fuhrer, *Nano Letters*, **2004**, *4*, 35-39.

52. S. Berson, R. de Bettignies, S. Bailly, S. Guillerez and B. Jousselme, *Advanced Functional Materials*, **2007**, *17*, 3363-3370.

53. I. Khatri, S. Adhikari, H. R. Aryal, T. Soga, T. Jimbo and M. Umeno, *Applied Physics Letters*, **2009**, *94*, 093509.

54. D. S. Hecht, L. B. Hu and G. Irvin, *Advanced Materials*, **2011**, *23*, 1482-1513.

55. Z. C. Wu, Z. H. Chen, X. Du, J. M. Logan, J. Sippel, M. Nikolou, K. Kamaras, J. R. Reynolds, D. B. Tanner, A. F. Hebard and A. G. Rinzler, *Science*, **2004**, *305*, 1273-1276.

56. T. M. Barnes, J. D. Bergeson, R. C. Tenent, B. A. Larsen, G. Teeter, K. M. Jones, J. L. Blackburn and J. van de Lagemaat, *Applied Physics Letters*, **2010**, *96*, 243309.

57. B. Pradhan, S. K. Batabyal and A. J. Pal, *Applied Physics Letters*, **2006**, *88*, 093106.

58. M. S. Arnold, J. D. Zimmerman, C. K. Renshaw, X. Xu, R. R. Lunt, C. M. Austin and S. R. Forrest, *Nano Letters*, **2009**, *9*, 3354-3358.

59. A. J. Ferguson, J. L. Blackburn, J. M. Holt, N. Kopidakis, R. C. Tenent, T. M. Barnes, M. J. Heben and G. Rumbles, *Journal of Physical Chemistry Letters*, **2010**, *1*, 2406-2411.

60. T. Hasobe, S. Fukuzumi and P. V. Kamat, *Journal of Physical Chemistry B*, **2006**, *110*, 25477-25484.

61. M. H. Ham, G. L. C. Paulus, C. Y. Lee, C. Song, K. Kalantar-zadeh, W. Choi, J. H. Han and M. S. Strano, *Acs Nano*, **2010**, *4*, 6251-6259.

62. E. Shafran, B. D. Mangum and J. M. Gerton, *Nano Letters*, **2010**, *10*, 4049-4054.

63. A. Kongkanand, K. Tvrdy, K. Takechi, M. Kuno and P. V. Kamat, *Journal of the American Chemical Society*, **2008**, *130*, 4007-4015.

64. G. Girishkumar, M. Rettker, R. Underhile, D. Binz, K. Vinodgopal, P. McGinn and P. Kamat, *Langmuir*, **2005**, *21*, 8487-8494.

65. A. Kongkanand, K. Vinodgopal, S. Kuwabata and P. V. Kamat, *Journal of Physical Chemistry B*, **2006**, *110*, 16185-16188.

66. G. G. Wildgoose, C. E. Banks and R. G. Compton, *Small*, **2006**, *2*, 182-193.

67. A. Star, V. Joshi, S. Skarupo, D. Thomas and J.-C. P. Gabriel, *The Journal of Physical Chemistry B*, **2006**, *110*, 21014-21020.

68. N. Jia, Q. Lian, H. Shen, C. Wang, X. Li and Z. Yang, *Nano Letters*, **2007**, *7*, 2976-2980.

69. K. Kostarelos, L. Lacerda, G. Pastorin, W. Wu, S. Wieckowski, J. Luangsivilay, S. Godefroy, D. Pantarotto, J. P. Briand, S. Muller, M. Prato and A. Bianco, *Nature Nanotechnology*, **2007**, *2*, 108-113.

70. D. M. Guldi, G. M. A. Rahman, V. Sgobba, N. A. Kotov, D. Bonifazi and M. Prato, *J. Am. Chem. Soc.*, **2006**, *128*, 2315-2323.

71. L. Sheeney-Haj-Khia, B. Basnar and I. Willner, *Angewandte Chemie-International Edition*, **2005**, *44*, 78-83.

72. C. Schulz-Drost, V. Sgobba, C. Gerhards, S. Leubner, R. M. K. Calderon, A. Ruland and D. M. Guldi, *Angewandte Chemie-International Edition*, **2010**, *49*, 6425-6429.

73. B. R. Azamian, K. S. Coleman, J. J. Davis, N. Hanson and M. L. H. Green, *Chemical Communications*, **2002**, 366-367.

74. S. Banerjee and S. S. Wong, *Nano Letters*, **2002**, *2*, 195-200.

75. S. Ravindran, K. N. Bozhilov and C. S. Ozkan, *Carbon*, **2004**, *42*, 1537-1542.

76. L. Hu, Y. L. Zhao, K. Ryu, C. Zhou, J. F. Stoddart and G. Gruner, *Advanced Materials*, **2008**, *20*, 939-946.

77. V. Biju, T. Itoh, Y. Baba and M. Ishikawa, *Journal of Physical Chemistry B*, **2006**, *110*, 26068-26074.

78. B. F. Pan, D. X. Cui, C. S. Ozkan, M. Ozkan, P. Xu, T. Huang, F. T. Liu, H. Chen, Q. Li, R. He and F. Gao, *Journal of Physical Chemistry C*, **2008**, *112*, 939-944.

79. N. Cho, K. R. Choudhury, R. B. Thapa, Y. Sahoo, T. Ohulchanskyy, A. N. Cartwright, K. S. Lee and P. N. Prasad, *Advanced Materials*, **2007**, *19*, 232-236.

80. D. M. Guldi, G. M. A. Rahman, V. Sgobba, N. A. Kotov, D. Bonifazi and M. Prato, *Journal of the American Chemical Society*, **2006**, *128*, 2315-2323.

81. X. L. Li, Y. Jia and A. Y. Cao, *Acs Nano*, **2010**, *4*, 506-512.

82. X. L. Li, Y. Jia, J. Q. Wei, H. W. Zhu, K. L. Wang, D. H. Wu and A. Y. Cao, *Acs Nano*, **2010**, *4*, 2142-2148.

83. B. J. Landi, S. L. Castro, H. J. Ruf, C. M. Evans, S. G. Bailey and R. P. Raffaelle, *Solar Energy Materials and Solar Cells*, **2005**, *87*, 733-746.

84. J. E. Weaver, M. R. Dasari, A. Datar, S. Talapatra and P. Kohli, *Acs Nano*, **2010**, *4*, 6883-6893.

85. Y. Wu, J. Xiang, C. Yang, W. Lu and C. M. Lieber, *Nature*, **2004**, *430*, 61-65.

86. Y. Y. Wu, R. Fan and P. D. Yang, *Nano Letters*, **2002**, *2*, 83-86.

87. E. C. Garnett and P. D. Yang, *Journal of the American Chemical Society*, **2008**, *130*, 9224-9225.

88. X. N. Wang, H. J. Zhu, Y. M. Xu, H. Wang, Y. Tao, S. Hark, X. D. Xiao and Q. A. Li, *Acs Nano*, **2010**, *4*, 3302-3308.

89. J. A. Goebl, R. W. Black, J. Puthussery, J. Giblin, T. H. Kosel and M. Kuno, *Journal of the American Chemical Society*, **2008**, *130*, 14822-14833.

90. Y. Huang, X. F. Duan, Q. Q. Wei and C. M. Lieber, *Science*, **2001**, *291*, 630-633.

91. D. J. Milliron, S. M. Hughes, Y. Cui, L. Manna, J. B. Li, L. W. Wang and A. P. Alivisatos, *Nature*, **2004**, *430*, 190-195.

92. G. Z. Shen, D. Chen and C. J. Lee, *Journal of Physical Chemistry B*, **2006**, *110*, 15689-15693.

93. M. S. Gudiksen, L. J. Lauhon, J. Wang, D. C. Smith and C. M. Lieber, *Nature*, **2002**, *415*, 617-620.

94. J. Wang, *Journal of Materials Chemistry*, **2008**, *18*, 4017-4020.

95. A. J. Mieszawska, R. Jalilian, G. U. Sumanasekera and F. P. Zamborini, *Small*, **2007**, *3*, 722-756.

96. H. J. Fan, M. Knez, R. Scholz, K. Nielsch, E. Pippel, D. Hesse, M. Zacharias and U. Gosele, *Nature Materials*, **2006**, *5*, 627-631.

97. F. Xu, V. Volkov, Y. M. Zhu, H. Y. Bai, A. Rea, N. V. Valappil, W. Su, X. Y. Gao, I. L. Kuskovsky and H. Matsui, *Journal of Physical Chemistry C*, **2009**, *113*, 19419-19423.

98. D. V. Talapin, R. Koeppe, S. Gotzinger, A. Kornowski, J. M. Lupton, A. L. Rogach, O. Benson, J. Feldmann and H. Weller, *Nano Letters*, **2003**, *3*, 1677-1681.

99. L. Wang, H. W. Wei, Y. J. Fan, X. Gu and J. H. Zhan, *Journal of Physical Chemistry C*, **2009**, *113*, 14119-14125.

100. C. J. Brumlik and C. R. Martin, *Journal of the American Chemical Society*, **1991**, *113*, 3174-3175.

101. C. R. Martin, *Science*, **1994**, *266*, 1961-1966.

102. B. K. Oh, S. Park, J. E. Millstone, S. W. Lee, K. B. Lee and C. A. Mirkin, *Journal of the American Chemical Society*, **2006**, *128*, 11825-11829.

103. B. R. Martin, D. J. Dermody, B. D. Reiss, M. M. Fang, L. A. Lyon, M. J. Natan and T. E. Mallouk, *Advanced Materials*, **1999**, *11*, 1021-1025.

104. D. J. Pena, J. K. N. Mbindyo, A. J. Carado, T. E. Mallouk, C. D. Keating, B. Razavi and T. S. Mayer, *Journal of Physical Chemistry B*, **2002**, *106*, 7458-7462.

105. S. Park, J. H. Lim, S. W. Chung and C. A. Mirkin, *Science*, **2004**, *303*, 348-351.

106. W. Zhu, G. Z. Wang, X. Hong and X. S. Shen, *Journal of Physical Chemistry C*, **2009**, *113*, 5450-5454.

107. P. K. Jain, L. Amirav, S. Aloni and A. P. Alivisatos, *Journal of the American Chemical Society*, **2010**, *132*, 9997-9999.

108. X. M. Shuai and W. Z. Shen, *The Journal of Physical Chemistry C*, **2011**, *115*, 6415-6422.

109. D. O. Demchenko, R. D. Robinson, B. Sadtler, C. K. Erdonmez, A. P. Alivisatos and L. W. Wang, *Acs Nano*, **2008**, *2*, 627-636.

110. R. D. Robinson, B. Sadtler, D. O. Demchenko, C. K. Erdonmez, L. W. Wang and A. P. Alivisatos, *Science*, **2007**, *317*, 355-358.

111. Y. T. Chong, D. Gorlitz, S. Martens, M. Y. E. Yau, S. Allende, J. Bachmann and K. Nielsch, *Advanced Materials*, **2010**, *22*, 2435-2439.

112. B. M. Kayes, H. A. Atwater and N. S. Lewis, *Journal of Applied Physics*, **2005**, *97*, 114302.

113. K. S. Leschkies, R. Divakar, J. Basu, E. Enache-Pommer, J. E. Boercker, C. B. Carter, U. R. Kortshagen, D. J. Norris and E. S. Aydil, *Nano Letters*, **2007**, *7*, 1793-1798.

114. L. E. Greene, M. Law, B. D. Yuhas and P. D. Yang, *Journal of Physical Chemistry C*, **2007**, *111*, 18451-18456.

115. M. Law, L. E. Greene, A. Radenovic, T. Kuykendall, J. Liphardt and P. D. Yang, *Journal of Physical Chemistry B*, **2006**, *110*, 22652-22663.

116. D. C. Lee, I. Robel, J. M. Pietryga and V. I. Klimov, *Journal of the American Chemical Society*, **2010**, *132*, 9960-9962.

117. D. D. Lin, H. Wu, R. Zhang, W. Zhang and W. Pan, *Journal of the American Ceramic Society*, **2010**, *93*, 3384-3389.

118. Z. Zhang, C. Shao, X. Li, C. Wang, M. Zhang and Y. Liu, *ACS Applied Materials & Interfaces*, **2010**, *2*, 2915-2923.

119. M. T. Niu, F. Huang, L. F. Cui, P. Huang, Y. L. Yu and Y. S. Wang, *Acs Nano*, **2010**, *4*, 681-688.

120. M. N. Moore, *Environment International*, **2006**, *32*, 967-976.

121. P. V. Kamat, R. Huehn and R. Nicolaescu, *Journal of Physical Chemistry B*, **2002**, *106*, 788-794.

122. M. Ovecka, I. Lang, F. Baluska, A. Ismail, P. Illes and I. K. Lichtscheidl, *Protoplasma*, **2005**, *226*, 39-54.

123. P. G. Barlow, K. Donaldson, J. MacCallum, A. Clouter and V. Stone, *Toxicology Letters*, **2005**, *155*, 397-401.

124. C. Ispas, D. Andreescu, A. Patel, D. V. Goia, S. Andreescu and K. N. Wallace, *Environmental Science & Technology*, **2009**, *43*, 6349-6356.

125. C. Carlson, S. M. Hussain, A. M. Schrand, L. K. Braydich-Stolle, K. L. Hess, R. L. Jones and J. J. Schlager, *Journal of Physical Chemistry B*, **2008**, *112*, 13608-13619.

126. A. Simon-Deckers, S. Loo, M. Mayne-L'Hermite, N. Herlin-Boime, N. Menguy, C. Reynaud, B. Gouget and M. Carriere, *Environmental Science & Technology*, **2009**, *43*, 8423-8429.

127. J. L. Elechiguerra, J. L. Burt, J. R. Morones, A. Camacho-Bragado, X. Gao, H. H. Lara and M. J. Yacaman, *Journal of nanobiotechnology*, **2005**, *3*, 1-6.

128. T. Mironava, M. Hadjiargyrou, M. Simon, V. Jurukovski and M. H. Rafailovich, *Nanotoxicology*, **2010**, *4*, 120-137.

129. E. V. Basiuk, O. E. Ochoa-Olmos and L. F. De la Mora-Estrada, *Journal of Nanoscience and Nanotechnology*, **2011**, *11*, 3016-3038.

130. X. S. Zhu, L. Zhu, Z. H. Duan, R. Q. Qi, Y. Li and Y. P. Lang, *Journal of Environmental Science and Health Part a-Toxic/Hazardous Substances & Environmental Engineering*, **2008**, *43*, 278-284.

131. L. K. Limbach, P. Wick, P. Manser, R. N. Grass, A. Bruinink and W. J. Stark, *Environmental Science & Technology*, **2007**, *41*, 4158-4163.

132. E. Navarro, F. Piccapietra, B. Wagner, F. Marconi, R. Kaegi, N. Odzak, L. Sigg and R. Behra, *Environmental Science & Technology*, **2008**, *42*, 8959-8964.

133. N. S. Fisher, G. J. Jones and D. M. Nelson, *Journal of Experimental Marine Biology and Ecology*, **1981**, *51*, 37-56.

134. T. Li, B. Albee, M. Alemayehu, R. Diaz, L. Ingham, S. Kamal, M. Rodriguez and S. W. Bishnoi, *Analytical and Bioanalytical Chemistry*, **2010**, *398*, 689-700.

135. R. J. Griffitt, J. Luo, J. Gao, J. C. Bonzongo and D. S. Barber, *Environmental Toxicology and Chemistry*, **2008**, *27*, 1972-1978.

136. V. K. Sharma, *Journal of Environmental Science and Health Part a-Toxic/Hazardous Substances & Environmental Engineering*, **2009**, *44*, 1485-1495.

137. A. R. Petosa, D. P. Jaisi, I. R. Quevedo, M. Elimelech and N. Tufenkji, *Environmental Science & Technology*, **2010**, *44*, 6532-6549.

138. J. Liu, D. M. Aruguete, M. Murayama and M. F. Hochella, *Environmental Science & Technology*, **2009**, *43*, 8178-8183.

139. T. D. Zaveri, N. V. Dolgova, B. H. Chu, J. Y. Lee, J. E. Wong, T. P. Lele, F. Ren and B. G. Keselowsky, *Biomaterials*, **2010**, *31*, 2999-3007.

140. V. Aruoja, H. C. Dubourguier, K. Kasemets and A. Kahru, *Science of the Total Environment*, **2009**, *407*, 1461-1468.

Chapter 2 Hierarchical Synthesis of Carbon Nanotube – Nanocrystal Heterostructures and Investigation into Controlling Nanocrystal Density and Spatial Location on the Surfaces of Carbon Nanotubes

2.1 Introduction

As discussed in the Introduction chapter, CNT–nanocrystal heterostructures have been of great interest for a wide variety of applications. Selective functionalization of CNTs with precise control over the location as well as the density of nanocrystals can potentially advance practical application of such heterostructures as building blocks in electronic devices. Prior studies have examined the idea of selective functionalization of CNTs with nanocrystals. For instance, by making use of sidewall protection using a polystyrene matrix, selective bi-functionalization of the ends of CNTs with carboxylate groups at one end and thiol groups at the other has been elegantly demonstrated.[141] Moreover, a combination of focused-ion-beam (FIB) irradiation and subsequent mild chemical treatments was used to specifically anchor nanoparticles, fluorescent nanospheres, amino acids, as well as proteins onto pre-treated sites on the CNT surface through electrostatic and covalent interactions.[142] In addition, the use of biologically specific recognition strategies, involving small, amphiphilic proteins, has been demonstrated to create hybrid nanostructures of CNTs and Au nanoparticles.[143] While all of these methods clearly offer a viable route forward, it is also useful to develop such a protocol, which would be neither tedious nor expensive, and would involve the use of ambient experimental conditions without requiring complicated instrumental facilities.

Owing to the obvious reactivity of CNTs subject to covalent functionalization as implied in Chapter 1, the synthesis of CNT–nanocrystal heterostructures by covalent approaches has offered potential advantages in terms of capabilities of controlling the spatial coverage and location of nanocrystals on the CNT surfaces. Specifically, the tips of CNTs can be preferentially functionalized, attaining a higher density of functional moieties (e.g. carboxylic groups) there, as opposed to relatively inert sidewalls. In this regard, we have attempted to achieve site-selective placement of two types of nanocrystals onto CNTs by systematically exploring a number of different reaction conditions (e.g. the degree of oxidation treatment, particle concentration, and reaction time). A more rigorous and quantifiable correlation between chemical treatment and attachment strategy of nanoparticles/QDs onto CNT surfaces is demonstrated herein.

Specifically, we have used multi-walled carbon nanotubes (MWNTs) as a model template with which to construct complex hierarchical assembles of nanotube–nanocrystal heterostructures. That is, building on prior studies,[144] we initially oxidized our CNTs with carboxylic groups and then covalently functionalized the oxidized MWNT surfaces with either pre-synthesized Au NPs or CdSe QDs. The key step forward was that we could reliably alter the positions and densities of these NPs and QDs through appropriate variations in oxidation treatments and overall reaction conditions. For instance, one structure we have produced consists of Au NPs mainly localized at carbon nanotube tips with an over-coating of QDs along the nanotube sidewalls. We can also form the converse structure, consisting of QDs immobilized at the tips and Au NPs concentrated along the sidewalls.

To the best of our knowledge, such a generalized approach to the site-selective placement of both nanoparticles and quantum dots, i.e. either at the ends or sidewalls of nanotubes, using simple chemistry, has not as yet been reported. As such, our work is highly relevant not only

from the fundamental idea of tailoring chemical groups and moieties on nanotubes through a facile protocol but also from the practical notion of using the nanotube surface as a platform with which to precisely add specific functionalities. Moreover, to the best of our knowledge, very little has been published on the covalent fabrication of CNT-based nanocomposites containing two or more different types of nanocrystals. These structures are fascinating because of their potential for multi-functionality. Given that precise manipulation and placement of nanoscale building blocks represent a key goal of nanoscience, our effort in this work implies a predictable site-specific functionalization of CNTs with two or more different types of nanoparticles.

2.2 Experimental Section

2.2.1 *Materials preparation*

2.2.1.a Synthesis of Au nanoparticles (NPs)

Au nanocrystals (~12.7 nm) were prepared by a standard protocol[145] in aqueous media by the reduction of $HAuCl_4$ in the presence of sodium citrate. Specifically, 5 mL of 1% sodium citrate was added to 95 mL of aqueous $HAuCl_4$ solution containing 5 mg of Au, followed by heating to 80ºC for 20 min to ultimately yield colloidal gold.

2.2.1.b Synthesis of CdSe QDs

CdSe QDs (~ 4.2 nm) were prepared by a method[146] adapted as a safer, easier, and faster alternative to conventional syntheses. Specifically, 30 mg Se was dissolved in 5 mL of 1-octadecence (ODE) containing trioctylphosphine (TOP). 13 mg of CdO was subsequently added into a 25 mL round-bottom flask containing 10 mL ODE and 0.6 mL oleic acid (OA). CdO was

then dissolved into the mixture, remaining colorless as the flask was heated. When the temperature attained 225˚C, 1 mL of as-prepared Se solution was injected. A noticeable color change, indicative of nanocrystal formation, was observed immediately.

2.2.1.c Ligand exchange of CdSe QDs (Functionalized, amine-terminated CdSe)

10 mL of chloroform and 20 mL of a 0.5 M methanol solution of 2-aminoethanethiol (AET) were added to 10 mL of ODE solution containing as-prepared CdSe QDs. As a result, the mercapto groups associated with the thiol bonded to the Cd atoms, whereas the pendant amine groups rendered the modified QDs hydrophilic so that QDs can be dispersible in aqueous solution. These amine-terminated nanocrystals, namely AET-CdSe, were then precipitated out of solution by centrifugation upon ligand exchange, followed by subsequent washing with methanol and ultimately, stored in distilled water.

2.2.1.d MWNT Oxidation

Pristine MWNTs were oxidized by a variety of oxidation treatments, by which nanotubes were not only purified but also coated with carboxylic groups for further conjugation with nanocrystals. Essentially, we systematically increased the strength of nanotube oxidation according to known protocols. For instance, it is known that (i) gas-phase oxidation introduces very few defect sites, (ii) refluxing in dilute nitric acid is a form of mild oxidation, and (iii) sonication in H_2SO_4/H_2O_2 is a more robust oxidative method for increasing the number of carboxylic acid groups.[147] The subsequent presence of nanocrystals permitted the direct observation of the density distribution of defects following each of these specific treatments, which we now describe.

Wet air treatment:

100 mg MWNTs was placed at the bottom of a 100 mL two-neck flask. The flask was then heated to 200ºC. Water steam, produced by boiling distilled water in a 500 mL Erlenmeyer flask, was subsequently passed through the flask for 5 h as a means of mildly functionalizing the nanotube surface.

Ozonolysis / H_2O_2 treatment:

MWNTs were oxidized by a modified ozonolysis method[148-151] based on techniques developed for SWNTs. Specifically, 100 mg of pristine MWNTs were dispersed in 150 mL methanol by extensive sonication. The resulting reaction mixture was stirred vigorously during ozonolysis, which was carried out by placing the reaction flask in an ice/acetone bath. A 25% aqueous H_2O_2 solution was then added and heated to 70ºC for 4 h so as to cleave the generated ozonide intermediate. The ozonized MWNTs were finally vacuum filtered using a 0.2 μm polycarbonate membrane (Millipore, type GTTP), extensively washed with distilled water, and finally dried in an oven.

Dilute HNO_3 treatment:

MWNTs were refluxed in either a 3 M or 9 M solution of HNO_3 for 36 h. The oxidized MWNTs were subsequently filtered, washed, and dried, prior to subsequent use.

$KMnO_4$ / H_2SO_4 treatment:

100 mg of as-prepared MWNTs were dispersed in 20 mL of 0.5 M sulfuric acid. Separately, 1.98 g of potassium permanganate was dissolved in 20 mL of 0.5 M sulfuric acid and placed in a funnel fitted to the side neck of the reaction flask. The flask was then heated to 150˚C with vigorous stirring. $KMnO_4$ solution was added dropwise through the side funnel. The solution was refluxed for an additional 5 h. The mixture was then cooled and filtered. The filtrate was further washed with concentrated hydrochloric acid and distilled water in order to remove

as-generated manganese oxide.[152] Oxidized MWNTs were subsequently filtered, washed, and dried, prior to further use.

H_2SO_4 / HNO_3 treatment:

100 mg MWNTs were sonicated in a solution mixture of H_2SO_4 / HNO_3 (v : v = 3 : 1) for 2 h, and then refluxed for 2 h. These acid-treated MWNTs were subsequently filtered, washed, and dried, prior to use.

2.2.1.e Thiolation of oxidized MWNTs

10 mg of oxidized MWNTs were dispersed in 50 mL methanol by sonication, after which an aliquot of 0.1 M 2-(*N*-morpholino) ethanesulfonic acid (MES) buffer solution (pH = 6.0) was added, followed by activation through the addition of 57 mg *N*-hydroxysuccinimide (NHS) and 60 mg *N*-(3-dimethylaminopropyl)-*N'*-ethylcarbodiimide (EDC). The solution was then stirred for 30 min at room temperature. Afterwards, 200 mg AET was added with the reaction lasting for 12 h. The solution mixture was filtered through a polycarbonate membrane and washed with a large excess of water to remove excess NHS, EDC, and AET.

2.2.1.f Synthesis of MWNT–Au heterostructures

0.1 mg of thiolated MWNTs were dispersed in ~1 mL of distilled water by sonication. An aqueous solution of Au nanoparticles (NPs) was then added to the above solution and incubated for 2 h to promote gold-thiol bond formation. The final concentration of Au NPs in solution was 100 nM. After reaction, the solution was subsequently filtered and washed with an excess of water.

2.2.1.g Synthesis of MWNT–Au–CdSe heterostructures

Prior to reaction with CdSe, 0.1 mg of MWNT–Au heterostructures were further oxidized in 1 M HNO_3 for 0.5 h, 1 h, 6 h, 12 h, and 24 h in separate experiments, after which they were extensively washed with distilled water, oven dried, and re-dispersed in distilled water. An aliquot of 0.1 M MES buffer (pH = 6.0), EDC and NHS was then added to the above acid-treated MWNT–Au heterostructures in order to activate these structures for further coupling with AET-CdSe. The solution was stirred for 2 days. The resulting material was subsequently filtered and washed to remove loosely bound aggregates.

2.2.1.h Synthesis of MWNT–CdSe heterostructures

0.1 mg of oxidized MWNTs were dispersed in ~1 mL distilled water by sonication. An aliquot of 0.1 M MES buffer (pH = 6.0), EDC, and NHS in aqueous solution was added to the above solution, followed by the addition of AET-CdSe. The solution was then stirred for 2 days.

2.2.1.i Synthesis of MWNT–CdSe–Au heterostructures

0.1 mg of MWNT–CdSe heterostructures were further oxidized in 1 M HNO_3 for 0.5 h, 1 h, 6 h, 12 h, and 24 h in separate experiments, followed by extensive washing with distilled water and oven drying. Subsequent thiolation of acid-treated MWNT–CdSe heterostructures can create additional active sites for coupling with Au NPs. Afterwards, an aqueous solution of Au nanoparticles was added to a dispersed suspension of thiolated MWNT–CdSe heterostructures and subsequently incubated for 2 h. The resulting material was subsequently filtered and washed to remove loosely bound aggregates.

2.2.2 *Materials characterization*

2.2.2.a Powder X-ray diffraction

X-ray diffraction is a non-destructive analytical technique, which reveals information about the crystallographic structure and chemical composition of solid materials. The principle is that when an incident x-ray beam interacts with atoms periodically arranging in crystals, diffracted waves from different atoms can interfere with each other, resulting in the diffraction pattern highly correlated with lattice planes following the well-known Bragg's law. In general, the crystallographic structure (e.g. space group and crystal phase) of tested materials can be identified by comparing diffraction patterns, encompassing peak position and intensity, against a standard database. The crystallite size (grain size) of materials can be derived from the width of diffraction peaks by means of the Scherrer equation.

In our work, to analyze these heterostructures, as-prepared samples were sonicated and dispersed in ethanol, and finally air-dried upon deposition onto glass slides. Diffraction patterns of these materials were collected using a Scintag diffractometer, operating in the Bragg configuration using Cu K_α radiation (λ = 1.54 Å) from 20^o to 80° at scanning rates of 0.25° per minute.

2.2.2.b Electron microscopy

An electron microscope is an instrument that uses an electron beam to illuminate the specimen and produce a magnified image of samples. Two common types of electron microscopes used in our studies are the transmission electron microscope (TEM) and the scanning electron microscope (SEM). For TEM, a beam of electrons is transmitted through an ultra thin specimen. An image is formed as a result of interactions of electrons with the specimen,

which is then magnified by an objective lens and projected onto a fluorescent viewing screen. The resolution of a modern TEM is about 0.2 nm. The morphology, chemical composition, as well as crystallographic information can be obtained if relevant modules are placed with the scope. At lower magnifications, TEM image contrast arises from the difference in absorption of electrons in the material, due to the thickness and composition of the material.

By contrast, SEM produces images by probing the specimen with a beam of electrons, and then collecting signals produced in the form of low-energy secondary electrons (SE), back-scattered electrons (BSE), or characteristic X-rays, which contain information about the sample's surface topography and chemical composition. The resulting SEM images yield a characteristic three-dimensional appearance useful for understanding the surface structure of a sample. Generally, the image resolution of a SEM is about an order of magnitude poorer than that of a TEM. Because the intensity of the BSE signal is strongly correlated with the atomic number of elements, BSE images can provide information about the distribution of different elements in the samples. In addition, the characteristic X-rays, emitted upon interaction between the electron beam and inner shell electrons of the sample, can be used to identify the chemical composition and abundance of elements in the sample.

In our study, morphologies of MWNTs were characterized using a field emission scanning electron microscopy instrument (FE-SEM Leo 1550), operating at an accelerating voltage of 2.0 kV and equipped with energy-dispersive X-ray spectroscopy (EDS) capabilities. Samples for SEM were prepared by dispersing nanostructures in ethanol, and then depositing the sample onto either a copper grid or a silicon wafer, attached to a SEM brass stub.

Low magnification TEM images were taken at an accelerating voltage of 80 kV on a FEI Tecnai12 BioTwinG^2 instrument, equipped with an AMT XR-60 CCD Digital Camera System.

High-resolution images were obtained on a JEOL 2010F instrument, equipped with an INCA EDS system, at accelerating voltages of 200 kV. Specimens for all of these TEM experiments were prepared by dispersing the as-prepared product in ethanol, sonicating to ensure adequate dispersion of the nanostructures, and dipping one drop of solution onto a 300 mesh Cu grid, coated with a lacey carbon film.

2.2.2.c Optical spectroscopy

FTIR data were obtained on a Nexus 670 (Thermo Nicolet) equipped with a single reflectance zinc selenide (ZnSe) ATR accessory, a KBr beam splitter, and a DTGS KBr detector. Solid samples were placed onto a ZnSe crystal. Measurements were obtained in absorbance mode using the Smart Performer module. UV-visible spectra were collected using a Thermospectronics UV1 with quartz cells having a 10-mm path length. Samples were prepared by sonication in distilled water. Data were corrected to account for the solvent background. Samples for photoluminescence (PL) spectra were initially dispersed in deionized water. Fluorescence data were obtained at room temperature on a Jobin Yvon Spex Fluorolog 3 instrument with a 1 s integration time, using excitation wavelengths of 400 nm.

2.2.3 *Basis of calculations*

As-obtained, commercial pristine MWNTs measured 16.3 ± 5.1 nm in diameter and ~1–5 μm in length. As a rough guide to the extent of our functionalization protocol, we approximated the tips and sidewalls of the CNTs as hemispheres and cylinders, respectively, whose intrinsic structure presumably remained relatively intact during the entire functionalization process. Our calculations showed that the surface area ratio of tips to sidewalls of MWNT spanned from 1:

122 to 1: 613, reinforcing the conclusion that the surface area available to the nanoparticles was considerably higher along the nanotube sidewalls than at the tips. The number of nanoparticles localized at the tips and sidewalls of the tubes was counted from 20 nanotubes randomly selected for each type of heterostructures investigated.

In this work, we characterized the nature of our heterostructures using a number of different parameters. For instance, the percentage of nanoparticles at the tips was obtained by dividing the number of nanoparticles at the tips by the total number of nanoparticles on the entire CNT surface. By analogy, the percentage of nanoparticles along the sidewalls could be computed by dividing the number of nanoparticles along the nanotube sidewalls by the total number of nanocrystals on the entire CNT surface. The average nanocrystal coverage of each type of heterostructure investigated was calculated by dividing the total number of nanoparticles attached to the CNT surface by the corresponding length of the MWNTs in microns. For practical purposes, because of the significantly high surface area along the sidewalls of CNTs as compared with that at the tips, we could reasonably ignore the latter quantity in our overall nanocrystal density computation.

2.3 Results and Discussion

2.3.1 *Synthesis of Au NPs and ligand exchange of CdSe QDs.*

As-prepared Au NPs capped with citrate possessed a size of 12.7 ± 1.1 nm (Figure 2.1A) exhibiting a typical plasmon resonance peak centered at 520 nm (Figure 2.1B). As-prepared CdSe QDs capped with hydrophobic capping ligands (e.g. trioctylphosphine oxide (TOPO) oleic acid) were well dispersed in non-polar solvents such as hexane, toluene, and ODE. Upon ligand

exchange with 2-aminoethanethiol (AET), AET-CdSe QDs became hydrophilic due to the presence of charged amine groups on the surface.[153] TEM images of as-prepared CdSe QDs (Figure 2.1C) revealed that QDs were monodisperse with a diameter range of 4.22 ± 0.79 nm. The diameter of AET-CdSe, measuring 4.21 ± 0.62 nm, suggested that ligand exchange has little influence upon the overall size of QDs. The absorption spectrum of CdSe QDs shows a prominent excitonic absorption at 610 nm, corresponding to a bandgap of 2.04 eV. A slight blue shift of absorption of AET-CdSe QDs as compared with that of as-prepared CdSe QDs suggested a small increase in the band gap of the CdSe QDs after ligand exchange (Figure 2.1D). This observation could be attributed to the photo-oxidation of CdSe QDs induced by the presence of ligands.[154] It is also worth noting that the CdSe solution after ligand exchange was unstable and that the CdSe QDs precipitated after a few weeks in solution.

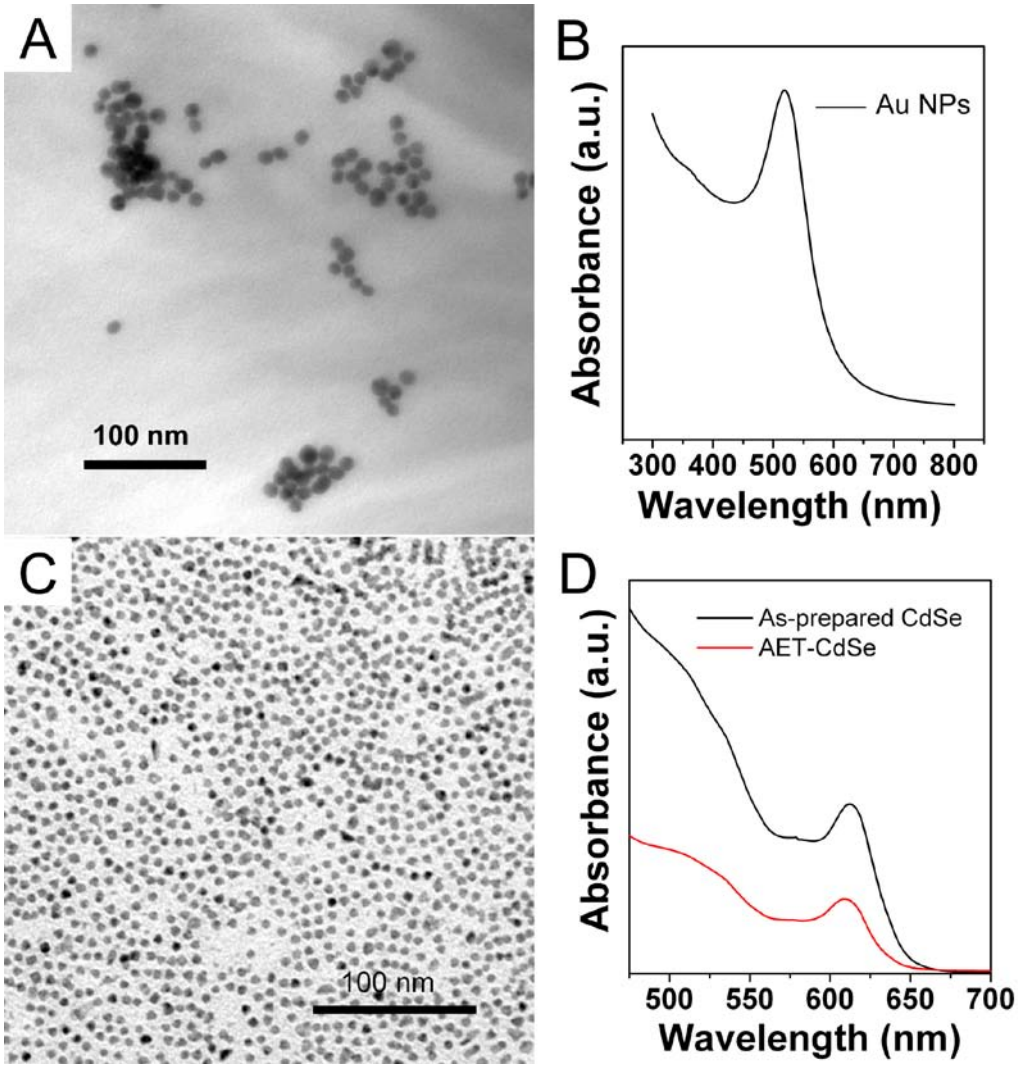

Figure 2.1: (A) TEM image and (B) UV-visible absorbance spectrum of as-prepared Au NPs. (C) TEM image of as-prepared CdSe nanocrystals. (D) UV-visible absorbance spectra of CdSe nanocrystals before and after ligand exchange.

2.3.2 *Oxidation and thiolation of MWNTs.*

The commercial MWNTs were produced by arc-discharge, with an overall nanotube content of 20 – 30 wt %. The major impurities in the pristine MWNTs consisted of multi-layered polygonal structures ("bucky onions") and graphitic particles. Based on SEM data along with EDS data highlighted in Figure 2.2, we concluded that no metal catalysts were present in the pristine MWNT sample. Since graphitic particles are believed to be more active than MWNTs, all of the oxidation processes employed in this work generally yielded relatively pure MWNTs.

In this work, several oxidation treatments using a variety of oxidants were applied, with the idea of systematically proceeding from a relatively mild oxidizing agent to progressively stronger oxidizing regimes. Therefore, the subsequent nanocrystal density can be tuned and correlated with the coverage and distribution of oxygenated functionalities on the CNT surface. In our series of experiments, the treatments we used, in order of increasing oxidizing strength, are: (a) oxygen in a wet air flow, (b) ozone/ H_2O_2, (c) 3 M nitric acid, (d) 9 M nitric acid, (e) $KMnO_4$ / H_2SO_4 (0.5 M), and (f) H_2SO_4 (18 M) / HNO_3 (16 M) mixture.

FT-IR results confirmed the success of the oxidation of MWNTs. For instance, for H_2SO_4/ HNO_3 treated MWNTs, a peak belonging to the C=O stretching vibration at 1691 cm^{-1} can be observed in its spectrum, indicating the presence of carboxylic groups on the CNT surface after oxidation (Figure 2.3A). The broad band between 3100 and 3500 cm^{-1} occurs as a result of the O-H stretching vibration emanating from the carboxylic acid groups. The peak at 2200 cm^{-1} could be attributed to the presence of CO_2 in the environment. Similar results were obtained for other oxidized MWNTs subjected to different oxidation treatments (Figure 2.3B). However, we note that the results cannot sufficiently provide for a quantitative determination of the extent of

oxidation treatment due to a lack of a practical standard as well as efficient calibration of experimental conditions.

In order to successfully attach Au NPs onto MWNTs, oxidized MWNTs were further thiolated with AET (Figure 2.4). Therefore, dangling thiol groups on the nanotube surface could serve as active sites for NP attachment. Upon thiolation of MWNTs, the formation of amide bonds led to a shift of carbonyl peaks to 1600 cm^{-1}. The peaks at 2910 and 2846 cm^{-1} correspond to aliphatic C-H stretching modes associated with the alkyl groups of AET (Figure 2.3A). As evidence for the validity of this entire approach, we note a far more successful attachment of Au NPs onto the MWNT surface after oxidation and thiolation as compared with merely using unoxidized, pristine MWNTs.

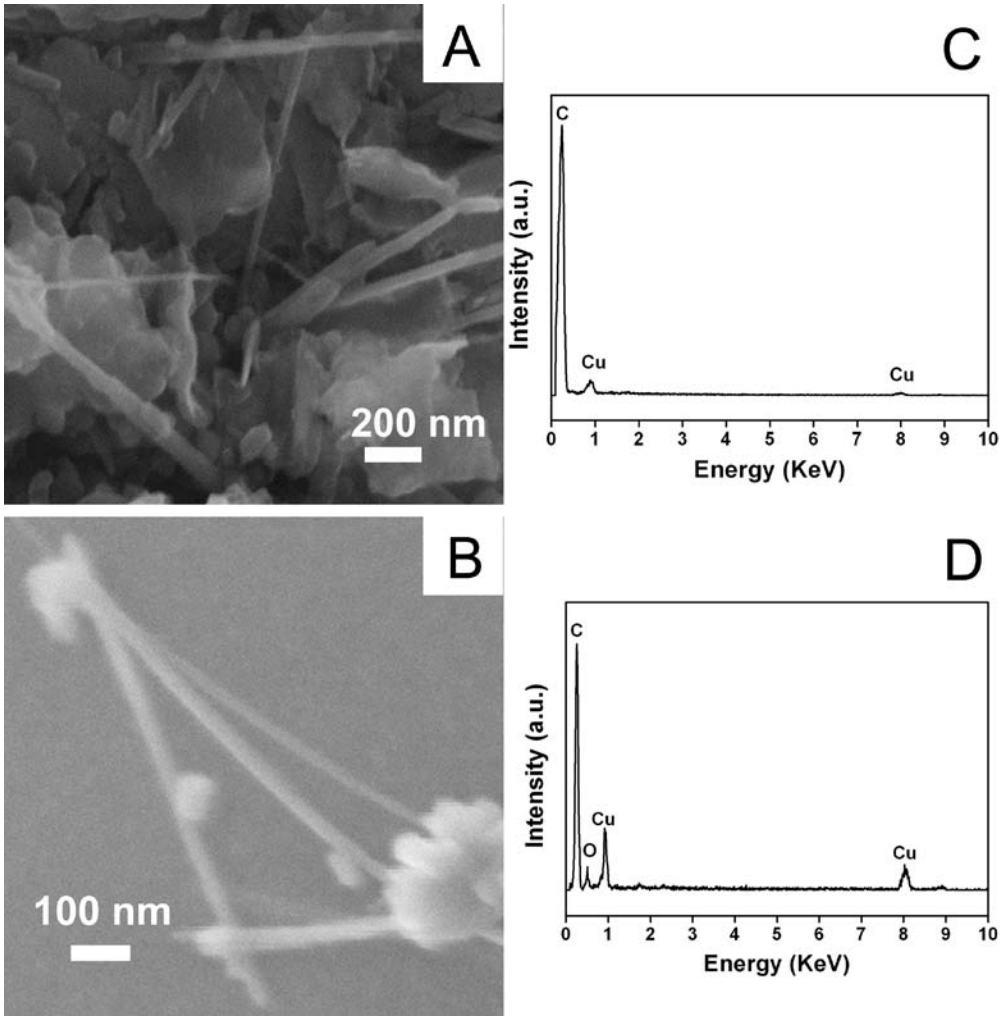

Figure 2.2: (A) SEM image of pristine MWNTs, showing an estimated overall nanotube content of 20-30 wt %. (B) SEM image of HNO_3/H_2SO_4 oxidized MWNTs. Acid purification treatment clearly removed the majority of graphitic nanoparticulate impurities but in spite of a lot of unpublished experimental effort, it was not 100% effective. (C-D) EDS of pristine MWNTs and HNO_3/H_2SO_4 oxidized MWNTs. The Cu signal originates from copper TEM grids used for SEM sample preparation.

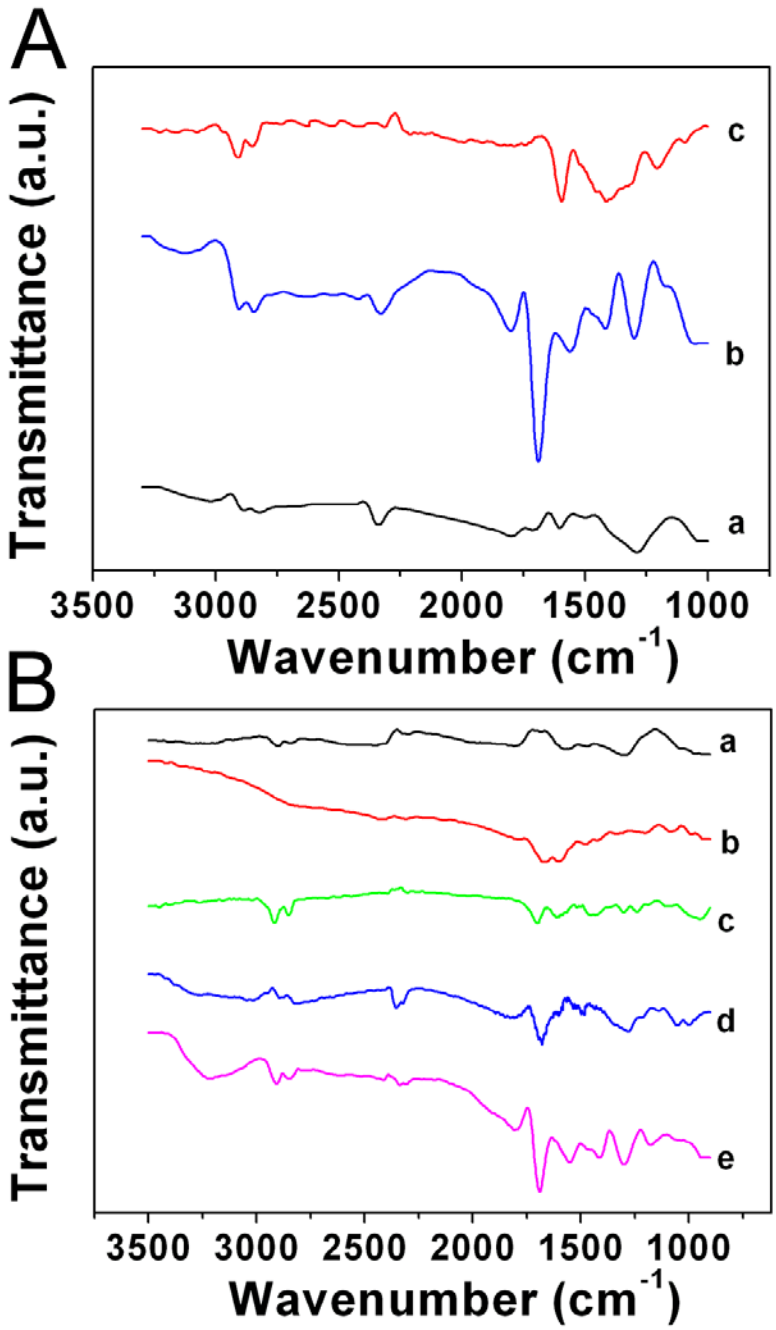

Figure 2.3: (A) FT-IR spectra of (a) pristine MWNTs, (b) oxidized MWNTs, and (c) thiolated-MWNTs, in which MWNTs were initially oxidized using a H_2SO_4/ HNO_3 treatment.
(B) FT-IR spectra of oxidized MWNTs upon different oxidation treatments: (a) wet air, (b) ozonolysis, (c) 3M HNO_3, (d) 9M HNO_3 and (e) $KMnO_4$/ H_2SO_4.

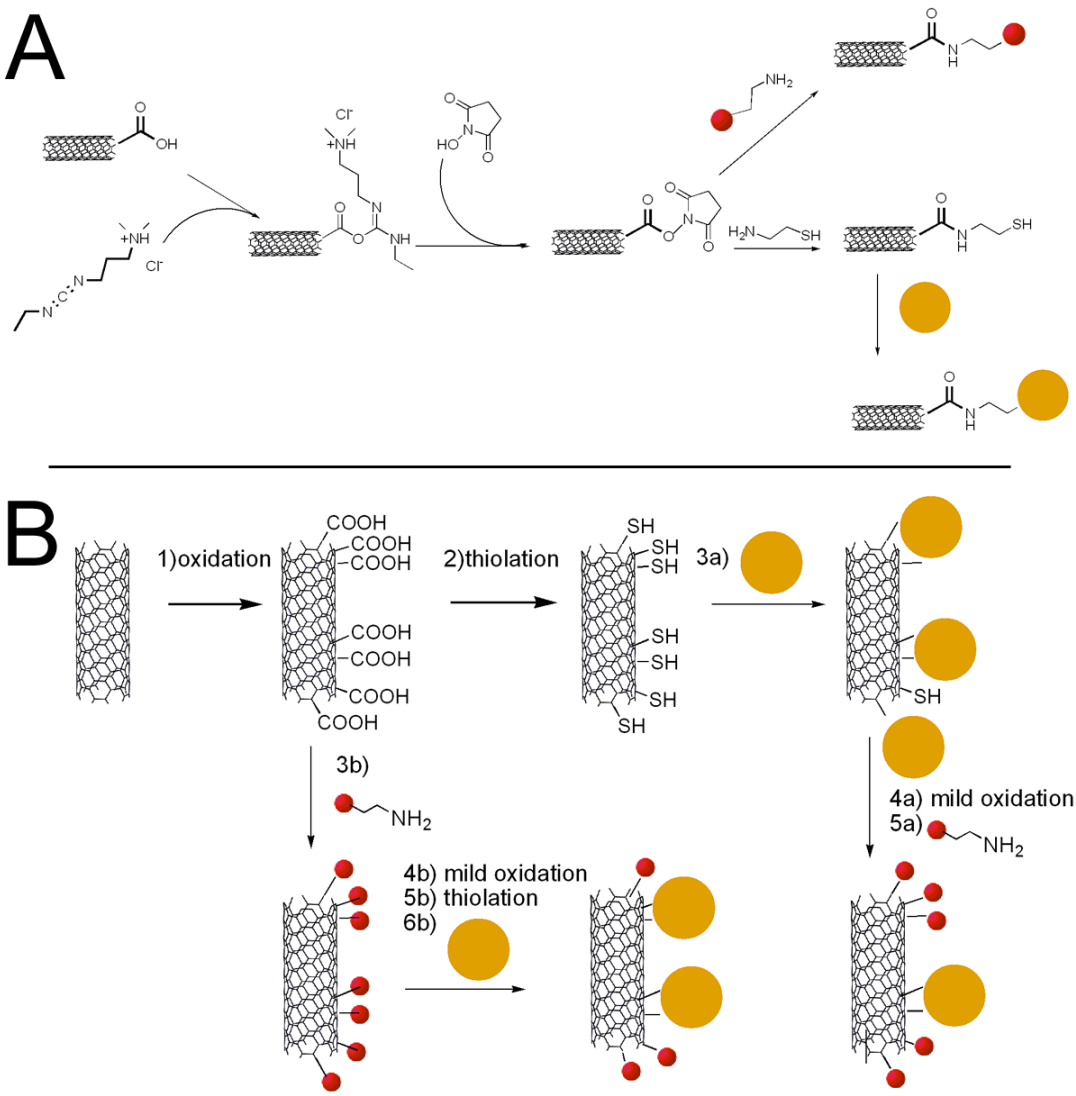

Figure 2.4: (A) Synthetic route associated with the preparation of MWNTs coupled with (i) thiol groups, (ii) Au NPs (large orange spheres) and (iii) AET-CdSe QDs (small red spheres). (B) Summary of synthetic strategies proposed for the formation of either MWNT–Au–CdSe or MWNT–CdSe–Au heterostructures.

2.3.3 *Synthesis of MWNT–Au heterostructures.*

TEM images (Figure 2.5) evince the presence of a series of MWNT–Au heterostructures, prepared using different oxidation treatments from a relatively mild wet air treatment to comparatively stronger acid protocols. High-resolution TEM images show the successful formation of MWNT–Au heterostructures, wherein Au nanoparticles were bound to MWNTs along the sidewall (Figure 2.6A and B). Lattice fringes associated with Au nanoparticles as well as the interfaces between the nanoparticles and the MWNT surface were clearly discernible. Similarly, well-defined lattice fringes corresponding to CdSe nanocrystals were also observed in MWNT–CdSe heterostructures, as shown in Figure 2.5C and D.

The results (Table 2.1) confirmed that the density of Au nanoparticles on the tube surface strongly correlated with the nature of the oxidative treatment.[147, 155, 156] For instance, the control experiment in the presence of unoxidized MWNTs showed no obvious attachment of Au NPs (Figure 2.5A), indicating that the weak non-covalent interaction between Au NPs and pristine MWNTs was not sufficient to achieve effective attachment of NPs onto the MWNT surface. We also found that the MWNT–Au heterostructures originating from a wet air treatment possessed the lowest surface coverage of Au NPs (1.0 particle/μm) due to its relatively low extent of oxidation. An average of 12.0 nanoparticles of Au /μm was observed when a mild oxidative treatment, such as 9 M nitric acid, was used. By contrast, H_2SO_4 /HNO_3 -treated MWNTs possessed a relatively high density of functional groups, and hence the highest density of Au nanoparticles (20.3 particles/μm). It is worth noting that although the statistical error on some of our measurements was relatively high, partly because of a large degree of polydispersity in

nanotube length and diameter, the trend of Au NP coverage on the MWNT surface clearly correlated with the strength of the oxidation treatment.

Apart from reactive sites created upon the oxidation of nanotubes, the change in solubility of CNTs in the reaction medium associated with the extent of oxidative treatment also affected the subsequent coverage of nanoparticles. In this study, for instance, Au NPs were incubated with thiolated MWNTs in aqueous solution. The nature of pristine CNTs is hydrophobic. In that case, a poor dispersion of these CNTs in solution would have hampered the diffusion of NPs into the spaces between individual CNTs, thereby limiting the chances of reacting NPs with CNTs. By contrast, a high concentration of carboxylic groups on the surfaces of the CNTs treated by the strong oxidation process rendered these modified MWNTs far more hydrophilic and therefore soluble in the reaction medium (e.g. methanol and water), which, in turn, would lead to a greater probability of interaction with Au nanoparticles.

2.3.3.a Spatial distribution of nanoparticle coverage correlates with strength of oxidative method.

The spatial coverage of Au nanoparticles on the nanotube surface was also found to correlate strongly with the nature of the oxidative treatment. For instance, the mechanism of ozonolysis of CNTs has been proposed to involve ozone addition to the conjugated double bonds of the outer CNT circumference through a facile 1,3-dipolar cycloaddition reaction.[148] Therefore, one would theorize that the distribution of oxygenated functional groups would favor a higher density of Au NPs along the sidewalls of CNTs as compared with that at the tips. In fact, not surprisingly, the experimental results showed that 92.4% of Au nanoparticles are apt to attach onto the nanotube sidewall.

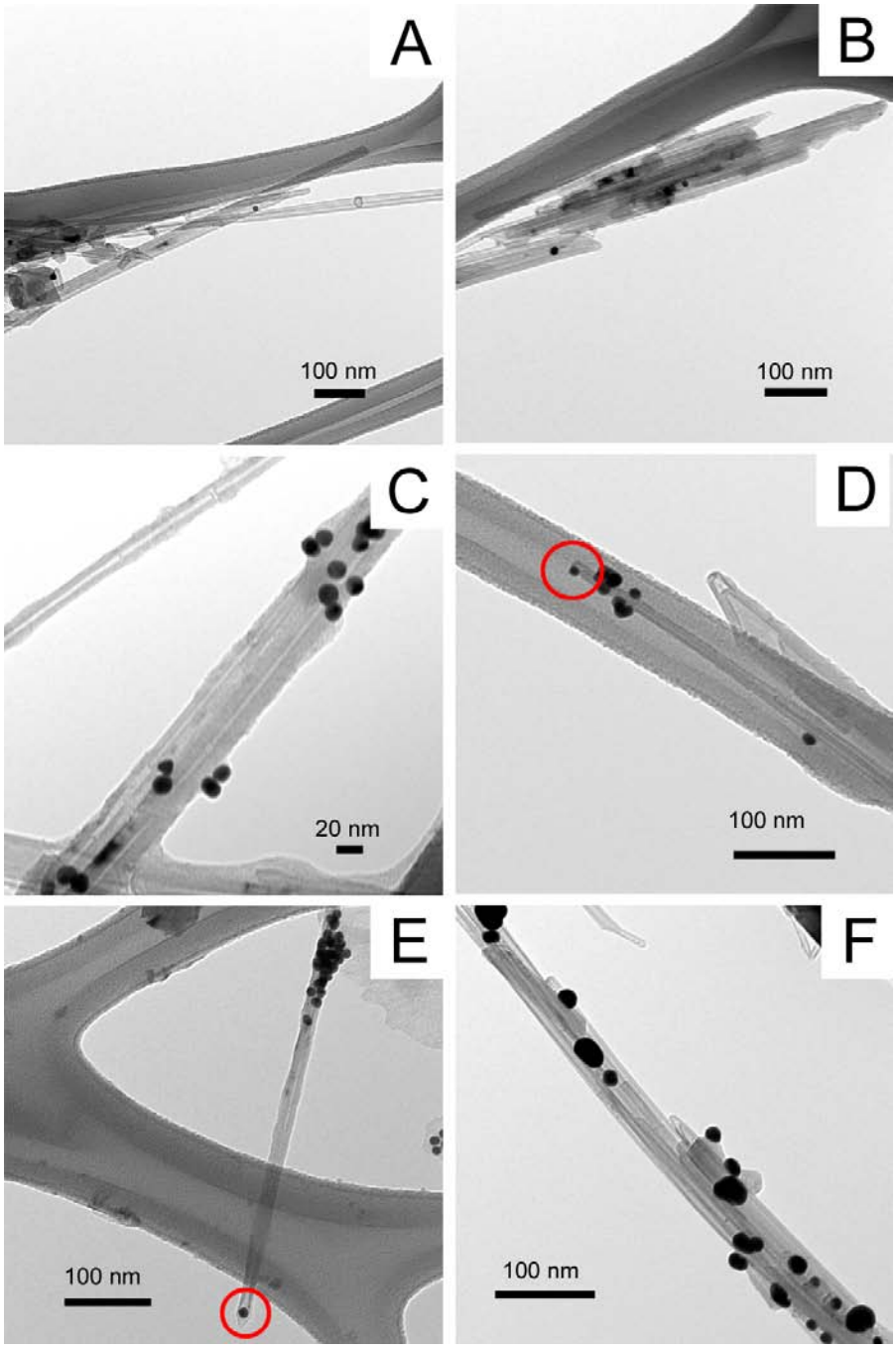

Figure 2.5: (A) TEM images of unoxidized MWNTs incubated with Au nanocrystals. MWNT–Au heterostructures generated after various different oxidation treatments: (B) wet air; (C) ozonolysis; (D) 9 M HNO_3; (E) $KMnO_4/H_2SO_4$; and (F) H_2SO_4/ HNO_3. Red circles highlight the locations of Au nanoparticles anchored at the tips of carbon nanotubes.

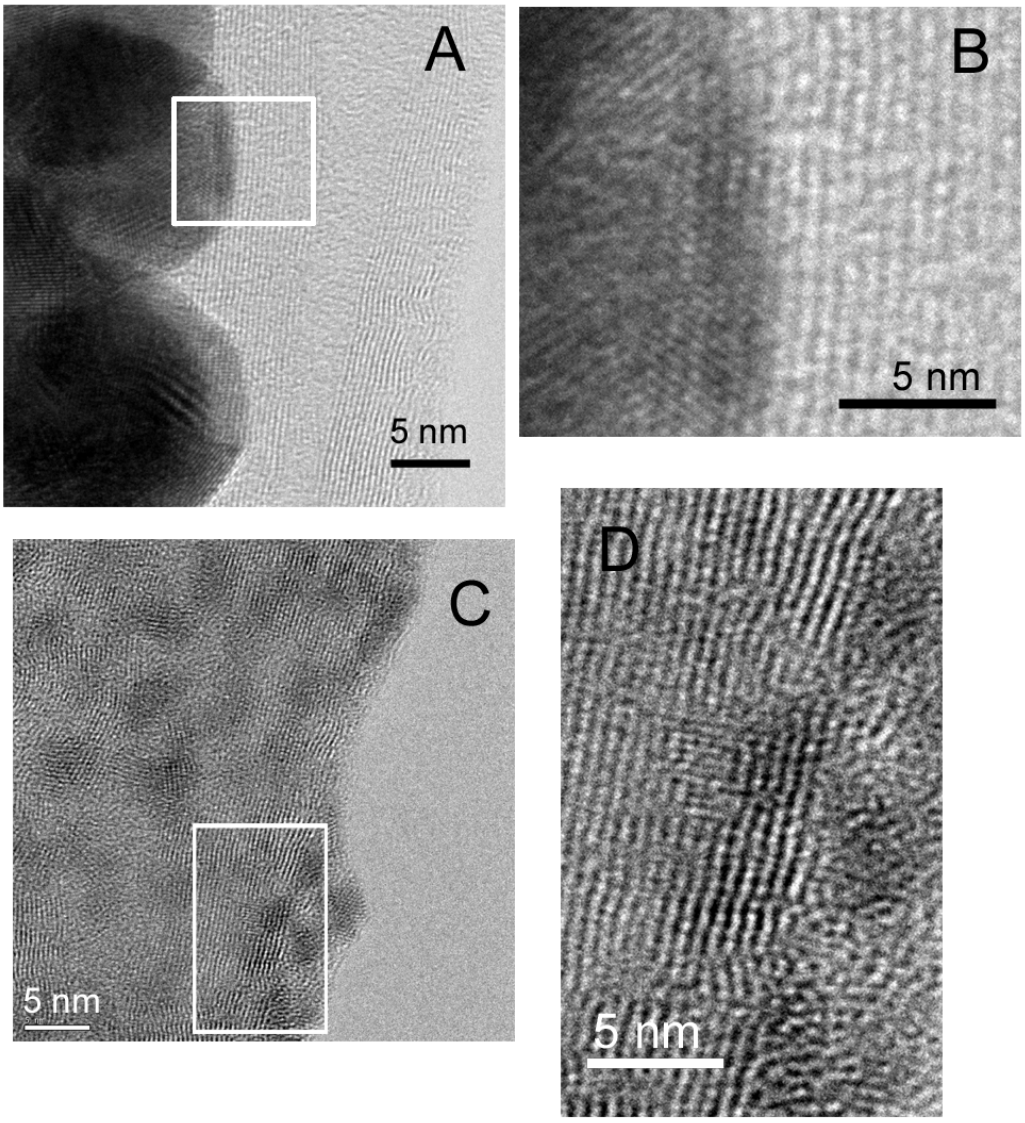

Figure 2.6: High-resolution TEM image of either Au (A) or CdSe (C) nanocrystals bound onto the surface of MWNTs. (B) Magnified image of the area indicated by the white square in (A). (D) Magnified image of the area outlined by the white square in (C).

Table 2.1: Spatial distribution and coverage of Au Nanoparticles on CNT Surfaces subjected to different oxidation treatments.

MWNT-Au heterostructures	**Oxidation treatment**	**Percentage of NPs along the sidewalls (%)**	**Percentage of NPs at the tips (%)**	**Overall Density of Nanocrystals (μm^{-1})**
0	Unoxidized	---	---	0
1	Wet air	100	0	1.0 ± 0.5
2	Ozonolysis/H_2O_2	92.4	7.6	7.8 ± 3.0
3 (a)	3 M HNO_3 at 50^oC	90.9	9.1	6.9 ± 3.1
3 (b)	9 M HNO_3 at 50^oC	69.1	30.9	12.0 ± 2.4
4	$KMnO_4$/ H_2SO_4	86.8	13.2	12.7 ± 4.4
5	H_2SO_4 /HNO_3	94.6	5.4	20.3 ± 8.5

By analogy, acid oxidation treatments are thought to preferentially open the more reactive end caps of nanotubes as well as to etch away defect sites along the sidewalls, and then coat the nanotubes with reasonable quantities of keto, carboxylic, aldehyde and alcoholic groups.[152, 157] Therefore, selective introduction of oxygenated groups onto the ends of CNTs with either minimal or no damage to the sidewalls can be theoretically achieved by carefully choosing different oxidation protocols. We expected that the treatment using 9 M nitric acid reflux at 50ºC preferentially oxidized MWNTs at their ends, thereby leading to the highest density of Au NPs (30.9 %) as compared with any other treatment method. This observation is highlighted in Figure 2.5 D, where the red circles correspond to Au NPs anchored at the tips of the carbon nanotubes.

By contrast, a stronger acid treatment, such as a combined $KMnO_4$ /H_2SO_4 treatment, not only introduced reactive acid groups at the ends of the CNT but also had a higher possibility of attacking defect sites along the tube sidewalls. Consequently, in this case, the probability of attachment of Au NPs along the sidewalls increased to 86.8% as compared with 69.1 % for 9 M HNO_3 treated MWNTs. Similarly, a combined H_2SO_4 / HNO_3 treatment followed by sonication non-discriminately and aggressively attacked the entire CNT surface, creating a large number of defect sites not only at the ends but also along the sidewalls. In fact, this harsh protocol led to the highest density of Au NPs (94.6%) observed along the sidewalls of the MWNTs among all the oxidation treatment we tested.

Interestingly, when a considerably milder treatment (e.g. 3 M HNO_3 at 50˚C and wet air oxidation) was used, the percentage of Au NPs at the tips unexpectedly decreased. As mentioned above, the hydrophilicity of mildly oxidized nanotubes in the reaction medium can influence the degree of nanoparticle attachment. Thus, a high degree of aggregation of MWNTs in these

specific cases likely prevented individual nanotube tips from being adequately exposed to the presence of Au NPs, thereby dramatically reducing the probability of attaching NPs at these end sites and hence leading to a <10% of loading at the tips.

2.3.3.b Observed nanoparticle coverage depends upon particle concentration.

By increasing concentrations of Au NPs present from 50, 100, to 200 nM, a correspondingly higher density of Au NPs could be achieved on the nanotube surface (Figure 2.7A-C and Table 2.2). Meanwhile, the actual spatial distribution of nanocrystals at the ends, defect sites, and sidewalls was not noticeably affected by changes in the concentration of Au NPs. One could make the argument that an increase in the NP concentration increases the probability of NP attachment both at the tips and along the sidewalls.

2.3.3.c Increasing incubation time yields higher nanoparticle coverages.

H_2SO_4 /HNO_3-treated MWNTs were incubated with AET-CdSe nanocrystals for different incubation/reaction time of 0.5, 2, and 48 h with a constant CdSe concentration of 100 nM. The density of QDs increased significantly from as low as zero particles per micron on the CNT surface to ~71.3 particles μm^{-1} upon increasing incubation time of 0.5 to 48 h (Figure 2.7D-F and Table 2.3). By contrast, for the MWNT–Au heterostructures, in which the MWNTs were oxidized by 9 M HNO_3 and the concentration of Au was 100 nM, the coverage density remained relatively stable at about 12 –14 particles μm^{-1} over the entire incubation time range of from 0.5 h to 48 h (Table 2.4).

It is worth noting that even though the MWNTs in these two types of heterostructures were modified by different oxidation treatments, that fact alone likely cannot fully explain the clear difference in attachment rate between the two different heterostructures. We note the

formation of nanotube–nanocrystal heterostructures in these two cases relied on two distinctive chemical processes. Specifically, in the MWNT–CdSe conjugate system, the attachment rate was determined by the rate of amide bond formation between carboxylic acids on the MWNT and amine groups on the CdSe, whereas creation of Au–S bonds governed the production of thiolated MWNT–Au heterostructures. Hence, it is likely due to binding affinity and kinetic rate constant data that the formation of Au–S bonds[158] is faster than that of amide bond production.[159]

More importantly, the MWNT–CdSe system showed a substantially greater coverage of QDs on the tubes (71.3 particles μm^{-1}) as compared with its MWNT–Au analogue (20.3 particles μm^{-1}) under similar reaction conditions. This observation could be ascribed to a potentially better diffusion of QDs through the MWNT framework, because of the relatively smaller size of these CdSe QDs. In addition, it is highly possible that there was a dense quantity of either thiol or carboxylic groups dangling at either the defect sites or the ends of the oxidized MWNTs. Therefore, the larger Au NPs (12.7 nm) attached to the reactive sites might have posed a steric hindrance factor, thereby preventing additional nanoparticles from approaching and coordinating onto the remaining reactive thiol sites available. By contrast, the CdSe QDs with a relatively smaller size, measuring 4.2 nm, would have a greater likelihood of generating a dense coating on the nanotube surface without a high degree of spatial impediment.

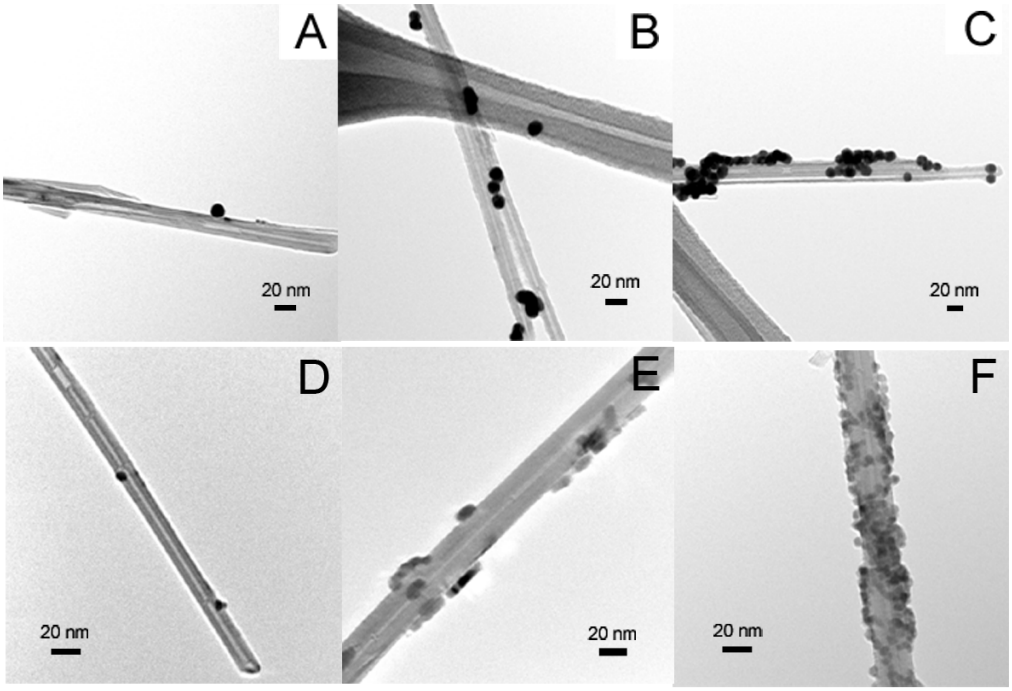

Figure 2.7: (A-C) The effect of nanocrystal concentration. TEM images of MWNT–Au heterostructures incubated with a concentration of Au NPs set at (A) 50 nM, (B) 100 nM and (C) 200 nM. Fixed incubation time: 2 h. MWNTs were initially oxidized with H_2SO_4 /HNO_3. (D-F) The effect of reaction time. TEM images of MWNT–CdSe heterostructures with incubation time of (D) 0.5 h, (E) 2 h, and (F) 48 h. Fixed concentration of CdSe nanocrystals: 100 nM. MWNTs were initially oxidized using a H_2SO_4 /HNO_3 treatment.

Table 2.2: Spatial distribution and coverage of Au nanoparticles with different nanoparticle concentrations on carbon nanotube templates

Concentration of Au Nanoparticles (nM)	**Percentage of Nanoparticles along the sidewall (%)**	**Percentage of Nanoparticles at the tips and ends (%)**	**Density Coverage of Nanoparticles on MWNTs (μm^{-1})**
50	100	0	1.0 ± 0.5
100	94.6	5.4	20.3 ± 8.5
200	98.0	2.0	48.0 ± 6.9

Table 2.3: Spatial distribution and coverage of CdSe nanocrystals onto carbon nanotube templates with different incubation time

Incubation time (h)	**Percentage of nanocrystals along the sidewall (%)**	**Percentage of nanocrystals at the tips (%)**	**Coverage of nanocrystals on MWNTs (μm^{-1})**
0.5	100	0	1.0 ± 1.0
2	98.5	1.5	15.4 ± 3.7
48	96.6	3.4	71.3 ± 14.2

Table 2.4: Spatial distribution and coverage of Au nanocrystals onto carbon nanotube templates with different incubation time*

Incubation time (h)	**Percentage of nanocrystals along the sidewall (%)**	**Percentage of nanocrystals at the tips (%)**	**Coverage of nanocrystals on MWNTs (μm^{-1})**
0.5	82.0	18.0	13.4 ± 3.4
2	69.1	30.9	12.0 ± 2.43
48	74.7	25.3	14.5 ± 3.8

(*Data were obtained from MWNT–Au heterostructures, in which MWNTs were initially oxidized by 9 M HNO_3.)

2.3.4 *Hierarchical synthesis of MWNT–Au–CdSe heterostructures*

Since Au NPs had the highest spatial preference for the tube sidewalls in MWNT–Au heterostructures using MWNTs pre-treated with H_2SO_4/HNO_3, this type of MWNT–Au heterostructures were used as the starting material in order to synthesize more sophisticated structures with different types of nanoparticles. Moreover, the higher hydrophilicity of these specifically oxidized MWNTs likely enabled a better dispersibility of MWNTs in reaction solution, thereby increasing the probability of interaction between the tips of the MWNTs and the additional CdSe nanocrystals.

Experimentally, as-prepared MWNT–Au heterostructures were further oxidized in 1 M HNO_3 so as to generate additional reactive sites for the subsequent attachment of CdSe nanocrystals (Figure 2.4B). TEM images shown in Figure 2.8 highlight the formation of MWNT-Au-CdSe heterostructures associated with different oxidation time in 1 M HNO_3. The red arrows denote the presence of Au NPs whereas the blue arrows indicate the location of CdSe QDs. It can be noted that upon prolonged reaction in dilute acid, we gradually lost Au NP coverage on the CNT surface (Table 2.5). Specifically, the density of Au NPs dropped from 20.3 particles μm^{-1} to 1 particle μm^{-1} within 24 h of reaction. Our observations can be ascribed to two factors. First, although the use of dilute acid was necessary in order to prevent excessive damage of pre-formed amide bonds, it is unlikely that all pre-formed amide bonds remained intact during the entire reaction process, as amide bonds are easily hydrolyzed under either acidic or basic conditions. Second, it has been previously reported that dissociation of the thiol ligand from the surface of NPs can be induced by lowering the pH of the reaction solution, as the added hydrogen ions can compete for the surface ligands with pre-attached nanoparticles.[160] In any event, two different

sets of reactive sites on the nanotubes were available upon further oxidation treatment with 1 M HNO_3: (i) one group, which had been unoccupied by Au NPs prior to the 1 M HNO_3 oxidation step, and (ii) an additional group of sites, which became available as Au NPs were lost upon exposure to 1 M HNO_3 oxidation. Both sets of sites nonetheless provided locations at which CdSe QDs could be subsequently bound onto the surfaces of the CNTs.

Upon incubation of oxidized MWNT–Au heterostructures with CdSe QDs, the coverage of CdSe QDs increased dramatically in the MWNT–Au templates with oxidation time of 1 h in 1 M HNO_3 and then leveled off, even after oxidation time of 24 h. Correspondingly, the portion of Au NPs in the resulting MWNT–Au–CdSe heterostructures decreased with additional oxidation time. With respect to the spatial distribution of either NPs or QDs, the number of Au NPs at the tips gradually decreased with increasing oxidation time in 1 M HNO_3, with a concomitant increase of CdSe QDs on the resulting MWNT–Au–CdSe surface. A maximum level of up to 9.0% of total CdSe QDs was observed at the tips upon 1 h oxidation of MWNT–Au in the presence of 1 M HNO_3. Essentially, we observed that the majority of the tips of MWNTs ended up being occupied by CdSe QDs after their introduction into the reaction medium, while the remaining Au NPs were primarily distributed along the MWNT sidewalls, as illustrated in Figure 2.8. With an increase in oxidation time of the MWNT–Au template, Au NPs along the CNT sidewalls were “replenished” with CdSe QDs, ultimately leading to an overall increase in the percentage of CdSe QDs along the nanotube sidewalls. It should be mentioned that there was insufficient evidence to support a faster dissociation rate of Au NPs at the tips as compared with the sidewalls. Nonetheless, given the same intrinsic probability of losing Au NPs at both the tips and the sidewalls, the lower quantity of particles localized at the tips, as compared with the

sidewalls, would have led to a more rapid replacement rate at the tips with CdSe QDs, which explains our data.

2.3.5 *Hierarchical synthesis of MWNT–CdSe–Au heterostructures.*

The converse reaction was also carried out to test the flexibility of our synthetic strategy. Specifically, H_2SO_4 /HNO_3-treated MWNTs were first coated with CdSe QDs, followed by an additional oxidation process in 1 M HNO_3, and finally, incubation with Au NPs, so as to prepare MWNT–CdSe–Au heterostructures. As seen in Table 2.5, even though the loss of CdSe was large, i.e. from 71.3 particles μm^{-1} to 9.8 particles μm^{-1}, the coverage of Au did not increase in a proportionate manner, consistent with a previous inference that the intrinsic size difference between Au and CdSe nanocrystals affected their overall density of coverage on the nanotube surface. Therefore, not surprisingly, we noted the portion of CdSe QDs relative to Au NPs in the resulting MWNT–CdSe–Au heterostructures attained a value of no less than 40%, even after a prolonged oxidation treatment of 24 h (Figure 2.9).

With respect to the spatial distribution of nanocrystals on the surfaces of the MWNTs, an initially high percentage of CdSe QDs along the sidewalls of MWNTs (Table 2.6) was observed, an observation similar to the findings in MWNT–Au heterostructures. Subsequently, approximately 6 hours of 1 M HNO_3 treatment of MWNT–CdSe heterostructures resulted in a larger fraction of added Au NPs localized at tip regions (up to levels as high as 10.3%). At longer oxidation time of MWNT–CdSe in 1 M HNO_3, i.e. up to 12 hours, defect sites, localized at the sidewalls, also began to fill up with added Au NPs as CdSe QDs in these regions were being continuously removed by acid.

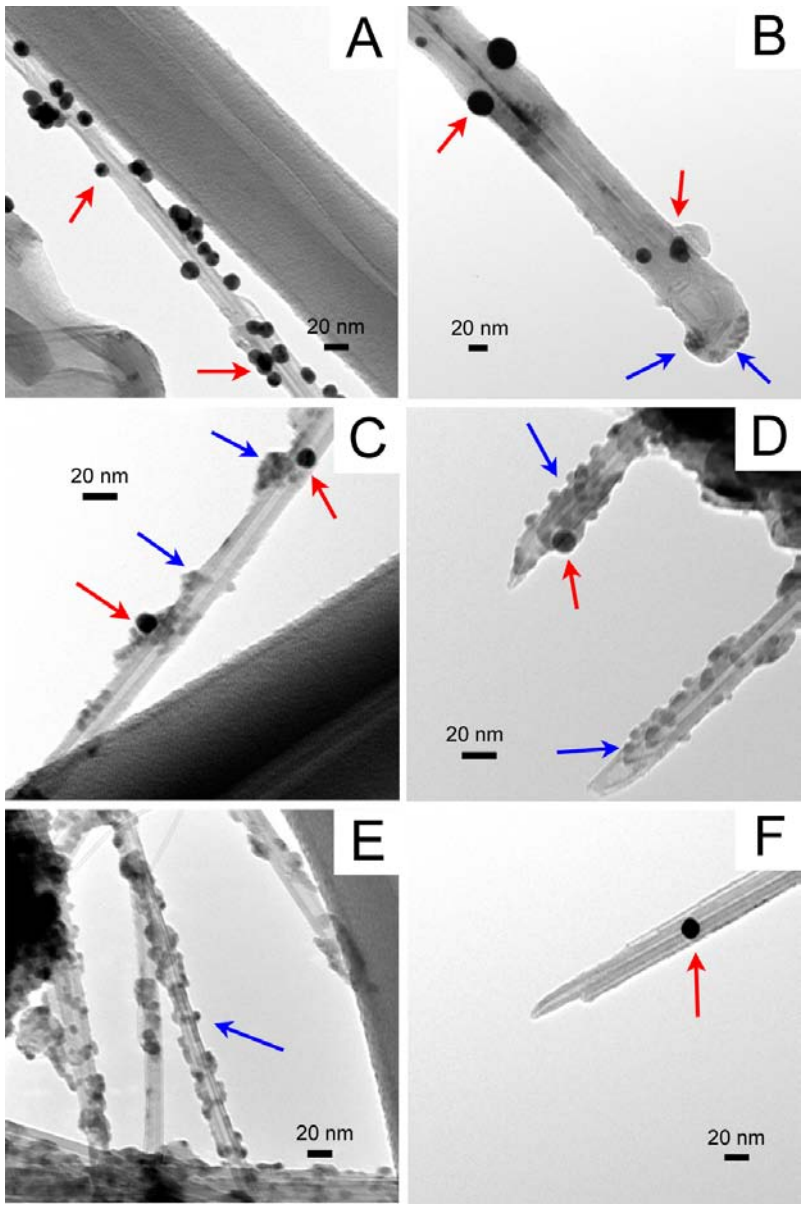

Figure 2.8: (A-E) TEM images of MWNT–Au–CdSe heterostructures. MWNT–Au heterostructures (red arrows) were initially oxidized in 1 M HNO_3 for (A) 0.5 h, (B) 1 h, (C) 6 h, (D) 12 h, and (E) 24 h, respectively, followed by reaction with AET-CdSe nanocrystals (blue arrows). (F) MWNT–Au heterostructures after 1 M HNO_3 oxidation for 24 h without incubation with AET-CdSe nanocrystals. MWNTs were initially oxidized using a H_2SO_4 /HNO_3 treatment.

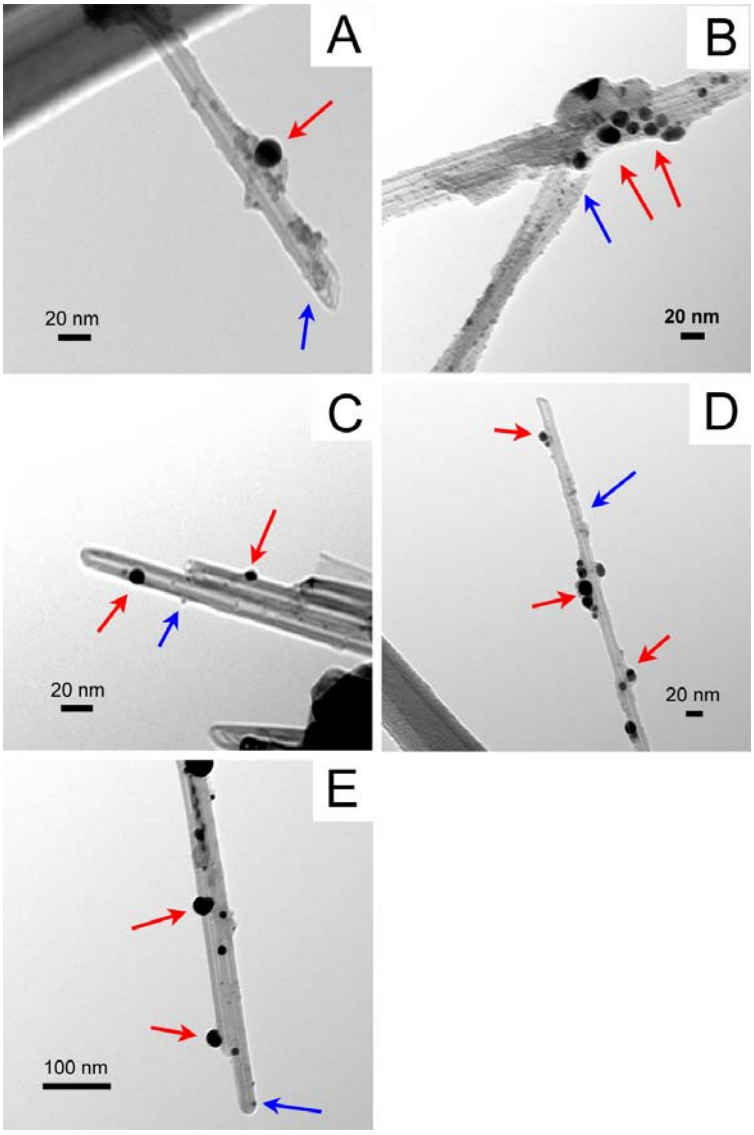

Figure 2.9: (A-E) TEM images of MWNT–CdSe–Au heterostructures. MWNT–CdSe heterostructures (blue arrows) were initially oxidized in 1 M HNO_3 for (A) 0.5 h, (B) 1 h, (C) 6 h, (D) 12 h, and (E) 24 h, respectively, followed by thiolation and subsequent reaction with Au NPs (red arrows). MWNTs were initially oxidized by a H_2SO_4 /HNO_3 treatment.

Table 2.5: Spatial distribution and coverage of Au NPs and CdSe QDs in MWNT–Au–CdSe heterostructures as a function of oxidation time of the MWNT–Au templates in 1 M HNO_3

	Oxidation time of the MWNT–Au template (h)	**Percentage of nanocrystals along the sidewall (%)**	**Percentage of nanocrystals at the tips and ends (%)**	**Coverage of nanocrystals on MWNT surfaces (μm^{-1})**
Au NPs	0	94.6	5.4	20.3 ± 8.5
	0.5	93.3	6.7	18 ± 4.7
	1	94.5	5.5	12.0 ± 3.2
	6	95.0	5.0	5.0 ± 1.5
	12	100	0	2.3 ± 1.0
	24	---	0	0.0
CdSe Nano-crystals	0	---	---	0
	0.5	100	0	0.5 ± 0.3
	1	91.0	9.0	48.0 ± 13.6
	6	94.9	5.1	48.2 ± 15.4
	12	94.2	5.8	50.0 ± 15.1
	24	94.1	5.9	50.9 ± 15.0

Table 2.6: Spatial distribution and coverage of Au NPs and CdSe QDs in MWNT–CdSe–Au heterostructures as a function of oxidation time of the MWNT–CdSe templates in 1 M HNO_3

	Oxidation time of the MWNT–CdSe template (h)	**Percentage of nanocrystals along the sidewall (%)**	**Percentage of nanocrystals at the tips and ends (%)**	**Coverage of nanocrystals on MWNT Surface (μm^{-1})**
Au Nano-Particles	0	-	-	0
	0.5	100	0	8.0 ± 2.1
	1	91.7	8.3	8.7 ± 2.0
	6	89.7	10.3	13.4 ± 4.3
	12	96.3	3.7	12.0 ± 3.9
	24	95.2	4.8	13.0 ± 6.0
CdSe Nano-particles	0	96.6	3.4	71.3 ± 14.2
	0.5	97.8	3.2	50.0 ± 15.9
	1	89.5	10.5	32.2 ± 15.0
	6	96.9	3.1	29.0 ± 10.9
	12	97.5	2.5	25.0 ± 12.7
	24	96.8	3.2	9.8 ± 10.1

2.3.6 *Other characterization protocols used*

2.3.6.a X-ray Diffraction

XRD data (Figure 2.10) show that oxidized MWNTs possessed no obvious diffraction feature in the 2θ range between 30˚ and 80˚. Additional peaks appearing in the heterostructure samples confirmed the presence of Au NPs and/or CdSe QDs. For comparison, the XRD pattern of AET-CdSe displayed in Figure 2.10b was consistent with literature values of the CdSe bulk (JCPDS File No. 02-0330). Bragg diffraction peaks were all relatively broad because of the extremely small dimensions of the CdSe nanocrystals. For the MWNT–CdSe heterostructures, peaks corresponding to CdSe crystal planes of (110) and (112) indicated that CdSe QDs were anchored onto CNT surfaces. For the MWNT–Au heterostructures, peaks positioned at (111), (200), (220), and (311) can be assigned to reflections of gold. Diffraction peaks for both Au NPs and CdSe QDs, though weak, suggested the successful formation of both MWNT–Au–CdSe and MWNT–CdSe–Au heterostructures, respectively.

2.3.6.b Optical measurements

Oxidized MWNTs appeared featureless in the absorption spectra (Figure 2.11). Relatively weak absorption peaks of MWNT–Au heterostructures and MWNT–CdSe heterostructures were noted at 520 nm and 600 nm, respectively. The lower intensity of absorption may likely be due to an intrinsically lower concentration of nanocrystals on the MWNT surface. In addition, the absorption of CdSe in MWNT–CdSe heterostructures was slightly blue-shifted as compared with that associated with as-prepared CdSe QDs, an observation that has been ascribed to the photo-oxidation of CdSe, as discussed previously. The

broad peak of MWNT–Au–CdSe centered at 576 nm was attributed to collective absorption due to both Au nanoparticles and CdSe QDs (Figure 2.11). UV-visible data for all of our MWNT-based heterostructures do not show any extraneous features that would typically arise from an electronic interaction between nanotubes and quantum dots in their ground states.[161]

The photoluminescence behavior (PL) of AET-CdSe, MWNT–CdSe and MWNT–Au–CdSe heterostructures was measured upon illumination at 400 nm. A substantial decrease in the PL intensity was observed for both MWNT–CdSe and MWNT–Au–CdSe heterostructures as compared with the AET-CdSe, which possessed an intense band-edge emission peak at 612 nm (Figure 2.12). The significant suppression of emission of the CdSe upon covalent conjugation with MWNTs suggested a strong excited state interaction with the nanotubes. This observation was in agreement with prior literature on SWNTs, including our own prior work.[79, 162] That is, the de-excitation process of excited CdSe QDs can be attributed to a rapid charge transfer from the excited semiconductors to the MWNT platform.[163, 164] Specifically, the photoinduced excition (a electron-hole pair) generated upon illumination of CdSe could undergo a normal radiative recombination process. However, once MWNTs were brought into contact with these excited QDs, the non-radiative quenching process, due to electron flow from the conduction band of electron donating QDs to the empty electronic states of the electron accepting nanotube, became competitive with the intrinsic radiative decay process, thereby resulting in the observed decrease in the PL intensity of the CdSe.[161] In addition, it has been proposed that nanotubes can also act as energy sinks for attached nanoparticles/nanocrystals through an energy transfer mechanism.[52] That provides for an alternative pathway for quenching of the CdSe emission.[78] In our case, the PL of CdSe QDs could also have been quenched by our use of relatively short linkers (e.g. AET)

bridging the CdSe and oxidized MWNTs. More detailed investigation of optical properties of CNT–CdSe heterostructures will be discussed in Chapter 3.

To rule out the possibility that the removal of ligands from the QD surface due to the presence of CNTs might have partially offset the observed emission of CdSe QDs, the PL spectrum of MWNT–CdSe heterostructures was taken in the presence of free AET molecules at a concentration of 0.5 M. No obvious change was noted as compared with that in the absence of AET solution. Moreover, we should note that any unbound CdSe QDs as well as free ligands were likely removed from the system by extensive washing steps, prior to our optical experiments. As such, it is less likely that the presence of either free CdSe QDs or free ligands interfered with the observed, intrinsic optical signature associated with our nanotube-nanocrystal heterostructures.

For our MWNT–Au–CdSe heterostructures, we noted that CdSe QDs were in close physical proximity to Au NPs in some cases. Therefore, the observation of a further depression of QD emission in our MWNT–Au–CdSe heterostructures could be attributed to additional non-radiative pathways, e.g. either energy transfer[165] or electron transfer[166] between CdSe QDs and Au NPs.

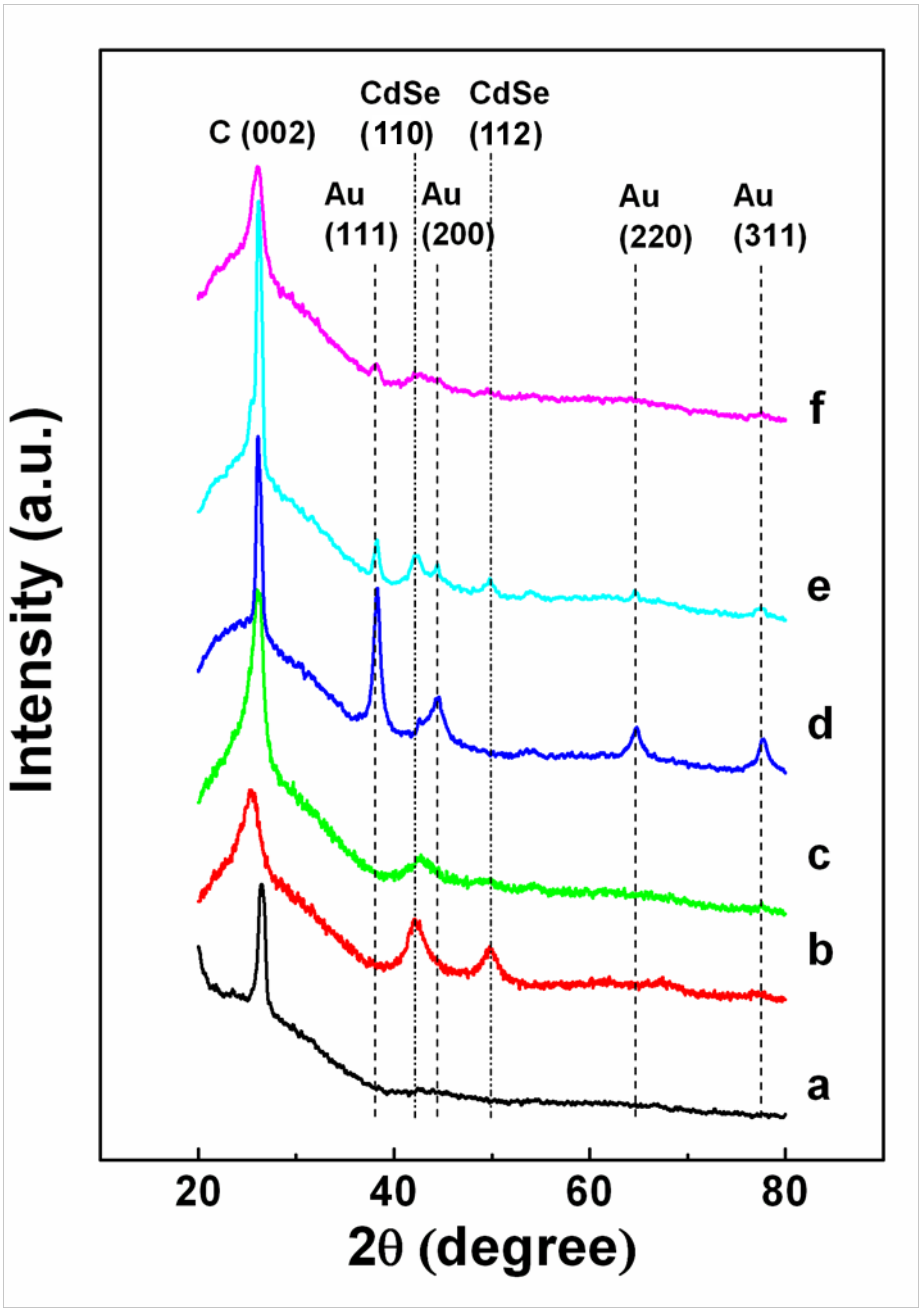

Figure 2.10: XRD patterns of (a) oxidized MWNTs, (b) AET-CdSe nanocrystals, (c) MWNT–CdSe heterostructures, (d) MWNT–Au heterostructures, (e) MWNT–Au–CdSe heterostructures, and (f) MWNT–CdSe–Au heterostructures. MWNTs were oxidized by H_2SO_4 / HNO_3. For MWNT–Au–CdSe heterostructures, MWNTs were first coated with Au NPs, oxidized in 1 M HNO_3 for 1 h, and finally coated with CdSe QDs. For MWNT–CdSe–Au heterostructures, MWNTs were first coated with AET-CdSe, oxidized in 1 M HNO_3 for 1 h, and finally coated with Au NPs.

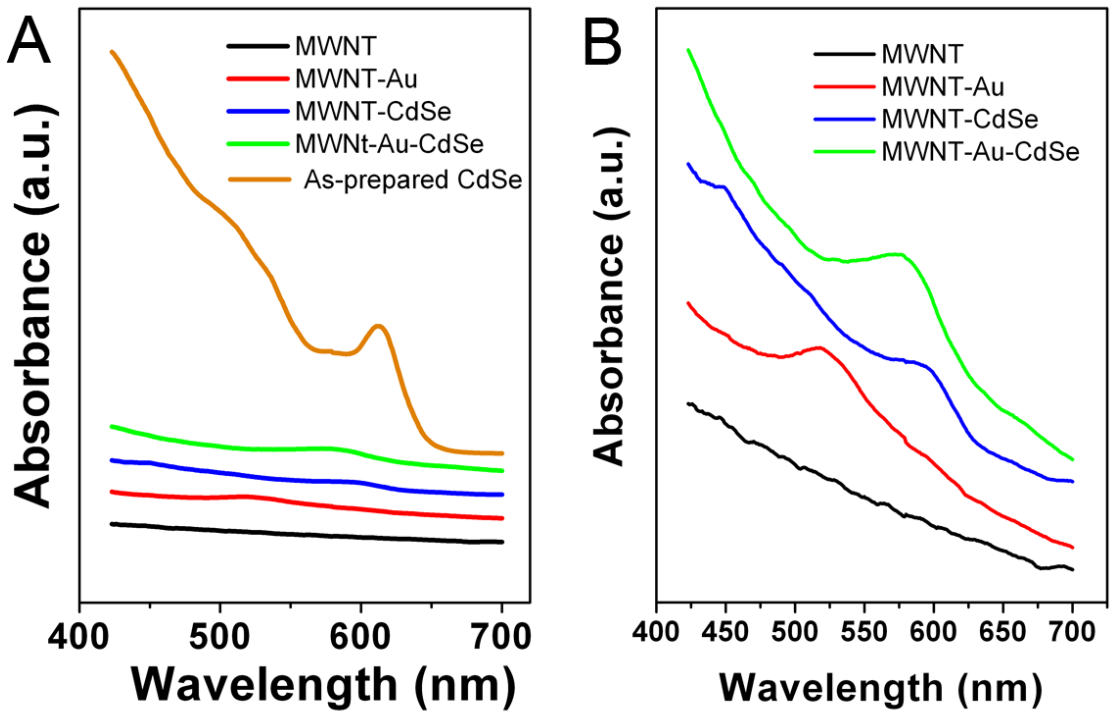

Figure 2.11: (A) UV-visible spectra of oxidized MWNTs, MWNT–Au heterostructures, MWNT–CdSe heterostructures, MWNT–Au–CdSe heterostructures, and CdSe QDs. MWNTs were initially oxidized by H_2SO_4/HNO_3. (B) Magnified absorption spectra corresponding to nanotube-based heterostructures.

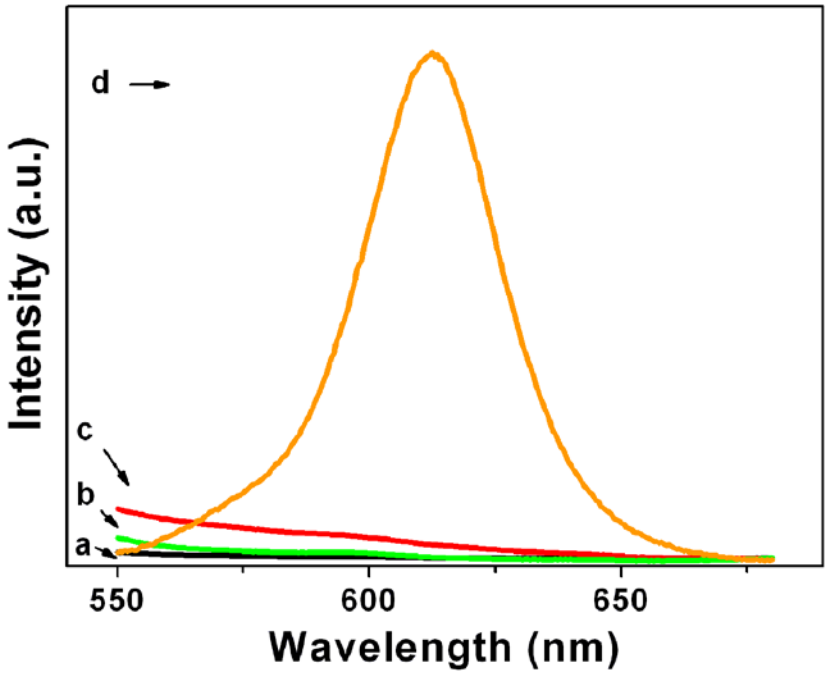

Figure 2.12: Photoluminescence spectra of (a) raw MWNTs (black curve), (b) MWNT–Au–CdSe heterostructures (green curve), (c) MWNT–CdSe heterostructures (red curve), and (d) AET-CdSe nanocrystals (orange curve). MWNTs were initially oxidized by H_2SO_4/HNO_3. Excitation wavelength is 400 nm.

2.4 Conclusions

We have demonstrated a covalent route towards the site-selective synthesis of MWNT–nanoparticle heterostructures containing two different types of nanoscale species, i.e. Au nanoparticles and CdSe QDs. We have quantitatively probed the effects of varying oxidation treatments, precursor concentrations, and incubation time in order to rationally affect the spatial coverage and distribution of either Au NPs or semiconducting QDs on the MWNT sidewalls and tips. The degree of NP coverage was found to primarily vary with the intensity of the oxidation treatments. In general, the stronger the oxidation treatment, the denser the coating of nanoparticles and/or quantum dots on the nanotube surface. In addition, the use of larger concentrations of precursor nanocrystals along with longer incubation time also led to the observation of higher nanoparticle densities on our nanotube templates.

While none of these trends were perfect, our findings suggest a reasonable way of fabricating a series of novel CNT–nanocrystal/nanoparticle heterostructures with potentially tailorable electronic or optical properties. By controlling the oxidation time of MWNT–Au/CdSe templates, MWNT–Au–CdSe and MWNT–CdSe–Au heterostructures with various spatial locations and coverages of NPs and QDs could be obtained. Potential charge-transfer as well as energy transfer between CNTs and the corresponding nanoparticles/quantum dots, as evidenced by the suppression of QD emission, will likely render such heterostructures as key components in nanoscale devices and/or solar applications.

2.5 References

52. S. Berson, R. de Bettignies, S. Bailly, S. Guillerez and B. Jousselme, *Advanced Functional Materials*, **2007**, *17*, 3363-3370.

78. B. F. Pan, D. X. Cui, C. S. Ozkan, M. Ozkan, P. Xu, T. Huang, F. T. Liu, H. Chen, Q. Li, R. He and F. Gao, *Journal of Physical Chemistry C*, **2008**, *112*, 939-944.

79. N. Cho, K. R. Choudhury, R. B. Thapa, Y. Sahoo, T. Ohulchanskyy, A. N. Cartwright, K. S. Lee and P. N. Prasad, *Advanced Materials*, **2007**, *19*, 232-236.

141. N. Chopra, M. Majumder and B. J. Hinds, *Advanced Functional Materials*, **2005**, *15*, 858-864.

142. M. S. Raghuveer, A. Kumar, M. J. Frederick, G. P. Louie, P. G. Ganesan and G. Ramanath, *Advanced Materials*, **2006**, *18*, 547-552.

143. K. Kurppa, H. Jiang, G. R. Szilvay, A. G. Nasibulin, E. L. Kauppinen and M. B. Linder, *Angewandte Chemie-International Edition*, **2007**, *46*, 6446-6449.

144. S. Banerjee and S. S. Wong, *Journal of the American Chemical Society*, **2003**, *125*, 10342-10350.

145. B. V. Enustun and J. Turkevich, *Journal of the American Chemical Society*, **1963**, *85*, 3317-3328.

146. E. M. Boatman, G. C. Lisensky and K. J. Nordell, *Journal of Chemical Education*, **2005**, *82*, 1697-1699.

147. X. H. Li, J. L. Niu, J. Zhang, H. L. Li and Z. F. Liu, *Journal of Physical Chemistry B*, **2003**, *107*, 2453-2458.

148. S. Banerjee and S. S. Wong, *Journal of Physical Chemistry B*, **2002**, *106*, 12144-12151.

149. S. Banerjee and S. S. Wong, *Nano Letters*, **2004**, *4*, 1445-1450.

150. L. C. Teague, S. Banerjee, S. S. Wong, C. A. Richter, B. Varughese and J. D. Batteas, *Chemical Physics Letters*, **2007**, *442*, 354-359.

151. T. Hemraj-Benny, T. J. Bandosz and S. S. Wong, *Journal of Colloid and Interface Science*, **2008**, *317*, 375-382.

152. H. Hiura, T. W. Ebbesen and K. Tanigaki, *Advanced Materials*, **1995**, *7*, 275-276.

153. S. Ravindran, S. Chaudhary, B. Colburn, M. Ozkan and C. S. Ozkan, *Nano Letters*, **2003**, *3*, 447-453.

154. J. Aldana, Y. A. Wang and X. G. Peng, *Journal of the American Chemical Society*, **2001**, *123*, 8844-8850.

155. J. Zhang, H. L. Zou, Q. Qing, Y. L. Yang, Q. W. Li, Z. F. Liu, X. Y. Guo and Z. L. Du, *Journal of Physical Chemistry B*, **2003**, *107*, 3712-3718.

156. S. Banerjee and S. S. Wong, *Chemical Communications*, **2004**, 1866-1867.

157. J. Liu, A. G. Rinzler, H. J. Dai, J. H. Hafner, R. K. Bradley, P. J. Boul, A. Lu, T. Iverson, K. Shelimov, C. B. Huffman, F. Rodriguez-Macias, Y. S. Shon, T. R. Lee, D. T. Colbert and R. E. Smalley, *Science*, **1998**, *280*, 1253-1256.

158. S. Liao, Y. Shnidman and A. Ulman, *Journal of the American Chemical Society*, **2000**, *122*, 3688-3694.

159. G. K. Kouassi and J. Irudayaraj, *journal of Nanobiotechnology*, **2006**, *4*, 1-10.

160. J. Aldana, N. Lavelle, Y. J. Wang and X. G. Peng, *Journal of the American Chemical Society*, **2005**, *127*, 2496-2504.

161. M. Olek, T. Busgen, M. Hilgendorff and M. Giersig, *Journal of Physical Chemistry B*, **2006**, *110*, 12901-12904.

162. I. Robel, B. A. Bunker and P. V. Kamat, *Advanced Materials*, **2005**, *17*, 2458-2463.

163. A. Kongkanand, R. M. Dominguez and P. V. Kamat, *Nano Letters*, **2007**, *7*, 676-680.

164. F. Vietmeyer, B. Seger and P. V. Kamat, *Advanced Materials*, **2007**, *19*, 2935-2940.

165. M. Kondon, J. Kim, N. Udawatte and D. Lee, *Journal of Physical Chemistry C*, **2008**, *112*, 6695-6699.

166. R. Costi, A. E. Saunders, E. Elmalem, A. Salant and U. Banin, *Nano Letters*, **2008**, *8*, 637-641.

Chapter 3 Synthesis of Double-walled Carbon Nanotube – Quantum Dot Heterostructures and Photophysical Studies of Carrier Dynamics in Heterostructures

3.1 Introduction

3.1.1 *Double-walled carbon nanotubes (DWNTs)*

In recent years, double-walled carbon nanotubes (DWNTs), consisting of two coaxial tubules, have attracted significant attention due to their unique properties.[167-169] Indeed, because of the fact that the outer and inner layers in a DWNT retain the basic electronic properties of each constituent graphene monolayer tubule, even though the detailed energy dispersion relations are affected by the interlayer interaction,[170, 171] the properties of DWNTs are predicted to be as promising as or superior to those of SWNTs and MWNTs.[172] For instance, with respect to field emission properties, it has been found that DWNTs not only maintain higher current densities but also combine the low threshold voltage for electron emission normally characteristic of SWNTs with the efficient emission stability typically associated with MWNTs.[173, 174] Moreover, the different permutations of interwall interactions between the inner and outer tubes of DWNTs also result in their electronic structure being somewhat different from that of SWNTs, thereby leading to their unique spectral features.[170, 175-178] By comparison with SWNTs shown to enhance electron transport,[53] DWNTs with a high charge mobility have been utilized to construct efficient solar cells by facilitating hole transport**.**[179, 180] Moreover, the advanced structural stability,[169]

decent thermal conductivity, and high mechanical stiffness[174] render DWNTs as promising candidates for numerous applications.[181, 182]

Most recently, chemical functionalization studies of DWNTs, including sidewall fluorination, have been carried out.[183] Raman and optical absorption spectra results have indicated that fluorination can be used to suppress the optical properties of carbon nanotubes without interfering with the properties of inner tubes.[184] That is, it is possible to suppress only the Raman radial breathing modes contributed by the outer tubes of DWNTs, while keeping intact the intrinsic electronic structure of the inner tubes, as demonstrated by photoluminescence maps and optical absorption spectra.[184] In the context of DWNT–NC heterostructures, fluorine atoms on the outer tubes of DWNTs have been found to more effective at nucleating and growing 5-7 nm CdSe nanoparticles *in situ* than oxygen-containing functional groups.[185] Nonetheless, the *in situ* chemical synthesis of semiconducting nanoparticles directly onto the surfaces of carbon nanotubes usually leads to inhomogeneities in shape and size.[186]

In this Chapter, we present the covalent, linker-mediated synthesis of a DWNT–NC heterostructure, prepared by anchoring surface-modified CdSe quantum dots (QDs) onto the surface of functionalized DWNTs. By applying a relatively mild treatment, the physical integrity and optoelectronic properties of the DWNT would not be necessarily compromised upon functionalization.

3.1.2 *Photophysical studies of CNT–QD heterostructures*

As discussed in Chapter 1, the fate of the electron-hole pair (exciton) highly depends upon the presence of radiative and non-radiative channels. Upon conjugation with CNTs, two external non-radiative channels, including Förster resonance energy transfer (FRET) and charge

transfer, can be taken into account. FRET is a non-radiative relaxation process wherein the energy is transferred from a photoexcited donor to a ground-state acceptor without the concomitant irradiation of a photon. The interaction is based on the coupling between dipoles of a donor and an acceptor. There are at least three basic requirements for FRET to occur: (i) overlap between the emission spectrum of a donor and absorption spectrum of an acceptor, (ii) coupling between donor and acceptor transition dipoles, and (iii) close proximity of donor and acceptor. The rate of energy transfer can be simplified as

$$K_{FRET} = \frac{1}{\tau_d}\left(\frac{R_0}{r}\right)^6 \qquad (3.1)$$

where τ_d is the radiative lifetime of a donor in the absence of an acceptor, R_0 is the Förster distance at which the efficiency of energy transfer is 50%, and r is the donor-to-acceptor distance. Generally, FRET interaction is weak when $r > 100$ Å. The estimation of R_0 involves a number of parameters including the spectral overlap integral, the orientation of donor-acceptor dipoles, the refractive index of the medium, and the fluorescence quantum efficiency of the donor.

On the other hand, charge transfer of one of the photogenerated charge carriers from QDs to an acceptor occurs via tunneling. The rate of charge transfer can be estimated based on the free energy change of the reaction, the reorganization energy, and the electronic coupling strength, as elaborated in the later section. Its kinetics has been found to depend exponentially on the distance between donors and acceptors. This means that the molecular linker between QDs and the acceptors plays a crucial role in determining the rate of interfacial electron transfer and offers a powerful handle for controlling interfacial electronic coupling. In addition to the

molecular length, the chemical nature of the functional groups as well as the molecular backbone can also have a profound effect upon the coupling strength and molecular conductance.

To date, suppression of fluorescence of QDs has been commonly observed upon conjugation with CNTs, which indicates strong coupling between them. However, it is still problematic to unambiguously attribute the reduced fluorescence to either charge or energy transfer between the QDs and CNTs. In some of the studies, the quenching of the QDs has been attributed to the charge transfer process[76] while others indicated that energy transfer is the main factor.[77] In one recent study, the authors have shown that the energy transfer efficiency from an individual quantum dot to a carbon nanotube can reach as much as 96%.[62] In order to effectively implement CNT–QD heterostructures in photovoltaic devices, efficient charge carrier extraction is a crucial step. While devices, which exploit FRET process, have been shown to be useful for solar harvesting,[187] such process is detrimental to a device based primarily upon charge transfer interactions. As charge and resonance energy transfer are competing with donor-acceptor interactions, it is essential to be able to understand the design rules which can favor one process over the other. Therefore, the investigation of the photophysical properties of QD–CNT heterostructures is crucial for developing a fundamental understanding of exciton dissociation via a charge/energy transfer process, thereby providing critical insights into the chemical modification of the QD surface as well as the rational design of QD-based heterostructures for the development of photovoltaic devices.

In order to experimentally resolve the dynamics of electron/energy transfer events, spectroscopic techniques employing sub-picosecond pulsed lasers are often necessary. As suggested in Chapter 1, those time-resolved spectroscopies usually utilize a pump-probe configuration, wherein the change in the signals (e.g. fluorescence and absorption) after

excitation by the pump pulse can be monitored by the probe pulse. In this Chapter, we have employed time-resolved photoluminescence spectroscopy (TRPL) to study the dynamics of excitons generated in QDs. Ideally, the excitons generated in well-passivated, defect-free quantum dots are expected to decay via a radiative recombination with a constant rate, therefore producing a single exponential decay trace. In fact, exciton decay is influenced by both radiative and non-radiative recombination events, the rate of which is fluctuated over time. As a result, a multi-exponential exciton decay of QDs is typically observed during time-resolved fluorescence measurements.

A number of groups have used TRPL to study the carrier dynamics in QD-acceptor systems. Watson and co-workers have studied electron transfer from CdS QDs capped with mercaptoalkanoic acid to TiO_2 nanoparticles by using TRPL, which complements transient absorption.[188] The rapid decay of CdS QDs upon addition of mercaptoalkanoic acid and TiO_2 has implied the presence of a dynamic quenching mechanism. By contrast, the time-resolved emission data of CdS–ZrO_2, wherein the conduction band of ZrO_2 is located above that of CdS, showed no additional dynamic quenching. It further confirmed that the quenching process was due to an interfacial electron transfer from CdS to TiO_2. Kamat and co-workers have used TRPL to investigate a size-dependent charge transfer rate from CdSe QDs to a TiO_2 nanotube array.[63] CdSe QDs with smaller size (e.g. 2.6 nm) exhibited faster decay with an average lifetime of 0.4 ns as compared with the 2.6 ns measured for bigger QDs (e.g. 3.7 nm). These results indicated that the charge injection process is highly affected by the energy difference in the conduction band between CdSe and TiO_2. It is also important to note that it can be difficult to distinguish charge transfer from the de-convolution of dynamic contributions from other non-radiative

channels such as charge trapping, energy transfer, and hot electron relaxation, especially if there is a lack of other complementary data.

3.2 Experimental Section

3.2.1 *Materials preparation*

3.2.1.a Synthesis of DWNT–CdSe (DWNT–CdSe/ZnS) heterostructures

Commercial DWNTs (Helix Material Solutions, Inc.) were purified in nitric acid so as to remove metal catalysts and carbonaceous impurities, including SWNTs and amorphous carbon. Specifically, 50 mg of DWNTs were dispersed in 8 M HNO_3 by sonication, and then stirred 60ºC for 30 h. The resulting, purified DWNTs have been filtered through a 0.2 μm polycarbonate membrane (Millipore), thoroughly washed by excess water, and ultimately dried, prior to TGA measurements.

CdSe quantum dots (CdSe QDs) have been prepared according to a well-known protocol in the prior literature.[146] Upon further processing, oleic acid capping agents of as-prepared CdSe QDs were replaced by 2-aminoethanethiol molecules (AET) via a ligand exchange reaction, resulting in water-soluble, amino-terminated CdSe quantum dots (AET-CdSe QDs). The resulting AET-CdSe QDs were finally re-dispersed in dimethyl sulfoxide (DMSO). Commercial CdSe/ZnS QDs (D = 5.4 nm with core diameter of 2.5 nm) capped with octadecylamine in toluene were purchased from NN lab. For CdSe/ZnS QDs, the aforementioned ligand-exchange procedure was repeated three times in order to ensure the complete replacement of octadecylamine with AET and obtain AET-CdSe/ZnS QDs.

The composites were synthesized by formation of amide bonds between the amino terminal groups on the surface of AET-CdSe QDs (or AET-CdSe/ZnS QDs) and the carboxylic groups on DWNTs with the assistance of 1-ethyl-3-(3-dimethylaminopropyl) carbodiimide (EDC)/*N*-hydroxysuccinimide (NHS) (or *N*,*N'*-Dicyclohexylcarbodiimide (DCC)). In a typical experiment, 1 mg of oxidized DWNTs was dispersed in 10 mL dimethylformamide (DMF) by sonication. A total of 80 mg of EDC/NHS and an aliquot of 2-(*N*-morpholino) ethanesulfonic acid (MES) buffer were subsequently added, followed by the addition of 1 mL of AET-CdSe QDs (or AET-CdSe/ZnS QDs) with an estimated concentration of 10^{-5} M. The resulting solution was stirred in the dark for 24 h. Upon completion of the reaction, the solution was vacuum filtered by using a 0.2 μm polycarbonate membrane (Millipore), extensively washed with DMF and distilled water, and finally oven-dried for subsequent measurements.

3.2.1.b Synthesis of CdTe QDs and AET-CdTe QDs

0.0128 g of CdO (0.1 mmol) and 0.057 g of tetradecylphosphonic acid (TDPA) (in order to slow down the reaction rate as compared with oleic acid) was dissolved in 5 ml of octadecene (ODE) at 250ºC under Ar atmosphere. 0.025 g of Te (0.196 mmol) was dissolved in 0.475 g of tributylphosphine (TBP), followed by the addition of 1.5 g of ODE. At 285ºC, the Te-TBP-ODE solution was swiftly injected into CdO-TDPA-ODE solution and heating was turned off immediately. The color of the solution gradually turned from yellow to orange and onwards to red and dark brown. When the solution cooled down, it was red with an absorption peak located at 594 nm. The unreacted precursor was then extracted by adding chloroform/methanol and the as-prepared CdTe solution was washed by acetone followed by centrifugation. The diameter of as-prepared CdTe nanocrystals is about 3.5 nm and the concentration of the CdTe solution is

estimated to be 7×10^{-5} M, according to the reported correlation between extinction coefficient and particle size. CdTe is unfortunately relatively unstable in air.

Ligand exchange was conducted in a glove box (air-free environment). 0.1 mL of CdTe stock solution was added into 2 mL of chloroform, followed by 0.1 mL of 0.5 M AET. The mixture was manually shaken prior to the subsequent addition of 1 mL of water. Once the water phase turned red, it was carefully separated from chloroform phase by pipette and kept in an inert atmosphere. We note that AET-CdTe is stable in water but not ethanol.

3.2.2 *Materials characterization*

3.2.2.a Electron microscopy

Low-magnification TEM images were taken at an accelerating voltage of 80 kV on a FEI Tecnai12 BioTwinG^2 instrument, equipped with an AMT XR-60 CCD digital camera system. High-resolution images were obtained on a JEOL 2010F instrument, equipped with an INCA EDS system, at accelerating voltages of 200 kV. Specimens for all of these TEM experiments were prepared by dispersing the as-prepared product in ethanol, sonicating to ensure adequate dispersion of the nanostructures, and dipping one drop of solution onto a 300 mesh Cu grid, coated with a lacey carbon film.

3.2.2.b Powder XRD

Crystallographic and purity information on nanotube–nanocrystal heterostructures were obtained using powder XRD. To analyze these materials, as-prepared samples were subsequently sonicated, and finally air-dried upon deposition onto glass slides. Diffraction patterns of these

materials were collected using a Scintag diffractometer, operating in the Bragg configuration using Cu K_α radiation (λ = 1.54 Å) from 20^o to 80° at scanning rates of 0.25° per minute.

3.2.2.c Optical spectroscopies and fluorescence microscopies

FT- IR data were obtained on a Nexus 670 (Thermo Nicolet) instrument equipped with a single reflectance zinc selenide (ZnSe) ATR accessory, a KBr beam splitter, and a DTGS KBr detector. Solid samples were placed onto a ZnSe crystal. Measurements were obtained in absorbance mode using the Smart Performer module. UV-visible spectra were collected at high resolution using a Thermospectronics UV1 apparatus with quartz cells maintaining a 10-mm path length. Data were corrected to account for the solvent background.

Composite samples for optical measurements were freshly prepared by dispersing CNT–QD heterostructures in ethanol by sonication. For AET-QD samples, the concentration of AET-QDs in ethanol solution was estimated to be similar to that in composite samples. Steady-state fluorescence data were obtained at room temperature on a home-built confocal microscope coupled to a high-repetition rate (250 kHz) ultrafast Ti : sapphire-based amplified laser system. An optical parametric amplifier was used to generate visible laser pulses (~200 fs) tuned to the appropriate region of the absorption spectrum of the quantum dots. Before photoexcitation, the laser pulses were temporally broadened and spectrally narrowed to a bandwidth of 2 nm, using a set of interference filters. The excitation wavelength was tuned to be 524 nm, close to the exciton absorption of our samples, thereby avoiding possible complications of our carrier dynamics with potential multi-exciton generation process. Emission from the QD solutions was collected into a single-grating spectrometer (iHR320, JY Horiba) equipped with both a liquid nitrogen cooled CCD (Symphony, JY Horiba) for acquiring data and an avalanche photodiode (Micro-Photon-

Devices) for dynamic measurements. Time-resolved PL data were acquired by using the time-correlated single photon counting technique using Picoharp 300 (Picoquant GmbH) photon counting instrumentation. Optical interference filters (Chroma) and the grating spectrometer were simultaneously employed for spectral filtering of the PL emission. Solutions were continuously stirred during data acquisition. The power density of laser remained sufficiently low so that less than one electron-hole pair per QD presumably was generated during each pulse period.

The resulting time-resolved fluorescence data can be fit by exponential decay functions with either one or more components.

$$I = \sum_{i}^{n} A_i e^{-t/\tau_i} \qquad (3.2)$$

wherein A_i is the amplitude and τ is the lifetime. For the average lifetime, it can be calculated according to an intensity-weighted approach

$$\tau = \sum_i A_i \tau_i^2 \Big/ \sum_i A_i \tau_i \qquad (3.3)$$

Fluorescence images were taken using a confocal fluorescence microscope (Leica, TCS SP5) equipped with an argon ion laser. Samples were excited under 488 nm irradiation, and data images were separately collected via two different output channels, which were monitored in the range of 590–620 nm and 570–800 nm, respectively.

3.3 Results and Discussion

3.3.1 *Preparation of purified, oxidized DWNTs*

As-obtained commercial DWNTs typically were contaminated with metal particles, amorphous carbon, and SWNTs, as illustrated in Figure 3.1. Based on the TGA data, upon heating pristine DWNTs to 800ºC under air, the remaining weight % of sample residue collected was ~10%, indicative of 10% metal content. Furthermore, the plot of derivative weight vs. temperature (Figure 3.1C) suggested that DWNTs were destroyed at ~560ºC, with a shoulder at around 476ºC, which can be attributed to the presence of amorphous carbon and SWNTs in the sample, likely due to the higher reactivity of amorphous carbon, defective graphitic carbon, and SWNTs as compared with DWNTs.[172, 189, 190] We note that metal particles present in pristine DWNTs, possessing a similar size to that of QDs, can interfere with the observation of DWNT–QD heterostructures under TEM, whereas the presence of SWNTs may affect the final properties of DWNT–QD heterostructures. Therefore, it was critical to remove those impurities prior to a further coupling reaction.

It is known that nitric acid can not only destroy the metal catalyst but also remove amorphous carbon and chemically active SWNTs. TGA measurements demonstrated that less than 1% of metal catalyst was contained in purified DWNTs along with the disappearance of the shoulder, previously observed at 476ºC (Figure 3.1D). These results indicated that our purified DWNTs were, to a certain extent, free from amorphous carbon and SWNTs as well. A comparison between TEM images of DWNTs before and after nitric acid treatment provides for visual confirmation of a much higher sample quality associated with our purified DWNTs.

3.3.2 *Characterization of DWNT–CdSe heterostructures*

The oxidation of DWNTs was confirmed by IR spectra as illustrated in Figure 3.2. The obvious peak for oxidized DWNTs at 1700 cm^{-1} is associated with the presence of carboxylic acid groups. Oxidized DWNTs also could be well-dispersed in ethanol and even water, as the presence of carboxylic groups on the surface of DWNTs enhances their solubility[191] in polar solvents. In addition, Figure 3.3 shows infrared spectra of CdSe QDs before and after ligand exchange. Specifically, peaks at 2926 cm^{-1} and 2858 cm^{-1} in oleic acid (OA) and OA-CdSe can be assigned to C-H stretching vibration associated with the alkyl chain; the C=O double bond stretching mode at 1700 cm^{-1}, originally shown in oleic acid ligands, shifts to 1535 cm^{-1} and is associated with the vibration of COO^- when oleic acid bonded onto the CdSe surface. It is suggested that the carboxylic group of oleic acid was de-protonated while interacting with the Cd atoms on the CdSe surface. A comparison of the infrared spectra before and after ligand exchange confirmed the presence of AET on the surface of CdSe after the ligand exchange process. It has been reported that the thiol ligands can be de-protonated to form thiolate molecules, which can then be bonded onto the QD surface.[28, 160] As such, peaks associated with S-H in the region of 2400 – 2600 cm^{-1} disappeared upon AET attachment to the CdSe surface. We also note that thiol-capped CdSe QDs were not temporally stable, losing solubility over time. This could be attributed to photocatalytic oxidation of the thiol ligands to disulfides, which do not attach well to the surfaces of nanocrystals.[154]

According to the same protocol of the coupling reaction discussed in Chapter 2, the formation of DWNT–CdSe heterostructures was based on the formation of amide bonds between the amino groups on the surface of CdSe and the carboxylic groups on the CNT surface. The appearance of peaks at 1656 and 1504 cm^{-1} in the infrared spectra of the as-obtained DWNT–QD

heterostructures suggested the formation of amide bonds. TEM images (Figure 3.4) show that upon conjugation, QDs with an average diameter of 3.4 nm were clearly visible along DWNT bundles. We note that the coverage of QDs on DWNTs was non-uniform, which could be attributed to (i) either non-uniform distribution of carboxylic groups on the CNT surface (ii) or an inefficient attachment of QDs as a result of steric hindrance arising from the possible aggregation of DWNTs. Figure 3.4B and C showed typical high-resolution TEM images of DWNT–CdSe heterostructures, wherein the distinctive double walls of carbon nanotubes and highly crystalline CdSe nanocrystals immobilized on the nanotube surface could be observed. It is worth noting that some of the tubes appeared to be wrapped in some amorphous coating, which most likely originated from solvent residue, incurred during the TEM sample preparation process.

Powder XRD (Figure 3.4D) confirmed the presence of CdSe in these as-prepared heterostructures. The peak at ca. 25.4º was associated with the presence of graphite (JCPDS No. 75-1621) in carbon nanotubes. We noted that for the DWNT–QD heterostructures, peaks at 42.5º and 48.8º, indicated by arrows, though weak, could be reliably assigned to the reflections of hexagonal würtzite CdSe QDs (JCPDS No. 02-0330), again consistent with the formation of DWNT–QD heterostructures.

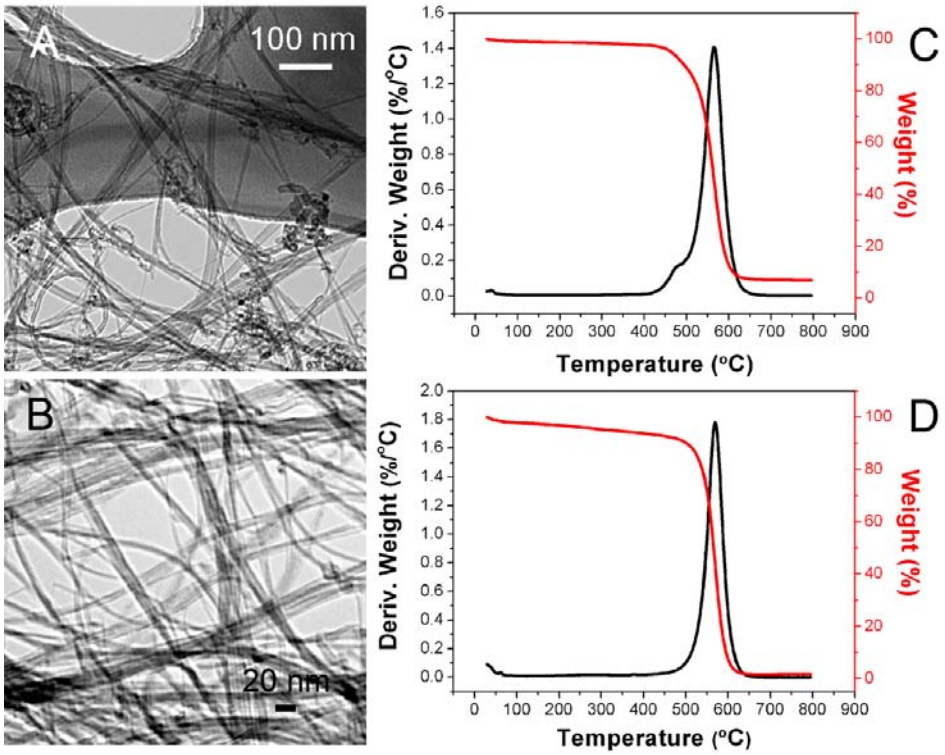

Figure 3.1: TEM images of (A) raw double-walled carbon nanotubes (DWNTs) and (B) the corresponding purified DWNTs (B). TGA data of (C) raw DWNTs and (D) the corresponding purified DWNTs.

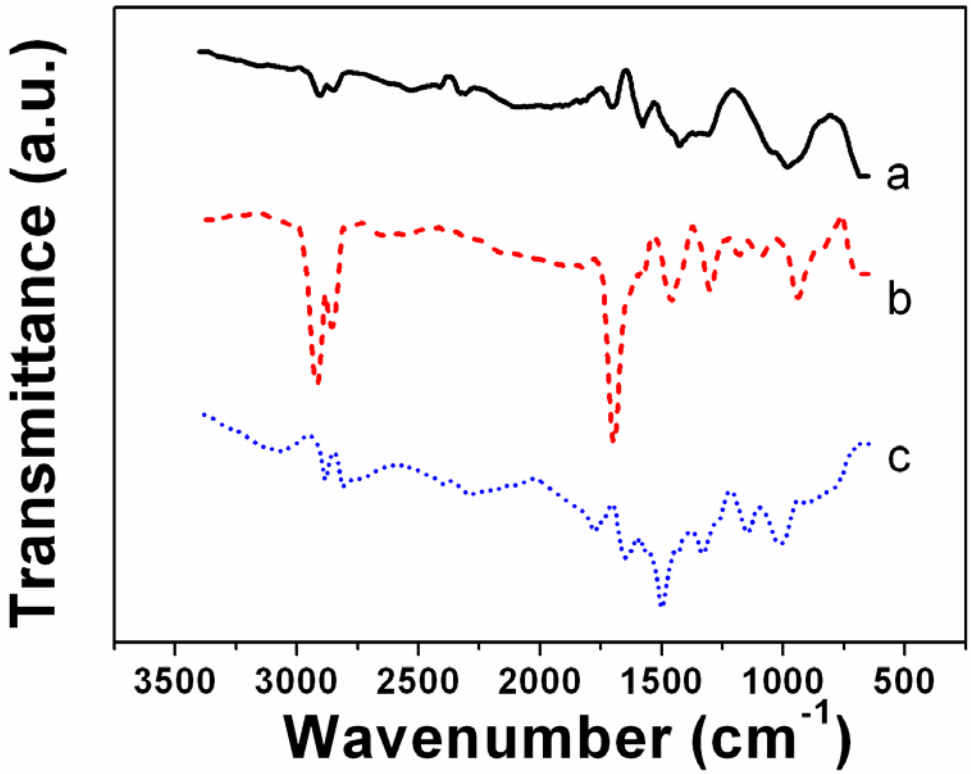

Figure 3.2: Infrared spectra of (a) raw DWNTs (black), (b) oxidized, purified DWNTs (red), and (c) DWNT-CdSe heterostructures (blue), respectively.

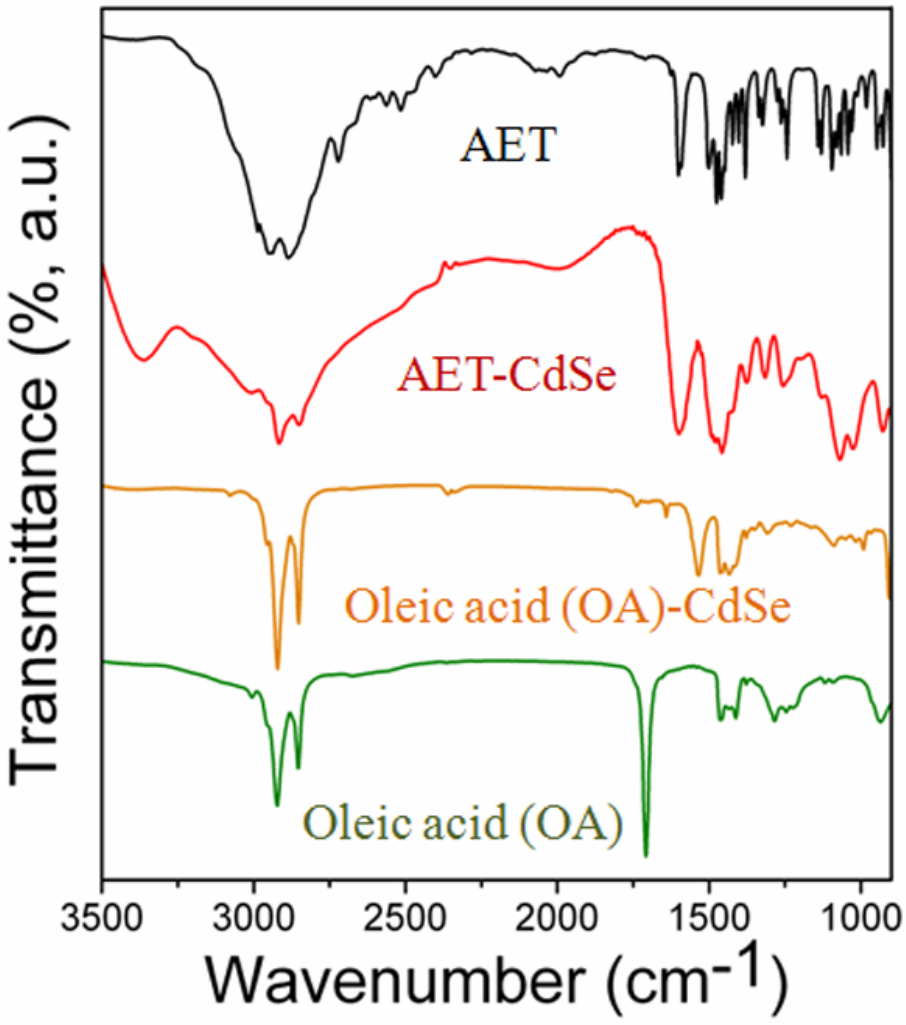

Figure 3.3: Infrared spectra of oleic acid (OA) (green), OA-CdSe (orange), AET-CdSe (red), and AET (black), respectively.

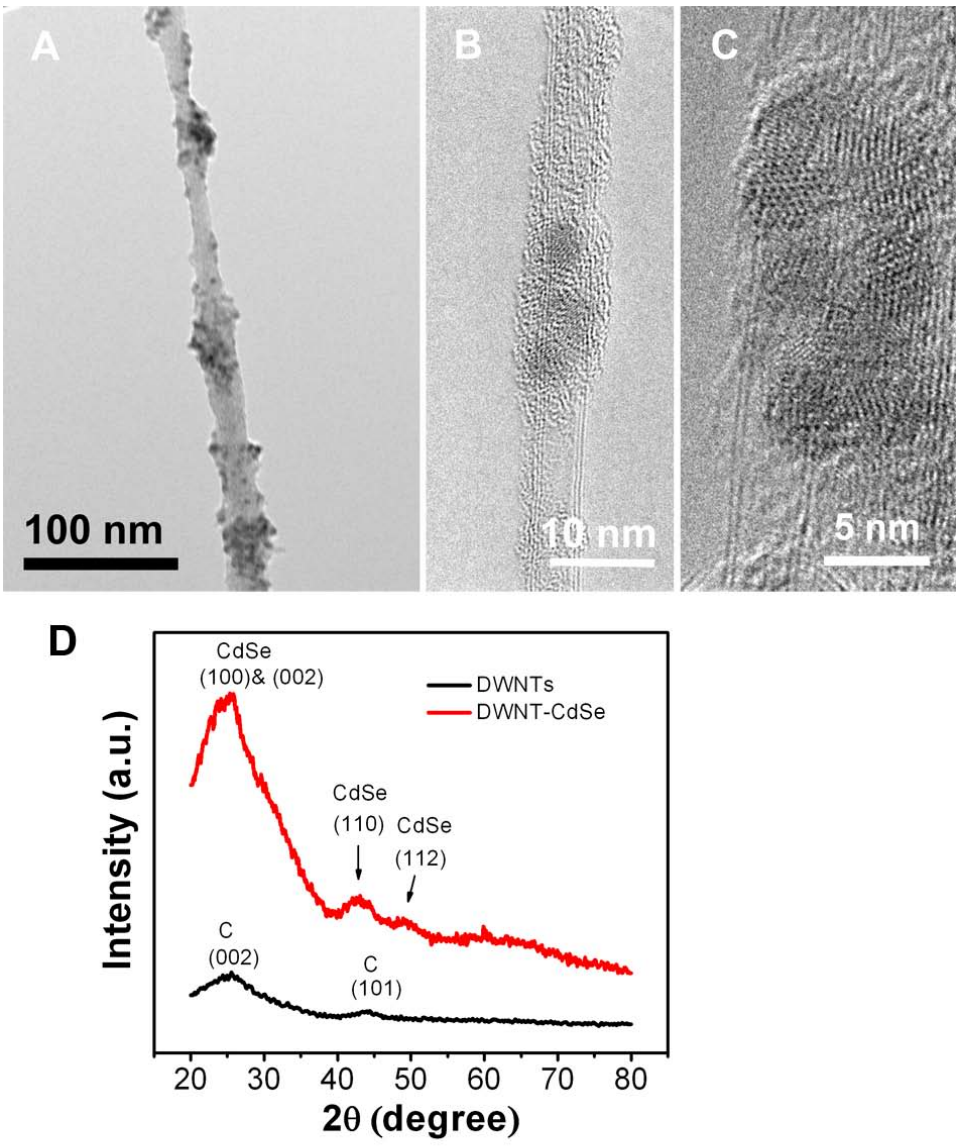

Figure 3.4: (A) TEM as well as (B and C) HRTEM images of DWNT-CdSe. (D) XRD patterns of raw DWNTs (black) and DWNT–CdSe heterostructures (red).

3.3.3 *Optical characterization of DWNT–CdSe heterostructures*

3.3.3.a Absorption and steady-state fluorescence

For absorption spectra, as-prepared CdSe nanocrystals (Figure 3.5) exhibited a well-pronounced absorption peak at ~580 nm, whereas a 5 nm red shift in peak position was noted for AET-CdSe, indicating a possible aggregation of QDs upon ligand exchange. Similarly, a physical mixture of oxidized DWNTs with the same concentration of AET-CdSe QDs yielded an identical absorption spectrum (Figure 3.5). However, the peak intensity was relatively weaker, an observation attributable to light scattering by DWNTs, causing less photons to be absorbed by AET-CdSe QDs themselves. No obvious spectral feature was noted in the absorption spectrum of DWNT–CdSe nanostructures, presumably due to the decreased CdSe concentration in the final composites, which might have been below the detection limit of UV-visible spectroscopy. In addition, the strong background due to scattering by DWNTs might have conceivably overwhelmed the signal generated by CdSe QDs.

In steady-state fluorescence measurements, as-prepared CdSe QDs exhibited a pronounced band-gap emission (excitonic emission) at 595 nm with only a small shoulder centered at 750 nm, merging with the long tail of the band-gap emission of CdSe (Figure 3.6). By contrast, the fluorescence spectrum of AET-CdSe QDs (Figure 3.6) consists of a high-energy peak, corresponding to band-gap emission at 600 nm, as well as a broad, low-energy emission band at 800 nm with significant intensity. As compared with that of as-prepared CdSe QDs, this emission appearing in the near infrared region is believed to originate from trap states on the surface induced by the surface ligand itself, namely AET. The asymmetric band-gap emission

profile is suggestive not only of the broad size distribution of CdSe QDs but also of spectral fluctuations in their microenvironment. Moreover, the broad trap emission centered at 795 nm indicated a wide energy distribution in the trap states, with the energy shift of > 0.4 eV relative to the excitonic emission.

Strikingly, even though the complete quenching of emission of QDs in CNT–QD heterostructures has been observed commonly, the excitonic emission of QDs by CNTs in our DWNT–CdSe heterostructures was still quite evident. Moreover, as compared with the emission profile of AET-CdSe alone, the excitonic peak position for DWNT-CdSe composites blue shifted by 20 nm. More interestingly, the trap emission from QDs was no longer observable, suggesting that the surface trap emission state was effectively quenched by the presence of DWNTs.

For comparison, a control sample consisting of a physical mixture of nanotubes and quantum dots, generated simply by adding DWNTs together with AET-CdSe QDs at the same concentration as the pure AET-CdSe solution, was also optically probed. It turns out that the observed peak position of the excitonic emission in the mixture was similar to that of AET-CdSe QDs alone; moreover, the trap emission state was still significant. Furthermore, the intensity ratio of the trap emission state to the excitonic emission state (I_t/I_e) for the mixture sample was smaller than that of the AET-CdSe solution. Interestingly, when an excess of AET ligands was added to the mixture solution, an increased I_t/I_e ratio was observed, once again suggesting that the presence of AET ligands contributed to an increase in trap sites as well as to the observed trap emission (Figure 3.7). Hence, it is reasonable to infer that the equilibrium associated with the association and dissociation kinetics of AET ligands on the CdSe QD surface was affected by the interaction between the nanotube and QDs, resulting in the observed changes in I_t/I_e. We note that the absolute value of the intensity difference of I_e between that of the AET-CdSe solution

and the corresponding physically mixed sample could be due to factors such as power fluctuation, scattering from the carbon nanotubes, as well as re-absorbed emission by the DWNTs themselves.

Confocal fluorescence images (Figure 3.8) of both AET-CdSe and DWNT-CdSe heterostructure composites were used to further confirm our findings in steady-state spectra. Images were collected at two different channels separately monitored at 600 nm and 800 nm, corresponding to excitonic emission and trap emission of CdSe, respectively. Not surprisingly, the AET-CdSe by themselves showed discernible fluorescence in images obtained at both ca. 600 nm and ca. 800 nm emission wavelengths (Figure 3.8). For the DWNT–CdSe heterostructures, as expected, fluorescence can be observed in the 600 nm channel but not at the 800 nm channel, in excellent agreement with our steady-state fluorescence spectra results. Moreover, the overlapping images of fluorescence images and bright-field images clearly correlated the spectral overlap of the CdSe excitonic fluorescence with the spatial localization of the DWNTs. We note that the distribution of fluorescence of CdSe along the DWNTs themselves was not uniform, an observation fully consistent with our TEM data. We also cannot rule out the possible existence of either small clusters or single CdSe nanocrystals exhibiting weak fluorescence beyond the functional capabilities of our detector.

Based on all of these data, we can conclude that the conjugation of DWNTs with CdSe plays a significant role in affecting the surface-state emission of the QDs and also, profoundly alters the dominant relaxation pathway of photogenerated charge carriers within the QDs themselves.

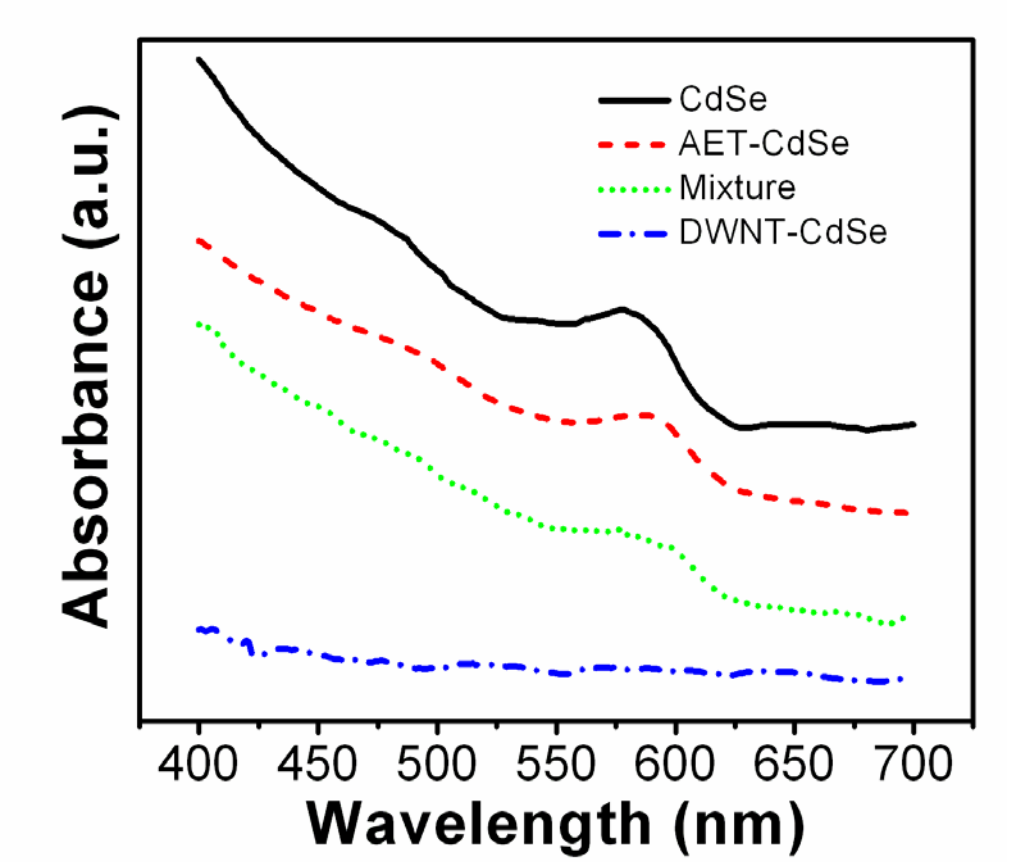

Figure 3.5: UV-visible spectra of as-prepared CdSe (black), AET-CdSe (red), a physical mixture of DWNTs and AET-CdSe (green), and DWNT-CdSe (blue).

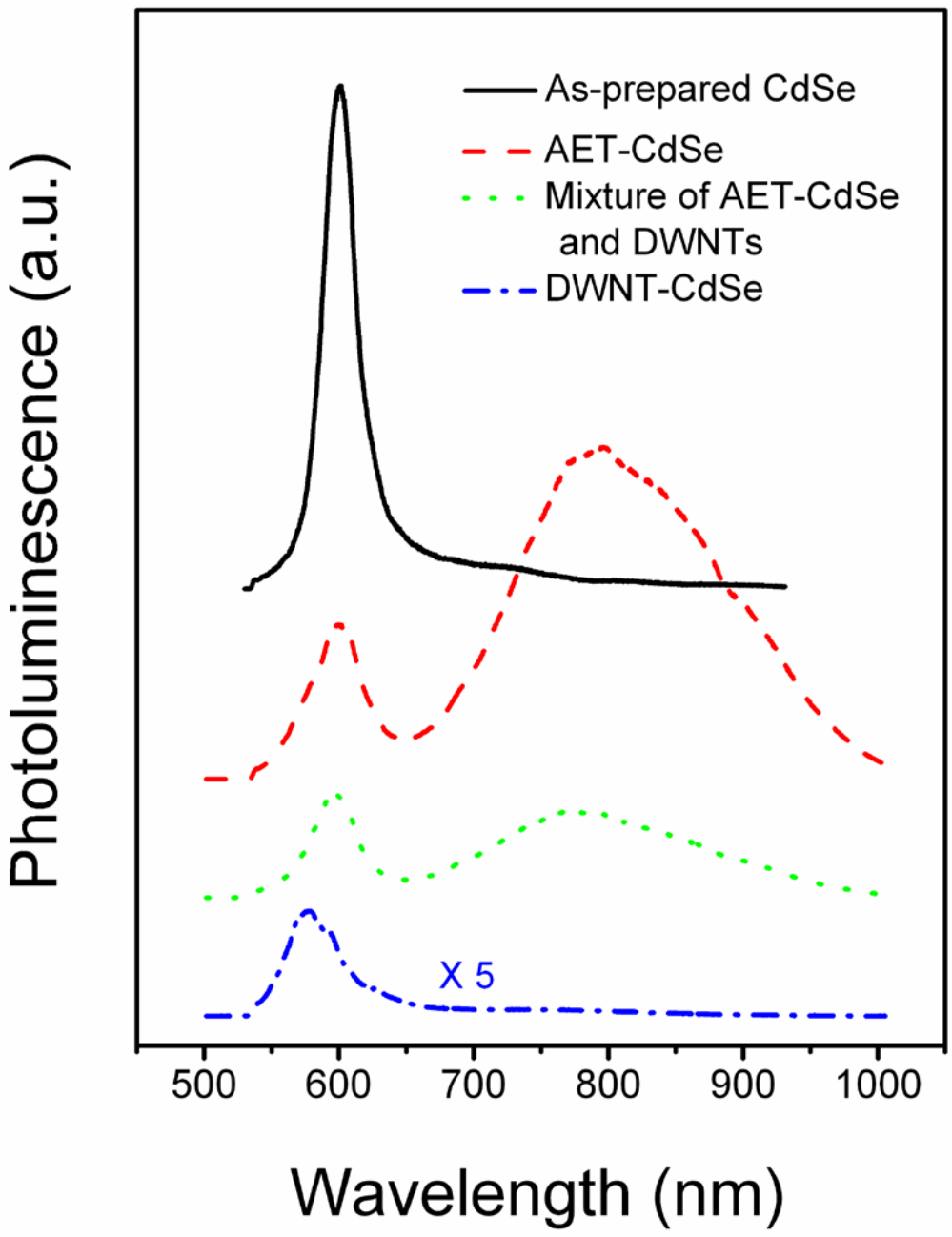

Figure 3.6: Steady-state photoluminescence spectra of as-prepared CdSe (black), AET-CdSe (red), a physical mixture of DWNTs and AET-CdSe (green), and DWNT–CdSe heterostructures (blue), respectively.

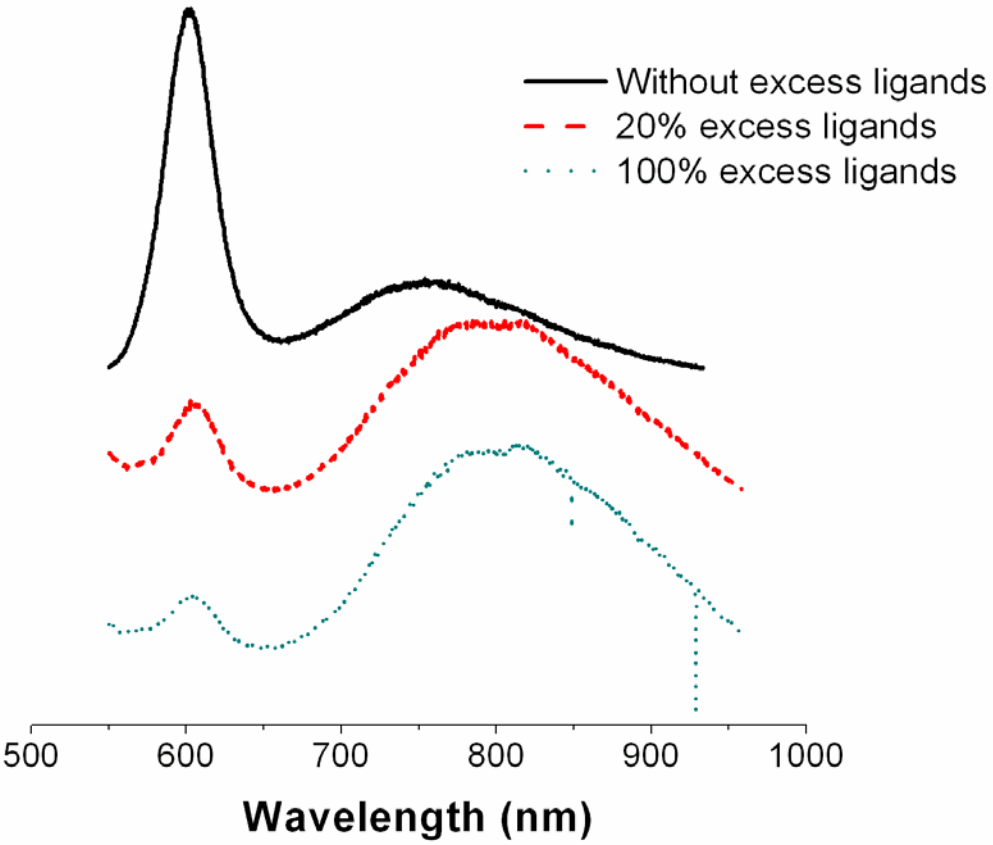

Figure 3.7: Influence of surface ligands upon the surface trap states. A rise in the excess amount of AET ligands in the solution correspondingly increased the ratio of trap emission to excitonic emission.

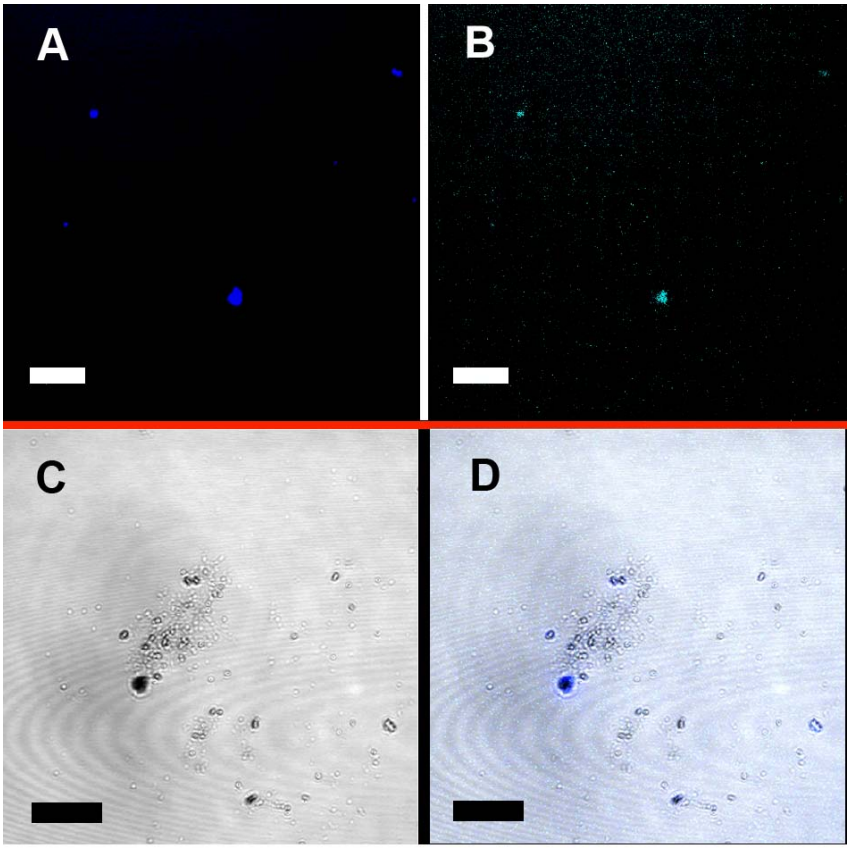

Figure 3.8: Confocal scanning fluorescence microscopy images. (A-B) fluorescence images of AET-CdSe QDs collected at ca. 600 nm (A) and ca. 800 nm (B). (C) The bright field image of DWNT–CdSe heterostructures. (D) Merged image of DWNT–CdSe heterostructures, including (C) and the corresponding fluorescence images collected at both ~ 600 and ~ 800 nm. No detectable signal was observed in the near-infrared channel. Scale bars are 10 µm.

3.3.3.b Time-resolved fluorescence

Time-resolved fluorescence spectroscopy was used to reveal more information about the dynamics of charge carriers within the heterostructures probed. First, we monitored the decay of exciton emission and trap emission of isolated AET-CdSe QDs. Figure 3.9A shows time-resolved emission measurements for each of these bands on a log-log scale in order to highlight the different decay components and the overall time window difference in the visible and NIR regions. The exciton luminescence was multi-exponential with a relatively short total lifetime, with early time decay dynamics occurring faster than the instrument responsive function, which was indicative of a very efficient non-radiative contribution. Given the risen of trap emission observed in the steady-state spectrum, this ultrafast process could be ascribed to the trapping process induced by the presence of AET ligands. On the other hand, the NIR trap emission was found to exhibit a long lifetime relative to the intrinsic radiative processes in CdSe QDs, with significant recombination still occurring on μs timescales. The recombination kinetics in the NIR can be compared directly with quantitative models that consider the effect on the QD PL of both the quantity and energy distributions of surface traps [192].

As such, both the energy shift associated with the trap emission (> 0.4 eV) and its decay kinetics are consistent with the presence of deep carrier traps. This is consistent with reports of thiol ligands as hole acceptors since their redox energy level is situated at a noticeably higher energy level than that of the valence band of CdSe[193]; moreover, it is partially due to the low electronegativity of sulfur as compared with oxygen in either oleic acid or TOPO.[21] Therefore, the presence of the AET-induced NIR emission and associated exciton kinetics provides a direct

optical signature for the presence of deeply trapped carriers in the vicinity of the QD surface and therefore allows us to monitor what happens to these trapped carriers upon functionalization.

When the CdSe-AET complex was covalently linked to DWNTs, the optical signature of these trapped charges disappeared, affecting both the steady-state and time-resolved PL. We note that as opposed to the multi-exponential decay behavior observed in the AET-CdSe sample, the exciton now decayed nearly mono-exponentially (Figure 3.9B), an optical signature indicative of charged exciton (trion) photoluminescence rather than a species with a nearby trapped charge. These types of exciton ion (trion) complexes form upon photoexcitation of a charged QD and have been shown to be weakly emissive. In our system, the observed TRPL kinetics is consistent with previous reports of trion emission in both films [194] and isolated[195, 196] CdSe-based QDs. In general, we observed double-exponential kinetic behavior similar to what has been reported, with average lifetimes that were shorter than the neutral radiative lifetime (typically 5 – 9 ns). Specifically, the luminescence decay curve can be perfectly fit by a double-exponential function as shown in the Figure 3.9B, revealing that more than 90% of the emission is contained in a single exponential function with a lifetime of ~ 2.7 ns. In addition, a small amount of carrier recombination was found to occur with a lifetime of ~ 11 ns (leading to an average total lifetime of 3.5 ns). Moreover, the failure of the recovery of nearly-mono-exponential decay in the physically mixed sample suggested that this unique optical signature was particularly intrinsic to the heterostructures of DWNT–CdSe (Figure 3.9B). In all cases, the results were found to be independent of incident laser power.

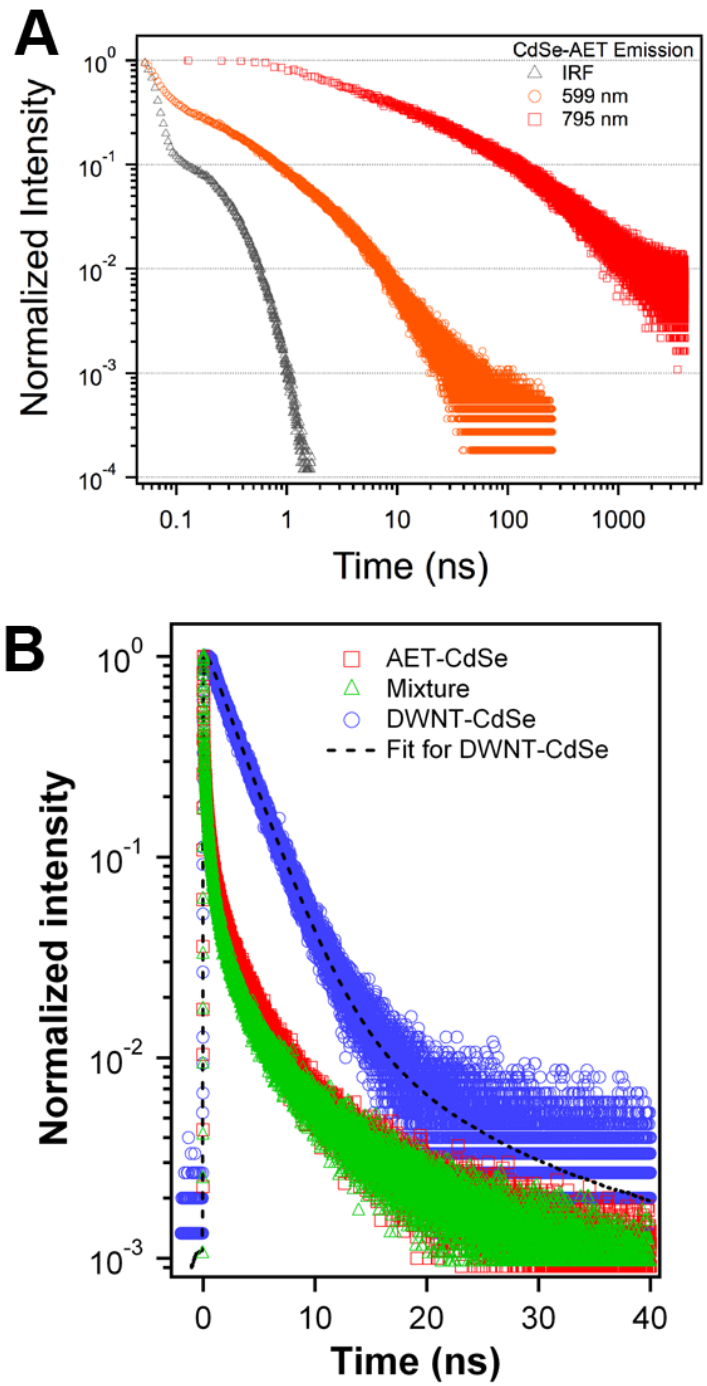

Figure 3.9: (A) Normalized exciton (orange at 599 nm) and trap (red at 795 nm) emission decay of CdSe-AET on a log scale. The instrument response function is shown as a reference (black). (B) Normalized time-resolved photoluminescence measurements of the exciton decay in AET-CdSe (red), a physical mixture of AET-CdSe and DWNTs (green), and DWNT–CdSe heterostructures (blue), respectively.

It is important to note that while previous reports have relied upon statistical fluctuations of the QD charge state for the observation of the trion luminescence, this species was isolated in our assembled heterostructure. The observed nearly-monoexponential decay implies that the rate of the non-radiative contribution, usually attributed to Auger recombination involving the extra charge carrier, was no longer fluctuating in time. Instead, the emission rate appeared to be time-independent, suggesting a long-lived (nearly permanent) charge separated state between the QD and the DWNTs. In addition, it is usually expected that the presence of CNTs would shorten the overall PL lifetime by providing additional nonradiative recombination channels. However, we note that the exciton in the DWNT–CdSe heterostructures had a significantly longer average lifetime as compared with that associated with AET-CdSe nanocrystals alone. Therefore, this provides further proof that we were likely observing the emission of trion formed in charged QDs. Both the disappearance of trap emission and the observation of the optical feature of charged QDs suggested that the electronic interaction between the QD and DWNT was dominated by a surface-mediated charge transfer process rather than by resonance energy transfer interaction.

Moreover, it is important to note that a low laser power of 5 – 500 μW was typically used in our measurements, corresponding to pulse energies of 0.2 – 2 nJ. If we used a value of 10^{-15} cm^2 as an upper bound on estimates of our absorption cross-sections[197] at 520 nm and a spot size of ~ 25 microns, the average number of carriers <N> expected from statistics is 0.015 – 1.5. This is well below the regime where multiple carrier interactions will become significant. In addition, samples were kept stirring in order to prevent charge buildup during measurements. Therefore, we believed that the observed kinetics were trustworthy without interference with multiple-exciton interactions.

3.3.4 *Calculation of distance-dependent kinetic rates*

To support our hypothesis above, we have analyzed the rates of different possible decay channels of the quantum dot excitation into the nanotube, including resonance energy transfer (RET) of both charge carriers via a near-field electromagnetic interaction and charge transfer (CT) of one of the charge carriers. Both of these processes are highly dependent upon the physical separation between donor and acceptor, and can potentially compete with each other. In the dipole limit, the RET rate is inversely proportional to the sixth order of magnitude of distance,[77] whereas the interfacial charge transfer rate decays much more rapidly, falling off exponentially with the tunneling distance.[198, 199]

3.3.4.a Determination of resonance energy transfer rates

The calculation of energy transfer rate has been conducted by our collaborator, Dr. Matthew Sfeir. The calculation process is briefly described here and the results are illustrated in Figure 3.10. Specifically, since the physical size of the nanotube is larger than the surface-to-surface distance (r) to the QD, the typical dipole approximation (and corresponding r^{-6} rate dependence) is no longer valid. As such, we have followed the methodology of Swathi and Sebastian[200] to more precisely treat the transition density in the nanotube. In this calculation, the QD is approximated as an ideal dipole, with a transition moment taken from calculations provided by Govorov et al. [201] We have modeled the DWNT as two non-interacting semiconducting SWNTs, (*14, 13*) and (*9, 8*), with the appropriate chiral vectors to give a NT–NT spacing of ~ 0.34 nm. We have simplified the calculation by using the single-electron picture to calculate the electronic structure of the nanotube (ignoring many-body effects). We argue that

the error introduced by this treatment is compensated for by the variation in the type (metallic, semiconducting) and size (1 – 4 nm) of the nanotubes likely present in our sample.

3.3.4.b Determination of charge transfer rates

Electron (charge) transfer kinetics of a donor-bridge-acceptor system in solution are often evaluated by Marcus theory,[202] in which the rate of ET can be estimated by the expression[203]

$$k_{ET} = \frac{2\pi}{\hbar} H_{DA}{}^{2} \frac{1}{\sqrt{4\pi\lambda k_B T}} \exp\left(\frac{-(\Delta G + \lambda)^2}{4\lambda k_B T} \right) \qquad (3.4)$$

wherein H_{DA} is the electronic coupling matrix element, λ is the total reorganization energy, ΔG is the free energy change of the electron transfer reaction, and k_B is Boltzmann constant. According to Marcus theory,[202] the rate of CT between CdSe and CNTs can be estimated based upon the free energy change of the reaction, the reorganization energy, and the electronic coupling strength.

Detailed calculations show that the amplitudes of the wave functions decrease exponentially with distance, and thus, the magnitude of $H_{DA}{}^{2}$ also decays exponentially as a function of distance.

$$H_{DA}^{2} = H_{DA,\max}^{2} \exp(-\beta r) \qquad (3.5)$$

wherein r is the separation between donor and acceptor or the length of the bridge, $H_{DA,\max}^{2}$ is the electronic coupling element at the contact distance for the donor and acceptor, and β is a structure-dependent attenuation factor which correlates with the rate of electron transfer with the chemical structure of the bridge.[204] In the case where the saturated hydrocarbon molecules, such as alkanethiol, are used as the bridge, β has been reported to be in the range of 0.8 –1.0Å [204, 205]

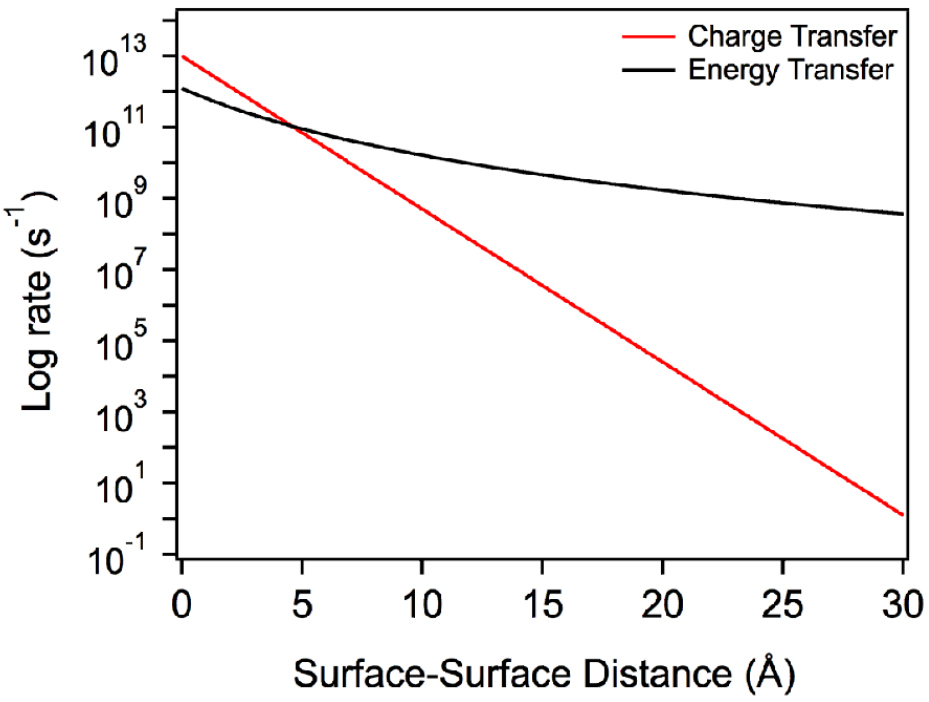

Figure 3.10: Calculations of the distance-dependent charge (red) and energy transfer (black) rates for an ideal dipole (p = 13 D) and a DWNT composed of (14, 13) and (9, 8) chiral vectors. The dielectric medium was set to be slightly higher than water (ε = 2).

Determination of λ

The total reorganization energy λ usually includes contributions from the molecular vibrations, λ_i, and solvent oscillators, λ_s, which strongly depends on the dielectric constants of the medium.[203] λ_i which involves the nuclear relaxation within nanocrystals, is usually considered to be small,[206, 207] on the order of 0.01 eV or smaller.[208] Kamat and co-workers have estimated that the reorganization energy was 10 meV for the electron transfer between QDs and metal oxide thin film.[209] In our study, we believe that charge transfer is surface-mediated. Therefore, the extent of the nuclear reorganization within the lattice of CdSe involved in charge transfer is likely to be negligible. For the sake of simplicity, it is reasonable for us to assume that λ_i is very small and close to 0 eV.

The parameter λ_s can be determined by the dielectric continuum model of a solvent, [203, 210] which is expressed as

$$\lambda_s = \frac{e^2}{4\pi\varepsilon_0}\left(\frac{1}{2r_D}+\frac{1}{2r_A}-\frac{1}{r_c}\right)\left(\frac{1}{n_D{}^2}-\frac{1}{\varepsilon}\right) \qquad (3.6)$$

where ε_0 is the permittivity constant of vacuum; r_D and r_A are the radii of the donor and acceptor, respectively; n_D and ε are the refractive index and the dielectric constant of the medium (ethanol), respectively; and r_c is the center-to-center distance between the donor and the acceptor. In our study, the edge-to-edge distance between CdSe and CNTs is estimated to be 4.7Å upon the formation of amide bonds between 2-aminoethanethiol and carboxylic groups on the surfaces of the carbon nanotubes. According to this model, in ethanol, λ_s is 0.22 eV. Thus, the total reorganization energy λ can be calculated to be around 0.22 eV. This value is also consistent

with the reorganization energy of 0.2-0.6 eV, estimated for the electron transfer from CdSe to Rhodamine B.[206] To this end, equation (3.4) can be rewritten as

$$\lg k_{ET} = 17 + \lg H_{DA,\max}^{2} - \frac{\beta}{2.3} r - \frac{4.2(\Delta G + \lambda)^2}{\lambda} \qquad (3.7)$$

where $H_{DA,max}$, ΔG, and λ are in eV and r is in Å.

Determination of ΔG

The driving force ΔG is associated with the difference in the redox potentials of CdSe and CNTs.[206, 210] The CB and VB potentials of CdSe with a size of 3.48 nm have been reported as -3.5 and -5.6 eV versus vacuum (or -1.0 and 1.1 V versus NHE, respectively).[211, 212] According to the trap emission peak centered at 800 nm, observed in steady state photoluminescence spectra, the hole trap states can be estimated to be around -5.1– (-5.2) eV. On the other hand, the reported work function for acid-oxidized multi-walled CNTs is -5.1 eV versus vacuum.[213] Therefore, the driving force of the hole transfer from the surface trap states of CdSe to CNT can be estimated as 0 – (-0.1) eV.

Determination of $H_{DA,max}$

$H_{DA,}$is an indicator of the extent of overlap between the donor and acceptor electronic wavefunctions. It has been reported that the electronic coupling energy between CdTe with a size of 3.4 nm and a inter-particle distance of 0.4 nm was 20 meV.[214] For hole transfer, the coupling energy should be smaller due to the high effective hole mass. In our case, 10^{-2} eV would be a fairly good approximation for $H_{DA,max}$

Given that $\beta = 1.0$ Å^{-1} and $\lambda = 0.22$ eV, equation (3.7) can be reformulated as

$$\lg k_{ET} = 13 - 0.43r, \Delta G = -0.1eV \qquad (3.8)$$

We note that although the total reorganization energy has a minor distance dependence, the electronic coupling element generally governs the distance-dependence of charge transfer dynamics. The length scales for charge transfer between the surface states of CdSe and CNTs is illustrated in Figure 3.10. At r = 4.7 Å, we estimate that $k_{ET} = 10^{10} \sim 10^{11}$ s^{-1}

3.3.4.c Insights into mechanism

Comparisons between the RET and CT scaling behavior are supportive of the hypothesis that we are observing predominantly trion emission as the observed changes in the PL kinetics cannot be explained by invoking a simple quenching process (e.g. CT or RET) alone. For example, if we assume that the carriers were located near the center of the QD, then the expected charge transfer rate was too low ($< 10^5$ s^{-1}) to effectively compete with either RET or radiative recombination. In this scenario, RET should dominate and led to an overall shortening of the total lifetime. According to the above calculations, we can determine the expected RET rate for the DWNT–CdSe. The surface-to-surface distance is 2.17 nm and the calculated rate is 1.3 ns^{-1}; this is ~5X faster than the observed total lifetime (3.5 ns). Regardless of the exact numbers given by the calculations, it is abundantly clear that a faster overall rate should be observed upon binding to the DWNT, in contradiction with the experimental results. However, if a photoexcited carrier can be efficiently trapped in a surface state, the rate of the CT process to a NT acceptor can enhanced significantly by several orders of magnitude, whereas radiative recombination and RET were no longer viable due to the poor spatial overlapping of hole and electron wavefunctions upon trapping. As a result, CT became the dominant relaxation pathway for the excitons generated in the CNT–CdSe hybrids and effectively competes with trap recombination

(given by our time-resolved PL measurements on the NIR emission band to be $10^6 – 10^7$ s^{-1}). To reinforce this, our calculations show that charge transfer can be quite an efficient process (~ 10^{11} s^{-1}) for a carrier trapped at the QD surface that is closest to the NT, owing to the short length of the molecular linker. Due to the high mobility of holes in the nanotube,[215] the probability of back electron transfer from the CNTs to CdSe QDs was much less likely than the forward rate, again due to the dramatic distance scaling. Consequently, quasi-permanent QD ions were generated via a surface-mediated charge transfer process (Figure 3.11), thereby giving rise to the optical feature observed in the time-resolved photoluminescence measurement.

In addition, we note that the rate of the initial surface trapping step will depend highly upon the number of traps and their energy distribution. In our material, we have tried to engineer an ultrafast trapping process, by maximizing the coverage of AET molecules on the surface of the particle. As such, we would not expect this surface trapping process, thought to be localized at the sulfur-QD interface, to be affected by the presence of the DWNT, which was bonded through the nitrogen atom of the AET. To this end, we conclude that, in this system, we were observing the long-lived negatively charged state of CdSe. The whole process can be summarized by the following equations:

$$\text{CdSe (exciton)}^{*} + \text{CdSe-AET (trap)} + \text{DWNT} \rightarrow \text{CdSe (exciton)}^{-} + \text{CdSe-AET (trap)}^{+} + \text{DWNT} \rightarrow \text{CdSe (exciton)}^{-} + \text{CdSe-AET (trap)} + \text{DWNT}^{+} \quad (3.9)$$

Furthermore, we note that if the back transfer rate was slow enough, then it is likely that the charge-separated state was achieved through incidental excitation (either from ambient illumination or laser alignment) before PL measurements occurred. As such, it is reasonable that the NIR signature of trap recombination disappeared in the DWNT–CdSe heterostructures. During laser studies, a subsequent electron-hole pair was generated via photon absorption by the

CdSe anion, creating a negative exciton ion (trion), which emitted light with a characteristic nearly mono-exponential decay behavior. [195, 196] We note that a recent result from the Lian group[206] has demonstrated that achieving asymmetric charge transfer rates in CdSe QD based complexes was feasible. Using an adsorbed Rhodamine B molecule, these researchers observed that charge transfer interactions accounted for 84% of the exciton quenching in QDs with a ratio of the forward/back charge rates of $> 10^4$.[206]

3.3.5 *Optical characterization of DWNT–CdSe/ZnS heterostructures*

As an additional check on our work, we generated an analogous heterostructure using core-shell CdSe/ZnS QDs after ligand exchange with AET. Given that the bandgap of ZnS is wider than that of CdSe, forming a type-I core-shell structure, the electrons and holes are expected to be more confined within the CdSe core by the ZnS shell. In particular, the hole wave function has a negligible probability of spreading into the ZnS layer,[216] thereby lowering the probability of hole trapping onto the surface of QDs. For a material without an effective charge trapping step, we expect that RET will dominate the electronic interaction and effectively shorten the total lifetime. Similar experiments in this regime have recently been reported for CdSe/ZnS QDs on graphene.[217] Experimentally, the as-prepared CdSe/ZnS QDs exhibited highly efficient emission with nearly mono-exponential decay due to the improved surface passivation provided by the ZnS shell. Upon AET ligand exchange, a multi-exponential decay of the exciton of AET-CdSe/ZnS suggested that the relaxed, lowest-lying core exciton remained weakly coupled to the surface states. However, no obvious trap emission was observed in AET-CdSe/ZnS, even upon an extensive ligand exchange process (Figure 3.12A).

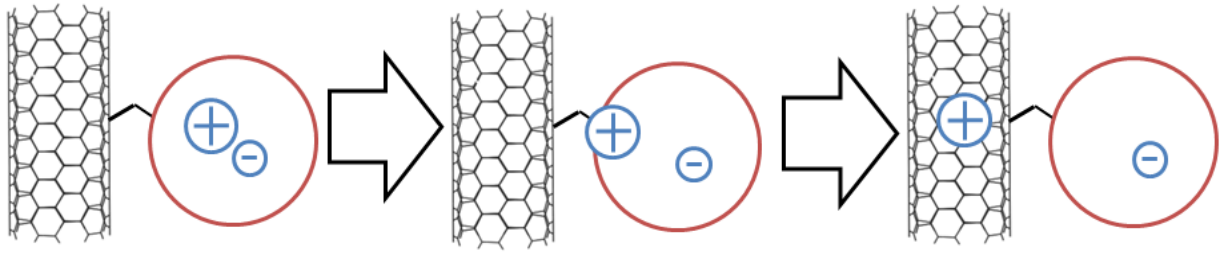

Figure 3.11: A schematic of the plausible surface-mediated charge transfer mechanism occurring in our DWNT–CdSe heterostructures.

Similar to the CdSe QDs, covalent conjugation of the AET-CdSe/ZnS to DWNTs resulted in a noticeable decrease in emission intensity. However, a significant difference was observed in the time-resolved photoluminescence data (Figure 3.12B), where the kinetics of the exciton reveals the presence of an additional quenching channel resulting in a smaller average total lifetime. In addition, by contrast with DWNT–CdSe, the exciton decay of CdSe/ZnS-AET–DWNT remained a multi-exponential process. Based on these overall observations, it is conceivable that the charge-separated state could not be formed within the CdSe/ZnS-AET–DWNT heterostructures, due to the substantial impairment of the surface trapping process.

As a consequence, RET became a more probable relaxation pathway and can account for the significant decrease of exciton emission. From the observed TRPL decays, it is possible to estimate the RET rate from the CdSe/ZnS QD to the DWNT and the overall decrease in quantum yield. Although the decays were multi-exponential, we can assume that the additional nonradiative relaxation process affected each component identically:

$$\bar{\Gamma}_{tot}[QD-NT] = \bar{\Gamma}_{tot}[QD] + \Gamma_{RET};\ \bar{\Gamma}_{tot} = \frac{1}{\bar{\tau}} = \sum_i A_i\tau_i \Big/ \sum_i A_i\tau_i^2 \qquad (3.10)$$

where $\bar{\Gamma}_{tot}[QD-NT]$, $\bar{\Gamma}_{tot}[QD]$, and Γ_{RET} represent the total decay rate of CNT-QD heterostructures, the total decay rate of QDs alone, and the rate of RET, respectively. The amplitudes (*A*) and lifetimes (τ) can be extracted by fitting each of the data sets (with and without DWNTs). The decay traces of AET-CdSe/ZnS and DWNT–CdSe/ZnS can be fit using a multi-exponential function with three components, respectively. The lifetimes and amplitudes obtained by these fitting protocols can be used to compute the RET rate; it is determined to be 0.22 ns^{-1}. This should give a corresponding reduction in the quantum yield of ~ 2.3X before

accounting for the absorption of the incident and emitted light by the presence of the broadly absorbing nanotube species. In practice, it is difficult to accurately resolve the absolute absorbance of the QDs from the DWNT baseline. However, our best estimate gave a change in PL intensity of ~ 3.5. Using our kinetic models, the CdSe/ZnS-AET–DWNT complexes, with a surface-to-surface distance of 3.17 nm, had a calculated RET rate of 0.3 ns^{-1}. This value matched very well with the experimental value (0.2 ns^{-1}) and was well within the expected error.

Since we have already established that charge transfer from the interior of the dot was inefficient, all of these results explain why the charged-separated state can be formed in CdSe but not CdSe/ZnS complexes. Taken all together, these results provide strong evidence that an ultrafast trapping process was a crucial intermediate in the formation of the observed long-lived charge-separated state, and an efficient solar device based on these inorganic nanostructures.

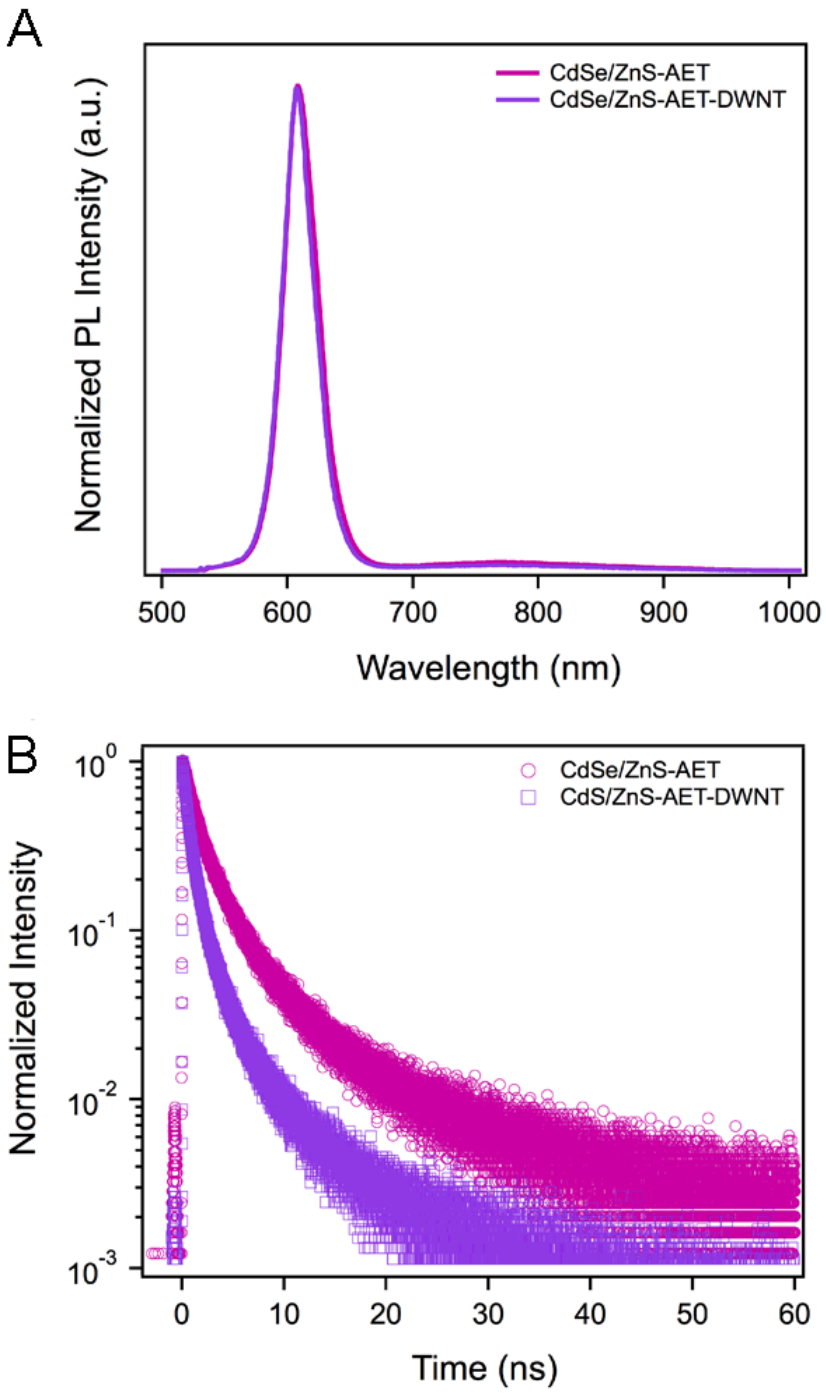

Figure 3.12: (A) The steady-state photoluminescence spectra of CdSe/ZnS-AET (pink) and CdSe/ZnS-AET–DWNT composites (purple). (B) Normalized time-resolved photoluminescence measurements of the exciton decay in CdSe/ZnS-AET (red circle) and CdSe/ZnS-AET–DWNT composites (purple square).

3.3.6 *Optical characterization of CdTe and AET-CdTe*

To further back up our hypothesis of hole trapping on CdSe QDs induced by AET ligands, we prepared CdTe QDs and tested the influence of AET on their optical properties. The as-prepared CdTe QDs have an average size of 3.5 nm (Figure 3.13A), therefore possessing surface area-to volume ratio similar to that of CdSe QDs used in DWNT–CdSe heterostructures discussed before. Moreover, the excitonic absorption of as-prepared CdTe QDs at 597 nm (Figure 3.13B) suggested that it had similar band gap energy to that of CdSe as well. As both the energies of conduction band and valence band of CdTe QDs were found to be higher than those associated with CdSe QDs, similar trap emission is expected to be observed in AET-CdTe QDs if the electron traps account for the original trap emission in AET-CdSe QDs. However, upon ligand exchange, as opposed to the observation found in AET-CdSe, no trap emission was arisen in the steady-state fluorescence spectrum of AET-CdTe QDs as illustrated in Figure 3.13C. This suggested that electron traps should not be responsible for the observed trap emission in AET-CdSe. The symmetric broadening of steady state spectrum of AET-CdTe could be plausibly attributed to the disturbance of size distribution of CdTe by interaction with AET. In addition, the almost identical exciton decay traces (Figure 3.13D) of both CdTe and AET-CdTe QDs indicated that AET had little influence on exciton dynamics within CdTe. Therefore, the absence of additional non-radiative pathway associated with AET in AET-CdTe further confirmed that it was photogenerated holes, instead of electrons, being trapped on the surface of CdSe in the presence of surface ligands, AET.

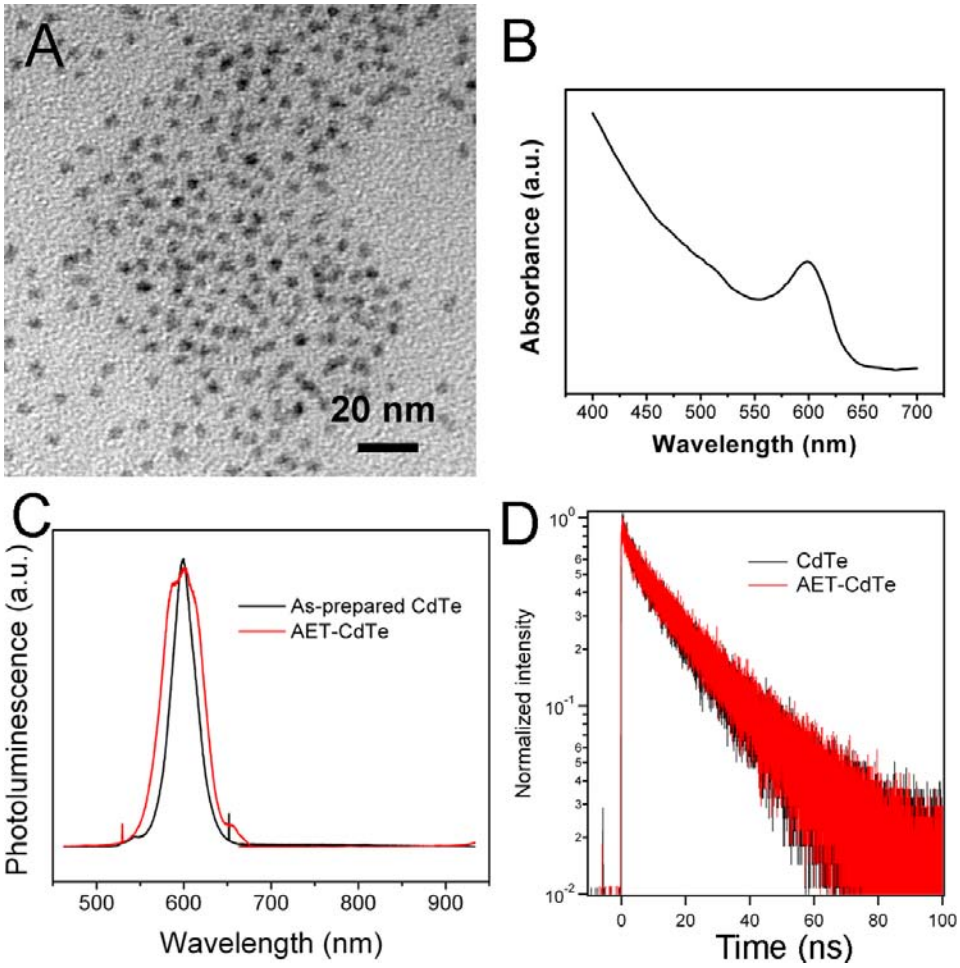

Figure 3.13: (A) TEM image of as-prepared CdTe QDs. (B) UV-visible spectrum of as-prepared CdTe QDs. (C) Steady-state spectra of as-prepared CdTe and AET-CdTe QDs. (D) Exciton decay curves of as-prepared CdTe and AET-CdTe QDs.

3.4 Conclusions

In order to take advantage of the unique properties of DWNTs for diverse applications, it has been critical to explore the chemical modification of DWNTs with other functional moieties, such as quantum dots. Herein, we demonstrated that a conventional covalent approach can be applied to reliably synthesize DWNT–CdSe heterostructures. The use of surface ligands, AET, induced hole trapping process at the CdSe surface, thereby leading to trap emission in near-infrared region, which was then completely quenched upon conjugation with CNTs. In addition, we observed nearly mono-exponential charged exciton photoluminescence upon conjugation of CdSe QDs with DWNTs, suggesting the formation of a long-lived charge-separated state within DWNT–CdSe heterostructures. An efficient surface-mediated charge transfer from CdSe QDs to the DWNTs is suggested to account for the optical observation, as supported by theoretical calculations. In addition, we note a high coverage of AET on the surface of CdSe ensured not only the high efficiency of surface trapping process but also the high statistical probability that one particular type of charge carriers localized near the interface. Moreover, it cannot be overemphasized that precise control of both the proximity of QDs to the DWNTs and the surface chemistry is crucial for controlling the different kinetic pathways.

While additional experimental and theoretical studies on the effect of chemical functionalization on the properties of DWNTs are still needed, the experimental evidence presented herein suggests that DWNT–QD heterostructures mediated by the electronically active molecular linker, AET, exhibit potential for incorporation into devices such as photovoltaic cells, especially considering the observation of effective charge separation between CdSe and DWNTs.

3.5 References

21. P. Guyot-Sionnest, M. Shim, C. Matranga and M. Hines, *Physical Review B*, **1999**, *60*, R2181-R2184.

28. S. Jeong, M. Achermann, J. Nanda, S. Ivanov, V. I. Klimov and J. A. Hollingsworth, *Journal of the American Chemical Society*, **2005**, *127*, 10126-10127.

53. I. Khatri, S. Adhikari, H. R. Aryal, T. Soga, T. Jimbo and M. Umeno, *Applied Physics Letters*, **2009**, *94*, 093509.

62. E. Shafran, B. D. Mangum and J. M. Gerton, *Nano Letters*, **2010**, *10*, 4049-4054.

63. A. Kongkanand, K. Tvrdy, K. Takechi, M. Kuno and P. V. Kamat, *Journal of the American Chemical Society*, **2008**, *130*, 4007-4015.

76. L. Hu, Y. L. Zhao, K. Ryu, C. Zhou, J. F. Stoddart and G. Gruner, *Advanced Materials*, **2008**, *20*, 939-946.

77. V. Biju, T. Itoh, Y. Baba and M. Ishikawa, *Journal of Physical Chemistry B*, **2006**, *110*, 26068-26074.

146. E. M. Boatman, G. C. Lisensky and K. J. Nordell, *Journal of Chemical Education*, **2005**, *82*, 1697-1699.

154. J. Aldana, Y. A. Wang and X. G. Peng, *Journal of the American Chemical Society*, **2001**, *123*, 8844-8850.

160. J. Aldana, N. Lavelle, Y. J. Wang and X. G. Peng, *Journal of the American Chemical Society*, **2005**, *127*, 2496-2504.

167. Y. Tison, C. E. Giusca, V. Stolojan, Y. Hayashi and S. R. P. Silva, *Advanced Materials*, **2008**, *20*, 189-194.

168. A. Hashimoto, K. Suenaga, K. Urita, T. Shimada, T. Sugai, S. Bandow, H. Shinohara and S. Iijima, *Physical Review Letters*, **2005**, *94*, 045504/045501-045504.

169. R. Saito, R. Matsuo, T. Kimura, G. Dresselhaus and M. S. Dresselhaus, *Chemical Physics Letters*, **2001**, *348*, 187-193.

170. R. Pfeiffer, C. Kramberger, F. Simon, H. Kuzmany, V. N. Popov and H. Kataura, *European Physical Journal B*, **2004**, *42*, 345-350.

171. R. Pfeiffer, H. Kuzmany, C. Kramberger, C. Schaman, T. Pichler, H. Kataura, Y. Achiba, J. Kurti and V. Zolyomi, *Physical Review Letters*, **2003**, *90*, 225501/225501-225504.

172. M. Endo, H. Muramatsu, T. Hayashi, Y. A. Kim, M. Terrones and N. S. Dresselhaus, *Nature*, **2005**, *433*, 476-476.

173. B. Ha, D. H. Shin, J. Park and C. J. Lee, *Journal of Physical Chemistry C*, **2008**, *112*, 430-435.

174. Y. W. Son, S. Oh, J. Ihm and S. Han, *Nanotechnology*, **2005**, *16*, 125-128.

175. Y. H. Ho, C. P. Chang, F. L. Shyu, R. B. Chen, S. C. Chen and M. F. Lin, *Carbon*, **2004**, *42*, 3159-3167.

176. I. Maeng, C. Kang, S. J. Oh, J. H. Son, K. H. An and Y. H. Lee, *Applied Physics Letters*, **2007**, *90*, 051914/051911-051913.

177. F. Villalpando-Paez, H. Son, D. Nezich, Y. P. Hsieh, J. Kong, Y. A. Kim, D. Shimamoto, H. Muramatsu, T. Hayashi, M. Endo, M. Terrones and M. S. Dresselhaus, *Nano Letters*, **2008**, *8*, 3879-3886.

178. G. W. Ho, Y. H. Ho, T. S. Li, C. P. Chang and M. F. Lin, *Carbon*, **2006**, *44*, 2323-2329.

179. S. P. Somani, P. R. Somani, E. Flahaut, G. Kalita and M. Umeno, *Japanese Journal of Applied Physics*, **2008**, *47*, 1219-1222.

180. Y. Jia, J. Q. Wei, K. L. Wang, A. Y. Cao, Q. K. Shu, X. C. Gui, Y. Q. Zhu, D. M. Zhuang, G. Zhang, B. B. Ma, L. D. Wang, W. J. Liu, Z. C. Wang, J. B. Luo and D. Wu, *Advanced Materials*, **2008**, *20*, 4594-4598.

181. Y. C. Jung, D. Shimamoto, H. Muramatsu, Y. A. Kim, T. Hayashi, M. Terrones and M. Endo, *Advanced Materials*, **2008**, *20*, 4509-4512.

182. R. B. Koizhaiganova, H. J. Kim, T. Vasudevan and M. S. Lee, *Synthetic Metals*, **2009**, *159*, 2437-2442.

183. H. Muramatsu, Y. A. Kim, T. Hayashi, M. Endo, A. Yonemoto, H. Arikai, F. Okino and H. Touhara, *Chemical Communications*, **2005**, 2002-2004.

184. T. Hayashi, D. Shimamoto, Y. A. Kim, H. Muramatsu, F. Okino, H. Touhara, T. Shimada, Y. Miyauchi, S. Maruyama, M. Terrones, M. S. Dresselhaus and M. Endo, *Acs Nano*, **2008**, *2*, 485-488.

185. Y. A. Kim, H. Muramatsu, K. C. Park, D. Shimamoto, Y. C. Jung, J. H. Kim, T. Hayashi, Y. Saito, M. Endo, M. Terrones and M. S. Dresselhaus, *Applied Physics Letters*, **2008**, *93*, 051901/051901-051903.

186. S. Banerjee and S. S. Wong, *Chem. Commun.*, **2004**, 1866-1867.

187. Y. Liu, M. A. Summers, C. Edder, J. M. J. Fréchet and M. D. McGehee, *Advanced Materials*, **2005**, *17*, 2960-2964.

188. R. S. Dibbell and D. F. Watson, *Journal of Physical Chemistry C*, **2009**, *113*, 3139-3149.

189. T. Murakami, K. Matsumoto, K. Kisoda, R. Naito, K. Nishio, T. Isshiki and H. Harima, *Journal of Applied Physics*, **2008**, *103*, 114305/114301-114308

190. T. Sugai, H. Yoshida, T. Shimada, T. Okazaki and H. Shinohara, *Nano Letters*, **2003**, *3*, 769-773.

191. H. Muramatsu, T. Hayashi, Y. A. Kim, D. Shimamoto, Y. J. Kim, K. Tantrakarn, M. Endo, M. Terrones and M. S. Dresselhaus, *Chemical Physics Letters*, **2005**, *414*, 444-448.

192. M. Jones, S. S. Lo and G. D. Scholes, *Proceedings of the National Academy of Sciences of the United States of America*, **2009**, *106*, 3011-3016.

193. S. F. Wuister, C. D. Donega and A. Meijerink, *Journal of Physical Chemistry B*, **2004**, *108*, 17393-17397.

194. P. P. Jha and P. Guyot-Sionnest, *ACS nano*, **2009**, *3*, 1011-1015.

195. D. E. Gomez, J. van Embden, P. Mulvaney, M. J. Fernee and H. Rubinsztein-Dunlop, *ACS nano*, **2009**, *3*, 2281-2287.

196. P. Spinicelli, S. Buil, X. Quelin, B. Mahler, B. Dubertret and J. P. Hermier, *Physical Review Letters*, **2009**, *102*, 136801.

197. C. A. Leatherdale, W. K. Woo, F. V. Mikulec and M. G. Bawendi, *Journal of Physical Chemistry B*, **2002**, *106*, 7619-7622.

198. E. Bakkers, A. W. Marsman, L. W. Jenneskens and D. Vanmaekelbergh, *Angewandte Chemie-International Edition*, **2000**, *39*, 2297-2299.

199. R. S. Dibbell, D. G. Youker and D. F. Watson, *Journal of Physical Chemistry C*, **2009**, *113*, 18643-18651.

200. R. S. Swathi and K. L. Sebastian, *Journal of Chemical Physics*, **2010**, *132*, 104502.

201. A. Govorov, G. Bryant, W. Zhang, T. Skeini, J. Lee, N. Kotov, J. Slocik and R. Naik, *Nano Lett*, **2006**, *6*, 984-994.

202. R. A. Marcus, *Journal of Chemical Physics*, **1965**, *43*, 679-701.

203. M. R. Wasielewski, *Chemical Reviews*, **1992**, *92*, 435-461.

204. M. A. Rampi and G. M. Whitesides, *Chemical Physics*, **2002**, *281*, 373-391.

205. J. F. Smalley, S. W. Feldberg, C. E. D. Chidsey, M. R. Linford, M. D. Newton and Y.-P. Liu, *The Journal of Physical Chemistry*, **1995**, *99*, 13141-13149.

206. A. Boulesbaa, Z. Q. Huang, D. Wu and T. Q. Lian, *Journal of Physical Chemistry C*, **2010**, *114*, 962-969.

207. W. A. Tisdale, Doctor of Philosophy, University of Minnesota, 2010.

208. Z.-J. Jiang and D. F. Kelley, *The Journal of Physical Chemistry C*, **2011**, *115*, 4594-4602.

209. K. Tvrdy, P. A. Frantsuzov and P. V. Kamat, *Proceedings of the National Academy of Sciences of the United States of America*, **2011**, *108*, 29-34.

210. K. Pettersson, J. Wiberg, T. Ljungdahl, J. Martensson and B. Albinsson, *Journal of Physical Chemistry A*, **2006**, *110*, 319-326.

211. E. Kucur, J. Riegler, G. A. Urban and T. Nann, *Journal of Chemical Physics*, **2003**, *119*, 2333-2337.

212. I. Robel, M. Kuno and P. V. Kamat, *Journal of the American Chemical Society*, **2007**, *129*, 4136-4137.

213. H. Ago, T. Kugler, F. Cacialli, W. R. Salaneck, M. S. P. Shaffer, A. H. Windle and R. H. Friend, *The Journal of Physical Chemistry B*, **1999**, *103*, 8116-8121.

214. R. Koole, P. Liljeroth, C. de Mello Donegá, D. Vanmaekelbergh and A. Meijerink, *Journal of the American Chemical Society*, **2006**, *128*, 10436-10441.

215. T. Dürkop, S. A. Getty, E. Cobas and M. S. Fuhrer, *Nano Letters*, **2003**, *4*, 35-39.

216. B. O. Dabbousi, J. RodriguezViejo, F. V. Mikulec, J. R. Heine, H. Mattoussi, R. Ober, K. F. Jensen and M. G. Bawendi, *Journal of Physical Chemistry B*, **1997**, *101*, 9463-9475.

217. Z. Chen, S. p. Berciaud, C. Nuckolls, T. F. Heinz and L. E. Brus, *ACS nano*, **2010**, *4*, 2964-2968.

Chapter 4 Fabrication of Inorganic Core-shell Nanofibers by Coaxial Electrospinning and Their Potential Applications in the Photo-degradation of Organic Pollutants

4.1 Introduction

One-dimensional nanoscale heterostructures have been of particular interest due to their composite intriguing properties that often go beyond a simple linear sum of their multiple constituent functionalities. In fact, the most interesting science often occurs at interfaces. Indeed, the unique properties of these materials, which cannot necessarily be realized in single-component structures, render them attractive in a broad range of applications. These include their incorporation as building blocks in nanoscale electronics as well as in photonics devices,[218], catalysts,[219, 220] sensors,[221] as well as solar cells.[115, 222]

As suggested in Chapter 1, considerable research efforts have been expended towards the synthesis and manufacturing of one-dimensional heterostructures possessing various chemical compositions, including metals[219, 220] and semiconductors.[223-231] In general, a core-shell heterostructure can be generated by two-step synthetic protocols, wherein the initial one-dimensional core template is pre-synthesized prior to the subsequent shell coating.[225, 228, 230] However, such approaches based upon solution-phase manipulations often require either (a) tedious purification steps in order to obtain pure core materials and/or (b) a very careful experimental design in order to efficaciously apply a secondary homogeneous, contiguous coating of shell materials. Alternatively, epitaxial growth based upon a two-step deposition process, employing either chemical vapor deposition,[218, 223, 232] pulsed laser deposition,[224,227] or

atomic layer deposition[115] techniques can provide the heterostructure with a well-defined interface. However, these gas phase processes usually require highly specialized equipment in order to achieve the high temperatures and/or low vacuum environments that are needed. Such an approach therefore can be potentially be energy-intensive and expensive. By contrast, simpler template-assisted methods usually are low-throughput in nature and can also be costly and time-consuming in terms of mass generation of product. Furthermore, chemical conversion processes (e.g. sulfidation[108] and the Kirkendall effect[96]) have been successfully exploited for the preparation of core-shell heterostructures. However, such strategies are highly limited in scope as they depend upon the precise nature of the materials synthesized. As such, developing generalizable and facile practical protocols that will fabricate one-dimensional well-defined core-shell nanostructures consisting of two chemically different materials still poses a significant challenge.

4.1.1 *Electrospinning*

Electrospinning has been of interest as it is a relatively simple, environmentally friendly, and versatile technique for generating highly uniform one-dimensional nanofibers composed of a variety of materials including polymer and inorganic composites.[233, 234] Its attractive advantages include not only its high throughput in a continuous process under mild conditions but also its inherent flexibility in terms of controlling the fiber diameter from the micron to nanometer scales. Briefly speaking, electrospinning is a process using electrical stress to generate fibers from liquids. In a typical electrospinning setup, the syringe pump is used to supply precursor solution into a metallic spinneret at a constant rate. When high voltage is applied, the liquid solution coming out of the spinneret is stretched into a conical shape under charge repulsion. This conical

shape is named Taylor cone. Once the charge repulsion force reaches a threshold value under which the electrostatic forces balances out the surface tension, a fiber jet will be ejected from the Taylor cone. Subsequently, the solvent is evaporated during the whipping process, leading to the formation of solid fibers collected on the grounded substrates. A number of processing parameters (e.g. applied voltage, flowing rate, and spinneret-collector distance) as well as material parameters (e.g. precursor concentration and solvent conductivity) play an important role in fiber formation and structure. For example, an increase in the strength of the applied electrical field can more likely lead to greater stretching of the solution due to the large Coulombic force between surface charges, therefore resulting in a decrease in the diameter of electrospun fibers. Similarly, the decrease in the flowing rate of the precursor solution can potentially lead to the reduction of the fiber diameter under the conditions wherein the Taylor cone can be maintained. It is also important to note that the exact relationship between each parameter variable and the resulting fiber morphology can differ for each system.

To date, electrospun inorganic nanofibers such as TiO_2, ZnO, V_2O_5, and Fe_3O_4 have been demonstrated to not only possess the unique properties of the individual materials themselves but also incorporate outstanding attributes associated with the one-dimensional morphology.[235, 236] Moreover, in recent years, the state-of-the-art configuration of the nozzle has advanced in a way such that the structure and morphology (and hence, overall functionality) of the resulting nanofibers can be precisely altered. For example, the coaxial nozzle configuration has been developed, allowing for the simultaneous coaxial electrospinning of two distinctive components. This technique stands out from other methods, owing to its ability to very easily prepare one-dimensional core-shell nanoscale heterostructures on a large scale in a one-step synthetic process. To date, electrospun polymer nanofibers with either core-shell or tubular structures have been

fabricated for a wide variety of applications including drug delivery devices,[237, 238] and electrodes.[239] However, to the best of our knowledge, fabrication of inorganic nanofibers with a well-defined core-shell structure by coaxial electrospinning has not as yet been reported.

4.1.2 *The use of TiO_2-based systems for photo-degradation*

TiO_2, as a well-known photocatalyst, has been widely used for the treatment of organic pollutants in water and air.[240] However, the drawback of TiO_2 photocatalysts is that the rate of electron transfer from TiO_2 to either oxygen or the electron acceptor on the surface of TiO_2 is much slower than that of the recombination of the electron-hole pair, a fact which impairs the photocatalytic activity of TiO_2.[240] To address this problem, coupling TiO_2 with another component, either a semiconductor or a metal, has been proposed as a means of preventing charge carriers from fast recombination by achieving efficient charge separation between TiO_2 and the other material. Among coupled semiconductor photocatalysts, the TiO_2/SnO_2 system in particular has been extensively studied, as it has demonstrated high photocatalytic activity due to fast electron transfer from TiO_2 to SnO_2.[241-244] SnO_2 is a common semiconductor used as a component of transparent conductors, electrodes, and sensors, due to its excellent conductivity.[245, 246] The band-gap energies of TiO_2 and SnO_2 are 3.2 and 3.8 eV, respectively. Hence, the energy offset between TiO_2 and SnO_2 allows photogenerated electrons to accumulate onto SnO_2 whereas holes will accrue onto TiO_2 upon formation of a heterojunction at the TiO_2/SnO_2 interface (Scheme 1).

Various TiO_2/SnO_2 binary oxide nanostructures have been prepared including films,[244, 247] nanoparticles,[248-250] nanotubes,[241] and nanowires.[224] However, one-dimensional nanostructures in particular have attracted a significant amount of interest, because of their

higher aspect ratios, large surface area-to-volume ratios, and potentially high conductivity. Studies have shown that well-ordered and aligned nanoparticles encapsulated within one-dimensional nanofibers can facilitate interparticle charge transfer along the nanofiber framework as compared with randomly packed nanoparticles.[233, 235] Moreover, apart from the necessity for reasonable interfacial contact between TiO_2 and SnO_2 for efficient charge separation, it is believed that full exposure of both components to the reaction medium would allow for both photogenerated holes and electrons to take part in the photocatalytic reactions, thereby enhancing the observed photocatalytic efficiency. In order to achieve this requirement, a bi-component nanowire structure of TiO_2 and SnO_2 has been realized by electrospinning with a side-by-side dual spinneret.[242] However, the fragile nature of this side-by-side design may result in poor catalyst durability, an essential property for catalysts. In order to mitigate this potentially damaging flaw, a core-shell architecture is preferable, owing to its greater stability and larger interfacial contact.

In this Chapter, we have demonstrated that core-shell SnO_2/TiO_2 nanofibers can be successfully fabricated by coaxial electrospinning. This simple, straightforward method yields highly uniform coaxial nanoscale heterostructures with well-defined interfaces between components. By rationally and precisely controlling material parameters and electrospinning conditions, the resulting morphology of coaxial SnO_2/TiO_2 nanofibers can be altered as either tubular coaxial, peapod-like, or solid coaxial architectures. Furthermore, due to the interesting electronic properties of SnO_2 and TiO_2 discussed above, the resulting core-shell nanofibers, incorporating both materials, can potentially be used as promising materials for photon energy conversion applications, including as solar devices and photocatalysts.

In particular, we have tested the photocatalytic activity of our novel tubular SnO_2/TiO_2 coaxial heterostructure fibers generated in this study. The enhanced photocatalytic activity of our tubular SnO_2/TiO_2 systems as compared with commercial TiO_2 photocatalysts can be attributed to a number of factors: (i) the dual layer structure ensures a well-defined heterojunction between TiO_2 and SnO_2, which allows for an increase in charge-separation efficiency; (ii) one-dimensional nanofibers facilitate efficient interparticle charge transfer along the nanoscale fiber framework; and (iii) the hollow structure allows for full exposure of both the TiO_2 outer layer and SnO_2 inner layer to the reaction medium, thereby allowing for both photogenerated electrons and holes to participate in the photocatalysis reaction. Hence, due to the versatility in our choice of materials as well as the flexibility of morphology control, our work has demonstrated that coaxial electrospinning can be considered to be an excellent and facile alternative route towards the fabrication of one-dimensional coaxial heterostructures with different chemical compositions and configurations, thereby providing the opportunity for the development of unique nanoscale devices. In particular, tubular coaxial structures prepared by coaxial electrospinning, which cannot be easily obtained by conventional synthetic routes, would be significantly beneficial for a broad range of applications, wherein it is desirable to have access to both materials, while maintaining a large and stable interface.

4.2 Experimental Section

4.2.1 *Preparation of TiO_2 and SnO_2 precursor solutions*

The TiO_2 electrospinning solution was prepared by first dissolving 0.175 g of poly(vinyl pyrrolidone) (PVP) (M_w = 1,300,000, Acros Organic) in 2 mL of ethanol with stirring, followed

by the addition of 0.5 mL of acetic acid. Once the PVP was completely dissolved and the solution became transparent, 0.25 mL of titanium isopropoxide (98+%, Acros Organic), $Ti(OiPr)_4$, was added and kept stirring in solution in order to obtain a homogeneous solution with a final concentration of Ti at 3×10^{-4} mol/mL. Subsequently, the precursor solution was loaded into a 3 mL plastic syringe. SnO_2 precursor solutions with varying concentrations were prepared by adding selective aliquots of tin ethylhexanoate (96%, Alfa Aesar) to light mineral oil (LMO, Lot A0251014, Acros Organic), followed by stirring in order to create a homogeneous solution. The precursor solution was also loaded into a separate 3 mL plastic syringe.

4.2.2 *Electrospinning*

In order to fabricate co-axial fibers, a home-made dual spinneret with the coaxial geometry was used, as shown in Figure 4.1. In a typical experiment, the TiO_2 precursor solution was fed into the outer 16 G spinneret with a feeding rate of 1.0 mL/h. At the same time, the SnO_2 precursor solution was run into the inner 23 G spinneret with a feeding rate of 0.1 mL/h. A high voltage was applied between the tip of the spinneret and the aluminum foil collector with a voltage/distance profile in the range of 5 kV / 3 inch. As-spun nanofibers were left to 'air dry' for one day in order to allow for the hydrolysis of $Ti(OiPr)_4$ to proceed to completion, followed by calcination in air at 500°C for 2 h. All as-generated nanofibers were prepared under identical electrospinning conditions, unless otherwise noted.

4.2.3 *Materials characterization*

Crystallographic and purity information on the prepared nanofibers were obtained using a Scintag diffractometer, operating in the Bragg configuration using Cu Kα radiation (λ = 1.54 Å).

SEM images were processed with a field emission (FE) SEM instrument (Leo 5050), operating at an accelerating voltage of 20 kV and equipped with EDS capabilities. HRTEM images and selected area electron diffraction (SAED) patterns were gathered using a JEOL 2010F instrument, equipped with a Gatan high-angle annular dark field detector (HAADF) for performing either incoherent HAADF or Z-contrast imaging in scanning TEM mode at accelerating voltages of 200 kV. Specimens for cross-sectional TEM experiments were prepared by embedding samples in Epon resin, which was then cut by a Reichert-Jung UltracutE ultramicrotome and placed onto Formvar-coated copper grids.

N_2 absorption profiles were measured with a NOVA 2200e Surface Area & Pore Size Analyzer. Multipoint Brunauer-Emmett-Teller (BET) method was used to determine the surface area of the electrospun fibers. The BET equation is present as follows,

$$\frac{1}{W\left(\left(P_0/P\right)-1\right)} = \frac{1}{W_m C} + \frac{C-1}{W_m C}\left(\frac{P}{P_0}\right) \qquad (4.1)$$

wherein W is the weight of gas adsorbed at a relative pressure P/P_0 and W_m is the weight of adsorbate constituting a monolayer of surface coverage. C is the constant related to the energy of adsorption in the first adsorbed layer, indicative of the magnitude of the adsorbent-adsorbate interactions. In the linear range of BET plot, where P/P_0 is usually in the range of 0.05 to 0.35 when using N_2 as the adsorbate, W_m can be obtained by the equation

$$W_m = \frac{1}{s+i} \qquad (4.2)$$

wherein *s* and *i* are the slope and intercept, respectively, of the BET plot. The total surface area (S) of the sample can be expressed as:

$$S = \frac{W_m N A_{cs}}{M} \quad (4.3)$$

wherein N is Avogadro's number and M is the molecular weight of the adsorbate. A_{cs} is the molecular cross-sectional area of the adsorbate molecule. For the hexagonal close-packed nitrogen monolayer at 77 K, the cross-sectional area, A_{cs}, for N_2 is 16.2 $Å^2$. The pore sizes for each sample were calculated, according to Barrett-Joyner-Halenda (BJH) theory.[235]

4.2.4 *Photocatalytic degradation activity*

In typical experiments, 4 mg of either tubular SnO_2/TiO_2 nanofibers, solid SnO_2/TiO_2 nanofibers, TiO_2 nanofibers, or commercial TiO_2 nanoparticles (P25) were dispersed, by sonication for 5 min, in separate, aqueous solutions of 5 mg/L Rhodamine B (RhB). The solutions were magnetically stirred in the dark for 30 min so as to establish an adsorption-desorption equilibrium of reactants with the photocatalysts. After exposure to UV light (~ 3 mW/cm^2) at 366 nm, the UV-visible absorption spectra of RhB were monitored at different time intervals. The photocatalytic performance of nanofibers was evaluated by the change in the intensity of the optical absorption peak at 555 nm. In terms of a control experiment, RhB solution was treated under the identical conditions without the addition of any photocatalysts.

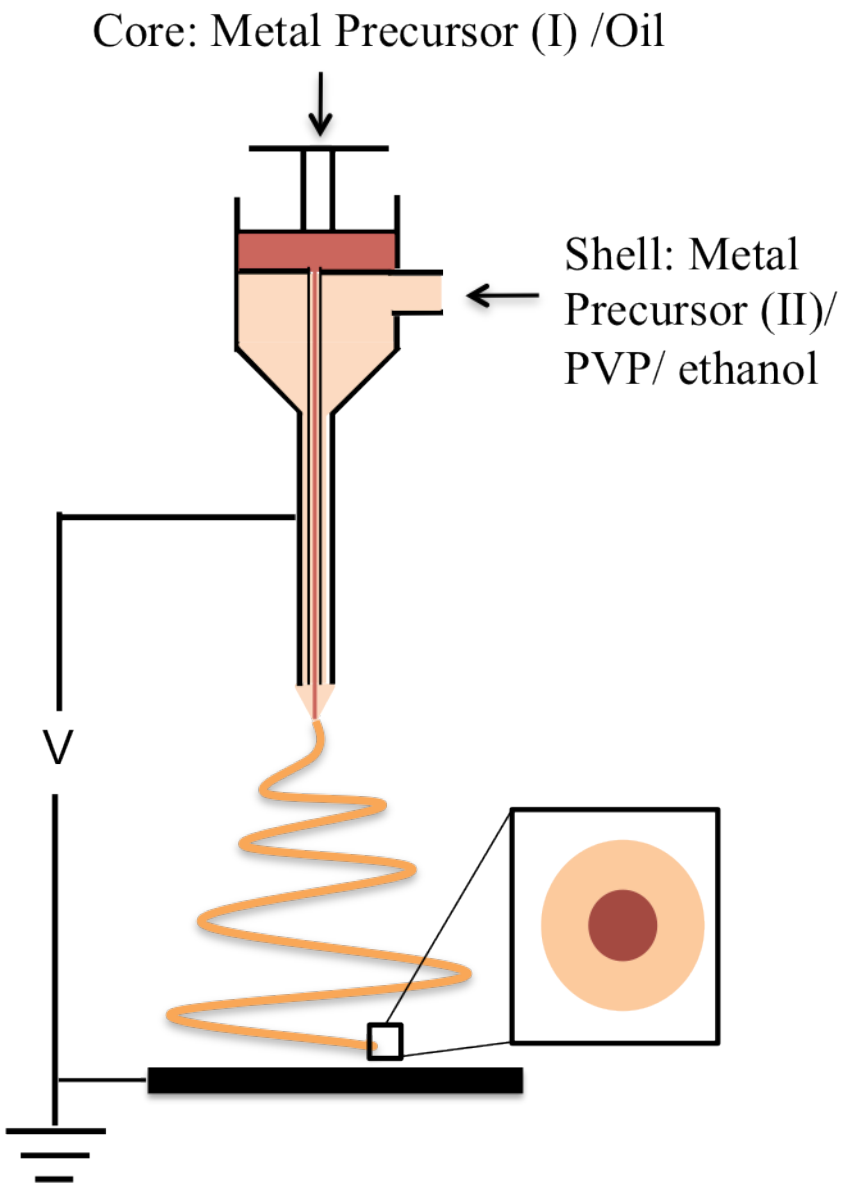

Figure 4.1: A simple schematic illustration of the experimental set-up associated with co-axial electrospinning. The core solution is fed into the inner spinneret while the shell solution is transported into the outer one. Coaxial fibers are collected on the metal substrate under high-voltage conditions.

4.3 Results and Discussion

4.3.1 *Effect of concentration of tin precursor solution upon the internal morphology of electrospun SnO_2/TiO_2 nanofibers*

In order to create a distinctive boundary between the core and shell materials, it has been previously suggested that physical mixing between two solutions during the electrospinning process should be eliminated by using two immiscible solvents for the core solution and the shell solution, respectively.[251] Hence, in our study, ethanol was chosen as the solvent for the shell precursor solution whereas LMO, which is not miscible with ethanol, was used for the core precursor solution. The morphologies of the resulting SnO_2/TiO_2 nanofibers have been evaluated by SEM with a backscattering detector, wherein titanium and tin elements could be distinguished by the differential contrast in these images owing to their substantial difference in atomic number.

We have noted that the concentration of tin precursor solution maintains a significant influence upon the internal morphology of the resulting SnO_2/TiO_2 coaxial fibers. Specifically, highly uniform SnO_2/TiO_2 nanofibers with unique tubular coaxial structures can be formed when the concentration of tin (II) precursor solution is 1.6 mmol/mL. As shown in Figure 4.2A-B, a smooth thin layer was found to coat the interior wall of the tubular nanofibers possessing an overall outer diameter of 285 ± 45 nm and an inner diameter of 122 ± 36 nm; this thin layer was continuous along the entire inner surface of fibers. A cross-sectional SEM image (inset) of fractured nanofibers unambiguously shows the presence of an integral bright ring, concentric with the hollow outer fiber.

In addition, the cross-sectional TEM image along with the corresponding EDS line scan across the structure confirmed the overall elemental distribution in our samples. Specifically,

Figure 4.2C highlights a representative cross-sectional TEM view of a single nanofiber. An inner concentric SnO_2 layer, consisting of densely packed nanoparticles, with a diameter of 20 ± 5 nm, was observed within the less-dense but thicker circular TiO_2 shell. Particle-like aggregates in the hollow central core region most likely corresponded to the fragments of fibers generated during the TEM sample preparation process. The size of the inner hollow region is 141 nm, consistent with the results obtained from the SEM images. In addition, the outer TiO_2 shell consists of loosely packed small nanoparticles with diameters of about 15 nm, indicative of the polycrystallinity of the nanofibers. The EDS line scan results (Figure 4.2D), collected from the area indicated by the red dotted line in Figure 2C, showed that the intensity of the Sn L signal reached a maximum in the inner layer region whereas the Ti Kα signal profile dramatically increased at the location of the outer shell, in excellent agreement with SEM observations. All of these data are consistent with the formation of tubular TiO_2 nanofibers consisting of a thin inner layer of SnO_2.

Such a structure has potential advantages in terms of applications associated with sensing, catalysis, and energy conversion, because it possesses not only a well-defined heterojunction comprised of two distinctive components but also an open inner channel which provides for high surface area and also direct access to the interior material. Not surprisingly, this unusual architecture gave rise to superior photocatalytic activity, as compared with either the individual single-component analogues or its solid wirelike counterparts, as will be further elaborated in a later section. Importantly, to the best of our knowledge, such tubular coaxial nanofibers consisting of two distinctive metal oxides fabricated by coaxial electrospinning have not been previously reported.

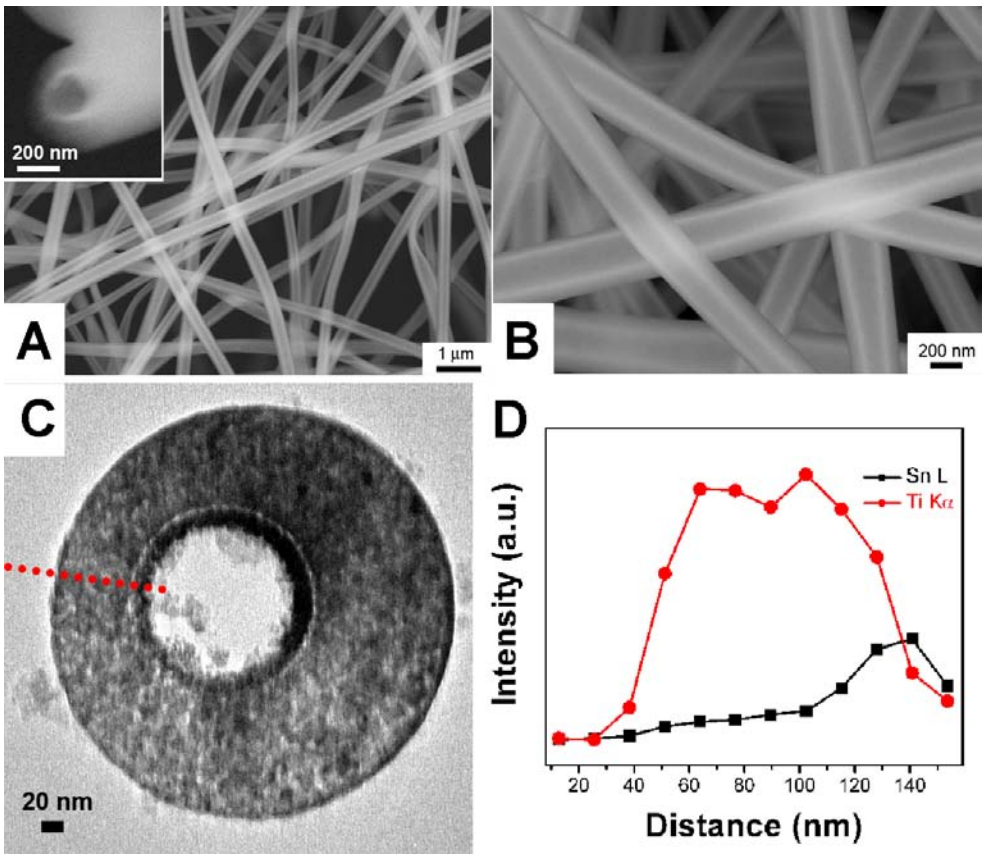

Figure 4.2: (A-B) SEM images of hollow SnO_2/TiO_2 coaxial nanofibers obtained when the concentration of tin (II) precursor is 1.6 mmol/mL. Inset is an SEM image of a typical cross-sectional view of hollow SnO_2/TiO_2 coaxial nanofibers. (C) Cross-sectional TEM image of coaxial SnO_2-TiO_2 core-shell nanofibers. (D) The signal intensity profile of Sn L and Ti Kα derived from EDS line scanning profiles collected along the red dotted line in (C). Each data point corresponds to the red dot along the line drawn from left to right across the image.

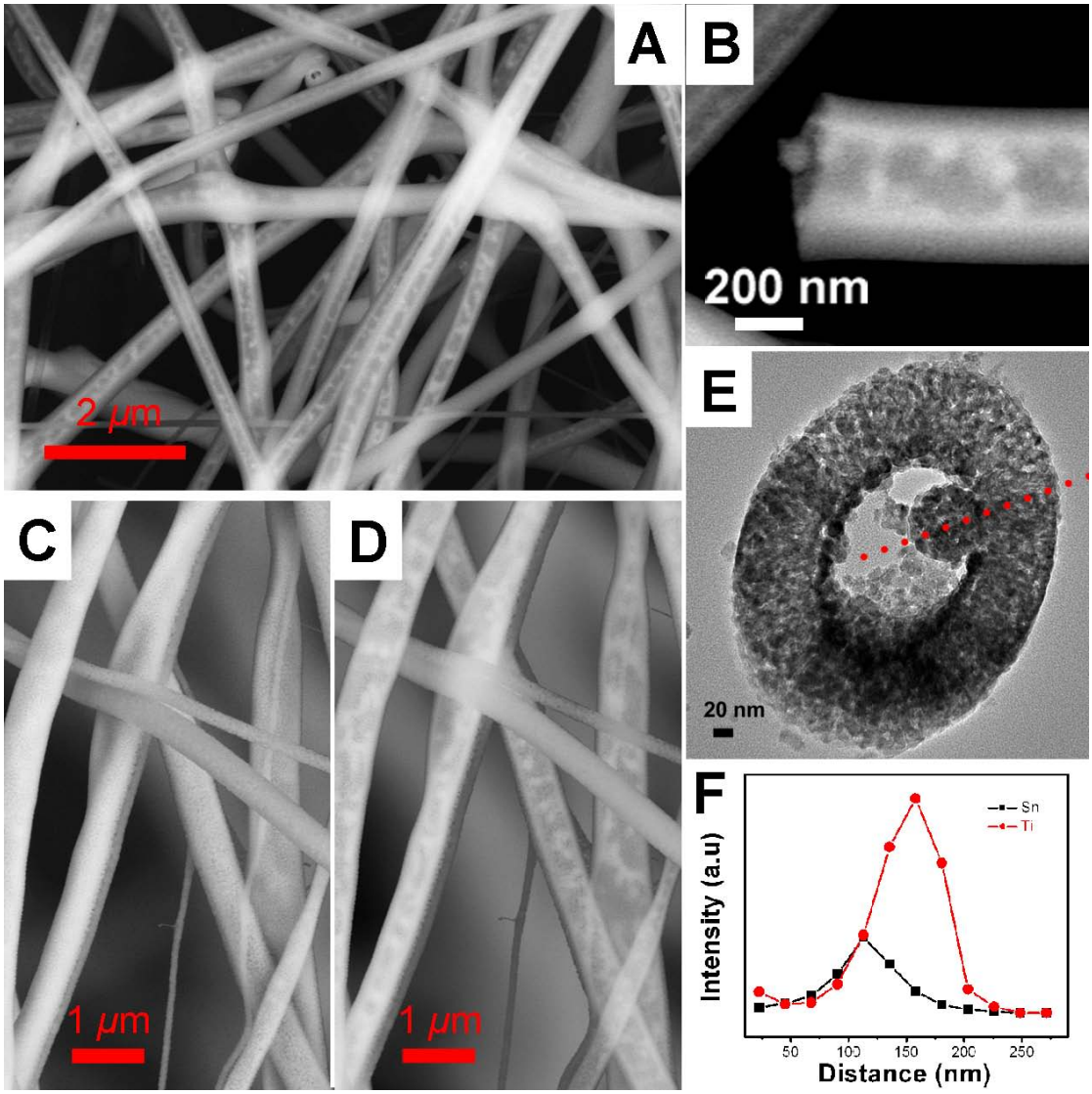

Figure 4.3: (A and B) SEM images of peapod-like SnO_2/TiO_2 nanofibers created when the concentration of tin (II) precursor is 2.2 mmol/mL. SEM images of the same sample area were taken at accelerating electron voltages of 10 kV (C) and 20 kV (D), respectively. (E) Cross-sectional TEM image of peapod-like SnO_2/TiO_2 nanofibers, illustrating particle-like features attached to the inner hollow wall of the fibers. (F) The signal intensity profile of Sn L and Ti Kα derived from EDS line scanning profiles collected along the red dotted line in (E). Each data point corresponds to the red dot along the line drawn from left to right.

When the concentration of the tin (II) precursor solution was increased to 2.2 mmol/mL, we begin to see the formation of SnO_2 nanoparticles within the inner cavity of the nanowires. Representative SEM images (Figure 4.3A-B) highlight the presence of these nanoparticles, possessing a size of 58 ± 13 nm. These peapod structures maintain overall widths of 284 ± 36 nm, similar to previous tubular fibers. However, they possess a slightly decreased inner cavity, measuring only 99 ± 16 nm. We attribute this reduction of the inner cavity size to the proportionally lower LMO content in the tin precursor solution. In order to verify that the observed SnO_2 nanoparticles were in fact inside the tubular fibers, as opposed to on the external surfaces of the TiO_2 nanofibers, SEM images of the same sample area were taken under different accelerating electron voltages. In principle, an increase in accelerating electron voltage allows us to visualize regions within the fiber interior.

As illustrated in Figure 4.3C, nanofibers with a smooth exterior were observed at an accelerating voltage of 10 kV, whereas the hollow features as well as nanoparticles themselves became more readily apparent upon increasing the accelerating voltage to 20 kV (Figure 4.3D). These results confirmed that SnO_2 nanoparticles were encapsulated within the tubular fibers, instead of physically localizing on the exterior surface of the fibers. Additional proof was provided using cross-sectional TEM. A representative cross-sectional TEM image (Figure 4.3E) shows that particle aggregate attached to the interior wall of fibers possesses a size of about 70 nm, consistent with findings from SEM. Aggregates were composed of smaller nanoparticles, measuring ~12 nm. In addition to these nanoparticles, the thin inner SnO_2 coating, present within the hollow nanotubes, is maintained within these peapod-like nanostructures. This is suggestive that upon the formation of a contiguous inner coating of SnO_2, excess tin precursors began to fill

in the actual inner cavity. An EDS line scan result (Figure 4.3F) again demonstrated that Sn was localized in the region of the inner particle, whereas the Ti signal was more dominant in the outer shell area, in spite of the sample drifting caused by charging, as well as the potential signal interference associated with the presence of fragments of fibers generated during the sample preparation.

Upon application of the tin precursor without the addition of mineral oil, we were able to form solid SnO_2/TiO_2 coaxial nanofibers. Typical SEM images (Figure 4.4A-B) show that as-prepared SnO_2/TiO_2 core-shell nanofibers are highly uniform with a discernible core-shell structure. The overall diameter is 275 ± 30 nm, with an average core size of 53 ± 13 nm. The contrast noted in the SEM images arising from the difference in the atomic number between Sn and Ti highlights a clearly distinctive boundary between the shell and the core, which is continuous along the entire length of fibers. Particularly, in the image (Figure 4.4B) where the fibers were fractured and the cross sections of the fibers can be visualized, it is evident that the bright central core is concentrically wrapped by the shell materials. EDS spectrum associated with SEM images (Figure 4.4C) indicates that the fibers contain both Ti and Sn without the presence of any distinguishable impurities.

The cross-sectional TEM image (Figure 4.5A) suggests that these SnO_2/TiO_2 nanofibers were composed of a thick shell, consisting of loosely packed nanoparticles with an average diameter of about 20 nm, and a denser circular core with a size of about 50 nm. This is in good agreement with the SEM data. The loosely packed particles in the shell likely gave rise to the overall porosity of these SnO_2/TiO_2 nanofibers, which is potentially beneficial for their applicability in photocatalysts and in solar cells. EDS spectra (Figure 4.5B) were taken at selected areas of the shell and core, respectively. As expected, the strong Sn signal collected

from the center area confirmed that the core of nanofibers was primarily comprised of SnO_2, whereas the shell was dominated by the presence of Ti, indicative of the TiO_2 shell. We also noted that a weak Sn signal is present in the shell region. This implies that Sn was likely doping TiO_2.

The electron diffraction patterns of the selected sections of the core and shell regions, respectively, (Figure 4.5C and D) also confirm that both the core and shell of SnO_2/TiO_2 nanofibers were polycrystalline and that the five most distinctive diffraction rings of the core (or shell) can be assigned, moving concentrically and sequentially from the center outwards, to (110), (101), (200) (or (111)), (211), and (301) planes of rutile phase SnO_2 (or TiO_2). In addition, the fringe spacing has been determined to be 3.30 Å for the shell materials, a value which is slightly larger than the expected d_{110} = 3.25 Å associated with phase-pure rutile TiO_2.[248] This slight lattice expansion may be partially attributed to Sn doping of TiO_2, whose likelihood have already been implied by the aforementioned EDS results.

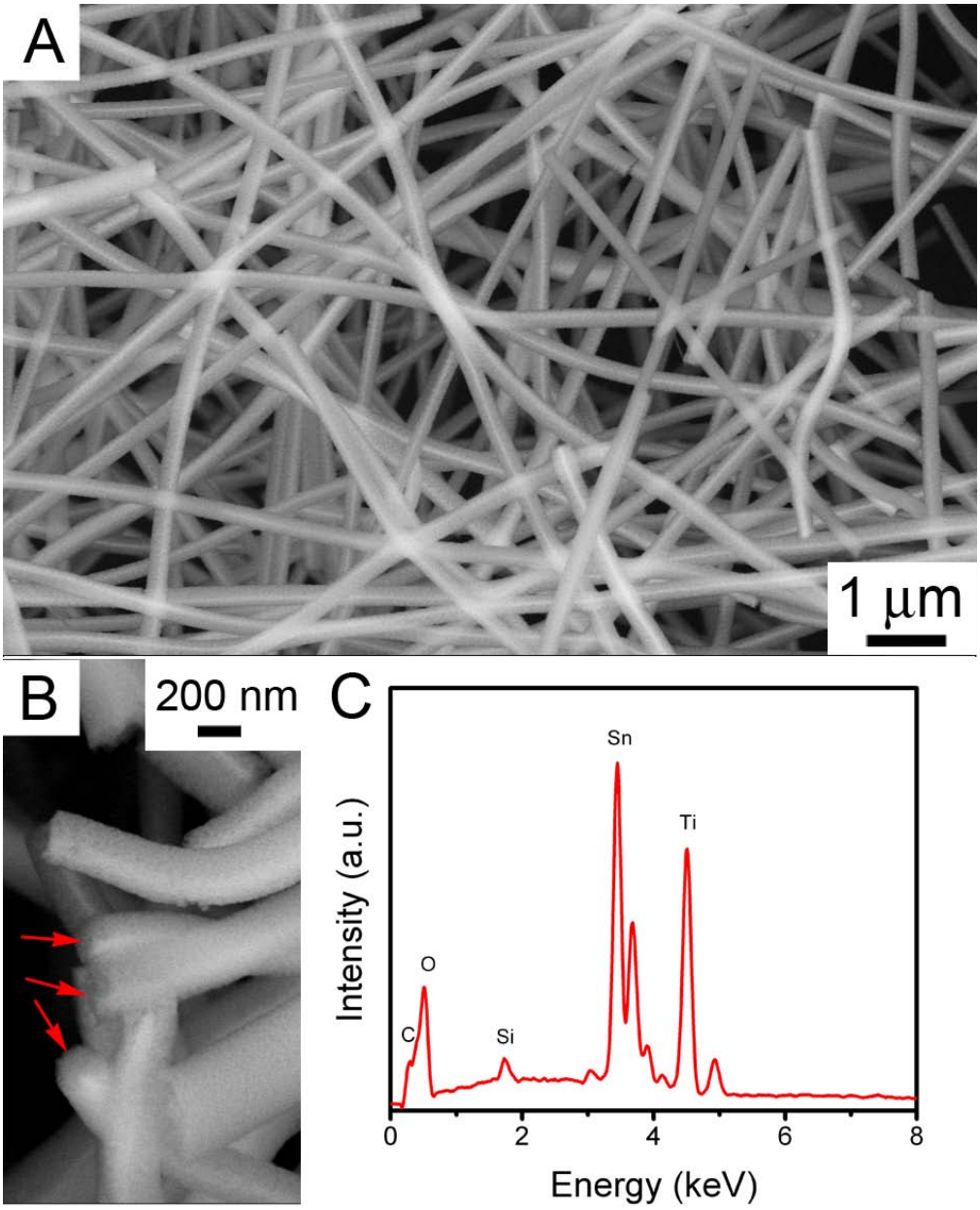

Figure 4.4: (A) Low-magnification SEM image of highly uniform SnO_2/TiO_2 core-shell nanofibers generated when the concentration of tin (II) precursor is 3.0 mmol/mL. (B) High-magnification SEM image of SnO_2/TiO_2 core-shell nanofibers. Red arrows indicate the presence of fractured fibers, wherein the core shell structure can be clearly observed. (C) EDS profile collected from the SnO_2/TiO_2 core-shell nanofibers.

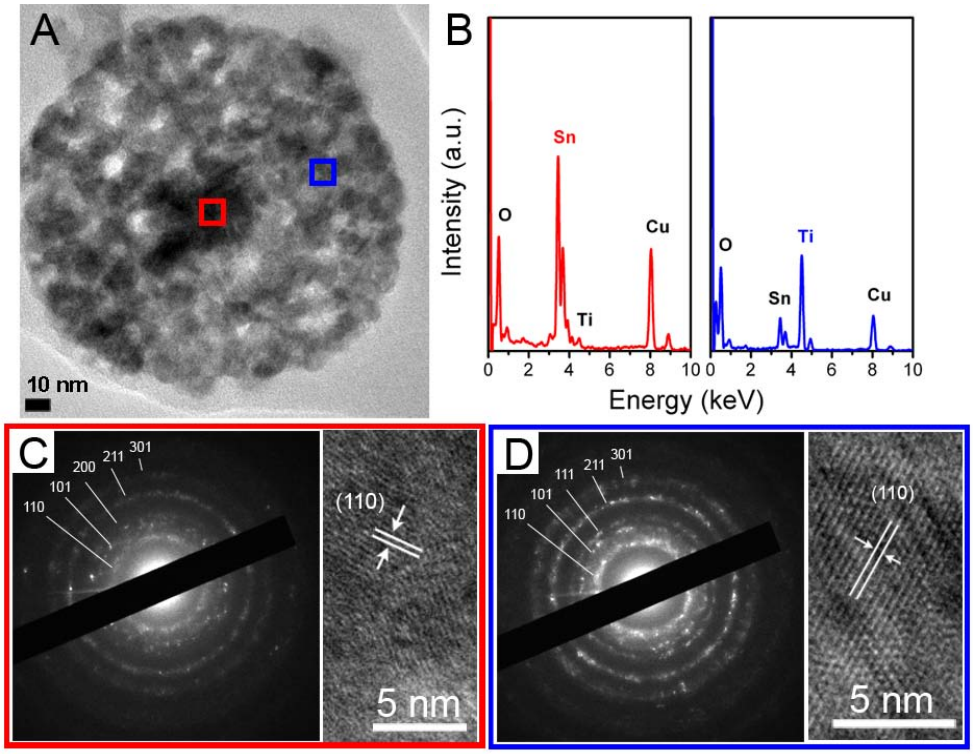

Figure 4.5: (A) Cross-sectional TEM image of a representative SnO_2/TiO_2 core shell nanofiber, prepared at a concentration of tin (II) precursor of 3.0 mmol/mL. (B) EDS profiles collected from the corresponding frames indicated in TEM image. (C) SAED and HRTEM data obtained from the core component. (D) SAED and HRTEM taken from the shell region.

4.3.2 *Crystal structure of SnO_2/ TiO_2 nanofibers*

The crystallographic information associated with SnO_2/TiO_2 nanofibers has been investigated by means of XRD. As illustrated in Figure 4.6, the pure TiO_2 nanofibers, calcinated at 500°C, exhibited a pure anatase phase (JCPDS No. 21-1272), whereas the pure rutile phase of TiO_2 nanofibers could be obtained upon calcination at 800°C. Surprisingly, the calcinated SnO_2/TiO_2 nanofibers possessed a pure rutile phase for both SnO_2 and TiO_2 components, even at a relatively low calcination temperature of 500°C. All peaks in fact could be indexed to the tetragonal rutile phase of TiO_2 (JCPDS No. 21-1276) and SnO_2 (JCPDS No. 72-1147). As the peaks corresponding to rutile TiO_2 lie very close to those of rutile SnO_2, the observed peak pattern of SnO_2/TiO_2 was broader than that associated with their individual constituent components. A phase transition of TiO_2 from the anatase phase to the rutile phase, which can plausibly be ascribed to the doping of Sn^{4+} ions, has been previously reported.[248, 252]

In our case, we speculate that some Sn^{4+} ions might have migrated into the Ti-O-Ti network during the electrospinning and subsequent calcination processes. This latter step could then have facilitated further diffusion of tin ions at the interface and inside the Ti-O-Ti network, thereby inducing the phase transition of TiO_2 at the relatively low temperature we observed.[252] Such speculation also explains our observations in the EDS spectra. In addition, it has been observed that rutile SnO_2 can promote the preferential growth of rutile TiO_2, owing to the fact that the lattice difference between rutile SnO_2 and TiO_2 is only about 2%.[253] Hence, the influence of the SnO_2 lattice could likely be another important factor in promoting the observed phase transition of TiO_2.

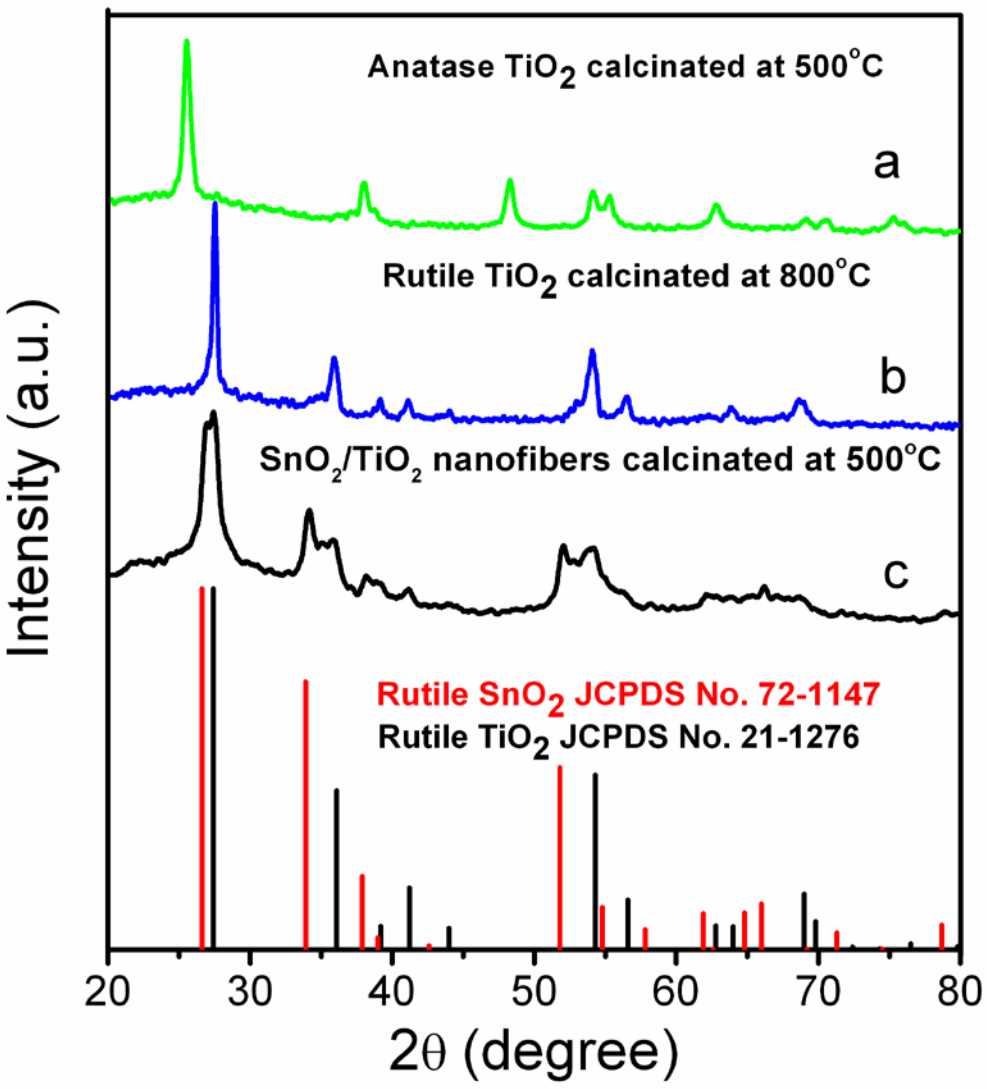

Figure 4.6: XRD patterns of TiO_2 fibers sintered at 500°C (a) and 800°C (b), as well as of hollow SnO_2/TiO_2 coaxial nanofibers (c).

4.3.3 *Effect of electrospinning conditions upon the morphology of SnO_2/TiO_2 electrospun nanofibers*

The subtle influence of other factors such as feeding rate and the applied voltage upon the morphologies of SnO_2/TiO_2 nanofibers was also investigated. By contrast with the importance of the concentration of the tin (II) precursor solution upon structure, changing either the feeding rate or applied voltage does not appear to substantially impact upon the inherent morphologies of SnO_2/TiO_2 nanofibers. Nonetheless, as the feeding rate necessarily affects the precursor supply during the electrospinning process, that factor can play an important role in determining the resulting dimensions of the fibers. Indeed, the size of the inner diameter of nanofibers increases directly as a function of inner feeding rate, as summarized in Tables 4.1 and 2. In the case where the concentration of the tin (II) precursor solution was 1.6 mmol/mL with an inner feeding rate of 0.15 mL/h, a hollow co-axial structure was retained, whereas the diameter of the inner cavity increased in magnitude by 134% to 164 ± 43 nm as compared with only 122 ± 36 nm when the inner feeding rate was 0.10 mL/h. Similarly, when the inner feeding rate was decreased to ~0.03 mL/h, the overall diameter of the fibers as well as their inner cavity diameter diminished to 236 nm and 60 nm, respectively.

It is also worth mentioning that at a constant feeding rate of the shell precursor solution, a minimum feeding rate of the core precursor solution was required in order to ensure the formation of fibers with continuous inner features. For example, if the inner shell feeding rate were too low, i.e. below 0.03 mL/h, shorter hollow segments could potentially form inside each of the fibers.[251] On the other hand, if the inner oil-phase solution were injected at a substantially high rate, for example, 0.5 mL/h in our case, no fibers were collected, as the supply of shell

precursor solution would not have been sufficient to completely coat the oil phase with shell material during electrospinning. Similarly, solid SnO_2/TiO_2 nanofibers exhibited the same trend in that a decrease in the inner feeding rate can lead to a decrease in the diameter of the core and in the overall dimension of the as-produced fibers. The reduction in the dimension of fibers correlated with a decrease in the outer feeding rate as well. Therefore, in this study, we were able to vary the core diameter of solid SnO_2/TiO_2 nanofibers in the range of 30 – 60 nm by altering the inner feeding rate between 0.05 – 2 mL/h.

By contrast with the substantial effect of feeding rate upon the resulting fiber diameter, the magnitude of the applied voltage was found to exert little influence upon the dimensions of fibers synthesized under our experimental conditions (Table 4.3). Specifically, at a given feeding rate, the average diameter of fibers varied within a relatively narrow range of 272 to 285 nm, whereas the inner diameter slightly widened from 104 to 122 nm when the applied voltage was reduced from 7 to 5 kV. Previous studies[251] have demonstrated that the enhancement of local electrical field can result in a significant decrease in fiber diameter when fibers with a single composition are fabricated. In our case herein, the magnitude of the electrical field was limited to a relatively narrow range of 5 – 7 kV in order to achieve the formation of a stable co-axial jet, which would ultimately yield co-axial fibers. We noted that below the minimum voltage of the critical range necessary to form the electrospun fibers, the reagent solutions tended to drip haphazardly from the spinnerets without the formation of a fiber jet. By contrast, the use of voltages above the critical range would cause recession of the Taylor cone, which would therefore inhibit production of a co-axial jet. In fact, we have noted that our considerably limited ability to vary the applied voltage in our case precluded us from deducing a definitive relationship between the magnitude of the electrical field and the resulting fiber dimension.

Table 4.1: The influence of inner feeding rate upon the resulting dimensions of as-prepared tubular TiO_2/SnO_2 nanofibers.

Feeding rate (mL/h)		**Diameter of inner tubes (nm)**	**Diameter of fibers (nm)**
Outer needle	**Inner needle**		
1.0	0.15	164 ± 43	301 ± 50
	0.10	122 ± 36	285 ± 45
	0.03	60 ± 16	236 ± 23

Table 4.2: The influence of feeding rate upon the resulting dimensions of TiO_2/SnO_2 nanofibers.

Feeding rate (mL/h)		**Diameter of core (nm)**	**Diameter of fibers (nm)**
Outer needle	Inner needle		
2.0	0.20	63 ± 19	345 ± 54
1.0	0.10	53 ± 13	275 ± 30
	0.05	32 ± 5	236 ± 23
0.5	0.05	37 ± 7	194 ± 20

Table 4.3: The influence of the voltage profile upon the resulting dimensions of tubular TiO_2/SnO_2 nanofibers

Voltage (kV)	Diameter of inner tubes (nm)	Overall Diameter of fibers (nm)
5	122 ± 36	285 ± 45
6	104 ± 23	280 ± 48
7	104 ± 25	272 ± 37

4.3.4 *Plausible mechanism*

In a previous study, a structure with SnO_2 nanoparticles encapsulated inside the hollow TiO_2 nanofibers was reported.[254] However, the unique tubular structure with dual co-axial layers formed in our study has not been previously synthesized. We note that tin ethylhexanoate as the tin precursor in our study has an appealing solubility due to its distinctive structure. It is an amphiphilic molecule consisting of a hydrophobic alkyl chain terminal group as well as a hydrophilic carboxylate terminal group, allowing it to dissolve and/or disperse in both nonpolar and polar solvents. A simple test performed by adding ethanol to a mixture of tin 2-ethylhexanoate and mineral oil showed that the tin precursor dispersed in mineral oil gradually accumulated at the interface between the ethanol layer and mineral oil layer, forming an intermediate layer (Figure 4.7). As such, it is highly likely that tin ethylhexanoate molecules migrate to the interface between the polar shell solution (ethanol) and the nonpolar core solution (mineral oil) during electrospinning prior to decomposition into SnO_2 under the heating treatment. Moreover, while the as-prepared fibers were air-dried at room temperature, allowing for hydrolysis of the titanium precursor, and subsequently heated at elevated temperature for annealing, small TiO_2 nanocrystals started to grow in the shell. Those TiO_2 nanocrystals could potentially provide active sites for the heterogeneous nucleation of SnO_2 since the carboxylate group of ethylhexanoate molecules in tin precursor is apt to anchor onto the surface of TiO_2.[255] Upon calcination, the metal precursors would then be converted into robust metal oxide layers, whereas the polymer and mineral oil would be removed. It is highly likely that the growth of metal oxide nanocrystals occurred simultaneously with, if not prior to, the combustion of

polymer and mineral oil. Hence, even though the calcination step led to the shrinkage of the overall dimension of fibers, the tubular structure was still retained.

In addition, the proportion of mineral oil within the tin precursor solution plays a key role in forming the tubular co-axial SnO_2/TiO_2 structure. For instance, the increase in the proportion of mineral oil, giving rise to the tin precursor concentration of 0.8 mmol/mL, resulted in the formation of "bead-like" fibers consisting of wider central cavities coated with a discontinuous inner SnO_2 layer (Figure 4.8). Since mineral oil cannot be readily electrospun, in this case, an increase in the proportion of mineral oil may reduce the interfacial stress generated between the core solution and shell solution in the co-axial Talyor cone. Therefore, the shell solution may not effectively confine the core solution within the co-axial cone. As a result, the inner jet can then undergo various break-up processes, leading to the formation of hollow bead fragments interconnected by solid fibers.[256] By contrast, an increase of the concentration of tin precursor to 1.6 mmol/mL provided for sufficient tin precursor materials to coat the inside wall of the tubular TiO_2, thereby resulting in the formation of the tubular co-axial SnO_2/TiO_2 structure we have observed. When the concentration of tin precursor was subsequently increased to 2.2 mmol/mL, the use of an excess amount of tin precursors led to the formation of SnO_2 nanoparticles in addition to the SnO_2 inner layer, accompanied by a shrinkage of the inner hollow channel. With a further increase (decrease) of the proportion of tin precursor (mineral oil) in the core precursor solution, a solid coaxial structure could be obtained, as summarized in Figure 4.9.

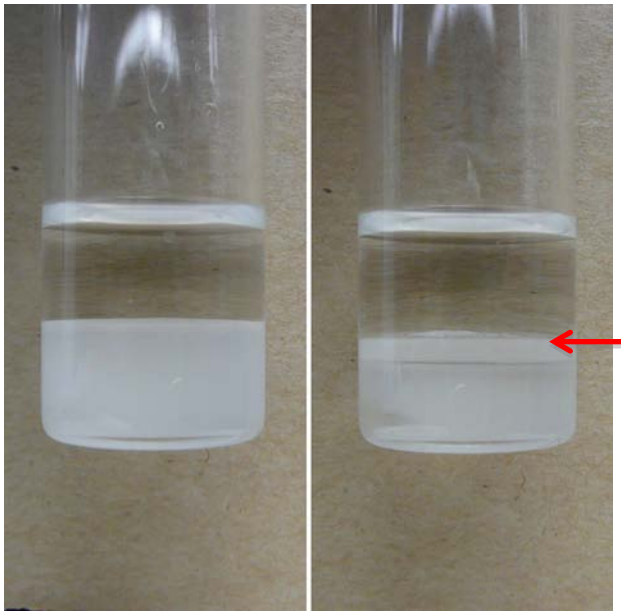

Figure 4.7: (Left) Photograph of ethanol (upper layer) and a mixture of tin 2-ethylhexanoate and mineral oil (bottom layer). (Right) Photograph of the identical solution after one hour. An intermediate layer has clearly formed between the ethanol and mineral oil layers (as indicated by the red arrow).

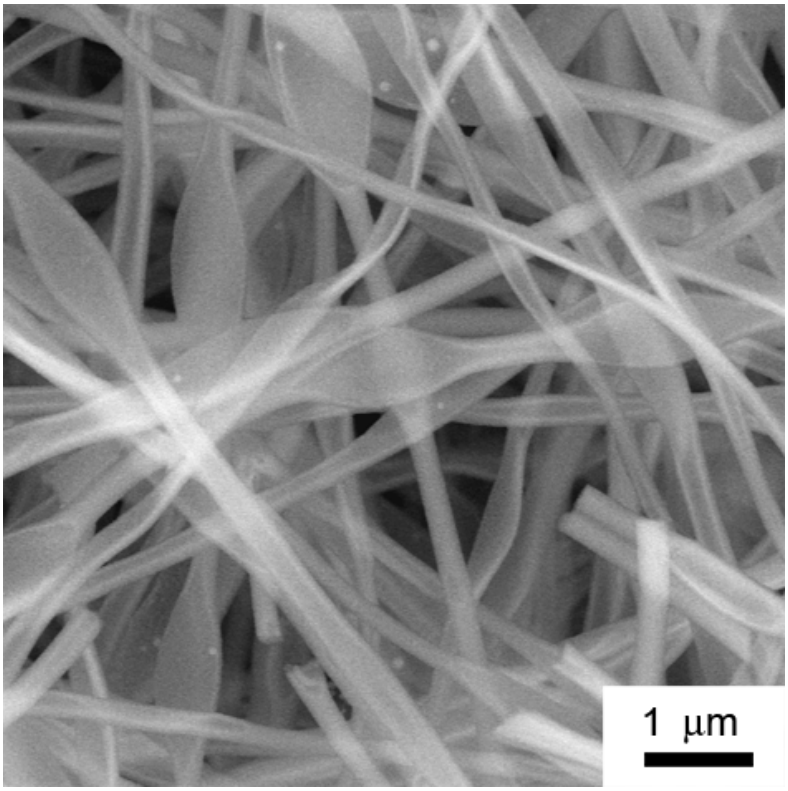

Figure 4.8: SEM image of SnO_2/TiO_2 nanofibers when the concentration of tin (II) precursor is 0.8 mmol/mL.

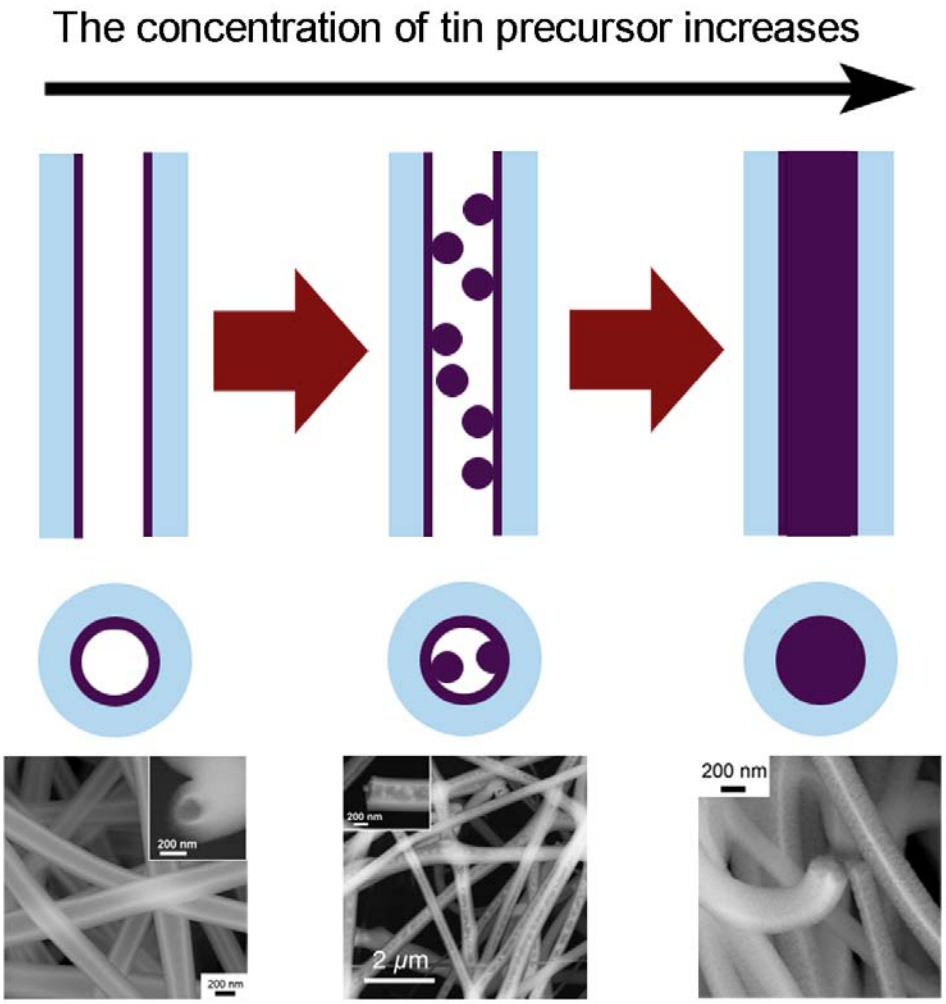

Figure 4.9: Effect of the concentration of tin precursor upon the morphology of the SnO_2/TiO_2 electrospun fibers. By increasing the concentration of tin precursor, the morphology of electrospun fibers evolves from that of a tubular coaxial structure to a peapod-like structure, and finally, onwards to a solid, filled core-shell structure.

4.3.5 *Photocatalytic Activity*

In order to test the practical applicability of electrospun coaxial heterostructures, the photocatalytic activities of SnO_2/TiO_2 nanofibers were evaluated by monitoring the degradation of an organic dye. Figure 4.10A highlights the degradation of RhB in the presence of tubular SnO_2/TiO_2 nanofiber photocatalysts under UV illumination over a time period of 150 min. By comparison, the photocatalytic activities of commercial TiO_2 nanoparticles (P25), electrospun TiO_2 nanofibers, as well as solid SnO_2/TiO_2 coaxial nanofibers were also tested under identical conditions. The data clearly show that the degradation of RhB catalyzed by tubular SnO_2/TiO_2 nanofibers is much faster than that associated with the three other types of photocatalysts, whereas the dye in the control experiment experiences little if any degradation upon UV exposure. The photocatalytic degradation reaction of RhB can be modeled as a pseudo-first-order reaction with the kinetics expressed by the equation, $\ln(C_0/C_t) = kt$, where C_0 represents the initial concentration of aqueous RhB, C_t denotes the concentration of RhB at a given reaction time "t", and k is the reaction rate constant. Derived from the plot as shown in Figure 4.10B, the computed reaction rate constants are 4.6×10^{-3}, 3.3×10^{-3}, 3.0×10^{-3} and 2.5×10^{-3} min^{-1} for tubular SnO_2 /TiO_2 nanofibers, solid SnO_2 /TiO_2 nanofibers, TiO_2 nanofibers, and P25, respectively. As we can see, our tubular SnO_2 /TiO_2 nanofibers exhibited a 1.5-fold higher intrinsic activity than TiO_2 nanofibers alone, and an almost 2-fold increase in photocatalytic activity as compared with commercial TiO_2 nanoparticles, under identical reaction conditions.

This substantial improvement in the activity of tubular SnO_2 /TiO_2 nanofibers can be attributed to a number of factors related to the unique structure of the fibers as well as to the energy level offset between SnO_2 and TiO_2, which is inherently beneficial for efficient charge

separation at the interface of these two components. First, nanoparticles spatially confined within nanofiber motifs likely experienced an efficient interparticle charge transport along its one-dimensional structure. A comparison between P25 nanoparticles and pure TiO_2 fibers implied that interparticle interactions may play an important role in facilitating charge transport between the particles, thereby enhancing photocatalytic efficiency. Specifically, trapping and detrapping processes induced by the surface defects of randomly packed nanoparticles have been found to dramatically undermine charge mobility and subsequently cause significant charge recombination. In particular, studies have shown that one-dimensional structures encapsulating closely packed nanoparticles can enhance the diffusion length and improve the degree of charge transport.[257, 258] For instance, the electrical conductivity of SnO_2 nanowires and polycrystalline nanotubes has been found to be more than 5x higher than that of SnO_2 nanoparticles alone.[259] A photocatalytic comparison between TiO_2 nanofibers and TiO_2 nanoparticles suggested that TiO_2 nanofibers possessed higher photocatalytic activity by a factor of 3 in terms of photocurrent generation as a result of the noticeable improvement in interparticle charge transport.[235] Therefore, in our photocatalytic reactions, a rapid interparticle transport of photogenerated charge carriers through the grain boundaries in SnO_2/TiO_2 fibers likely accounts for the improved activity as compared with TiO_2 nanoparticles alone.

Second, the tubular structure led to a remarkable increase in accessible surface area. The available surface area of tubular SnO_2/TiO_2 nanofibers was determined to be 87 m^2/g (Table 4.4), which is about 1.5-fold higher than that of P25 TiO_2 nanoparticles (55 m^2/g), solid TiO_2 nanofibers (52 m^2/g), and solid SnO_2/TiO_2 nanofibers (60 m^2/g), respectively. The high surface area of tubular SnO_2/TiO_2 fibers allowed for a correspondingly high adsorption of active species, thereby promoting the observed photocatalytic efficiency. Third, photogenerated electron

transfer from TiO_2 to SnO_2, due to the energy-level offset between the conduction bands of SnO_2 and TiO_2, greatly suppressed the possible recombination of charge carriers, as highlighted in Figure 4.11. A comparison between solid SnO_2 /TiO_2 coaxial nanofibers and anatase TiO_2 nanofibers also revealed the advantages of using heterojunctions. It has been suggested that the rutile phase TiO_2 possesses a lower activity than its anatase analogue.[260] Therefore, the slight enhancement in the activity of solid SnO_2 /TiO_2 coaxial nanofibers with a pure rutile phase as compared with its anatase counterpart strongly confirmed that the formation of heterojunction between TiO_2 and SnO_2 yielded a positive influence on the carrier separation efficiency, so as to enhance the photocatalytic activity.

Subsequently, the tubular structure tended to facilitate the photocatalytic process wherein not only holes on TiO_2 but also electrons accumulated on SnO_2 could react with active species in solution, thereby providing oxidizing radicals that could subsequently act to assist in the degradation of organic dyes. We note that though the phase transformation of TiO_2 from anatase to rutile may lower its intrinsic photocatalytic activity, the synergistic coupling of the tubular one-dimensional structure with favorable electron transfer from TiO_2 to SnO_2 can lead to the overall enhancement of photocatalytic activity as observed.

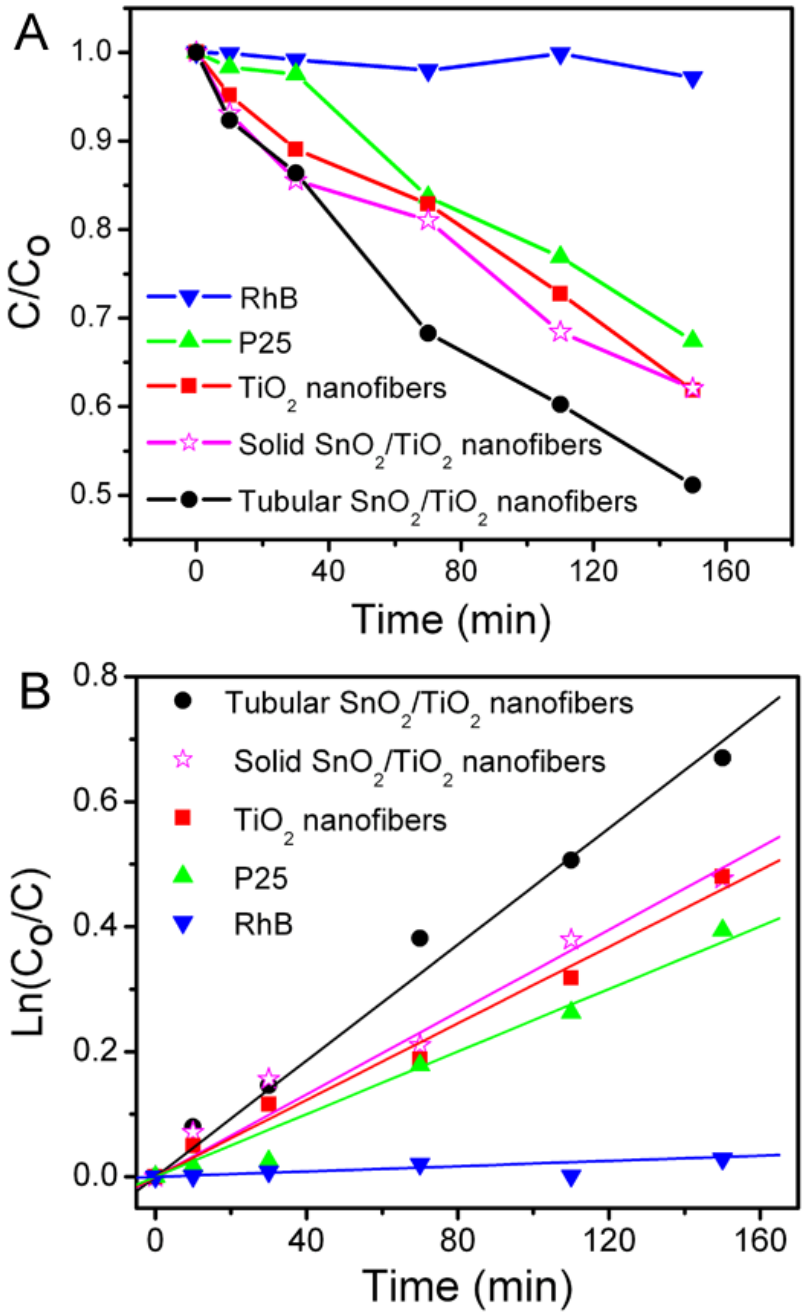

Figure 4.10: (A) Degradation profiles of Rhodamine B (RhB) in the presence of different photocatalysts under UV illumination. (B) First-order kinetic rate constant data associated with RhB photocatalytic degradation in the presence of different photocatalysts.

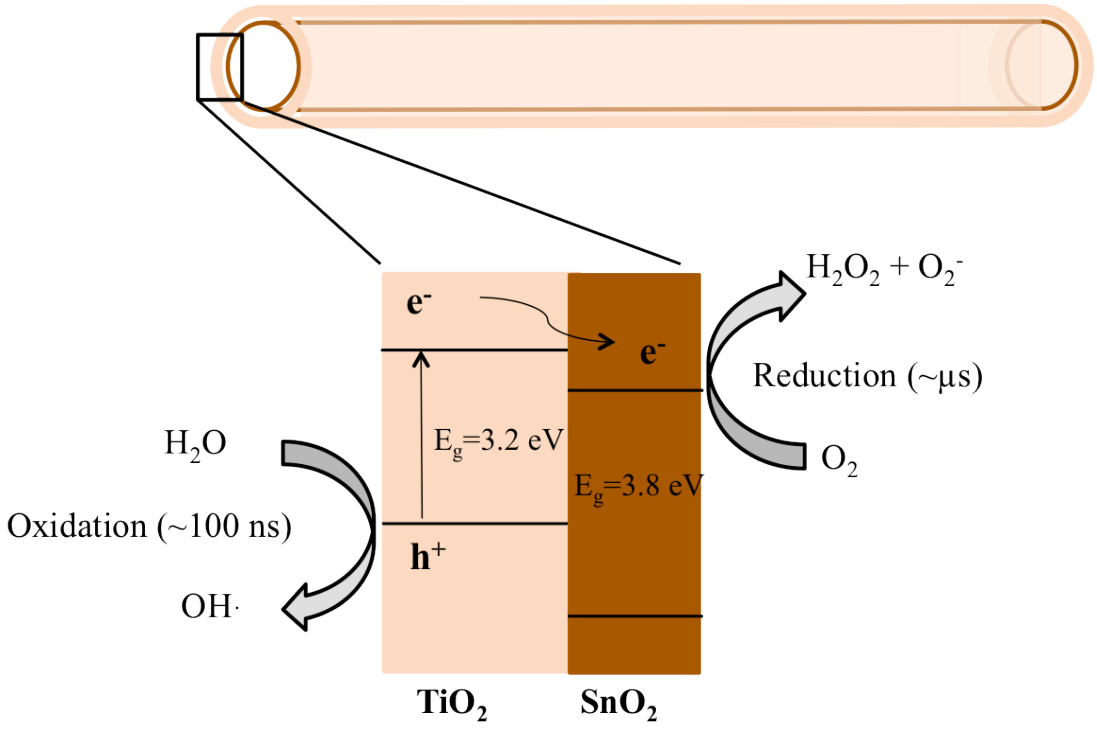

Figure 4.11: This cartoon represents a typical configuration of our as-prepared tubular SnO_2/TiO_2 coaxial electrospun fibers. The corresponding energy band diagram of SnO_2 and TiO_2 illustrates the principle of charge separation at the interface of SnO_2/TiO_2 as well as the subsequent photocatalytic reaction.

Table 4.4: Measured physicochemical properties of different photocatalysts used in our study.

Samples	**BET surface area (m^2/g)**	**BJH pore radius (nm)**
P25	55	1.4
Electrospun TiO_2 nanofibers	52	2.7
Solid SnO_2/TiO_2 nanofibers	60	2.0
Tubular SnO_2/TiO_2 nanofibers	87	2.7

4.4 Conclusions

In summary, this study has demonstrated that SnO_2/TiO_2 nanofibers with well-defined core-shell structures can be readily fabricated by coaxial electrospinning. Three different interior morphologies were prepared by appropriately varying the precursor concentration. Measurement of the photocatalytic activity of these materials has suggested that tubular coaxial nanofibers are superior to their compositional analogues as a result of the combination of the advantages associated with the formation of a heterojunction as well as a tubular motif. The established methodology reported herein is highly versatile and can be extended to different binary metal oxide systems, including SnO_2/Fe_2O_3[119] and ZnO/NiO[118], as well as to either metals or sulfides depending on appropriate post-treatments (e.g. annealing in a reducing atmosphere will generate metal nanofibers[261]). The important advantages of using coaxial electrospinning for the fabrication of inorganic heterostructures lie in its flexibility in terms of the choice of materials, synthetic simplicity, high yield, as well as the reliable generation of high-quality coaxial structures. Hence, the potential functionalities that can be incorporated into electrospun coaxial structures are essentially unlimited. In fact, these materials could readily encompass luminescent, magnetic, and ferroelectric moieties. Furthermore, the ability to tune the interior morphology all the way from hollow nanotubes to filled nanowires allows for the development of a host of useful applications.

4.5 References

96. H. J. Fan, M. Knez, R. Scholz, K. Nielsch, E. Pippel, D. Hesse, M. Zacharias and U. Gosele, *Nature Materials*, **2006**, *5*, 627-631.

108. X. M. Shuai and W. Z. Shen, *The Journal of Physical Chemistry C*, **2011**, *115*, 6415-6422.

115. M. Law, L. E. Greene, A. Radenovic, T. Kuykendall, J. Liphardt and P. D. Yang, *Journal of Physical Chemistry B*, **2006**, *110*, 22652-22663.

118. Z. Zhang, C. Shao, X. Li, C. Wang, M. Zhang and Y. Liu, *ACS Applied Materials & Interfaces*, **2010**, *2*, 2915-2923.

119. M. T. Niu, F. Huang, L. F. Cui, P. Huang, Y. L. Yu and Y. S. Wang, *Acs Nano*, **2010**, *4*, 681-688.

218. J. Xiang, W. Lu, Y. J. Hu, Y. Wu, H. Yan and C. M. Lieber, *Nature*, **2006**, *441*, 489-493.

219. X. W. Teng, Q. Wang, P. Liu, W. Han, A. Frenkel, W. Wen, N. Marinkovic, J. C. Hanson and J. A. Rodriguez, *Journal of the American Chemical Society*, **2008**, *130*, 1093-1101.

220. X. W. Teng, M. Feygenson, Q. Wang, J. Q. He, W. X. Du, A. I. Frenkel, W. Q. Han and M. Aronson, *Nano Letters*, **2009**, *9*, 3177-3184.

221. Y. H. Lin, Y. C. Hsueh, P. S. Lee, C. C. Wang, J. R. Chen, J. M. Wu, T. P. Perng and H. C. Shih, *Journal of the Electrochemical Society*, **2010**, *157*, K206-K210.

222. Y. J. Dong, B. Z. Tian, T. J. Kempa and C. M. Lieber, *Nano Letters*, **2009**, *9*, 2183-2187.

223. Q. Kuang, Z. Y. Jiang, Z. X. Xie, S. C. Lin, Z. W. Lin, S. Y. Xie, R. B. Huang and L. S. Zheng, *Journal of the American Chemical Society*, **2005**, *127*, 11777-11784.

224. R. He, M. Law, R. Fan, F. Kim and P. Yang, *Nano Letters*, **2002**, *2*, 1109-1112.

225. C. L. Zhu, M. L. Zhang, Y. J. Qiao, G. Xiao, F. Zhang and Y. J. Chen, *The Journal of Physical Chemistry C*, **2010**, *114*, 16229-16235.

226. J. Jun, C. Jin, H. Kim, S. Park and C. Lee, *Applied Surface Science*, **2009**, *255*, 8544-8550.

227. K. Nagashima, T. Yanagida, H. Tanaka, S. Seki, A. Saeki, S. Tagawa and T. Kawai, *Journal of the American Chemical Society*, **2008**, *130*, 5378-5382.

228. A. Datta, S. K. Panda and S. Chaudhuri, *The Journal of Physical Chemistry C*, **2007**, *111*, 17260-17264.

229. J. Cao, J.-Z. Sun, H.-Y. Li, J. Hong and M. Wang, *Journal of Materials Chemistry*, **2004**, *14*, 1203-1206.

230. X. Q. Meng, H. Peng, Y. Q. Gai and J. Li, *The Journal of Physical Chemistry C*, **2009**, *114*, 1467-1471.

231. J. M. Wu, *Journal of Physical Chemistry C*, **2008**, *112*, 13192-13199.

232. J. Hu, Y. Bando, Z. Liu, T. Sekiguchi, D. Golberg and J. Zhan, *Journal of the American Chemical Society*, **2003**, *125*, 11306-11313.

233. S. Ramakrishna, R. Jose, P. S. Archana, A. S. Nair, R. Balamurugan, J. Venugopal and W. E. Teo, *Journal of Materials Science*, **2010**, *45*, 6283-6312.

234. A. K. Moghe and B. S. Gupta, *Polymer Reviews*, **2008**, *48*, 353-377.

235. S. K. Choi, S. Kim, S. K. Lim and H. Park, *The Journal of Physical Chemistry C*, **2010**, *114*, 16475-16480.

236. V. Thavasi, G. Singh and S. Ramakrishna, *Energy & Environmental Science*, **2008**, *1*, 205-221.

237. Y. Z. Zhang, X. Wang, Y. Feng, J. Li, C. T. Lim and S. Ramakrishna, *Biomacromolecules*, **2006**, *7*, 1049-1057.

238. H. L. Jiang, Y. Q. Hu, Y. Li, P. C. Zhao, K. J. Zhu and W. L. Chen, *Journal of Controlled Release*, **2005**, *108*, 237-243.

239. Y. Yu, L. Gu, C. B. Zhu, P. A. van Aken and J. Maier, *Journal of the American Chemical Society*, **2009**, *131*, 15984-15985.

240. M. R. Hoffmann, S. T. Martin, W. Choi and D. W. Bahnemann, *Chemical Reviews*, **1995**, *95*, 69-96.

241. L. R. Hou, C. Z. Yuan and Y. Peng, *Journal of Hazardous materials*, **2007**, *139*, 310-315.

242. Z. Liu, D. D. Sun, P. Guo and J. O. Leckie, *Nano Letters*, **2006**, *7*, 1081-1085.

243. Y. Zhao, J. Liu, L. Y. Shi, S. A. Yuan, J. H. Fang, Z. Y. Wang and M. H. Zhang, *Applied Catalysis B-Environmental*, **2010**, *100*, 68-76.

244. K. Vinodgopal, I. Bedja and P. V. Kamat, *Chemistry of Materials*, **1996**, *8*, 2180-2187.

245. S. C. Ray, M. K. Karanjai and D. DasGupta, *Surface & Coatings Technology*, **1998**, *102*, 73-80.

246. Y. Liu, E. Koep and M. L. Liu, *Chemistry of Materials*, **2005**, *17*, 3997-4000.

247. D. G. Shchukin and R. A. Caruso, *Advanced Functional Materials*, **2003**, *13*, 789-794.

248. J. Li and H. C. Zeng, *Journal of the American Chemical Society*, **2007**, *129*, 15839-15847.

249. K. K. Akurati, A. Vital, R. Hany, B. Bommer, T. Graule and M. Winterer, *International Journal of Photoenergy*, **2005**, *7*, 153-161.

250. S. F. Chen, L. Chen, S. Gao and G. Y. Cao, *Materials Chemistry and Physics*, **2006**, *98*, 116-120.

251. D. Li and Y. N. Xia, *Nano Letters*, **2004**, *4*, 933-938.

252. Y. Q. Cao, T. He, L. S. Zhao, E. J. Wang, W. S. Yang and Y. A. Cao, *Journal of Physical Chemistry C*, **2009**, *113*, 18121-18124.

253. B. Liu and E. S. Aydil, *Journal of the American Chemical Society*, **2009**, *131*, 3985-3990.

254. D. Li, J. T. McCann and Y. N. Xia, *Small*, **2005**, *1*, 83-86.

255. I. Robel, V. Subramanian, M. Kuno and P. V. Kamat, *Journal of the American Chemical Society*, **2006**, *128*, 2385-2393.

256. J. E. Díaz, A. Barrero, M. Márquez and I. G. Loscertales, *Advanced Functional Materials*, **2006**, *16*, 2110-2116.

257. O. K. Varghese, M. Paulose and C. A. Grimes, *Nature Nanotechnology*, **2009**, *4*, 592-597.

258. J. R. Jennings, A. Ghicov, L. M. Peter, P. Schmuki and A. B. Walker, *Journal of the American Chemical Society*, **2008**, *130*, 13364-13372.

259. M.-S. Park, Y.-M. Kang, G.-X. Wang, S.-X. Dou and H.-K. Liu, *Advanced Functional Materials*, **2008**, *18*, 455-461.

260. N. G. Park, J. van de Lagemaat and A. J. Frank, *Journal of Physical Chemistry B*, **2000**, *104*, 8989-8994.

261. H. Wu, R. Zhang, X. X. Liu, D. D. Lin and W. Pan, *Chemistry of Materials*, **2007**, *19*, 3506-3511.

Chapter 5 Study of the Morphology Effect of ZnO Nanostructures upon Their Toxicity to Marine Organisms

5.1 Introduction

With an increase in commercial manufacturing of nanoparticle-containing goods and biomedical applications utilizing nanoparticles, there is a growing concern about the real and perceived environmental risks associated with exposure to nanomaterials. Indeed, the toxicity of a particular material may increase when its size decreases to the nanometer scale and this property may be related to the ability of nanoparticles to penetrate into and accumulate within cells and organisms.[124-126, 128, 262] Diverse physicochemical factors including morphology, encompassing issues related to the size, shape, and aspect ratio of nanoparticles, can influence the fate of nanoparticles in aquatic systems.[263] For example, the shape of nickel nanoparticles can affects their toxicity towards zebrafish embryos,[124] while the morphology of TiO_2 nanoparticles can also induce noticeable toxicity in bacteria or mammal cells.[126, 264, 265]

ZnO nanoparticles are widely incorporated in commercially available merchandise (e.g. sunscreen, coatings, and paints).[266] However, their environmental impact and the mechanism of their toxicity still have not been fully elucidated. A few studies involving marine and freshwater organisms have suggested that the dissolution of the Zn ions from ZnO nanoparticles can account for their toxicity.[140, 267-269] The effects of natural organic compounds (e.g. fulvic acid and cysteine) and pH upon the dissolution kinetics of ZnO nanoparticles in different types of water systems (e.g. deionized seawater and artificial seawater) have also been studied in order to shed

light upon the impact of ZnO nanoparticles in the environment.[270] However, the dissolution behavior of nanomaterials has also been found to be influenced inherently by their morphologies.[271] For instance, owing to their anisotropic structure and the presence of fewer surface defect sites, either one-dimensional wire-like or rod-like nanomaterials have exhibited higher resistance to dissolution than zero-dimensional spherical nanoparticles in fuel cell operations.[272] The dissolution of ZnO nanoparticles was also found to be size-dependent.[273] As such, engineering ZnO nanostructures may alter their intrinsic toxicity by influencing their inherent dissolution rate.

A recent report has suggested that both nanoscale particulate ZnO and dissolved Zn^{2+} could account for the toxicity of nanoscale ZnO aggregates to zebrafish embryos, because the presence of soluble Zn^{2+} alone could not fully explain the adverse effects induced in embryos by nanoscale ZnO aggregates.[274] Moreover, Miao *et al.* [270] have argued that the additional inhibitive effects observed for ZnO nanoparticles as compared with Zn^{2+} could be ascribed to the extra Zn^{2+} released from ZnO nanoparticles upon either their attachment to the cell surface or intracellular accumulation. Given that the morphology of nanoparticles can potentially affect their interaction with cell membranes as well as their ability to penetrate into cells and organisms, a true, verifiable morphological dependence of the toxicity of ZnO nanoparticles may exist in addition to the inherent toxic effect associated with the presence of dissolved metal ions. In fact, a recent study has suggested that the size dependence of the antibacterial activity of ZnO could be attributed to the faster movement and less spatial hindrance of smaller nanoparticles upon attachment to the bacterial surface as opposed to bulk materials.[275] Both *Escherichia coli* and *Pseudomonas fluorescens* have been found to exhibit a high tolerance to zinc ions at the tested ZnO concentration (20 mg L^{-1}). The physical attachment of ZnO nanoparticles onto the surface

of bacteria was ascribed as the main cause of ZnO toxicity to these bacterial species.[275] Brayner et al.[276] have investigated bacterial growth in the presence of ZnO, possessing various morphologies, and found that the surfactant used for regulating the shape of ZnO was primarily responsible for the observed toxicity. Thus far, however, little is known about the actual size- and shape-dependence of the observed toxicology of ZnO nanoparticles in the presence of marine organisms.

As such, in this Chapter, we have attempted to address two specific questions: (i) Would nanoscale ZnO with different morphologies result in intrinsically different toxic effects to marine diatoms by altering their dissolution behaviors on time scales relevant to biological systems? (ii) Apart from the soluble zinc that is released from ZnO nanoparticles, would the presence of nanoscale ZnO particles themselves induce an additional toxic effect in diatoms? If so, are the toxic effects of nanoparticles effectively morphology-dependent? To address all of these questions, we have synthesized ZnO nanoparticles of different morphologies without any surfactants, and examined the specific toxic effects of these nanoparticles upon marine diatoms, which represent prominent examples of phytoplankton assemblages in aquatic ecosystems. Three diatom species were compared. One of these diatoms possesses a much more lightly silicified frustule than the other two species. In our study, two different shapes as well as two different sizes of ZnO nanoparticles were examined for each algal species in order to determine whether ZnO toxicity could be systematically altered in a comprehensible fashion. The influence of particle concentration for each type of nanoparticle upon algal growth was examined as well.

5.2 Experimental Section

5.2.1 *Synthesis of ZnO nanostructures possessing different morphologies.*

The preparation of ZnO nanoparticles with different morphologies has been adapted from the reported literature.[277, 278] Specifically, existing methods were optimized in order to improve control over nanoparticle morphology by systematically varying solvent composition, precursor concentrations, and reaction time without the assistance of either any organic ligands or capping agents. We note that it was essential to prepare nanoparticles in the absence of organic capping ligands, since these organic compounds may exacerbate inherent toxic effects and thereby distort data interpretation.[279]

In a typical experiment, for spherical nanoparticles, 2.3 mL of 0.3 M NaOH in methanol was added dropwise to 4.2 mL of 0.1 M $ZnCl_2$ in methanol. The resulting solution was then heated at 60°C and stirred for 2 h, yielding small spherical nanoparticles (SS) and after 6 h, producing large spherical nanoparticles (LS). The white precipitate was subsequently washed several times with distilled water, and ultimately oven dried for further experiments. To obtain one-dimensional ZnO nanostructures, the nucleation and growth rates of ZnO were altered by increasing the concentration ratio of $[OH^-]$ to $[Zn^{2+}]$ to 20: 1 and by using a solvent mixture consisting of water and ethanol. Specifically, 0.0512 g of $ZnCl_2$ (0.38 mmol) and 0.3 g of NaOH (7.5 mmol) were dissolved in 0.75 mL of distilled water, followed by the addition of 8 mL of ethanol and sonication at 40°C for 35 min. To obtain ZnO nanoneedles (NN), the above solution was then stirred at 60°C overnight. The white precipitate was collected by centrifugation, washed several times with ethanol and distilled water, and finally oven dried prior to additional experiments.

5.2.2 *Materials characterization*

Crystallographic and purity information on the prepared nanomaterials were obtained using a Scintag diffractometer, operating in the Bragg configuration using Cu K_α radiation (λ = 1.54 Å) from 20º to 80° at scanning rates of 0.25° min^{-1}.

The size and shape of the nanostructures were determined by TEM analysis, with images taken at an accelerating voltage of 80 kV on an FEI Tecnai12 BioTwinG^2 instrument, equipped with an AMT XR-60 CCD digital camera system. Specimens for all of these TEM experiments were prepared by dispersing the nanoparticles in ethanol to ensure an adequate dispersion of the nanostructures, placing one drop of solution onto a 300 mesh Cu grid, coated with a lacey carbon film, and allowing for air drying to take place. The sizes of the nanoparticles were determined by statistically measuring 30 nanoparticles in TEM images by ImageJ. In addition, the interior morphology of diatoms after exposure to nanoparticles was also examined by TEM. Following exposure to ZnO nanostructures, the diatoms were centrifuged, fixed in 3% glutaraldehyde/0.05 M phosphate buffer (pH = 7), and kept at 4ºC. After fixation, samples were then placed in 2% osmium tetroxide in phosphate buffer, dehydrated using a graded series of ethyl alcohol, and embedded in Epon resin. Ultrathin sections of 80 nm were cut with a Reichert-Jung UltracutE ultramicrotome and placed onto Formvar-coated slot copper grids. Sections were then counter-stained with both uranyl acetate and lead citrate.

The actual sizes of the nanoparticles in medium were determined by dynamic light scattering (DLS) measurements (Brookhaven Instruments Corporation, 90Plus Particle Size Analyzer). Dynamic light scattering is a non-invasive technique that can be used to determine the hydrodynamic size distribution profile of small particles in solution. When the light from laser hits the small particles, a time-dependent fluctuation in the scattering intensity can be observed

due to the Brownian motion of small particles in solution, which therefore leads to the changes in the distance between the scatterers as a function of time. The dynamic information about the particles in solution can be derived from an autocorrelation of the scattering intensity trace recorded during the experiment. At short delay time, the correlation is high because the particles do not have a chance to move to a great extent from their initial state, whereas the degree of correlation diminishes to zero over time as the particles diffuse. The resulting exponential decay of the correlation function is characteristic of the diffusion coefficient of the particles, which can be used to determine the hydrodynamic radius of a sphere through the Stokes-Einstein equation. Experimentally, ZnO nanoparticles were dispersed in solutions of fresh medium at certain concentrations (e.g. 10 mg L^{-1}, 40 mg L^{-1}, and 80 mg L^{-1}). All solutions were subsequently sonicated for a few minutes to break up visible clumps of aggregates. Samples were then placed in a clean cuvette and five measurements were taken successively for each solution.

5.2.3 *Dissolution of ZnO nanoparticles*

The extent of dissolution of ZnO nanostructures in the seawater medium in the absence of algae was measured using graphite furnace atomic absorption spectrometry (GFAAS) (AAnalyst 800, Perkin Elmer). Specifically, ZnO nanostructures were dispersed by sonication into fresh growth medium (40 mg ZnO L^{-1}) for all shapes and sizes of the nanoparticles and held at room temperature for up to 3 d. At 1 h, 4 h, 24 h, and 72 h, an aliquot of solution was withdrawn and centrifuged at 8300 *g* for 30 min. The supernatant was then filtered through a 0.05 μm polycarbonate membrane in order to remove any remaining nanoparticles. The total amount of dissolved Zn in the filtrate was measured by GFAAS. The light source consisted of a hollow cathode lamp and the spectra were monitored at a wavelength of 213.9 nm, corresponding to

where Zn atoms maintain a characteristic absorption profile. Replicates were measured for each sample and the relevant metal concentration was calculated using a standard curve. In order to test the concentration effect of ZnO nanoparticles upon their dissolution rate, three different concentrations (e.g. 10 mg L^{-1}, 40 mg L^{-1}, and 80 mg L^{-1}) of ZnO small nanospheres (SS) and nanoneedles (NN) were investigated, following the procedure noted above.

5.2.4 *Nanoparticle exposure and algal growth studies*

We examined three marine diatoms possessing different morphologies, namely *Thalassiosira pseudonana*, *Chaetoceros gracilis*, and *Phaeodactylum tricornutum*. All diatom cultures were maintained in an f/2 medium,[280] prepared using filtered surface seawater collected 8 km off Southampton, NY and modified such that Mn, Co, Mo, and f/20 Fe were added but no EDTA was used. Specifically, f/2 denotes a tried and true medium for culturing marine phytoplankton. The term, F/20 of a certain nutrient, signifies that one tenth of the amount of that nutrient is added. Media for all algal cultures were sterilized by filtering through a sterile 0.2 μm filter. The starting cell density of *T. pseudonana* was $2 \cdot 10^3$ cells/mL. The corresponding, initial values for *C. gracilis* and *P. tricornutum* were $2 \cdot 10^4$ cells/mL and $3 \cdot 10^4$ cells/mL, respectively, so as to yield approximately the same initial biomass for all species. A calculated amount of each type of ZnO nanostructures was then re-dispersed in 1 mL of f/2 medium by sonication in order to ensure a homogeneous dispersion of ZnO by minimizing clumping; this was then added into the algal cultures. Four different concentrations of ZnO nanostructures were tested for all cell cultures, namely 10 mg L^{-1}, 20 mg L^{-1}, 40 mg L^{-1}, and 80 mg L^{-1}. All treatments were conducted in triple replicates. Once the diatoms were exposed to ZnO nanostructures, the cultures were incubated at 17ºC with light provided by cool-white fluorescence lamps (120 μmol quanta m^{-2} s^{-1})

on a 14 h: 10 h light: dark cycle. Two mL of algal cultures were sampled from each flask every 24 h and preserved with filtered Lugol's solution for further cell count measurements. Control algal cultures were treated under identical conditions without the addition of ZnO nanoparticles. Algal cell counts were obtained using a Coulter Counter (Coulter Multisizer III). Log-linear cell division rates were calculated between 24 and 72 h.

The diatom, *T. pseudonana*, was also exposed to radioactive ZnO nanostructures in order to determine the bioavailability of the Zn initially associated with the nanoparticles. ZnO nanostructures labeled by ^{65}Zn were prepared following the same procedure as the non-radioactive synthesis, except that the gamma-emitting radioisotope, ^{65}Zn, was added together with stable Zn salt for the synthesis of the nanoparticles. Specifically, stable Zn was combined with 26.2 kBq (0.436 nmoles) of ^{65}Zn for the synthesis of each type of ZnO nanoparticle. Two replicate cultures were then assessed for each treatment. The starting algal cell density was measured to be $3 \cdot 10^5$ cells mL^{-1}. The level of Zn bioaccumulation was determined, as described previously.[281] Briefly, at each sample time, a 5 mL sample from each culture was withdrawn, filtered through a 1 µm-pore-size polycarbonate membrane, and rinsed twice with 5 mL of unlabeled filtered seawater. Control cultures containing no diatom cells were also studied in order to differentiate the ^{65}Zn, collected on the filters and attributable to adsorption to the polycarbonate membrane, from that associated with the filtered cells. The net radioactivity of ^{65}Zn associated with the diatoms was calculated by subtracting the radioactivity from the control cultures. Radioactivity of the filters was measured at 1115 keV using an LKB 1282 CompuGamma equipped with a well-type NaI(Tl) detector. Counting time was 5 minutes and yielded propagated counting errors of <5%. The quantity of total Zn associated with the cells was

determined by considering the specific activity of ^{65}Zn in the experimental cultures. The specific activity of Zn on the date of experiments was noted to be 1.636 μCi/μg.

5.2.5 *Statistical analysis*

Data analysis was performed using Minitab 16.1.0 (LEAD Technologies, Inc.) software. One-way Analysis of Variance (ANOVA) with Tukey's method for multiple comparisons was used in order to evaluate the various responses induced by either different particle concentrations or particle morphologies, with *p*-values <0.05 considered to be significant.

ANOVA is a general technique that has been developed to test the hypothesis that the means among two or more groups are equal, under the assumption that the sampled populations are normally distributed. One-way ANOVA has been used to evaluate the effect of an independent treatment variable on the dependent variables. The *p*-value indicates the probability of obtaining a mean difference between the groups as high as what is observed by sampling variation. A low *p*-value suggests a more significant difference between the groups.

5.3 Results and Discussion

5.3.1 *Structural characterization of ZnO nanoparticles*

Figure 5.1 highlights representative XRD patterns of both ZnO nanorods and spherical nanoparticles, which agrees with a database standard previously reported (JCPDS No. 36-1451), confirming that the resulting products were crystalline hexagonal-phase ZnO. The enhanced intensity and narrow band width of the peak located at about 34°, associated with the (0002) plane, as shown in XRD pattern of ZnO nanorods, have suggested that the potential growth

direction of one-dimensional ZnO nanostructures was along the [0001] direction. All other ZnO nanostructures analyzed exhibited similar XRD patterns, confirming both the chemical composition and crystallographic phase of these nanomaterials.

To be precise, the size and shape of ZnO nanoparticles, as determined by TEM images, were uniform with a remarkably narrow size distribution. The sizes of small spherical and large spherical nanoparticles were measured to be 6.3 ± 1.1 nm and 15.7 ± 1.3 nm, respectively (Figure 5.2A-B). For one-dimensional nanoparticles, with a high ratio of $[OH^-]$ to $[Zn^{2+}]$ precursors, the excess of OH^- led to the formation of ZnO_2^{2-}, which is soluble in water. This provided for a supersaturated precursor solution, which would in turn give rise to the rapid formation of a number of ZnO cluster nuclei upon the addition of ethanol followed by ultrasonic treatment. ZnO_2^{2-} in aqueous solution provides the source of Zn, according to the following equation:

$$ZnO_2^{2-} + H_2O \leftrightarrow ZnO + 2OH^- \qquad (5.1)$$

Therefore, the addition of alcohol could deactivate OH^- and ensure that the reaction would shift towards the right. In fact, the growth rate of the ZnO nanostructure itself was controlled by the presence of an alcohol-water mixture, which could effectively control the inherent reactivity of ZnO_2^{2-} species. Therefore, usage of highly basic conditions coupled with an alcoholic environment was essential in separating the fast nucleation step from the subsequent slow growth of ZnO in order to ensure the formation of one-dimensional nanostructures. As such, ZnO nanorods and nanoneedles could be generated by varying the reaction time. ZnO nanorod lengths measured 242 ± 47 nm with diameters of 13.5 ± 2.7 nm (Figure 5.2C), with the latter

comparable in size with that of large spherical nanoparticles. By comparison, ZnO nanoneedles possessed lengths of 862 ± 301 nm with diameters of 29.5 ± 7.1 nm (Figure 5.2D).

According to the DLS data (Table 5.1), a wide size distribution of particles in the solution was observed for all four types of ZnO nanostructures, typically showing two distinctive populations in both the several hundred nanometers region and the several microns region, a result which is consistent with that reported previously.[267] In particular, the size increased by a factor of above 50 for spherical nanoparticles, indicative of a considerable degree of aggregation within nanoparticles as a consequence of the high surface-area-to-volume ratio of nanoparticles. In fact, it is not uncommon that the particles appear as agglomerates in solution since there was no surfactant capping on their external surfaces.[269, 282] As shown in the inset to Figure 5.2, both ZnO NRs and NNs tend to assemble as sub-micron-sized spherical aggregates. We have also noted that the concentration of ZnO did not exert a great influence upon the degree of aggregation observed. For example, the size ranges of ZnO SS in suspension were 313 – 1900 nm, 425 – 1599 nm, and 416 - 2149 nm, when the corresponding amounts of SS in suspension were 10 mg L^{-1}, 40 mg L^{-1}, and 80 mg L^{-1}, respectively. The aggregation effect should be taken into account for analyzing the extent of particle dissolution. Nevertheless, the surface topography and morphology of each type of ZnO aggregates can be distinctive, as observed in the associated TEM images

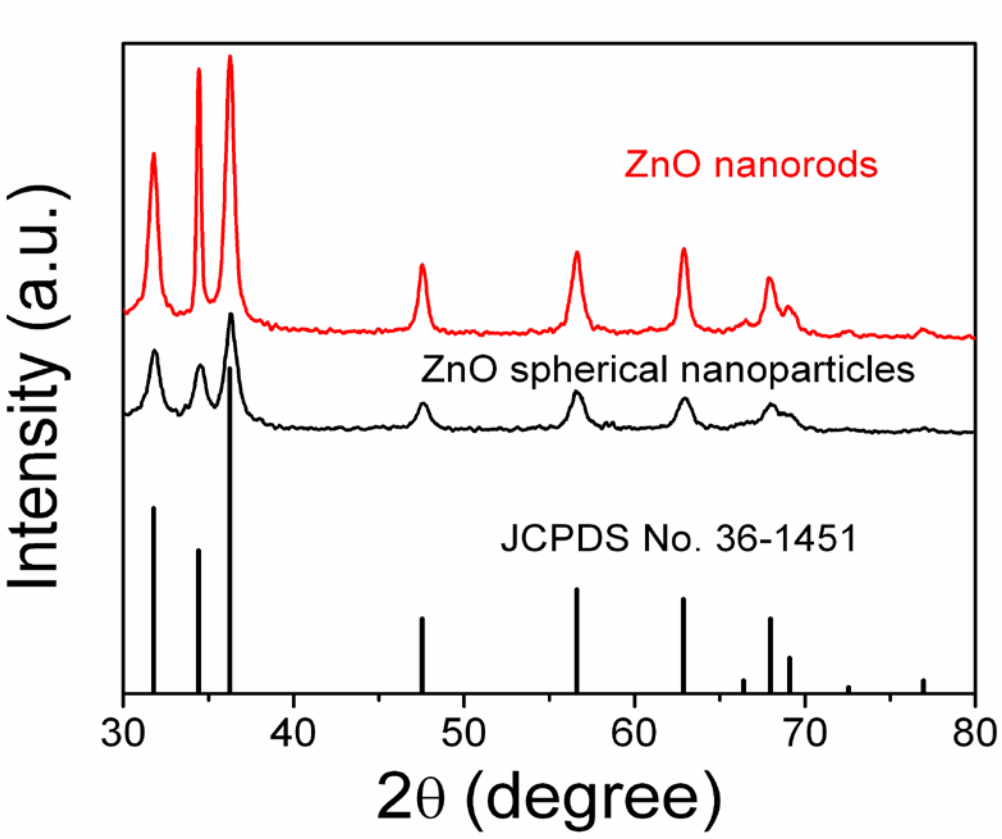

Figure 5.1: X-ray diffraction patterns of ZnO nanorods, ZnO spherical nanoparticles, and a database standard previously reported (JCPDS No. 36-1451).

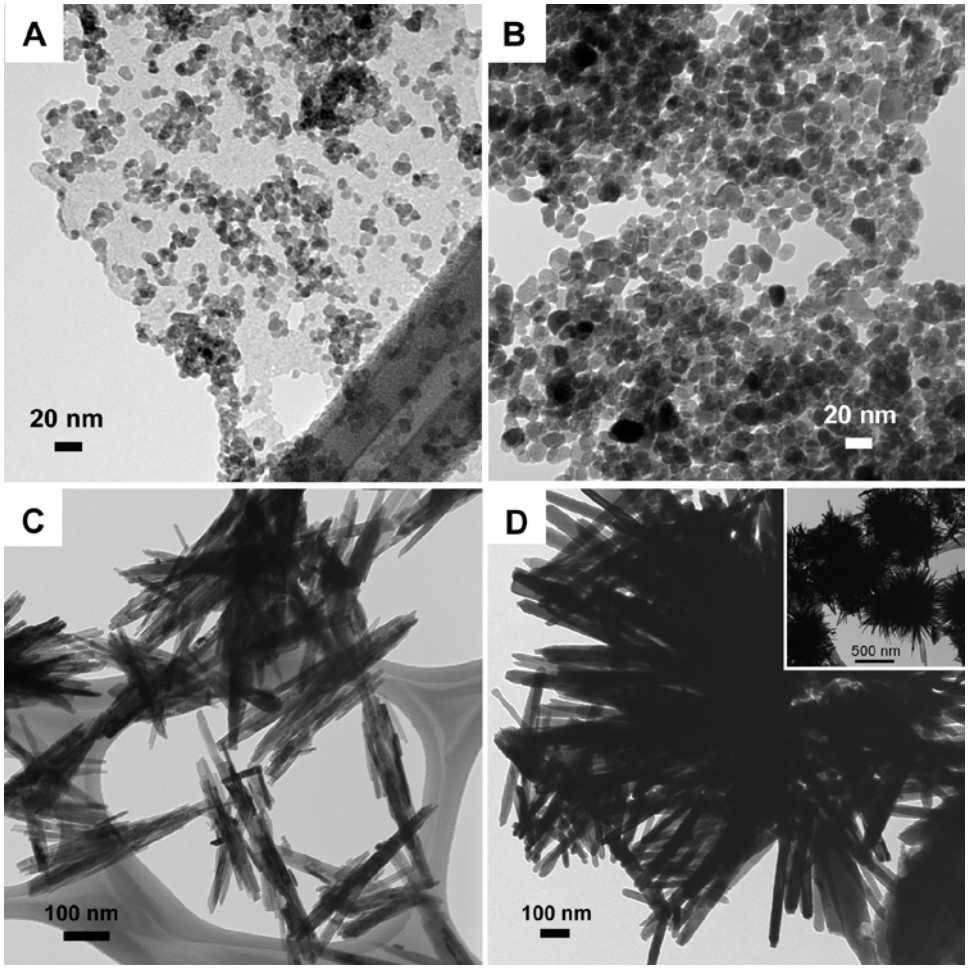

Figure 5.2: TEM images of ZnO nanoparticles possessing different morphologies. (A) small spheres, SS; (B) large spheres, LS; (C) nanorods, NR; and (D) nanoneedles, NN. Inset highlights low magnification TEM images of NN.

Table 5.1: Particle dimensions of ZnO nanostructures obtained by TEM and DLS.

Sample	Size estimated from TEM analysis (nm) (d: diameter; l: length)	Actual size range in suspension, as estimated from DLS (nm)
SS	6.3 ± 1.1	313 - 1900[a], 425 - 1599[b], 416 – 2149[c]
LS	15.7 ± 1.3	277 – 1186[a], 363 - 1588[b], 386 – 1653[c]
NR	242 ± 47 (l) 13.5 ± 2.7 (d)	504 – 1766[a], 459 - 1528[b], 320 – 1666[c]
NN	862 ± 301 (l) 29.5 ± 7.1 (d)	321 - 1344[a], 309 - 1223[b], 288 - 1239[c]

[a] The initial ZnO concentration in suspension is 10 mg L^{-1}.

[b] The initial ZnO concentration in suspension is 40 mg L^{-1}.

[c] The initial ZnO concentration in suspension is 80 mg L^{-1}.

5.3.2 *Dissolution of ZnO nanoparticles*

The dissolution of the ZnO nanoparticles (40 mg L^{-1}) occurred within the first few hours and slowed over time, so that equilibrium was generally achieved within 72 h (Figure 5.3). The pH of the ZnO suspensions was in the range of 8.2-8.3, close to the value obtained from the pure medium and independent of the initial concentration of ZnO nanoparticles. Considering that the dissolution of ZnO can be modeled as a first-order reaction, the dissolution profiles can be fit by the Noyes-Whitney equation [283].

$$C = C_s\left(1 - e^{-kt}\right) \qquad (5.2)$$

where C is the concentration of solute in solution at time t, C_s is the solubility of ZnO in equilibrium at the experimental temperature, and k is the first order release rate constant. Mathematically, $t_{1/2}$, the time taken to attain half of C_s, can be calculated by

$$t_{1/2} = \frac{\ln 2}{k} \qquad (5.3)$$

The estimated $t_{1/2}$ was 0.55 ± 0.04, 0.47 ± 0.03, 0.40 ± 0.28, and 0.38 ± 0.24 h for NR, NN, SS, and LS, respectively. Statistically, the dissolution kinetics of the various types of nanostructures tested did not significantly differ ($p > 0.05$). The calculated C_s was 1.42 ± 0.04, 1.33 ± 0.06, 1.59 ± 0.05, and 1.41 ± 0.09 mg L^{-1} for NR, NN, SS, and LS, respectively. That C_s was lowest for NN and highest for SS among the four different nanostructures tested is likely due to their different structural morphologies, as manifested by surface curvature, with a smaller radius of positive curvature thermodynamically leading to a higher equilibrium solubility.[271] The overall dissolution observed corresponded to ~4.1-4.9% of the total Zn added and was

comparable to findings reported elsewhere.[284] Recently, Miller et al.[269] have studied the dissolution of ZnO in seawater at four different initial nanoparticle concentrations. Specifically, 100% of the nanoparticles dissolved when the concentration of ZnO was lower than 1 mg L^{-1}, a result similar to an observation reported earlier,[268] whereas about 30% of these nanostructures dissolved at a concentration of 10 mg L^{-1}. It was not surprising that ZnO nanoparticles would continuously dissolve until the solution was saturated and attain dissolution equilibrium. In our study, a concentration of 10-40 mg L^{-1} of ZnO was used to ensure a considerable amount of ZnO, possessing the initial morphology, after the dissolution process.

Structural morphologies of ZnO after exposure to algal cultures after one week were evaluated by TEM, thereby confirming the integrity of ZnO nanoparticles after the dissolution process (Figure 5.4). In spite of the coagulation of nanoparticles due to the presence of organic residue from the algal culture on the ZnO nanostructures, the morphology of individual nanostructures was retained. The observation that the dissolution process did not result in either an overall decrease in the size or a substantial distortion of the shape of nanoparticles can be attributed to the Ostwald ripening phenomenon,[285] which suggests that smaller nanoparticles with higher surface energy thermodynamically dissolve significantly faster than bigger ones. As a result, we hypothesize that the smaller particles present in the ensembles were preferentially dissolved first and contributed a higher fraction to the overall dissolved Zn content present in solution, thereby leading to the preservation of the morphology of the remaining ZnO nanostructures.

We also examined the influence of the initial particle concentration on the dissolution kinetics of ZnO by monitoring the dissolution of 10 mg L^{-1}, 40 mg L^{-1}, and 80 mg L^{-1} of ZnO SS and NN in the medium, respectively. Values for C_s and $t_{1/2}$ for each treatment are summarized in

Table 5.2. For SS, $t_{1/2}$ was calculated to be 0.24 ± 0.15, 0.40 ± 0.28, and 0.35 ± 0.02 h for 10 mg L^{-1}, 40 mg L^{-1}, and 80 mg L^{-1} of ZnO SS, respectively. These results suggested that the dissolution rate was statistically independent of initial particle concentrations over the time scales we tested ($p > 0.05$). In another case, data with ZnO NN, possessing a distinctive one-dimensional structure with a high aspect ratio as opposed to spherical nanoparticles, showed that the initial particle concentration had little impact upon the dissolution rate of ZnO ($p > 0.05$). On the other hand, an increase of the initial ZnO concentration did not result in a significant increase in the amount of zinc ions in solution at equilibrium; this observation can be attributed to the fact that the lowest amount of ZnO added (10 mg L^{-1}) was expected to be higher than the inherent solubility of ZnO (C_s) under the experimental conditions tested. This overall observation was in agreement with other reports that ZnO particle concentrations have little influence upon their dissolution behaviors, as long as the amount of ZnO in the solution is substantially higher than the expected equilibrium value.[270, 274] In fact, the variation of C_s and $t_{1/2}$ between each treatment was well within experimental error and probably due to pH fluctuations in solution.[270]

The explanation for a lack of particle-morphology and particle-concentration dependence of dissolution kinetics of ZnO in our case could lie in the inherent aggregation effect of nanoparticles.[267, 271] As described in the aforementioned discussion, particles without surfactants on their surfaces tend to form aggregates in solution in spite of the variety of morphologies and concentrations tested. As noted from DLS measurements, those aggregates possessing similar sizes and size distributions could yield an overall similar surface area for all types of nanoparticle suspensions. Given that the dissolution rate is highly associated with the diffusion efficiency of dissolved solute, which in fact can be affected by the particle surface area, the

resultant similar surface area of all aggregates can potentially lead to a comparable overall dissolution kinetics among all of the ZnO suspensions analyzed.[271]

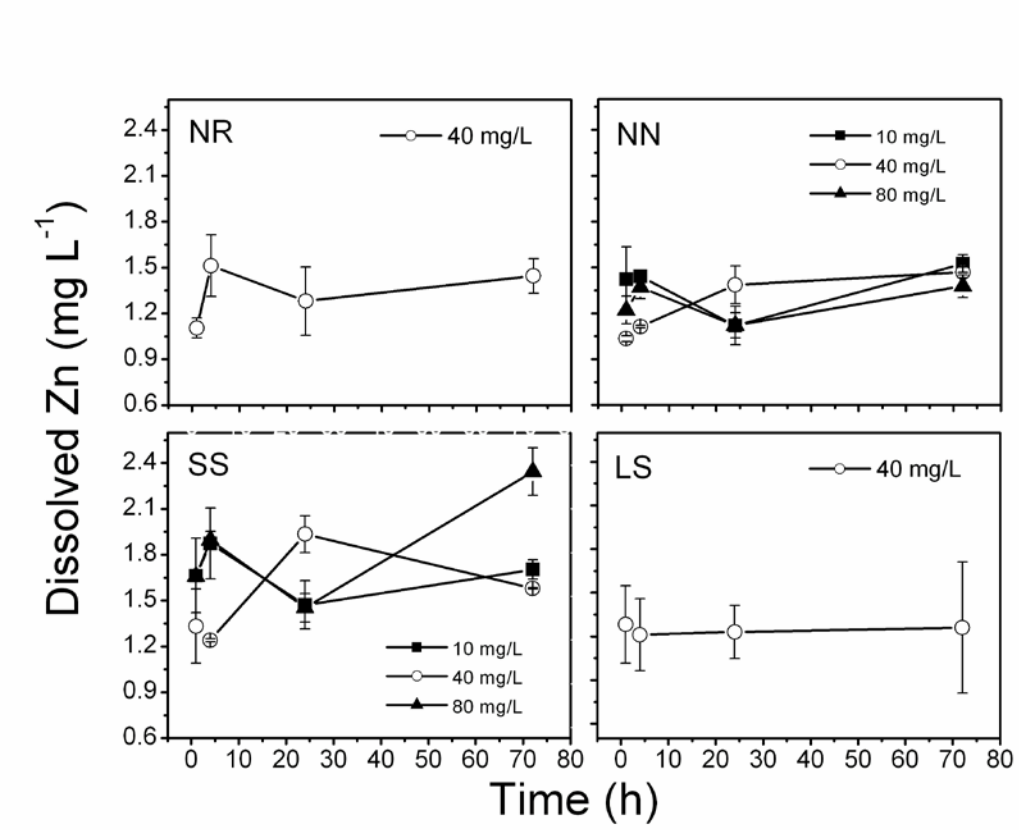

Figure 5.3: Dissolved Zn concentrations (mg L^{-1}) detected using GFAAS upon exposure of seawater to various ZnO nanostructures over time. Data points shown (n = 3) are within 1 SD error bar.

Table 5.2: The solubility of ZnO (C_s) and time for [Zn^{2+}] to reach half of C_s ($t_{1/2}$) in different dissolution experiments undertaken.

[ZnO] (mg L^{-1})	NN		SS	
	C_s (mg L^{-1})	$t_{1/2}$ (h)	C_s (mg L^{-1})	$t_{1/2}$ (h)
10	1.49 (0.03)[a]	0.32 (0.12)	1.79 (0.09)	0.24 (0.15)
40	1.33 (0.06)	0.47 (0.03)	1.59 (0.05)	0.40 (0.28)
80	1.31 (0.06)	0.26 (0.04)	1.93 (0.07)	0.35 (0.02)

[a] Values in parentheses denote 1 standard deviation.

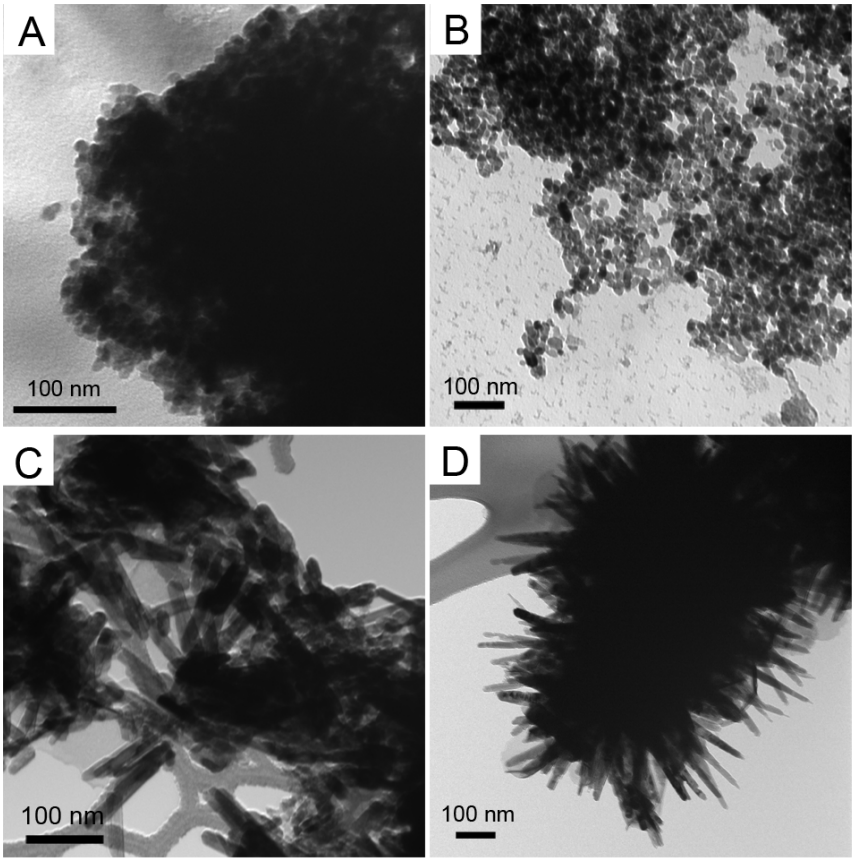

Figure 5.4: TEM images of ZnO nanoparticles possessing different morphologies after incubation with *P. tricornutum* cultures. (A) small spheres, SS; (B) large spheres, LS; (C) nanorods, NR; and (D) nanoneedles, NN.

5.3.3 *Toxicity of ZnO nanoparticles*

Figure 5.5 presents representative growth curves of *T. pseudonana* either with or without exposure to ZnO nanostructures. The log-linear cell division rates, calculated in a 24-72 h time frame (Table 5.3), decreased significantly after exposure to ZnO, regardless of the nanoparticle morphologies and of the initial particle concentration. It is not an unexpected result, given that the concentrations of dissolved Zn (after partial dissolution of the ZnO nanoparticles) are noted to be sufficiently high to interfere with the growth of *T. pseudonana*, according to EC_{50} (0.82 mg L^{-1}) and EC_0 (2.59 mg L^{-1}) values (concentrations leading to depression of cell division rates by 50% and 100%, respectively) reported for similar culture conditions.[281] A similar observation was determined for *C. gracilis*, showing a complete cessation of growth after 24 hours (Figure 5.6 and Table 5.3). Neither particle-concentration nor morphology dependence was observed for *C. gracilis.*

By contrast, *P. tricornutum* in the presence of ZnO nanostructures exhibited continuous growth at a relatively slow rate with respect to the algal cultures without nanoparticles (Figure 5.7). The inter-specific differences in algal sensitivity to ZnO nanoparticles are probably due to structural differences in their biological structures. Specifically, cells of *P. tricornutum* possess frustules that are more lightly silicified than those of the other species; the ash content of these cells contained 9% Si (0.30 pg Si $cell^{-1}$) as compared with 35% Si (1.66 pg Si $cell^{-1}$) for *T. pseudonana* cells.[286] Since Zn and Cu can interfere with diatom growth by disruption of Si uptake and frustule formation,[133] it is possible that *P. tricornutum* can more easily meet its cellular Si requirement than the other diatoms upon exposure to toxic metals. The log-linear cell division rates (Table 5.3) calculated over 72 hours decreased significantly with increasing

particle concentrations for all nanoparticle types, an observation not noted in the case of *T. pseudonana* and *C. gracilis*, as their growth was fully suppressed upon exposure to ZnO nanostructures under all tested concentrations. More importantly, the cell division rates between treatments, in which ZnO nanostructures with different morphologies were added, were significantly different when the particle concentration was $\geq$ 20 mg L^{-1}. Specifically, the inhibition effect on *P. tricornutum* caused by one-dimensional ZnO nanostructures was more substantial than that caused by spherical nanostructures, when the particle concentrations were $\geq$ 40 mg L^{-1} (Figure 5.8).

We have speculated that the morphology and particle-concentration dependence of ZnO toxicity to *P. tricornutum* cannot be solely explained by the presence of dissolved zinc in bulk solution. First, no systematic difference in the dissolution rate of ZnO was found to associate with either distinctive particle morphologies or particle concentrations. Second, we observed that SS particles released more Zn than rod-shaped particles and hence ought to have been more toxic than their NN analogues, which is in fact opposite to the pattern of algal toxicity caused by SS and NN particles. Third, the estimated $t_{1/2}$ suggested that the dissolution of particles occurred within one hour, which is much faster than the diatom cell division rate. Hence, assuming that even if the concentration of dissolved zinc were slightly different over a relatively short time period at the beginning of ZnO dissolution for each treatment, that fact may not be significant enough to result in such a profound difference in algal growth. In fact, the diatoms were likely exposed to about the same amount of dissolved zinc for all of the treatments during their growth. Therefore, we hypothesize that the physical structure of the particles themselves was also a important factor in determining the observed toxicity of ZnO nanoparticles. This hypothesis is

consistent with the observation that the morphology effect associated with ZnO toxicity became more profound with an increase of ZnO concentration.

In order to investigate the direct influence of nanoparticles upon toxicity to *P. tricornutum,* cells were examined by TEM after exposure to ZnO nanostructures for 4 days. For the diatoms growing in the absence of nanoparticles, defined and compact organelles were visible inside the cells possessing a distinctive silicon wall, indicative of healthy cells (Figure 5.9 Inset). By contrast, an internal degradation characterized by a lack of recognizable organelles and damage to the cell walls was observed in samples treated with ZnO nanoparticles. We noted the presence of ZnO aggregates, as indicated by the high-electron-density materials, either closely or directly attached to the cell walls of *P. tricornutum,* whereas ZnO nanoparticles were rarely observed inside the cells themselves (Figure 5.9A-D). However, because of their small size and/or further dissolution of ZnO intracellularly,[287, 288] we cannot completely rule out the possibility that free individual nanoparticles may have entered the cells.

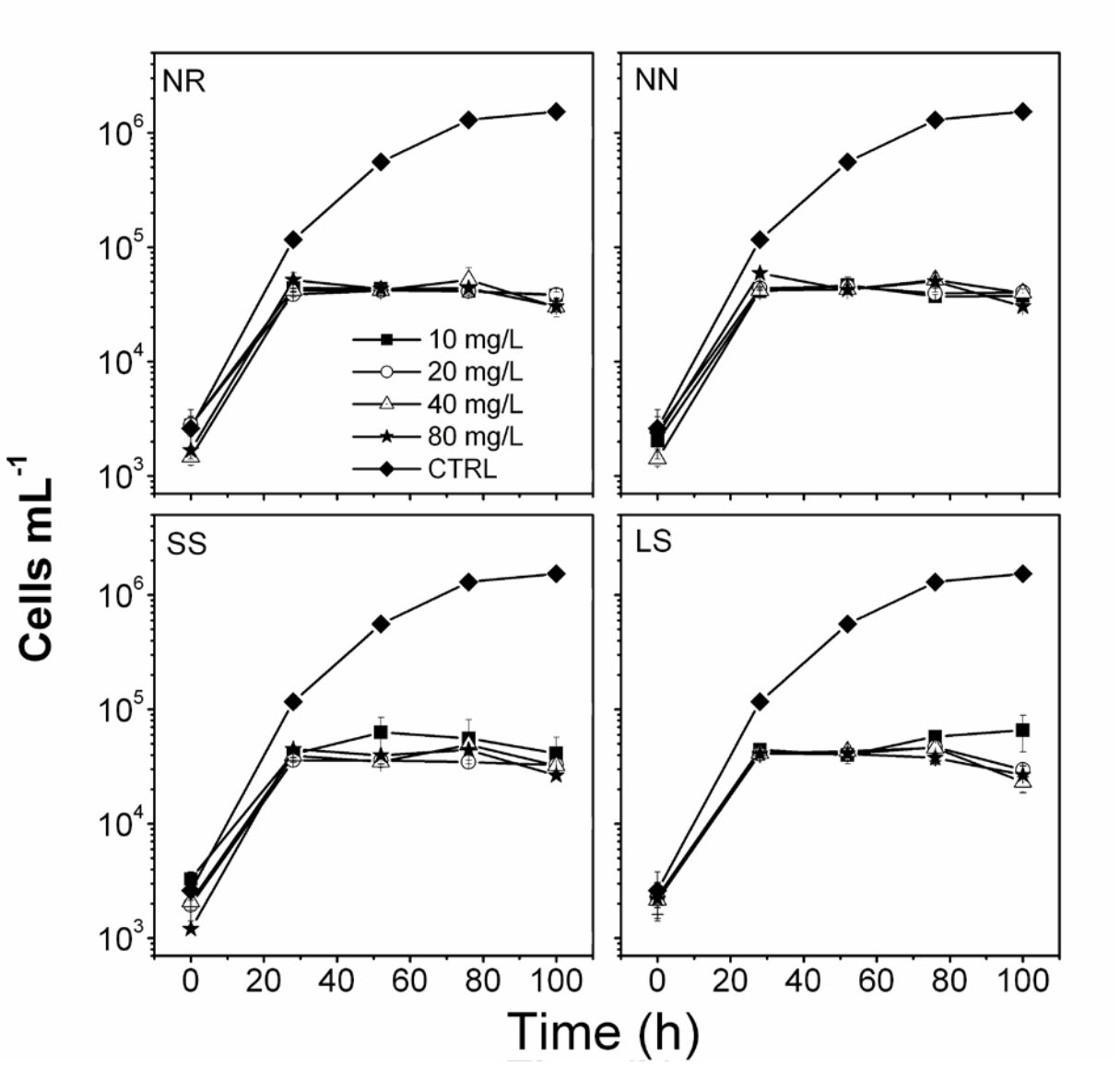

Figure 5.5: Growth of *T. pseudonana* in either the absence (◆) or presence of ZnO nanoparticles with different morphologies at different concentrations. 10 mg L^{-1} (■), 20 mg L^{-1} (○), 40 mg L^{-1} (△), and 80 mg L^{-1} (★), over 100 h.

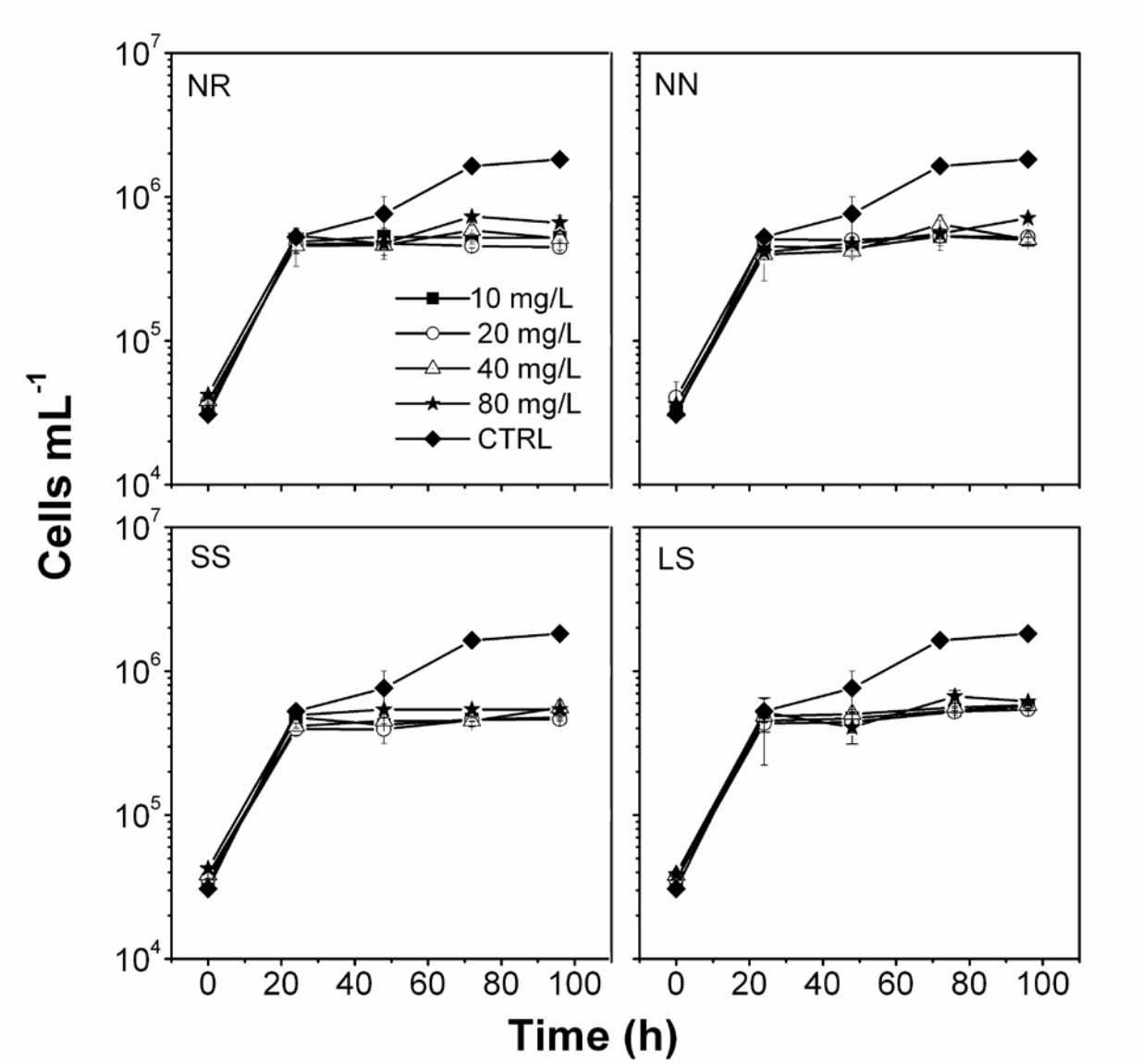

Figure 5.6: Growth of *C. gracilis* in the absence (◆) or presence of ZnO nanoparticles with different morphologies at different concentrations of 10 mg L^{-1} (■), 20 mg L^{-1} (○), 40 mg L^{-1} (△), and 80 mg L^{-1} (★), over 100 h.

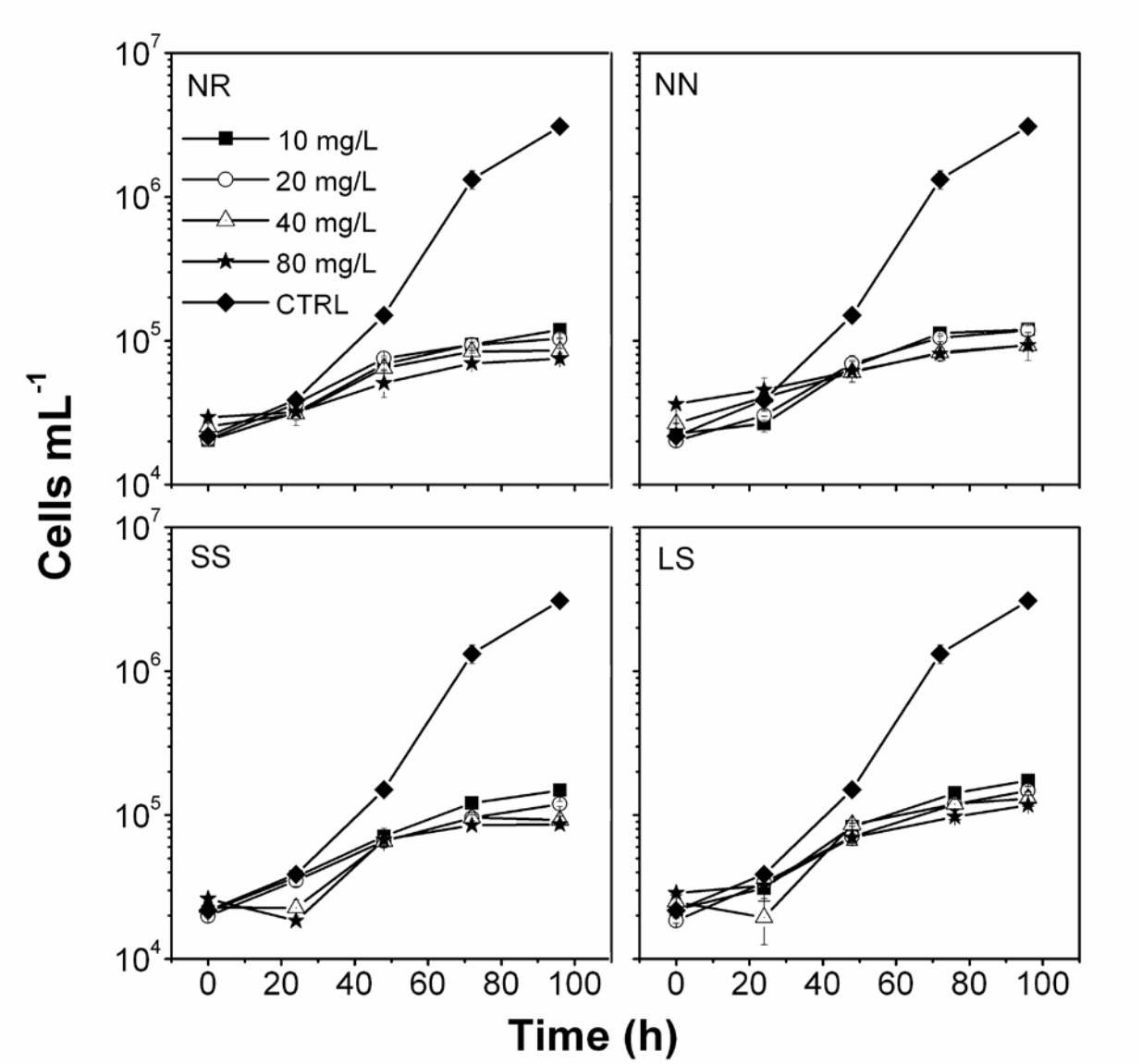

Figure 5.7: Growth of *P. tricornutum* in the absence (◆) or presence of ZnO nanoparticles with different morphologies at different concentrations of 10 mg L^{-1} (■), 20 mg L^{-1} (○), 40 mg L^{-1} (△), and 80 mg L^{-1} (★), over 100 h..

Table 5.3: Log-linear cell division rates (divisions day^{-1}) of *T. pseudonana*, *C. gracilis*, and *P. tricornutum* exposed to ZnO nanostructures at different particle concentrations within a 24-72 hour time frame.

Diatom species	*[ZnO] (mg L^{-1})*	*Control Sample*	*NR*	*NN*	*SS*	*LS*
T. pseudonana	10	1.74 (0.72)[a]	0 (0.04)*	0 (0.36)*	0.23 (0.56)*	0.19 (0.48)*
	20		0.05 (0.10)*	0 (0.16)*	0 (0.03)*	0.10 (0.14)*
	40		0.15 (0.21)*	0.15 (0.18)*	0.16 (0.47)*	0.07 (0.02)
	80		0 (0.20)*	0 (0.51)*	0 (0.24)*	0 (0.07)*
C. gracilis	10	0.82 (0.40)	0.05 (0.09)*	0.12 (0.22)*	0 (0.21)*	0.12 (0.08)*
	20		0 (0.06)*	0.03 (0.07)*	0.11 (0.16)*	0.13 (0.15)*
	40		0.18 (0.24)*	0.35 (0.38)*	0.06 (0.09)*	0.10 (0.08)*
	80		0.22 (0.56)*	0.21 (0.01)*	0.06 (0.09)*	0.19 (0.75)*
P. tricornutum	10	1.97 (0.10)	0.73 (0.09)	0.77 (0.07)	0.84 (0.09)	0.89 (0.03)
	20**		0.72 (0.05)	0.79 (0.02)	0.75 (0.07)	0.89 (0.07)
	40**		0.58 (0.03)	0.54 (0.09)	0.69 (0.02)	0.75 (0.02)
	80**		0.38 (0.07)	0.39 (0.06)	0.57 (0.06)	0.59 (0.02)

[a] Values in parentheses denote the standard deviation.
* The value is not significantly different from 0.
** $p < 0.05$. Division rates between treatments with different particle morphology within the fixed particle concentration are significantly different.

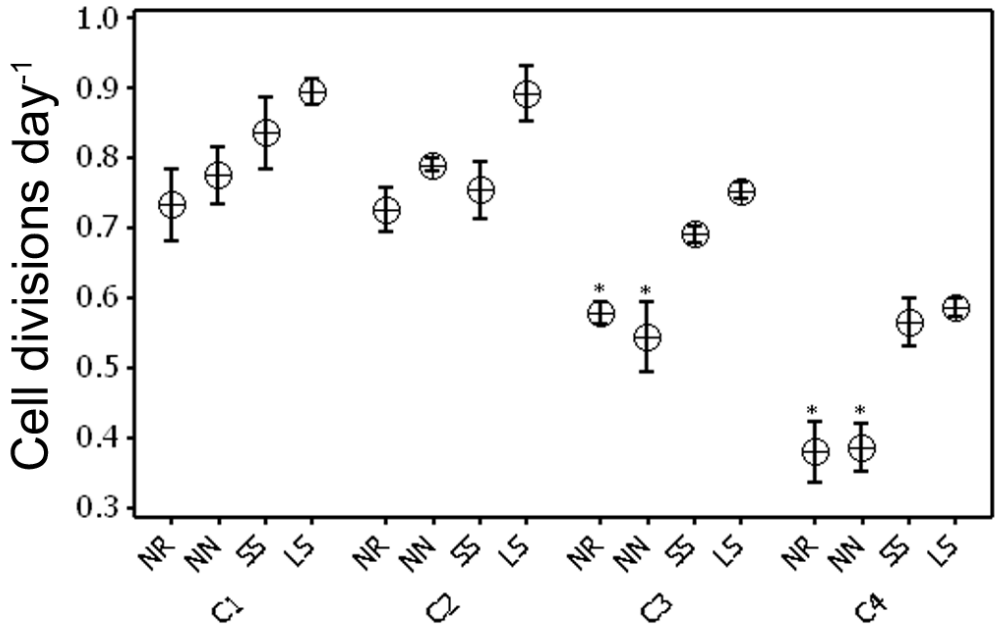

Figure 5.8: Log-linear cell division rate of *P. tricornutum* vs. particle concentration and particle morphology. Data points represent mean values (n = 3) with 1 SD error bars. C1 = ZnO concentration of 10 mg L^{-1}; C2 = 20 mg L^{-1}; C3 = 40 mg L^{-1}; C4 = 80 mg L^{-1}. The division rate of *P. tricornutum* in the absence of nanoparticles is 1.97 ± 0.10 divisions day^{-1}. Asterisk (*) indicates that the division rate is significantly different from that of SS.

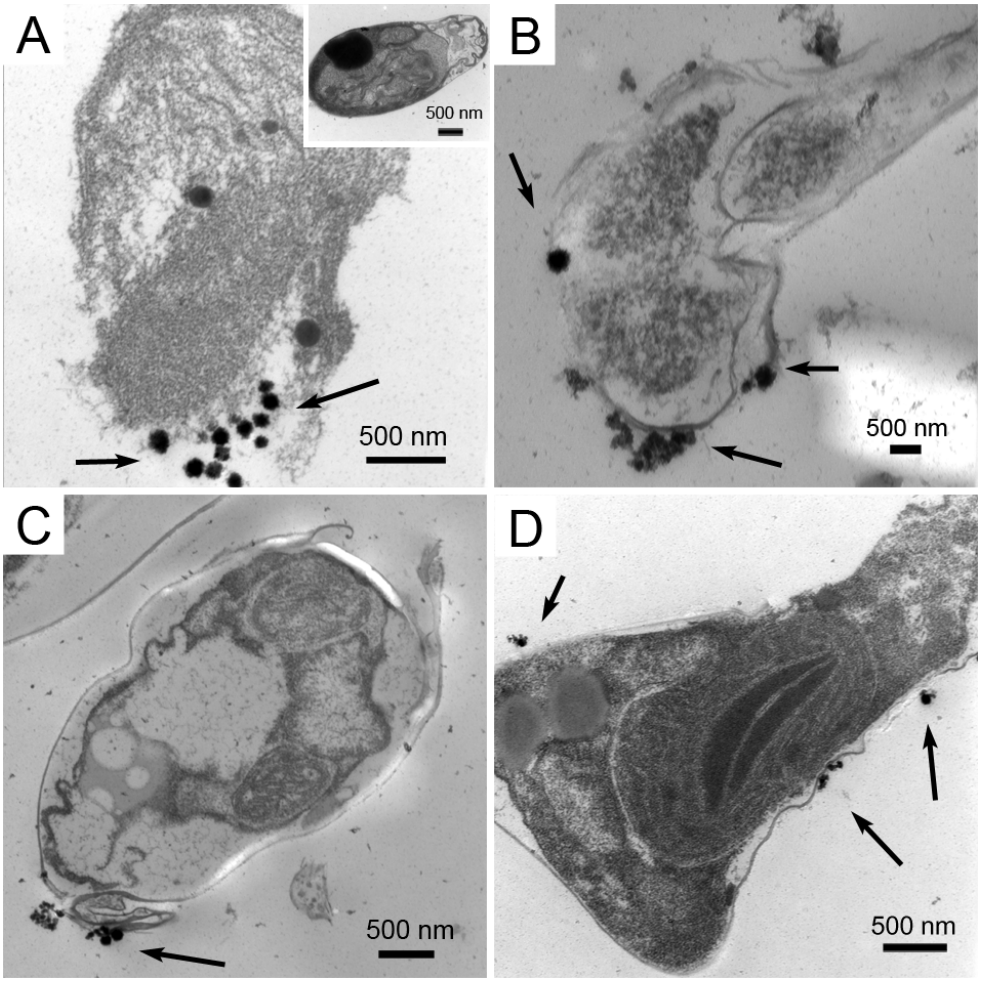

Figure 5.9: TEM images of *P. tricornutum* after exposure to ZnO nanostructures with initial particle concentration of 40 mg L^{-1} over a period of 100 h, (A) NR, (B) NN, (C) SS and (D) LS. The black arrows point to the location of ZnO nanoparticles. Inset is a typical TEM image of *P. tricornutum* growing in the absence of ZnO nanoparticles.

Nonetheless, it is reasonable to infer that the adhesion of nanoparticles onto the diatoms played an essential role in determining the toxicity of ZnO, either by causing mechanical damage[289] or by releasing zinc ions in the vicinity of metal transporting sites on the cell membrane, so as to enhance Zn^{2+} concentration near the cell surface and disrupt cellular metabolic processes. In any event, when the concentration of ZnO was increased, the diatoms were in fact exposed to a higher amount of nanoparticles, thereby enduring more severe damage arising from a physical interaction with the particles than in treatments in which a lower concentration of ZnO was present. Moreover, the morphology effect associated with the toxicity of ZnO revealed that the interaction between each type of ZnO nanoparticles/aggregates and *P. tricornutum* was intrinsically affected by the distinctive particle shape and surface morphology. Specifically, nanoscale ZnO with one-dimensional structures appeared to be more toxic than spheres, in spite of the formation of aggregates, whereas the size of nanoparticles had less influence upon the observed toxic effect. It has been reported that nanomaterials with one-dimensional structures can potentially enter the cell nucleus by penetrating through nucleopores.[263] ZnO nanowires also have been found to locate inside of either phagosomes or lysosomes upon incubation with human monocyte macrophages [287]. However, at this stage, we cannot unambiguously determine the actual mechanism of cellular interaction of ZnO nanoparticles.

Together with the dissolution results, the toxicity of ZnO to *T. pseudonana* and *C. gracilis* was most likely caused by the presence of high dissolved zinc concentrations upon partial dissolution of the ZnO nanoparticles. The cellular accumulation of Zn in *T. pseudonana* was further studied in order to confirm that the amount of dissolved zinc in solution was sufficient to account for the observed depression of cellular growth. After 21 h of exposure to the

radiolabeled ZnO nanoparticles, the concentration of total Zn associated with cells of the diatom, *T. pseudonana,* was 223 amol μm^{-3}, 392 amol μm^{-3}, 314 amol μm^{-3}, and 170 amol μm^{-3} for NR, NN, SS and LS, respectively. These cellular concentrations did not change appreciably over the following 2 days of treatment. The volume/volume concentration factor (VCF) of the Zn associated with these cells was calculated by dividing the Zn concentration in the cells by the dissolved Zn concentration, resulting from dissolution of the ZnO nanoparticles (VCF = mol Zn μm^{-3} cell divided by mol Zn μm^{-3} dissolved in seawater). VCF values were noted to be $10.2 \cdot 10^3$ for NR, $19.1 \cdot 10^3$ for NN, $12.8 \cdot 10^3$ for SS, and $7.8 \cdot 10^3$ for LS, respectively.

These VCF values were comparable with previous findings for Zn in *T. pseudonana* ($12 \cdot 10^3$),[281] suggesting that the Zn dissolution of the nanoparticles could be sufficient to account for all of the Zn uptake observed for these diatoms. Importantly, the cellular Zn concentrations present exceeded the Zn concentrations necessary to depress log-linear cell division rates in this species by 50% (EC_{50}, 16 amol μm^{-3}) and 100% (40 amol μm^{-3}), respectively.[281] In essence, the Zn uptake by *T. pseudonana* in the cultures exposed to the various nanoparticles exceeded sublethal and lethal doses by more than an order of magnitude, thereby accounting for the cessation of growth in this species. A similar argument has been made by Pipan-Tkalec et al. [290] who studied the bioaccumulation of Zn in isopods, exposed to ZnO nanoparticles. However, as noted for *P. tricornutum*, the Zn associated with these cells could be attributed to the presence of both ZnO particles/aggregates as well as to soluble zinc ions. Therefore, we could not fully exclude the possibility that the presence of ZnO aggregates on the cell surface may have also contributed to the depression of algal growth through the release of zinc ions.

5.4 Conclusions

In conclusion, the dissolution of ZnO nanostructures in our medium was found to occur within hours and to be essentially independent of either nanoparticle morphology or particle concentration. The lack of a particle concentration and morphology dependence of ZnO nanoparticle dissolution could be attributed to the aggregation effect, which inherently altered the surface area of nanoparticles in solution. The complete suppression of growth in *T. pseudonana* and *C. gracilis* could be explained solely on the basis of Zn dissolution since the lowest concentration of ZnO used (10 mg L^{-1}) released sufficient Zn ions to be acutely toxic to these cells. The more lightly silicified diatom, *P. triocornutum*, was less affected by the presence of Zn released into the aqueous phase, possibly because it required lower amounts of Si. For this diatom, the adverse growth effect induced by ZnO nanoparticles was found to be influenced by both particle concentration and morphology, wherein one-dimensional structures evinced greater toxicity. The overall results from this study suggest that not only dissolved zinc ions but also the nanoparticles themselves need to be carefully assessed in order to determine the specific toxicity of ZnO to marine organisms.

5.5 References

124. C. Ispas, D. Andreescu, A. Patel, D. V. Goia, S. Andreescu and K. N. Wallace, *Environmental Science & Technology*, **2009**, *43*, 6349-6356.

125. C. Carlson, S. M. Hussain, A. M. Schrand, L. K. Braydich-Stolle, K. L. Hess, R. L. Jones and J. J. Schlager, *Journal of Physical Chemistry B*, **2008**, *112*, 13608-13619.

126. A. Simon-Deckers, S. Loo, M. Mayne-L'Hermite, N. Herlin-Boime, N. Menguy, C. Reynaud, B. Gouget and M. Carriere, *Environmental Science & Technology*, **2009**, *43*, 8423-8429.

128. T. Mironava, M. Hadjiargyrou, M. Simon, V. Jurukovski and M. H. Rafailovich, *Nanotoxicology*, **2010**, *4*, 120-137.

133. N. S. Fisher, G. J. Jones and D. M. Nelson, *Journal of Experimental Marine Biology and Ecology*, **1981**, *51*, 37-56.

140. V. Aruoja, H. C. Dubourguier, K. Kasemets and A. Kahru, *Science of the Total Environment*, **2009**, *407*, 1461-1468.

262. J. L. Elechiguerra, J. L. Burt, J. R. Morones, A. Camacho-Bragado, X. Gao, H. H. Lara and M. J. Yacaman, *Journal of nanobiotechnology*, **2005**, *3*, 6.

263. H. Yang, C. Liu, D. F. Yang, H. S. Zhang and Z. G. Xi, *Journal of Applied Toxicology*, **2009**, *29*, 69-78.

264. R. F. Hamilton, N. Q. Wu, D. Porter, M. Buford, M. Wolfarth and A. Holian, *Particle and Fibre Toxicology*, **2009**, *6*, 35.

265. J. Chen, H. Zhou, A. C. Santulli and S. S. Wong, *Chemical Research in Toxicology*, **2010**, *23*, 871-879.

266. M. J. Osmond and M. J. McCall, *Nanotoxicology*, **2010**, *4*, 15-41.

267. N. M. Franklin, N. J. Rogers, S. C. Apte, G. E. Batley, G. E. Gadd and P. S. Casey, *Environmental Science & Technology*, **2007**, *41*, 8484-8490.

268. M. Heinlaan, A. Ivask, I. Blinova, H. C. Dubourguier and A. Kahru, *Chemosphere*, **2008**, *71*, 1308-1316.

269. R. J. Miller, H. S. Lenihan, E. B. Muller, N. Tseng, S. K. Hanna and A. A. Keller, *Environmental Science & Technology*, **2010**, *44*, 7329-7334.

270. A.-J. Miao, X.-Y. Zhang, Z. Luo, C.-S. Chen, W.-C. Chin, P. H. Santschi and A. Quigg, *Environ Toxicol Chem*, **2010**, *29*, 2814-2822.

271. P. Borm, F. C. Klaessig, T. D. Landry, B. Moudgil, J. Pauluhn, K. Thomas, R. Trottier and S. Wood, *Toxicological Sciences*, **2006**, *90*, 23-32.

272. Z. Chen, M. Waje, W. Li and Y. Yan, *Angewandte Chemie International Edition*, **2007**, *46*, 4060-4063.

273. E. A. Meulenkamp, *Journal of Physical Chemistry B*, **1998**, *102*, 7764-7769.

274. X. S. Zhu, J. X. Wang, X. Z. Zhang, Y. Chang and Y. S. Chen, *Nanotechnology*, **2009**, *20*, 195103.

275. W. Jiang, H. Mashayekhi and B. S. Xing, *Environmental Pollution*, **2009**, *157*, 1619-1625.

276. R. Brayner, R. Ferrari-Iliou, N. Brivois, S. Djediat, M. F. Benedetti and F. Fievet, *Nano Letters*, **2006**, *6*, 866-870.

277. C. Pacholski, A. Kornowski and H. Weller, *Angewandte Chemie International Edition*, **2002**, *41*, 1188-1191.

278. B. Liu and H. C. Zeng, *Langmuir*, **2004**, *20*, 4196-4204.

279. S. Nair, A. Sasidharan, V. V. D. Rani, D. Menon, S. Nair, K. Manzoor and S. Raina, *Journal of Materials Science: Materials in Medicine*, **2009**, *20*, 235-241.

280. R. R. Guillard and J. H. Ryther, *Canadian Journal of Microbiology*, **1962**, *8*, 229-239.

281. N. S. Fisher, M. Bohe and J. L. Teyssie, *Marine Ecology-Progress Series*, **1984**, *18*, 201-213.

282. L. K. Adams, D. Y. Lyon and P. J. J. Alvarez, *Water Research*, **2006**, *40*, 3527-3532.

283. P. Costa, J. Manuel and S. Lobo, *European Journal of Pharmaceutical Sciences*, **2001**, *13*, 123-133.

284. S. W. Y. Wong, P. T. Y. Leung, A. B. Djurisic and K. M. Y. Leung, *Analytical and Bioanalytical Chemistry*, **2010**, *396*, 609-618.

285. E. M. Wong, J. E. Bonevich and P. C. Searson, *Journal of Physical Chemistry B*, **1998**, *102*, 7770-7775.

286. N. S. Fisher, R. R. L. Guillard and D. C. Bankston, *Journal of Marine Research*, **1991**, *49*, 339-354.

287. K. H. Müller, J. Kulkarni, M. Motskin, A. Goode, P. Winship, J. N. Skepper, M. P. Ryan and A. E. Porter, *ACS Nano*, **2010**, *4*, 6767-6779.

288. T. Xia, M. Kovochich, M. Liong, L. Madler, B. Gilbert, H. B. Shi, J. I. Yeh, J. I. Zink and A. E. Nel, *ACS Nano*, **2008**, *2*, 2121-2134.

289. D. H. Lin and B. S. Xing, *Environmental Science & Technology*, **2008**, *42*, 5580-5585.

290. Z. Pipan-Tkalec, D. Drobne, A. Jemec, T. Romih, P. Zidar and M. Bele, *Toxicology*, **2010**, *269*, 198-203.

Chapter 6 Conclusions

Nanostructured materials have drawn research attention because of their unique and interesting electronic, optical, magnetic and catalytic properties, which are distinctive from their bulk counterparts. Numerous studies have unarguably implied that nanotechnology can potentially bring about revolutionary improvements in a wide variety of areas including catalysis, electronics, and renewable energy. For example, in the context of the exploitation of solar energy, the maximum theoretical efficiency of a standard silicon solar cell in use today is limited to ~31%, in part because of the loss of any photon energy that exceeds the semiconductor band gap. By contrast, the use of quantum dots can potentially increase the efficiency up to 66% due to the possibility of a multiexciton generation process and the exploitation of hot charge carriers as a result of the quantum confinement effect.[291, 292]

Despite the great promise of nanostructured materials in the application of photovoltaics, one of the main challenges in this field has been the need to rationally design and precisely fabricate nanostructured materials, especially heterostructures consisting of components with two or more distinctive chemical compositions, with precise control over chemical composition and physical dimensionality by facile, low-cost, and versatile approaches. Apart from materials' fabrication, a fundamental understanding of the electronic and optical properties of those nanostructures has become a more pressing concerning. In particular, unambiguously unraveling the underlying mechanisms of opto-electronic interactions between each component within a discrete multidimensional structure is crucial for providing valuable insight into the development

and construction of heterostructured assemblies as potential building blocks for highly efficient photovoltaic devices.

Hence, the synthesis and characterization of various nanoscale heterostructures along with the investigation of their novel properties for their potential applicability in energy conversion processes have been the focal point of my graduate study, as summarized in Figure 6.1. Specifically, the synthesis of carbon nanotube – nanocrystal heterostructures consisting one or more type of nanocrystals by covalent approaches was demonstrated in Chapter 2. A number of reaction conditions were extensively explored to reveal the potential for a rigorous and quantifiable correlation between the chemical treatment used and the resulting density and spatial distribution of nanoparticles/QDs on the CNT surfaces. In addition, the investigation of the optical properties of the quantum dots on the scaffold of CNTs has been described in detail in Chapter 3, highlighting the importance of the nature of the molecular linkers on the resulting charge transfer efficiency; the molecular linkers are crucial because of their chemical functionality in assembling the heterostructure as well as their electronic functionality by providing a discrete intermediate state. In Chapter 4, the fabrication of metal-oxide-based coaxial nanofibers by co-axial electrospinning has been successfully demonstrated, showing the potential advantages in energy conversion applications of combining both heterojunction chemistry as well as one-dimensional tubular structural motifs. Moreover, the morphology dependence of the toxicity of ZnO nanostructures to marine diatoms has been elucidated in Chapter 5, suggesting that the potential toxicological risk of nanostructures needs to be comprehensively assessed prior to their widespread use in a number of commercialized industrial applications.

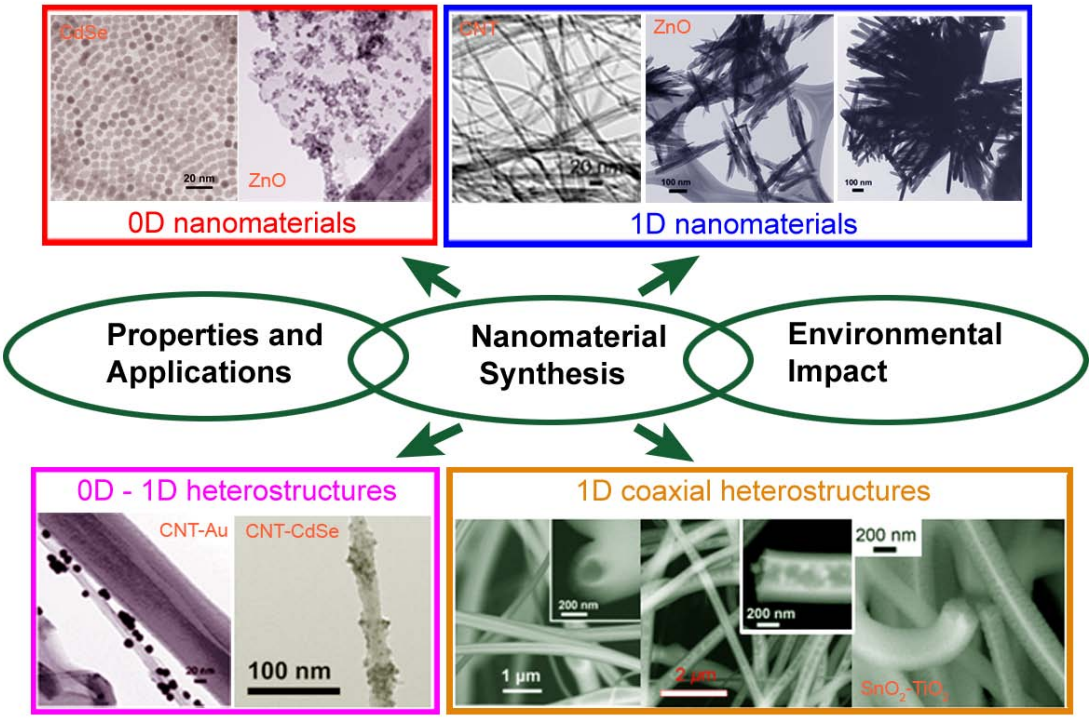

Figure 6.1: Representative electron microscopy images of various nanoscale materials and complex heterostructures.

With the emergence of nanotechnology and the ever-increasing demand for nanostructured materials for a host of applications, there has been a very pressing need to develop environmentally friendly and energy-efficient synthetic methods for the rational, controllable synthesis of nanomaterials. In our study, some limitations still exist in the chemical solution approach used for the synthesis of carbon nanotube – nanocrystal heterostructures, including (1) insufficient control over the uniformity in terms of the spatial distribution of nanocrystals on the nanotube surface, (2) the requirement of additional organic reagents in order to facilitate the reaction rate, and (3) the need for post-washing steps in order to separate the product from the reaction medium. However, our method offers the advantages of conducting all of these reactions under ambient conditions without relying on either vacuum or complex experimental protocols involving steps such as heating or the external application of electric and magnetic force fields. At the same time, we have demonstrated a high capability of controlling the spatial location and density of attached nanocrystals. On the other hand, the “green” merit of the electrospinning process, used for the fabrication of high-quality one-dimensional nanostructures in our study, lies in (1) the generation of few if any byproducts or hazardous wastes during the production process and (2) flexibility in terms of the choice of precursor materials, thereby allowing for the substitution of toxic reagents with more environmentally benign chemical alternatives. Indeed, it cannot be overemphasized that in addition to the development of facile and “green” techniques, substituting conventional toxic reagents and solvents with significantly safer replacements, including but not limited to biological reagents and ionic liquids, represents an alternative towards “green” synthesis.

In order to shed light on the charge/energy flow pathways, we have attempted to understand carrier dynamics in our multidimensional heterostructures by state-of-the art

instrumental techniques, such as time-resolved photoluminescence measurements. The different optical signatures we have observed for analogous heterostructures comprised of different chemical components (e.g. CdSe and CdSe/ZnS) reveal that the interfacial electronic interaction is fundamentally correlated with materials' composition as well as surface chemistry. We believe that the lessons learned from the photophysics of these CNT–QD heterostructures can be applied in general to the production of multidimensional device assemblies incorporating nanostructured semiconducting chromophores. A deeper understanding of the structure-property relationship will provide more valuable insights into the interfacial interactions between each component, so that we can more readily construct these types of heterostructured architectures with predictable properties in a rational manner.

In addition to these interfacial properties, we note that the surface properties and overall morphology of heterostructures can also play a key role in affecting their interactions with other components when they are incorporated into functional devices. For example, in our study, the surface area of one-dimensional heterostructures fabricated by electrospinning could be increased either by introducing the tubular structural motif or by modifying solution parameters (e.g. precursor and/or polymer concentration). In particular, the unique tubular heterostructures developed in our study, which possess hollow channels as well as a large-and-stable interface, can open up new opportunities for research in a host of various applications. Due to their versatility, methodologies based on the electrospinning technique established in our study can be exploited for many other systems, thereby providing unlimited possibilities for producing useful and interesting heterostructures for a wide variety of applications.

While improvements in energy conversion efficiency by the exploitation of heterostructures can be realized by efficient charge separation, several issues cannot be ignored

in achieving the construction of functional photovoltaic devices. For example, as we have noted, even though the surface modification of quantum dots can improve the electronic coupling between quantum dots themselves, or between quantum dots and energy/charge acceptors, the exciton lifetime and quantum yield can be also substantially undermined at the same time. Specifically, the poor passivation of the QD surface can increase the amount of surface states that act as recombination centers and decrease the chemical stability of quantum dots. Therefore, an appropriate chemical modification of quantum dots is also critical for improvement of the overall device performance. In addition, unexpected doping may occur when the heterojunction is formed between two elementally distinctive but chemically similar components. In particular, ion diffusion and subsequent doping effects during the processing step may result in the formation of undesired crystal phases or compounds, of which the advantageous electronic and optical properties are either significantly impaired or even diminished completely. Such adverse effects should be minimized and need additional investigation.

We are also aware that even though the use of nanoscale materials can lead to significant improvements in technologies for protecting the environment, including the areas of renewable energy and remediation of environmental contaminants, the novel characteristics of nanotechnology-related products in general may lead to unforeseen environmental problems. For instance, manufactured nanomaterials might pose risks to human health and other organisms due to their chemical composition, reactivity as well as unique size and shape. Our study implies that apart from the inherent dissolution of materials, possible aggregation effects, the actual morphology of materials, and the resulting surface topography of aggregates also contribute significantly to the potential toxicity of nanomaterials. Hence, a life-cycle risk assessment of nanotechnology-based devices is also important, especially when it comes to inevitable waste

disposal issues. In particular, the environmental risk of quantum dots and carbon-based nanostructures (e.g. fullerene, carbon nanotubes and graphene) needs comprehensive examination before they can be effectively utilized in the development of renewable energy.

Apart from 0D – 1D and 1D coaxial heterostructures we have explored in this dissertation, there are many other different types of heterostructures (e.g. 0D – 0D, 0D – 2D and 1D – 2D) that can be exploited for applications related to energy conversion. Future work will continue to focus on the development of rational synthetic strategies and fundamental property investigations. Efforts will be extended in particular towards the design and fabrication of photovoltaic devices based on the heterostructures we have either prepared or will develop according to the knowledge we and others have gained in the research.

References

291. M. C. Hanna and A. J. Nozik, *Journal of Applied Physics*, **2006**, *100*, 074510.

292. R. T. Ross and A. J. Nozik, *Journal of Applied Physics*, **1982**, *53*, 3813-3818.

References

1. G. W. Crabtree and N. S. Lewis, *Physics Today*, **2007**, *60*, 37-42.
2. M. Gratzel, *Inorganic Chemistry*, **2005**, *44*, 6841-6851.
3. U. Bach, D. Lupo, P. Comte, J. E. Moser, F. Weissortel, J. Salbeck, H. Spreitzer and M. Gratzel, *Nature*, **1998**, *395*, 583-585.
4. A. Hagfeldt, G. Boschloo, L. Sun, L. Kloo and H. Pettersson, *Chemical Reviews*, **2010**, *110*, 6595-6663.
5. G. Yu, J. Gao, J. C. Hummelen, F. Wudl and A. J. Heeger, *Science*, **1995**, *270*, 1789-1791.
6. W. U. Huynh, J. J. Dittmer and A. P. Alivisatos, *Science*, **2002**, *295*, 2425-2427.
7. R. Rossetti, S. Nakahara and L. E. Brus, *Journal of Chemical Physics*, **1983**, *79*, 1086-1088.
8. X. Peng, J. Wickham and A. P. Alivisatos, *Journal of the American Chemical Society*, **1998**, *120*, 5343-5344.
9. Z. A. Peng and X. G. Peng, *Journal of the American Chemical Society*, **2001**, *123*, 183-184.
10. Z. A. Peng and X. G. Peng, *Journal of the American Chemical Society*, **2002**, *124*, 3343-3353.
11. L. H. Qu and X. G. Peng, *Journal of the American Chemical Society*, **2002**, *124*, 2049-2055.
12. W. W. Yu, L. H. Qu, W. Z. Guo and X. G. Peng, *Chemistry of Materials*, **2003**, *15*, 2854-2860.
13. L. H. Qu, Z. A. Peng and X. G. Peng, *Nano Letters*, **2001**, *1*, 333-337.

14. W. W. Yu, Y. A. Wang and X. G. Peng, *Chemistry of Materials*, **2003**, *15*, 4300-4308.

15. J. S. Owen, E. M. Chan, H. Liu and A. P. Alivisatos, *Journal of the American Chemical Society*, **2010**, *132*, 18206-18213.

16. H. Liu, J. S. Owen and A. P. Alivisatos, *Journal of the American Chemical Society*, **2007**, *129*, 305-312.

17. C. B. Murray, C. R. Kagan and M. G. Bawendi, *Annual Review of Materials Science*, **2000**, *30*, 545-610.

18. A. M. Smith and S. M. Nie, *Accounts of Chemical Research*, **2010**, *43*, 190-200.

19. J. Z. Zhang, *Journal of Physical Chemistry B*, **2000**, *104*, 7239-7253.

20. W. A. Tisdale, K. J. Williams, B. A. Timp, D. J. Norris, E. S. Aydil and X. Y. Zhu, *Science*, **2010**, *328*, 1543-1547.

21. P. Guyot-Sionnest, M. Shim, C. Matranga and M. Hines, *Physical Review B*, **1999**, *60*, R2181-R2184.

22. T. C. Kippeny, M. J. Bowers, A. D. Dukes, J. R. McBride, R. L. Orndorff, M. D. Garrett and S. J. Rosenthal, *Journal of Chemical Physics*, **2008**, *128*, 084713.

23. M. Kuno, J. K. Lee, B. O. Dabbousi, F. V. Mikulec and M. G. Bawendi, *Journal of Chemical Physics*, **1997**, *106*, 9869-9882.

24. N. Y. Morgan, C. A. Leatherdale, M. Drndicacute, M. V. Jarosz, M. A. Kastner and M. Bawendi, *Physical Review B*, **2002**, *66*, 075339.

25. D. V. Talapin, J.-S. Lee, M. V. Kovalenko and E. V. Shevchenko, *Chemical Reviews*, **2009**, *110*, 389-458.

26. K. E. Knowles, D. B. Tice, E. A. McArthur, G. C. Solomon and E. A. Weiss, *Journal of the American Chemical Society*, **2009**, *132*, 1041-1050.

27. F. Dong, H. Y. Han, J. G. Liang and D. L. Lu, *Luminescence*, **2008**, *23*, 321-326.

28. S. Jeong, M. Achermann, J. Nanda, S. Ivanov, V. I. Klimov and J. A. Hollingsworth, *Journal of the American Chemical Society*, **2005**, *127*, 10126-10127.

29. M. A. Hines and P. Guyot-Sionnest, *Journal of Physical Chemistry*, **1996**, *100*, 468-471.

30. P. Reiss, M. Protiere and L. Li, *Small*, **2009**, *5*, 154-168.

31. A. J. Nozik, M. C. Beard, J. M. Luther, M. Law, R. J. Ellingson and J. C. Johnson, *Chemical Reviews*, **2010**, *110*, 6873-6890.

32. J. M. Luther, M. Law, M. C. Beard, Q. Song, M. O. Reese, R. J. Ellingson and A. J. Nozik, *Nano Letters*, **2008**, *8*, 3488-3492.

33. S.-Q. Fan, D. Kim, J.-J. Kim, D. W. Jung, S. O. Kang and J. Ko, *Electrochemistry Communications*, **2009**, *11*, 1337-1339.

34. Y. N. Xia, P. D. Yang, Y. G. Sun, Y. Y. Wu, B. Mayers, B. Gates, Y. D. Yin, F. Kim and Y. Q. Yan, *Advanced Materials*, **2003**, *15*, 353-389.

35. M. Law, L. E. Greene, J. C. Johnson, R. Saykally and P. D. Yang, *Nature Materials*, **2005**, *4*, 455-459.

36. Z. Y. Fan, H. Razavi, J. W. Do, A. Moriwaki, O. Ergen, Y. L. Chueh, P. W. Leu, J. C. Ho, T. Takahashi, L. A. Reichertz, S. Neale, K. Yu, M. Wu, J. W. Ager and A. Javey, *Nature Materials*, **2009**, *8*, 648-653.

37. S. Iijima, *Nature*, **1991**, *354*, 56-58.

38. S. Banerjee, T. Hemraj-Benny and S. S. Wong, *Advanced Materials*, **2005**, *17*, 17-29.

39. X. H. Peng and S. S. Wong, *Advanced Materials*, **2009**, *21*, 625-642.

40. M. Zheng, A. Jagota, M. S. Strano, A. P. Santos, P. Barone, S. G. Chou, B. A. Diner, M. S. Dresselhaus, R. S. McLean, G. B. Onoa, G. G. Samsonidze, E. D. Semke, M. Usrey and D. J. Walls, *Science*, **2003**, *302*, 1545-1548.

41. Y. B. Zhang, M. Kanungo, A. J. Ho, P. Freimuth, D. van der Lelie, M. Chen, S. M. Khamis, S. S. Datta, A. T. C. Johnson, J. A. Misewich and S. S. Wong, *Nano Letters*, **2007**, *7*, 3086-3091.

42. M. Alvaro, C. Aprile, B. Ferrer and H. Garcia, *Journal of the American Chemical Society*, **2007**, *129*, 5647-5655.

43. H. M. Li, F. O. Cheng, A. M. Duft and A. Adronov, *Journal of the American Chemical Society*, **2005**, *127*, 14518-14524.

44. N. W. S. Kam, T. C. Jessop, P. A. Wender and H. J. Dai, *Journal of the American Chemical Society*, **2004**, *126*, 6850-6851.

45. C. A. Dyke and J. M. Tour, *Journal of the American Chemical Society*, **2003**, *125*, 1156-1157.

46. J. L. Delgado, P. de la Cruz, F. Langa, A. Urbina, J. Casado and J. T. L. Navarrete, *Chemical Communications*, **2004**, 1734-1735.

47. T. Hemraj-Benny and S. S. Wong, *Chemistry of Materials*, **2006**, *18*, 4827-4839.

48. W. Zhang and T. M. Swager, *Journal of the American Chemical Society*, **2007**, *129*, 7714-7715.

49. D. Pantarotto, C. D. Partidos, R. Graff, J. Hoebeke, J. P. Briand, M. Prato and A. Bianco, *Journal of the American Chemical Society*, **2003**, *125*, 6160-6164.

50. J. J. Ge, H. Q. Hou, Q. Li, M. J. Graham, A. Greiner, D. H. Reneker, F. W. Harris and S. Z. D. Cheng, *Journal of the American Chemical Society*, **2004**, *126*, 15754-15761.

51. T. Durkop, S. A. Getty, E. Cobas and M. S. Fuhrer, *Nano Letters*, **2004**, *4*, 35-39.

52. S. Berson, R. de Bettignies, S. Bailly, S. Guillerez and B. Jousselme, *Advanced Functional Materials*, **2007**, *17*, 3363-3370.

53. I. Khatri, S. Adhikari, H. R. Aryal, T. Soga, T. Jimbo and M. Umeno, *Applied Physics Letters*, **2009**, *94*, 093509.

54. D. S. Hecht, L. B. Hu and G. Irvin, *Advanced Materials*, **2011**, *23*, 1482-1513.

55. Z. C. Wu, Z. H. Chen, X. Du, J. M. Logan, J. Sippel, M. Nikolou, K. Kamaras, J. R. Reynolds, D. B. Tanner, A. F. Hebard and A. G. Rinzler, *Science*, **2004**, *305*, 1273-1276.

56. T. M. Barnes, J. D. Bergeson, R. C. Tenent, B. A. Larsen, G. Teeter, K. M. Jones, J. L. Blackburn and J. van de Lagemaat, *Applied Physics Letters*, **2010**, *96*, 243309.

57. B. Pradhan, S. K. Batabyal and A. J. Pal, *Applied Physics Letters*, **2006**, *88*, 093106.

58. M. S. Arnold, J. D. Zimmerman, C. K. Renshaw, X. Xu, R. R. Lunt, C. M. Austin and S. R. Forrest, *Nano Letters*, **2009**, *9*, 3354-3358.

59. A. J. Ferguson, J. L. Blackburn, J. M. Holt, N. Kopidakis, R. C. Tenent, T. M. Barnes, M. J. Heben and G. Rumbles, *Journal of Physical Chemistry Letters*, **2010**, *1*, 2406-2411.

60. T. Hasobe, S. Fukuzumi and P. V. Kamat, *Journal of Physical Chemistry B*, **2006**, *110*, 25477-25484.

61. M. H. Ham, G. L. C. Paulus, C. Y. Lee, C. Song, K. Kalantar-zadeh, W. Choi, J. H. Han and M. S. Strano, *Acs Nano*, **2010**, *4*, 6251-6259.

62. E. Shafran, B. D. Mangum and J. M. Gerton, *Nano Letters*, **2010**, *10*, 4049-4054.

63. A. Kongkanand, K. Tvrdy, K. Takechi, M. Kuno and P. V. Kamat, *Journal of the American Chemical Society*, **2008**, *130*, 4007-4015.

64. G. Girishkumar, M. Rettker, R. Underhile, D. Binz, K. Vinodgopal, P. McGinn and P. Kamat, *Langmuir*, **2005**, *21*, 8487-8494.

65. A. Kongkanand, K. Vinodgopal, S. Kuwabata and P. V. Kamat, *Journal of Physical Chemistry B*, **2006**, *110*, 16185-16188.

66. G. G. Wildgoose, C. E. Banks and R. G. Compton, *Small*, **2006**, *2*, 182-193.

67. A. Star, V. Joshi, S. Skarupo, D. Thomas and J.-C. P. Gabriel, *The Journal of Physical Chemistry B*, **2006**, *110*, 21014-21020.

68. N. Jia, Q. Lian, H. Shen, C. Wang, X. Li and Z. Yang, *Nano Letters*, **2007**, *7*, 2976-2980.

69. K. Kostarelos, L. Lacerda, G. Pastorin, W. Wu, S. Wieckowski, J. Luangsivilay, S. Godefroy, D. Pantarotto, J. P. Briand, S. Muller, M. Prato and A. Bianco, *Nature Nanotechnology*, **2007**, *2*, 108-113.

70. D. M. Guldi, G. M. A. Rahman, V. Sgobba, N. A. Kotov, D. Bonifazi and M. Prato, *J. Am. Chem. Soc.*, **2006**, *128*, 2315-2323.

71. L. Sheeney-Haj-Khia, B. Basnar and I. Willner, *Angewandte Chemie-International Edition*, **2005**, *44*, 78-83.

72. C. Schulz-Drost, V. Sgobba, C. Gerhards, S. Leubner, R. M. K. Calderon, A. Ruland and D. M. Guldi, *Angewandte Chemie-International Edition*, **2010**, *49*, 6425-6429.

73. B. R. Azamian, K. S. Coleman, J. J. Davis, N. Hanson and M. L. H. Green, *Chemical Communications*, **2002**, 366-367.

74. S. Banerjee and S. S. Wong, *Nano Letters*, **2002**, *2*, 195-200.

75. S. Ravindran, K. N. Bozhilov and C. S. Ozkan, *Carbon*, **2004**, *42*, 1537-1542.

76. L. Hu, Y. L. Zhao, K. Ryu, C. Zhou, J. F. Stoddart and G. Gruner, *Advanced Materials*, **2008**, *20*, 939-946.

77. V. Biju, T. Itoh, Y. Baba and M. Ishikawa, *Journal of Physical Chemistry B*, **2006**, *110*, 26068-26074.

78. B. F. Pan, D. X. Cui, C. S. Ozkan, M. Ozkan, P. Xu, T. Huang, F. T. Liu, H. Chen, Q. Li, R. He and F. Gao, *Journal of Physical Chemistry C*, **2008**, *112*, 939-944.

79. N. Cho, K. R. Choudhury, R. B. Thapa, Y. Sahoo, T. Ohulchanskyy, A. N. Cartwright, K. S. Lee and P. N. Prasad, *Advanced Materials*, **2007**, *19*, 232-236.

80. D. M. Guldi, G. M. A. Rahman, V. Sgobba, N. A. Kotov, D. Bonifazi and M. Prato, *Journal of the American Chemical Society*, **2006**, *128*, 2315-2323.

81. X. L. Li, Y. Jia and A. Y. Cao, *Acs Nano*, **2010**, *4*, 506-512.

82. X. L. Li, Y. Jia, J. Q. Wei, H. W. Zhu, K. L. Wang, D. H. Wu and A. Y. Cao, *Acs Nano*, **2010**, *4*, 2142-2148.

83. B. J. Landi, S. L. Castro, H. J. Ruf, C. M. Evans, S. G. Bailey and R. P. Raffaelle, *Solar Energy Materials and Solar Cells*, **2005**, *87*, 733-746.

84. J. E. Weaver, M. R. Dasari, A. Datar, S. Talapatra and P. Kohli, *Acs Nano*, **2010**, *4*, 6883-6893.

85. Y. Wu, J. Xiang, C. Yang, W. Lu and C. M. Lieber, *Nature*, **2004**, *430*, 61-65.

86. Y. Y. Wu, R. Fan and P. D. Yang, *Nano Letters*, **2002**, *2*, 83-86.

87. E. C. Garnett and P. D. Yang, *Journal of the American Chemical Society*, **2008**, *130*, 9224-9225.

88. X. N. Wang, H. J. Zhu, Y. M. Xu, H. Wang, Y. Tao, S. Hark, X. D. Xiao and Q. A. Li, *Acs Nano*, **2010**, *4*, 3302-3308.

89. J. A. Goebl, R. W. Black, J. Puthussery, J. Giblin, T. H. Kosel and M. Kuno, *Journal of the American Chemical Society*, **2008**, *130*, 14822-14833.

90. Y. Huang, X. F. Duan, Q. Q. Wei and C. M. Lieber, *Science*, **2001**, *291*, 630-633.

91. D. J. Milliron, S. M. Hughes, Y. Cui, L. Manna, J. B. Li, L. W. Wang and A. P. Alivisatos, *Nature*, **2004**, *430*, 190-195.

92. G. Z. Shen, D. Chen and C. J. Lee, *Journal of Physical Chemistry B*, **2006**, *110*, 15689-15693.

93. M. S. Gudiksen, L. J. Lauhon, J. Wang, D. C. Smith and C. M. Lieber, *Nature*, **2002**, *415*, 617-620.

94. J. Wang, *Journal of Materials Chemistry*, **2008**, *18*, 4017-4020.

95. A. J. Mieszawska, R. Jalilian, G. U. Sumanasekera and F. P. Zamborini, *Small*, **2007**, *3*, 722-756.

96. H. J. Fan, M. Knez, R. Scholz, K. Nielsch, E. Pippel, D. Hesse, M. Zacharias and U. Gosele, *Nature Materials*, **2006**, *5*, 627-631.

97. F. Xu, V. Volkov, Y. M. Zhu, H. Y. Bai, A. Rea, N. V. Valappil, W. Su, X. Y. Gao, I. L. Kuskovsky and H. Matsui, *Journal of Physical Chemistry C*, **2009**, *113*, 19419-19423.

98. D. V. Talapin, R. Koeppe, S. Gotzinger, A. Kornowski, J. M. Lupton, A. L. Rogach, O. Benson, J. Feldmann and H. Weller, *Nano Letters*, **2003**, *3*, 1677-1681.

99. L. Wang, H. W. Wei, Y. J. Fan, X. Gu and J. H. Zhan, *Journal of Physical Chemistry C*, **2009**, *113*, 14119-14125.

100. C. J. Brumlik and C. R. Martin, *Journal of the American Chemical Society*, **1991**, *113*, 3174-3175.

101. C. R. Martin, *Science*, **1994**, *266*, 1961-1966.

102. B. K. Oh, S. Park, J. E. Millstone, S. W. Lee, K. B. Lee and C. A. Mirkin, *Journal of the American Chemical Society*, **2006**, *128*, 11825-11829.

103. B. R. Martin, D. J. Dermody, B. D. Reiss, M. M. Fang, L. A. Lyon, M. J. Natan and T. E. Mallouk, *Advanced Materials*, **1999**, *11*, 1021-1025.

104. D. J. Pena, J. K. N. Mbindyo, A. J. Carado, T. E. Mallouk, C. D. Keating, B. Razavi and T. S. Mayer, *Journal of Physical Chemistry B*, **2002**, *106*, 7458-7462.

105. S. Park, J. H. Lim, S. W. Chung and C. A. Mirkin, *Science*, **2004**, *303*, 348-351.

106. W. Zhu, G. Z. Wang, X. Hong and X. S. Shen, *Journal of Physical Chemistry C*, **2009**, *113*, 5450-5454.

107. P. K. Jain, L. Amirav, S. Aloni and A. P. Alivisatos, *Journal of the American Chemical Society*, **2010**, *132*, 9997-9999.

108. X. M. Shuai and W. Z. Shen, *The Journal of Physical Chemistry C*, **2011**, *115*, 6415-6422.

109. D. O. Demchenko, R. D. Robinson, B. Sadtler, C. K. Erdonmez, A. P. Alivisatos and L. W. Wang, *Acs Nano*, **2008**, *2*, 627-636.

110. R. D. Robinson, B. Sadtler, D. O. Demchenko, C. K. Erdonmez, L. W. Wang and A. P. Alivisatos, *Science*, **2007**, *317*, 355-358.

111. Y. T. Chong, D. Gorlitz, S. Martens, M. Y. E. Yau, S. Allende, J. Bachmann and K. Nielsch, *Advanced Materials*, **2010**, *22*, 2435-2439.

112. B. M. Kayes, H. A. Atwater and N. S. Lewis, *Journal of Applied Physics*, **2005**, *97*, 114302.

113. K. S. Leschkies, R. Divakar, J. Basu, E. Enache-Pommer, J. E. Boercker, C. B. Carter, U. R. Kortshagen, D. J. Norris and E. S. Aydil, *Nano Letters*, **2007**, *7*, 1793-1798.

114. L. E. Greene, M. Law, B. D. Yuhas and P. D. Yang, *Journal of Physical Chemistry C*, **2007**, *111*, 18451-18456.

115. M. Law, L. E. Greene, A. Radenovic, T. Kuykendall, J. Liphardt and P. D. Yang, *Journal of Physical Chemistry B*, **2006**, *110*, 22652-22663.

116. D. C. Lee, I. Robel, J. M. Pietryga and V. I. Klimov, *Journal of the American Chemical Society*, **2010**, *132*, 9960-9962.

117. D. D. Lin, H. Wu, R. Zhang, W. Zhang and W. Pan, *Journal of the American Ceramic Society*, **2010**, *93*, 3384-3389.

118. Z. Zhang, C. Shao, X. Li, C. Wang, M. Zhang and Y. Liu, *ACS Applied Materials & Interfaces*, **2010**, *2*, 2915-2923.

119. M. T. Niu, F. Huang, L. F. Cui, P. Huang, Y. L. Yu and Y. S. Wang, *Acs Nano*, **2010**, *4*, 681-688.

120. M. N. Moore, *Environment International*, **2006**, *32*, 967-976.

121. P. V. Kamat, R. Huehn and R. Nicolaescu, *Journal of Physical Chemistry B*, **2002**, *106*, 788-794.

122. M. Ovecka, I. Lang, F. Baluska, A. Ismail, P. Illes and I. K. Lichtscheidl, *Protoplasma*, **2005**, *226*, 39-54.

123. P. G. Barlow, K. Donaldson, J. MacCallum, A. Clouter and V. Stone, *Toxicology Letters*, **2005**, *155*, 397-401.

124. C. Ispas, D. Andreescu, A. Patel, D. V. Goia, S. Andreescu and K. N. Wallace, *Environmental Science & Technology*, **2009**, *43*, 6349-6356.

125. C. Carlson, S. M. Hussain, A. M. Schrand, L. K. Braydich-Stolle, K. L. Hess, R. L. Jones and J. J. Schlager, *Journal of Physical Chemistry B*, **2008**, *112*, 13608-13619.

126. A. Simon-Deckers, S. Loo, M. Mayne-L'Hermite, N. Herlin-Boime, N. Menguy, C. Reynaud, B. Gouget and M. Carriere, *Environmental Science & Technology*, **2009**, *43*, 8423-8429.

127. J. L. Elechiguerra, J. L. Burt, J. R. Morones, A. Camacho-Bragado, X. Gao, H. H. Lara and M. J. Yacaman, *Journal of nanobiotechnology*, **2005**, *3*, 1-6.

128. T. Mironava, M. Hadjiargyrou, M. Simon, V. Jurukovski and M. H. Rafailovich, *Nanotoxicology*, **2010**, *4*, 120-137.

129. E. V. Basiuk, O. E. Ochoa-Olmos and L. F. De la Mora-Estrada, *Journal of Nanoscience and Nanotechnology*, **2011**, *11*, 3016-3038.

130. X. S. Zhu, L. Zhu, Z. H. Duan, R. Q. Qi, Y. Li and Y. P. Lang, *Journal of Environmental Science and Health Part a-Toxic/Hazardous Substances & Environmental Engineering*, **2008**, *43*, 278-284.

131. L. K. Limbach, P. Wick, P. Manser, R. N. Grass, A. Bruinink and W. J. Stark, *Environmental Science & Technology*, **2007**, *41*, 4158-4163.

132. E. Navarro, F. Piccapietra, B. Wagner, F. Marconi, R. Kaegi, N. Odzak, L. Sigg and R. Behra, *Environmental Science & Technology*, **2008**, *42*, 8959-8964.

133. N. S. Fisher, G. J. Jones and D. M. Nelson, *Journal of Experimental Marine Biology and Ecology*, **1981**, *51*, 37-56.

134. T. Li, B. Albee, M. Alemayehu, R. Diaz, L. Ingham, S. Kamal, M. Rodriguez and S. W. Bishnoi, *Analytical and Bioanalytical Chemistry*, **2010**, *398*, 689-700.

135. R. J. Griffitt, J. Luo, J. Gao, J. C. Bonzongo and D. S. Barber, *Environmental Toxicology and Chemistry*, **2008**, *27*, 1972-1978.

136. V. K. Sharma, *Journal of Environmental Science and Health Part a-Toxic/Hazardous Substances & Environmental Engineering*, **2009**, *44*, 1485-1495.

137. A. R. Petosa, D. P. Jaisi, I. R. Quevedo, M. Elimelech and N. Tufenkji, *Environmental Science & Technology*, **2010**, *44*, 6532-6549.

138. J. Liu, D. M. Aruguete, M. Murayama and M. F. Hochella, *Environmental Science & Technology*, **2009**, *43*, 8178-8183.

139. T. D. Zaveri, N. V. Dolgova, B. H. Chu, J. Y. Lee, J. E. Wong, T. P. Lele, F. Ren and B. G. Keselowsky, *Biomaterials*, **2010**, *31*, 2999-3007.

140. V. Aruoja, H. C. Dubourguier, K. Kasemets and A. Kahru, *Science of the Total Environment*, **2009**, *407*, 1461-1468.

141. N. Chopra, M. Majumder and B. J. Hinds, *Advanced Functional Materials*, **2005**, *15*, 858-864.

142. M. S. Raghuveer, A. Kumar, M. J. Frederick, G. P. Louie, P. G. Ganesan and G. Ramanath, *Advanced Materials*, **2006**, *18*, 547-552.

143. K. Kurppa, H. Jiang, G. R. Szilvay, A. G. Nasibulin, E. L. Kauppinen and M. B. Linder, *Angewandte Chemie-International Edition*, **2007**, *46*, 6446-6449.

144. S. Banerjee and S. S. Wong, *Journal of the American Chemical Society*, **2003**, *125*, 10342-10350.

145. B. V. Enustun and J. Turkevich, *Journal of the American Chemical Society*, **1963**, *85*, 3317-3328.

146. E. M. Boatman, G. C. Lisensky and K. J. Nordell, *Journal of Chemical Education*, **2005**, *82*, 1697-1699.

147. X. H. Li, J. L. Niu, J. Zhang, H. L. Li and Z. F. Liu, *Journal of Physical Chemistry B*, **2003**, *107*, 2453-2458.

148. S. Banerjee and S. S. Wong, *Journal of Physical Chemistry B*, **2002**, *106*, 12144-12151.

149. S. Banerjee and S. S. Wong, *Nano Letters*, **2004**, *4*, 1445-1450.

150. L. C. Teague, S. Banerjee, S. S. Wong, C. A. Richter, B. Varughese and J. D. Batteas, *Chemical Physics Letters*, **2007**, *442*, 354-359.

151. T. Hemraj-Benny, T. J. Bandosz and S. S. Wong, *Journal of Colloid and Interface Science*, **2008**, *317*, 375-382.

152. H. Hiura, T. W. Ebbesen and K. Tanigaki, *Advanced Materials*, **1995**, *7*, 275-276.

153. S. Ravindran, S. Chaudhary, B. Colburn, M. Ozkan and C. S. Ozkan, *Nano Letters*, **2003**, *3*, 447-453.

154. J. Aldana, Y. A. Wang and X. G. Peng, *Journal of the American Chemical Society*, **2001**, *123*, 8844-8850.

155. J. Zhang, H. L. Zou, Q. Qing, Y. L. Yang, Q. W. Li, Z. F. Liu, X. Y. Guo and Z. L. Du, *Journal of Physical Chemistry B*, **2003**, *107*, 3712-3718.

156. S. Banerjee and S. S. Wong, *Chemical Communications*, **2004**, 1866-1867.

157. J. Liu, A. G. Rinzler, H. J. Dai, J. H. Hafner, R. K. Bradley, P. J. Boul, A. Lu, T. Iverson, K. Shelimov, C. B. Huffman, F. Rodriguez-Macias, Y. S. Shon, T. R. Lee, D. T. Colbert and R. E. Smalley, *Science*, **1998**, *280*, 1253-1256.

158. S. Liao, Y. Shnidman and A. Ulman, *Journal of the American Chemical Society*, **2000**, *122*, 3688-3694.

159. G. K. Kouassi and J. Irudayaraj, *journal of Nanobiotechnology*, **2006**, *4*, 1-10.

160. J. Aldana, N. Lavelle, Y. J. Wang and X. G. Peng, *Journal of the American Chemical Society*, **2005**, *127*, 2496-2504.

161. M. Olek, T. Busgen, M. Hilgendorff and M. Giersig, *Journal of Physical Chemistry B*, **2006**, *110*, 12901-12904.

162. I. Robel, B. A. Bunker and P. V. Kamat, *Advanced Materials*, **2005**, *17*, 2458-2463.

163. A. Kongkanand, R. M. Dominguez and P. V. Kamat, *Nano Letters*, **2007**, *7*, 676-680.

164. F. Vietmeyer, B. Seger and P. V. Kamat, *Advanced Materials*, **2007**, *19*, 2935-2940.

165. M. Kondon, J. Kim, N. Udawatte and D. Lee, *Journal of Physical Chemistry C*, **2008**, *112*, 6695-6699.

166. R. Costi, A. E. Saunders, E. Elmalem, A. Salant and U. Banin, *Nano Letters*, **2008**, *8*, 637-641.

167. Y. Tison, C. E. Giusca, V. Stolojan, Y. Hayashi and S. R. P. Silva, *Advanced Materials*, **2008**, *20*, 189-194.

168. A. Hashimoto, K. Suenaga, K. Urita, T. Shimada, T. Sugai, S. Bandow, H. Shinohara and S. Iijima, *Physical Review Letters*, **2005**, *94*, 045504/045501-045504.

169. R. Saito, R. Matsuo, T. Kimura, G. Dresselhaus and M. S. Dresselhaus, *Chemical Physics Letters*, **2001**, *348*, 187-193.

170. R. Pfeiffer, C. Kramberger, F. Simon, H. Kuzmany, V. N. Popov and H. Kataura, *European Physical Journal B*, **2004**, *42*, 345-350.

171. R. Pfeiffer, H. Kuzmany, C. Kramberger, C. Schaman, T. Pichler, H. Kataura, Y. Achiba, J. Kurti and V. Zolyomi, *Physical Review Letters*, **2003**, *90*, 225501/225501-225504.

172. M. Endo, H. Muramatsu, T. Hayashi, Y. A. Kim, M. Terrones and N. S. Dresselhaus, *Nature*, **2005**, *433*, 476-476.

173. B. Ha, D. H. Shin, J. Park and C. J. Lee, *Journal of Physical Chemistry C*, **2008**, *112*, 430-435.

174. Y. W. Son, S. Oh, J. Ihm and S. Han, *Nanotechnology*, **2005**, *16*, 125-128.

175. Y. H. Ho, C. P. Chang, F. L. Shyu, R. B. Chen, S. C. Chen and M. F. Lin, *Carbon*, **2004**, *42*, 3159-3167.

176. I. Maeng, C. Kang, S. J. Oh, J. H. Son, K. H. An and Y. H. Lee, *Applied Physics Letters*, **2007**, *90*, 051914/051911-051913.

177. F. Villalpando-Paez, H. Son, D. Nezich, Y. P. Hsieh, J. Kong, Y. A. Kim, D. Shimamoto, H. Muramatsu, T. Hayashi, M. Endo, M. Terrones and M. S. Dresselhaus, *Nano Letters*, **2008**, *8*, 3879-3886.

178. G. W. Ho, Y. H. Ho, T. S. Li, C. P. Chang and M. F. Lin, *Carbon*, **2006**, *44*, 2323-2329.

179. S. P. Somani, P. R. Somani, E. Flahaut, G. Kalita and M. Umeno, *Japanese Journal of Applied Physics*, **2008**, *47*, 1219-1222.

180. Y. Jia, J. Q. Wei, K. L. Wang, A. Y. Cao, Q. K. Shu, X. C. Gui, Y. Q. Zhu, D. M. Zhuang, G. Zhang, B. B. Ma, L. D. Wang, W. J. Liu, Z. C. Wang, J. B. Luo and D. Wu, *Advanced Materials*, **2008**, *20*, 4594-4598.

181. Y. C. Jung, D. Shimamoto, H. Muramatsu, Y. A. Kim, T. Hayashi, M. Terrones and M. Endo, *Advanced Materials*, **2008**, *20*, 4509-4512.

182. R. B. Koizhaiganova, H. J. Kim, T. Vasudevan and M. S. Lee, *Synthetic Metals*, **2009**, *159*, 2437-2442.

183. H. Muramatsu, Y. A. Kim, T. Hayashi, M. Endo, A. Yonemoto, H. Arikai, F. Okino and H. Touhara, *Chemical Communications*, **2005**, 2002-2004.

184. T. Hayashi, D. Shimamoto, Y. A. Kim, H. Muramatsu, F. Okino, H. Touhara, T. Shimada, Y. Miyauchi, S. Maruyama, M. Terrones, M. S. Dresselhaus and M. Endo, *Acs Nano*, **2008**, *2*, 485-488.

185. Y. A. Kim, H. Muramatsu, K. C. Park, D. Shimamoto, Y. C. Jung, J. H. Kim, T. Hayashi, Y. Saito, M. Endo, M. Terrones and M. S. Dresselhaus, *Applied Physics Letters*, **2008**, *93*, 051901/051901-051903.

186. S. Banerjee and S. S. Wong, *Chem. Commun.*, **2004**, 1866-1867.

187. Y. Liu, M. A. Summers, C. Edder, J. M. J. Fréchet and M. D. McGehee, *Advanced Materials*, **2005**, *17*, 2960-2964.

188. R. S. Dibbell and D. F. Watson, *Journal of Physical Chemistry C*, **2009**, *113*, 3139-3149.

189. T. Murakami, K. Matsumoto, K. Kisoda, R. Naito, K. Nishio, T. Isshiki and H. Harima, *Journal of Applied Physics*, **2008**, *103*, 114305/114301-114308

190. T. Sugai, H. Yoshida, T. Shimada, T. Okazaki and H. Shinohara, *Nano Letters*, **2003**, *3*, 769-773.

191. H. Muramatsu, T. Hayashi, Y. A. Kim, D. Shimamoto, Y. J. Kim, K. Tantrakarn, M. Endo, M. Terrones and M. S. Dresselhaus, *Chemical Physics Letters*, **2005**, *414*, 444-448.

192. M. Jones, S. S. Lo and G. D. Scholes, *Proceedings of the National Academy of Sciences of the United States of America*, **2009**, *106*, 3011-3016.

193. S. F. Wuister, C. D. Donega and A. Meijerink, *Journal of Physical Chemistry B*, **2004**, *108*, 17393-17397.

194. P. P. Jha and P. Guyot-Sionnest, *ACS nano*, **2009**, *3*, 1011-1015.

195. D. E. Gomez, J. van Embden, P. Mulvaney, M. J. Fernee and H. Rubinsztein-Dunlop, *ACS nano*, **2009**, *3*, 2281-2287.

196. P. Spinicelli, S. Buil, X. Quelin, B. Mahler, B. Dubertret and J. P. Hermier, *Physical Review Letters*, **2009**, *102*, 136801.

197. C. A. Leatherdale, W. K. Woo, F. V. Mikulec and M. G. Bawendi, *Journal of Physical Chemistry B*, **2002**, *106*, 7619-7622.

198. E. Bakkers, A. W. Marsman, L. W. Jenneskens and D. Vanmaekelbergh, *Angewandte Chemie-International Edition*, **2000**, *39*, 2297-2299.

199. R. S. Dibbell, D. G. Youker and D. F. Watson, *Journal of Physical Chemistry C*, **2009**, *113*, 18643-18651.

200. R. S. Swathi and K. L. Sebastian, *Journal of Chemical Physics*, **2010**, *132*, 104502.

201. A. Govorov, G. Bryant, W. Zhang, T. Skeini, J. Lee, N. Kotov, J. Slocik and R. Naik, *Nano Lett*, **2006**, *6*, 984-994.

202. R. A. Marcus, *Journal of Chemical Physics*, **1965**, *43*, 679-701.

203. M. R. Wasielewski, *Chemical Reviews*, **1992**, *92*, 435-461.

204. M. A. Rampi and G. M. Whitesides, *Chemical Physics*, **2002**, *281*, 373-391.

205. J. F. Smalley, S. W. Feldberg, C. E. D. Chidsey, M. R. Linford, M. D. Newton and Y.-P. Liu, *The Journal of Physical Chemistry*, **1995**, *99*, 13141-13149.

206. A. Boulesbaa, Z. Q. Huang, D. Wu and T. Q. Lian, *Journal of Physical Chemistry C*, **2010**, *114*, 962-969.

207. W. A. Tisdale, Doctor of Philosophy, University of Minnesota, 2010.

208. Z.-J. Jiang and D. F. Kelley, *The Journal of Physical Chemistry C*, **2011**, *115*, 4594-4602.

209. K. Tvrdy, P. A. Frantsuzov and P. V. Kamat, *Proceedings of the National Academy of Sciences of the United States of America*, **2011**, *108*, 29-34.

210. K. Pettersson, J. Wiberg, T. Ljungdahl, J. Martensson and B. Albinsson, *Journal of Physical Chemistry A*, **2006**, *110*, 319-326.

211. E. Kucur, J. Riegler, G. A. Urban and T. Nann, *Journal of Chemical Physics*, **2003**, *119*, 2333-2337.

212. I. Robel, M. Kuno and P. V. Kamat, *Journal of the American Chemical Society*, **2007**, *129*, 4136-4137.

213. H. Ago, T. Kugler, F. Cacialli, W. R. Salaneck, M. S. P. Shaffer, A. H. Windle and R. H. Friend, *The Journal of Physical Chemistry B*, **1999**, *103*, 8116-8121.

214. R. Koole, P. Liljeroth, C. de Mello Donegá, D. Vanmaekelbergh and A. Meijerink, *Journal of the American Chemical Society*, **2006**, *128*, 10436-10441.

215. T. Dürkop, S. A. Getty, E. Cobas and M. S. Fuhrer, *Nano Letters*, **2003**, *4*, 35-39.

216. B. O. Dabbousi, J. RodriguezViejo, F. V. Mikulec, J. R. Heine, H. Mattoussi, R. Ober, K. F. Jensen and M. G. Bawendi, *Journal of Physical Chemistry B*, **1997**, *101*, 9463-9475.

217. Z. Chen, S. p. Berciaud, C. Nuckolls, T. F. Heinz and L. E. Brus, *ACS nano*, **2010**, *4*, 2964-2968.

218. J. Xiang, W. Lu, Y. J. Hu, Y. Wu, H. Yan and C. M. Lieber, *Nature*, **2006**, *441*, 489-493.

219. X. W. Teng, Q. Wang, P. Liu, W. Han, A. Frenkel, W. Wen, N. Marinkovic, J. C. Hanson and J. A. Rodriguez, *Journal of the American Chemical Society*, **2008**, *130*, 1093-1101.

220. X. W. Teng, M. Feygenson, Q. Wang, J. Q. He, W. X. Du, A. I. Frenkel, W. Q. Han and M. Aronson, *Nano Letters*, **2009**, *9*, 3177-3184.

221. Y. H. Lin, Y. C. Hsueh, P. S. Lee, C. C. Wang, J. R. Chen, J. M. Wu, T. P. Perng and H. C. Shih, *Journal of the Electrochemical Society*, **2010**, *157*, K206-K210.

222. Y. J. Dong, B. Z. Tian, T. J. Kempa and C. M. Lieber, *Nano Letters*, **2009**, *9*, 2183-2187.

223. Q. Kuang, Z. Y. Jiang, Z. X. Xie, S. C. Lin, Z. W. Lin, S. Y. Xie, R. B. Huang and L. S. Zheng, *Journal of the American Chemical Society*, **2005**, *127*, 11777-11784.

224. R. He, M. Law, R. Fan, F. Kim and P. Yang, *Nano Letters*, **2002**, *2*, 1109-1112.

225. C. L. Zhu, M. L. Zhang, Y. J. Qiao, G. Xiao, F. Zhang and Y. J. Chen, *The Journal of Physical Chemistry C*, **2010**, *114*, 16229-16235.

226. J. Jun, C. Jin, H. Kim, S. Park and C. Lee, *Applied Surface Science*, **2009**, *255*, 8544-8550.

227. K. Nagashima, T. Yanagida, H. Tanaka, S. Seki, A. Saeki, S. Tagawa and T. Kawai, *Journal of the American Chemical Society*, **2008**, *130*, 5378-5382.

228. A. Datta, S. K. Panda and S. Chaudhuri, *The Journal of Physical Chemistry C*, **2007**, *111*, 17260-17264.

229. J. Cao, J.-Z. Sun, H.-Y. Li, J. Hong and M. Wang, *Journal of Materials Chemistry*, **2004**, *14*, 1203-1206.

230. X. Q. Meng, H. Peng, Y. Q. Gai and J. Li, *The Journal of Physical Chemistry C*, **2009**, *114*, 1467-1471.

231. J. M. Wu, *Journal of Physical Chemistry C*, **2008**, *112*, 13192-13199.

232. J. Hu, Y. Bando, Z. Liu, T. Sekiguchi, D. Golberg and J. Zhan, *Journal of the American Chemical Society*, **2003**, *125*, 11306-11313.

233. S. Ramakrishna, R. Jose, P. S. Archana, A. S. Nair, R. Balamurugan, J. Venugopal and W. E. Teo, *Journal of Materials Science*, **2010**, *45*, 6283-6312.

234. A. K. Moghe and B. S. Gupta, *Polymer Reviews*, **2008**, *48*, 353-377.

235. S. K. Choi, S. Kim, S. K. Lim and H. Park, *The Journal of Physical Chemistry C*, **2010**, *114*, 16475-16480.

236. V. Thavasi, G. Singh and S. Ramakrishna, *Energy & Environmental Science*, **2008**, *1*, 205-221.

237. Y. Z. Zhang, X. Wang, Y. Feng, J. Li, C. T. Lim and S. Ramakrishna, *Biomacromolecules*, **2006**, *7*, 1049-1057.

238. H. L. Jiang, Y. Q. Hu, Y. Li, P. C. Zhao, K. J. Zhu and W. L. Chen, *Journal of Controlled Release*, **2005**, *108*, 237-243.

239. Y. Yu, L. Gu, C. B. Zhu, P. A. van Aken and J. Maier, *Journal of the American Chemical Society*, **2009**, *131*, 15984-15985.

240. M. R. Hoffmann, S. T. Martin, W. Choi and D. W. Bahnemann, *Chemical Reviews*, **1995**, *95*, 69-96.

241. L. R. Hou, C. Z. Yuan and Y. Peng, *Journal of Hazardous materials*, **2007**, *139*, 310-315.

242. Z. Liu, D. D. Sun, P. Guo and J. O. Leckie, *Nano Letters*, **2006**, *7*, 1081-1085.

243. Y. Zhao, J. Liu, L. Y. Shi, S. A. Yuan, J. H. Fang, Z. Y. Wang and M. H. Zhang, *Applied Catalysis B-Environmental*, **2010**, *100*, 68-76.

244. K. Vinodgopal, I. Bedja and P. V. Kamat, *Chemistry of Materials*, **1996**, *8*, 2180-2187.

245. S. C. Ray, M. K. Karanjai and D. DasGupta, *Surface & Coatings Technology*, **1998**, *102*, 73-80.

246. Y. Liu, E. Koep and M. L. Liu, *Chemistry of Materials*, **2005**, *17*, 3997-4000.

247. D. G. Shchukin and R. A. Caruso, *Advanced Functional Materials*, **2003**, *13*, 789-794.

248. J. Li and H. C. Zeng, *Journal of the American Chemical Society*, **2007**, *129*, 15839-15847.

249. K. K. Akurati, A. Vital, R. Hany, B. Bommer, T. Graule and M. Winterer, *International Journal of Photoenergy*, **2005**, *7*, 153-161.

250. S. F. Chen, L. Chen, S. Gao and G. Y. Cao, *Materials Chemistry and Physics*, **2006**, *98*, 116-120.

251. D. Li and Y. N. Xia, *Nano Letters*, **2004**, *4*, 933-938.

252. Y. Q. Cao, T. He, L. S. Zhao, E. J. Wang, W. S. Yang and Y. A. Cao, *Journal of Physical Chemistry C*, **2009**, *113*, 18121-18124.

253. B. Liu and E. S. Aydil, *Journal of the American Chemical Society*, **2009**, *131*, 3985-3990.

254. D. Li, J. T. McCann and Y. N. Xia, *Small*, **2005**, *1*, 83-86.

255. I. Robel, V. Subramanian, M. Kuno and P. V. Kamat, *Journal of the American Chemical Society*, **2006**, *128*, 2385-2393.

256. J. E. Díaz, A. Barrero, M. Márquez and I. G. Loscertales, *Advanced Functional Materials*, **2006**, *16*, 2110-2116.

257. O. K. Varghese, M. Paulose and C. A. Grimes, *Nature Nanotechnology*, **2009**, *4*, 592-597.

258. J. R. Jennings, A. Ghicov, L. M. Peter, P. Schmuki and A. B. Walker, *Journal of the American Chemical Society*, **2008**, *130*, 13364-13372.

259. M.-S. Park, Y.-M. Kang, G.-X. Wang, S.-X. Dou and H.-K. Liu, *Advanced Functional Materials*, **2008**, *18*, 455-461.

260. N. G. Park, J. van de Lagemaat and A. J. Frank, *Journal of Physical Chemistry B*, **2000**, *104*, 8989-8994.

261. H. Wu, R. Zhang, X. X. Liu, D. D. Lin and W. Pan, *Chemistry of Materials*, **2007**, *19*, 3506-3511.

262. J. L. Elechiguerra, J. L. Burt, J. R. Morones, A. Camacho-Bragado, X. Gao, H. H. Lara and M. J. Yacaman, *Journal of nanobiotechnology*, **2005**, *3*, 6.

263. H. Yang, C. Liu, D. F. Yang, H. S. Zhang and Z. G. Xi, *Journal of Applied Toxicology*, **2009**, *29*, 69-78.

264. R. F. Hamilton, N. Q. Wu, D. Porter, M. Buford, M. Wolfarth and A. Holian, *Particle and Fibre Toxicology*, **2009**, *6*, 35.

265. J. Chen, H. Zhou, A. C. Santulli and S. S. Wong, *Chemical Research in Toxicology*, **2010**, *23*, 871-879.

266. M. J. Osmond and M. J. McCall, *Nanotoxicology*, **2010**, *4*, 15-41.

267. N. M. Franklin, N. J. Rogers, S. C. Apte, G. E. Batley, G. E. Gadd and P. S. Casey, *Environmental Science & Technology*, **2007**, *41*, 8484-8490.

268. M. Heinlaan, A. Ivask, I. Blinova, H. C. Dubourguier and A. Kahru, *Chemosphere*, **2008**, *71*, 1308-1316.

269. R. J. Miller, H. S. Lenihan, E. B. Muller, N. Tseng, S. K. Hanna and A. A. Keller, *Environmental Science & Technology*, **2010**, *44*, 7329-7334.

270. A.-J. Miao, X.-Y. Zhang, Z. Luo, C.-S. Chen, W.-C. Chin, P. H. Santschi and A. Quigg, *Environ Toxicol Chem*, **2010**, *29*, 2814-2822.

271. P. Borm, F. C. Klaessig, T. D. Landry, B. Moudgil, J. Pauluhn, K. Thomas, R. Trottier and S. Wood, *Toxicological Sciences*, **2006**, *90*, 23-32.

272. Z. Chen, M. Waje, W. Li and Y. Yan, *Angewandte Chemie International Edition*, **2007**, *46*, 4060-4063.

273. E. A. Meulenkamp, *Journal of Physical Chemistry B*, **1998**, *102*, 7764-7769.

274. X. S. Zhu, J. X. Wang, X. Z. Zhang, Y. Chang and Y. S. Chen, *Nanotechnology*, **2009**, *20*, 195103.

275. W. Jiang, H. Mashayekhi and B. S. Xing, *Environmental Pollution*, **2009**, *157*, 1619-1625.

276. R. Brayner, R. Ferrari-Iliou, N. Brivois, S. Djediat, M. F. Benedetti and F. Fievet, *Nano Letters*, **2006**, *6*, 866-870.

277. C. Pacholski, A. Kornowski and H. Weller, *Angewandte Chemie International Edition*, **2002**, *41*, 1188-1191.

278. B. Liu and H. C. Zeng, *Langmuir*, **2004**, *20*, 4196-4204.

279. S. Nair, A. Sasidharan, V. V. D. Rani, D. Menon, S. Nair, K. Manzoor and S. Raina, *Journal of Materials Science: Materials in Medicine*, **2009**, *20*, 235-241.

280. R. R. Guillard and J. H. Ryther, *Canadian Journal of Microbiology*, **1962**, *8*, 229-239.

281. N. S. Fisher, M. Bohe and J. L. Teyssie, *Marine Ecology-Progress Series*, **1984**, *18*, 201-213.

282. L. K. Adams, D. Y. Lyon and P. J. J. Alvarez, *Water Research*, **2006**, *40*, 3527-3532.

283. P. Costa, J. Manuel and S. Lobo, *European Journal of Pharmaceutical Sciences*, **2001**, *13*, 123-133.

284. S. W. Y. Wong, P. T. Y. Leung, A. B. Djurisic and K. M. Y. Leung, *Analytical and Bioanalytical Chemistry*, **2010**, *396*, 609-618.

285. E. M. Wong, J. E. Bonevich and P. C. Searson, *Journal of Physical Chemistry B*, **1998**, *102*, 7770-7775.

286. N. S. Fisher, R. R. L. Guillard and D. C. Bankston, *Journal of Marine Research*, **1991**, *49*, 339-354.

287. K. H. Müller, J. Kulkarni, M. Motskin, A. Goode, P. Winship, J. N. Skepper, M. P. Ryan and A. E. Porter, *ACS Nano*, **2010**, *4*, 6767-6779.

288. T. Xia, M. Kovochich, M. Liong, L. Madler, B. Gilbert, H. B. Shi, J. I. Yeh, J. I. Zink and A. E. Nel, *ACS Nano*, **2008**, *2*, 2121-2134.

289. D. H. Lin and B. S. Xing, *Environmental Science & Technology*, **2008**, *42*, 5580-5585.

290. Z. Pipan-Tkalec, D. Drobne, A. Jemec, T. Romih, P. Zidar and M. Bele, *Toxicology*, **2010**, *269*, 198-203.

291. M. C. Hanna and A. J. Nozik, *Journal of Applied Physics*, **2006**, *100*, 074510.

292. R. T. Ross and A. J. Nozik, *Journal of Applied Physics*, **1982**, *53*, 3813-3818.